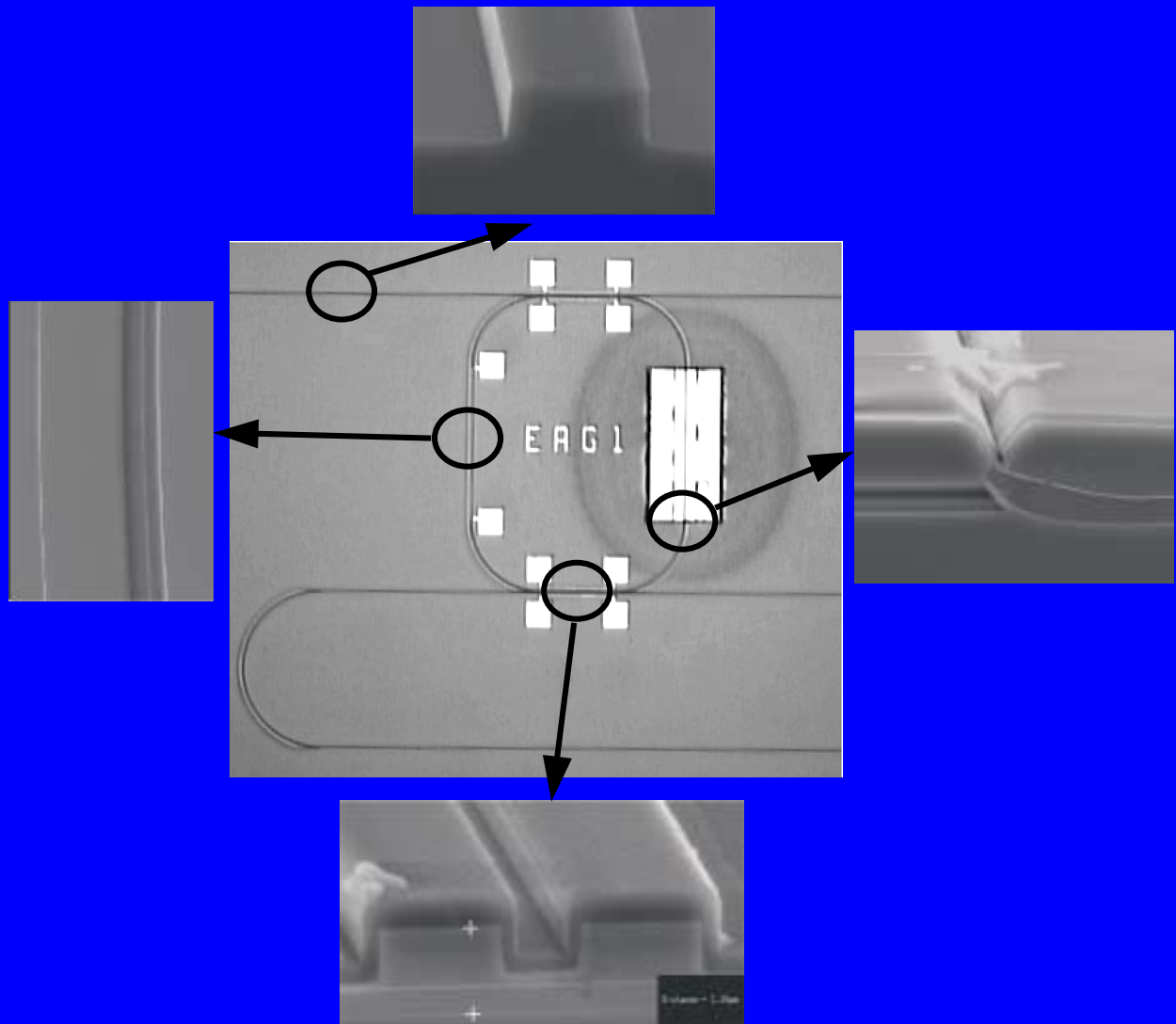


# **Realization of Optical Filters using Ring Resonators with integrated Semiconductor Optical Amplifiers in GaInAsP / InP**



**Dominik G. Rabus**



**Realization of Optical Filters using Ring Resonators  
with integrated Semiconductor Optical Amplifiers  
in GaInAsP / InP**

*vorgelegt von*

*Dipl.-Ing. Dominik G. Rabus*

*Vom Fachbereich IV -*

*Elektrotechnik und Informatik*

*der Technischen Universität Berlin*

*zur Erlangung des akademischen Grades*

*Doktor-Ingenieur*

*Dr.-Ing.*

*genehmigte Dissertation*

*Promotionsausschuss:*

*Vorsitzender: Prof. Dr.-Ing. Klar*

*Berichter: Prof. Dr.-Ing. Petermann*

*Berichter: Prof. Dr. rer. nat. Weber*

*Tag der wissenschaftlichen Aussprache:*

*05.07.2002*

*Berlin 2002*



Hinter der nächsten Biegung gleich  
Ein Tor führt ins geheime Reich  
Und ging ich oft auch dran vorbei  
Es kommt ein Tag, da steht mir frei  
Der Weg, den es zu gehen lohnt,  
Östlich der Sonn, westlich vom Monday

*J. R. R. Tolkien*

Still round the corner there may wait  
A new road or a secret gate;  
And though I oft have passed them by,  
a day will come at last when I  
shall take the hidden paths that run  
West of the Moon, East of the Sun.

*J. R. R. Tolkien*



## Zusammenfassung

Eine Schlüsselkomponente in einem optischen Netzwerk ist das optische Filter. Es gibt mehrere Arten von optischen Filtern, zum Beispiel Bragg – Gitter, Dünnschichtfilter, arrayed waveguide gratings (AWGs). Ein optisches Filter, dass in den letzten Jahren in der integrierten Optik hervorgetreten ist und welches in dieser Arbeit entworfen und untersucht wird auf der Basis von GaInAsP / InP, ist der **Ringresonator**. Filter auf der Basis von Ringresonatoren benötigen keine Spiegel oder Gitter für die optische Rückkopplung und eignen sich deshalb hervorragend für die monolithische Integration mit anderen Komponenten wie z. B. Laser und Photodetektoren.

Ein Filter mit einem benötigten bestimmten Transmissionsverhalten kann mit Hilfe mehrfach seriell oder parallel gekoppelter Ringresonatoren erreicht werden.

### ANFORDERUNGEN:

- Die Herstellung von Ringresonatoren in der integrierten Optik erfordert niedrig dämpfende, stark geführte Wellenleiter für die Realisierung kleiner Krümmungsradien ( $R \approx 100 \mu\text{m}$ ).
- Abstimmbarkeit ist essenziell für die Systemanwendung von optischen Filtern. Im Fall periodischer Filter, in unserem Fall Ringresonatoren, ist es wichtig das Transmissionsverhalten des Filters an ein bestimmtes Kanalaraster anzupassen (z. B. ITU - Raster).
- Die Filtereigenschaften passiver Ringresonatoren werden durch die internen Verluste eingeschränkt. Die Integration eines optischen Halbleiterverstärkers (SOA) ermöglicht nicht nur die Kompensation der internen Verluste, sondern auch zusätzliche Funktionalität (z. B. Schaltbarkeit).

### HERGESTELLTE BAUELEMENTE:

- **Passive einfache Ringresonatoren und Doppelringresonatoren** im Materialsystem GaInAsP / InP in der Form von Stadien, gekoppelt an Multimodeinterferenzkoppler (MMI) oder an Kodirektionalkoppler mit Radien von  $R = 100 \mu\text{m} - 200 \mu\text{m}$  und einem freien Spektralbereich (FSR) von 50 GHz und 100 GHz und On-Off Verhältnissen von mehr als 20 dB wurden realisiert.
- **Einfache Ringresonatoren und Dreifachringresonatoren** mit integrierten optischen **Halbleiterverstärkern** (Verstärkerlänge =  $100 \mu\text{m} - 800 \mu\text{m}$ ), gekoppelt an zwei Eingangs- und Ausgangswellenleiter unter der Verwendung von Kodirektionalkopplern mit Radien von  $R = 100 \mu\text{m} - 800 \mu\text{m}$  werden präsentiert. Die internen Verluste werden vollständig durch die Halbleiterverstärker ausgeglichen und On-Off Verhältnisse für den Durchgangskanal sowie für den Dropkanal von mehr als 20 dB wurden erreicht. Die Ringresonatoren besitzen einen freien Spektralbereich von 12,5 GHz, 25 GHz and 50 GHz.

■ Die **Abstimmbarkeit** auf eine bestimmte Wellenlänge sowie die **Resonanzanpassung** der Doppel- und Dreifachringresonatoren konnte mit Hilfe von integrierten **Platinwiderständen** erreicht werden.

■ Das Transmissionsverhalten hängt sehr von der Stärke der Interaktion der beteiligten Ringresonatoren untereinander und mit den verwendeten Kopplern ab. Eine Designregel wird beschrieben um ein quasi rechteckiges Transmissionsverhalten durch Verwendung von Doppel- und Dreifachringresonatoren zu erreichen.

⇒ Das Verhalten der hergestellten Bauelemente wird hinsichtlich ihrer Einfügedämpfung, Polarisationsabhängigkeit, Funktionalität und Einsatzmöglichkeit analysiert.





## Abstract

A key device in all-optical networks is the optical filter. There are different types of optical filters, for example, Bragg gratings, thin film filters, arrayed waveguide gratings (AWGs). An optical filter which has emerged in the last few years in integrated optics and which is designed and investigated on the basis of GaInAsP / InP in this thesis is the **ring resonator filter**. Ring resonator filters do not require facets or gratings for optical feedback and are thus particularly suited for monolithic integration with other components such as lasers and photodetectors for example.


A required passband shape of ring resonator filters can be custom designed by the use of multiple serial or parallel coupled resonators.


### REQUIREMENTS:

- The realization of ring resonators in integrated optics requires low loss waveguides with a strong confinement to achieve low bending radii ( $R \approx 100 \mu\text{m}$ ).
- Tuneability is essential for the system application of optical filters. In the case of periodic filters, in our case ring resonators, it is important to fit the transmission curve to the defined channel spacing (e.g. ITU-grid).
- The performance of passive ring resonators for filter applications is limited by internal losses. The incorporation of a semiconductor optical amplifier (SOA) enables additional functionality (e. g. switchability) including the compensation of internal losses.

### REALIZED DEVICES:

- **Passive single and double ring resonators** in the material system GaInAsP / InP in the form of racetracks, coupled to a multimode interference (MMI) coupler or a codirectional coupler (CC) with radii of  $R = 100 \mu\text{m} - 200 \mu\text{m}$  and free spectral ranges (FSRs) of 50 GHz and 100 GHz and on-off ratios of more than 20 dB are realized.
- **Single and triple ring resonators** with integrated SOAs (length =  $100 \mu\text{m} - 800 \mu\text{m}$ ), coupled to two input/output waveguides using codirectional couplers with radii of  $R = 100 \mu\text{m} - 800 \mu\text{m}$  are demonstrated. The ring losses are compensated by the SOA and an on-off ratio for the throughput and drop port of more than 20 dB is realized. The achieved free spectral range is 12.5 GHz, 25 GHz and 50 GHz.

 The **tuning** to a specific wavelength and the **resonance matching** of the double and triple ring resonators is demonstrated by using integrated **Pt – resistors**.

 The passband shape depends sensitively on the relative interactions between all resonators and the used couplers. In order to achieve a **box-like filter response**, a general design rule is developed for engineering definite filter shapes using **double** and **triple coupled ring resonators**.

⇒ *The performance of the devices is analyzed with respect to insertion loss, polarization dependence, functionality and application.*



## Acknowledgment

This work was performed at the Heinrich-Hertz-Institut für Nachrichtentechnik Berlin GmbH. First of all I thank M. Hamacher, H. Heidrich and U. Troppenz, H. Venghaus for their valuable support and helpful discussions which have enabled the realization of this thesis.

Further I would like to thank my roommates S. Fidorra, R. Stenzel and B. Hüttl, F. Boczianowski and my former roommates H. Bünning and H. Stolpe for their support and fruitful discussions and for creating a wonderful working atmosphere.

This work would not have been possible without the help and knowledge of my colleagues at the Heinrich-Hertz-Institute and their willingness and openness for discussions, especially P. Albrecht (optical measurement), R. Kaiser (“my famous teacher”), K. Janiak (reactive ion etching), W. Rehbein (optical measurement), J. Kreißl (laser fabrication), F. Fidorra (former project leader), G. Wache (draughtswoman), T. Gaertner and R. Türrck (anti reflection coating), W. Fürst (CAD mask design), M. Gravert and C. M. Weinert (finite difference and waveguide modeling software), C. Weimann (SEM and AFM), R. Steingrüber (electron beam writing), H. Schroeter-Janssen (SAMOVPE), F. Reier and H. Barsch (Epitaxy), I. Tiedke, Ch. Schulz, B. Reinsperger (Photolithography), K. Schweers and U. Knospe (secretary).

I would like to thank E. V. K. Rao and Y. Gottesman from France Telecom for performing the OLCR measurements.

Being a PhD student is not always an easy task and it is therefore important to have “fellow-sufferers” not only for helpful talks, beer drinking and badminton but for everything else which helps in accomplishing the “goal”. I therefore thank T. Tekin, O. Brox, R. Hauße, U. Siebel and L. Zei very much.

I would like to take this opportunity in thanking my parents and my sister who always believed in their son and brother which is a precious gift and gives tremendous motivation. Further I would like to thank my "big brother" Wolfram and my "big sister" Gabriele for their overwhelming support.

This work would not have been fulfilled without the patience, support, help and motivation of my beloved fiancée Regina.

Last but not least I would like to thank Prof. Dr. K. Petermann (TU - Berlin) for his valuable discussions and for supporting this thesis and Prof. Dr. H. G. Weber (HHI) for his willingness to supervise this thesis.



<b>1</b>	<b>INTRODUCTION .....</b>	<b>1</b>
1.1	THE OPTICAL NETWORK.....	1
1.1.1	<i>Optical filters.....</i>	3
1.2	THE RING RESONATOR - HISTORY.....	7
1.2.1	<i>Applications.....</i>	9
<b>2</b>	<b>COUPLED RING RESONATORS - THEORY AND SIMULATION MODEL .....</b>	<b>15</b>
2.1	INTRODUCTION .....	15
2.2	SYNTHESIS OF OPTICAL FILTERS USING RING RESONATORS.....	17
2.2.1	<i>Z - transform analysis of a ring resonator optical filter.....</i>	17
2.3	RING RESONATORS – THE USED MODEL .....	21
2.3.1	<i>The single ring resonator (SRR).....</i>	21
2.3.2	<i>The double ring resonator (DRR).....</i>	31
2.3.3	<i>The triple ring resonator (TRR).....</i>	36
<b>3</b>	<b>THE MATERIAL SYSTEM GaInAsP / InP .....</b>	<b>41</b>
3.1	THE QUATERNARY SEMICONDUCTOR COMPOUND GaInAsP .....	41
3.2	DISPERSION .....	43
3.2.1	<i>Dispersion in GaInAsP / InP .....</i>	44
<b>4</b>	<b>THE BUILDING BLOCKS OF THE RING RESONATOR .....</b>	<b>45</b>
4.1	THE WAVEGUIDE .....	45
4.1.1	<i>Concept of a strong guiding waveguide .....</i>	45
4.1.2	<i>The waveguide in the curvature.....</i>	49
4.1.3	<i>Fabrication of the waveguide .....</i>	53
4.2	THE MEASUREMENT METHOD .....	59
4.2.1	<i>The standard measurement setup for the characterization of the devices .....</i>	59
4.2.2	<i>The OLCR measurement setup .....</i>	60
4.2.3	<i>Specifications of optical performance .....</i>	61
4.2.4	<i>Experimental results.....</i>	62
4.3	COUPLERS .....	65
4.3.1	<i>Multimode – interference – coupler (MMI).....</i>	65
4.3.2	<i>Experimental results.....</i>	69
4.3.3	<i>The codirectional coupler.....</i>	71
4.3.4	<i>Experimental results.....</i>	73



<b>5</b>	<b>RING RESONATORS .....</b>	<b>77</b>
5.1	PASSIVE RING RESONATORS .....	77
5.1.1	<i>Integration of the elements</i> .....	77
5.1.2	<i>Experimental results</i> .....	78
5.1.3	<i>Results from the OLCR measurement</i> .....	84
5.1.4	<i>Tuneability and resonance trimming</i> .....	87
5.2	RING RESONATORS WITH INTEGRATED SOA.....	91
5.2.1	<i>The structure of the SOA</i> .....	91
5.2.2	<i>The integration process</i> .....	95
5.2.3	<i>The active – passive transition</i> .....	102
5.2.4	<i>Experimental results</i> .....	107
5.3	SYSTEM OPERATION – PERSPECTIVES .....	119
<b>6</b>	<b>SUMMARY .....</b>	<b>121</b>
	<b>APPENDIX.....</b>	<b>125</b>
	CALCULATION OF THE INTENSITY RELATIONS OF AN SRR WITH TWO INPUT/OUTPUT WAVEGUIDES .....	125
	CALCULATION OF THE INTENSITY RELATIONS OF A DRR.....	126
	CALCULATION OF THE INTENSITY RELATIONS OF A SERIALY COUPLED TRR.....	127
	CALCULATION OF THE INTENSITY RELATIONS OF A PARALLEL COUPLED TRR.....	128
	<b>SYMBOLS AND ABBREVIATIONS .....</b>	<b>129</b>
	<b>PUBLICATIONS.....</b>	<b>133</b>
	<b>LITERATURE.....</b>	<b>135</b>
	<b>INDEX .....</b>	<b>143</b>
	<b>CURRICULUM VITAE .....</b>	<b>144</b>





# 1 Introduction

## 1.1 The optical network

The primary role of optical fibers has long been to transmit high-speed bit streams from point to point, between nodes in the network. Electronics at the nodes have processed and switched the signals, multiplexing or demultiplexing them to different data rates, directing them to different nodes. In essence one can view the telecommunications network as built of two main components: pipes, which transmit signals, and switches which process and direct the signals. Fibers are representing the pipes for high-speed signals. The first big step towards optical networking was the advent of wavelength-division multiplexing (WDM). The initial attraction of WDM was its ability to multiply the capacity of a single fiber. Instead of carrying a single time-division multiplexed (TDM) channel at 2.5 or 10 Gbit/s or even more, a fiber could carry 4, 8, 16, 32, 40 or more optical channels at different wavelengths, each may be at a different data rate. WDM makes signal management and processing possible on the wavelength level. Combining four 10 Gbit/s signals into a single 40 Gbit/s data stream requires an expensive electronic TDM multiplexer and a 40 Gbit/s optical transmitter including a receiver and demultiplexers to pick out one of the signals. If the four 10 Gbit/s signals are sent on separate optical channels, a filter can pick off the desired optical channel without disturbing the rest of the channels. This principle is applied in any WDM system: optical filters are used for separating one optical channel from the combined signal without electronics. Optical filters are key devices for WDM systems. The most obvious application is for demultiplexing very closely spaced channels, however, they also play major roles in gain equalization and dispersion compensation. A simplified schematic of a WDM system is outlined in Fig. 1.

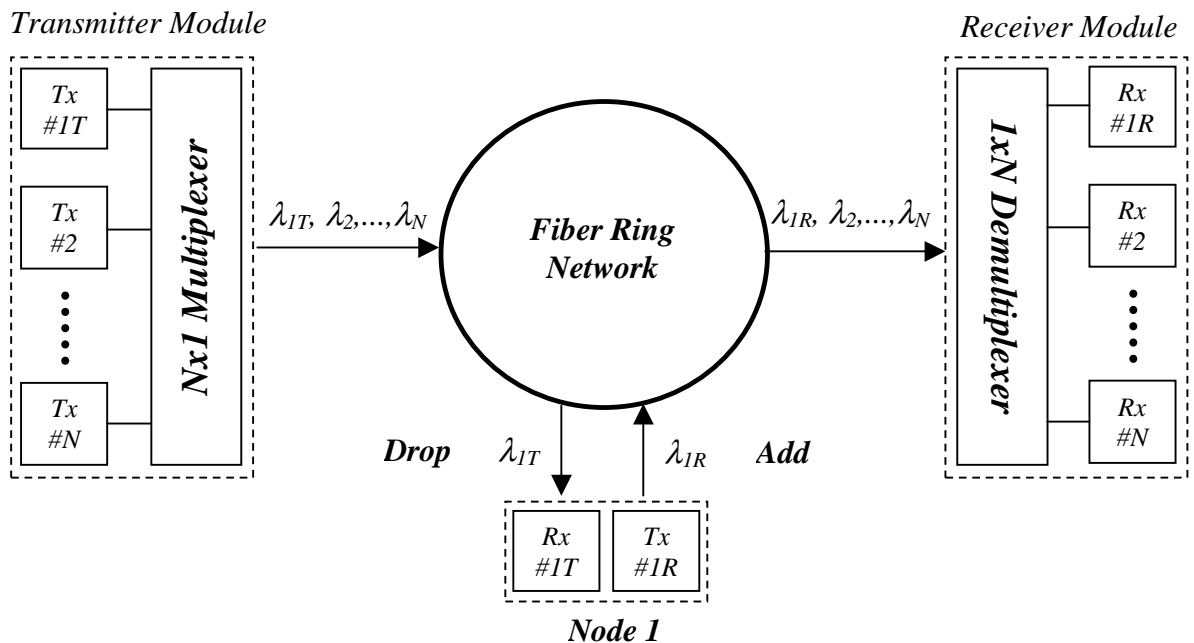


Fig. 1: Add/Drop filter application in a WDM system.

A filter referred to as an add/drop filter is required in an optical ring network to separate the channel to be dropped from those that pass through unaffected. Node 1 (Fig. 1) receives the dropped channel and may transmit its own information on a new signal at the same wavelength as that dropped or a new wavelength that does not interfere with those already used by the other channels on the through-path. Channel spacings are standardized based on the International Telecommunications Union (ITU) grid [1] defining 100 GHz spaced frequencies,  $f = 193.1 \pm m \times 0.1$  THz, where  $m$  is an integer. The center grid is 193.1 THz, which corresponds to a wavelength of 1552.524 nm in vacuum. Channel spacings for commercial systems are currently on the order of 100 GHz with bit rates up to 10 Gbit/s per channel. There are two ways to increase the capacity: increase the useable wavelength range and use the bandwidth already covered more efficiently, for example by decreasing the channel spacing to 50 GHz, 25 GHz or even 12.5 GHz. The increase in bit rate translates into a commensurate increase in the signal bandwidth. This means that there is less room to accommodate the signal bandwidth if the channel spacing is decreased. Closer channel spacing requires sharper filter responses and on-off ratios of more than 20 dB to separate the channels without introducing crosstalk from the other channels. The transmission spectrum from a periodic optical filter is shown in Fig. 2.

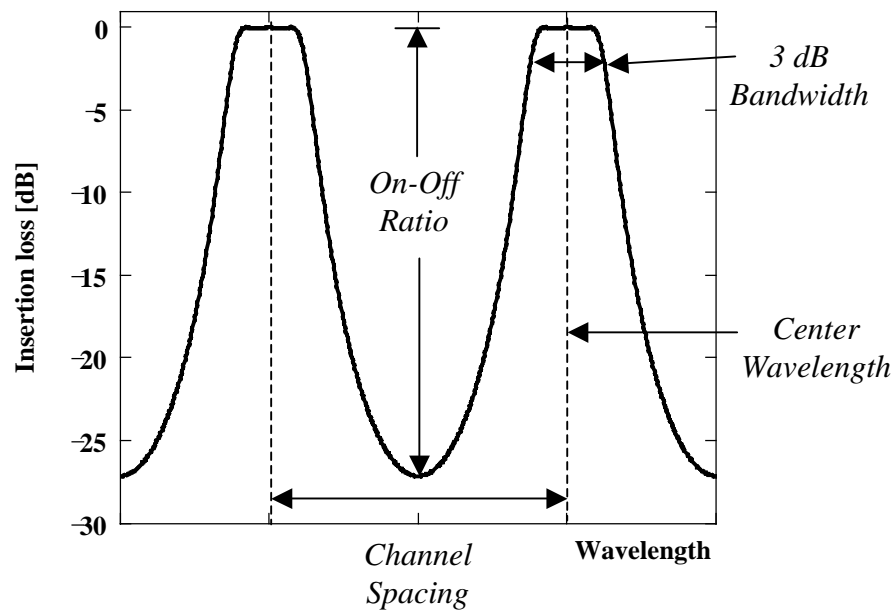


Fig. 2: Transmission characteristic of an optical filter.

### 1.1.1 Optical filters

A key element for controlling light in WDM systems is the optical filter. There are mainly two classes of optical filters.

- 1) Finite impulse response (FIR) / moving average (MA) filters: filters that do not rely on any feedback mechanism, i.e., do not rely on optical reflections. These filters are sometimes called feed-forward and examples are Mach-Zehnder based filters and waveguide grating routers (WGRs).
- 2) Infinite impulse response (IIR) / autoregressive (AR) filters: filters inherently based on multiple reflections. Examples of these include fiber Bragg gratings (FBGs), thin film filters (TFFs), and optical all-pass filters (APFs).

Ideally, a filter should have a rectangular amplitude response and zero dispersion (which corresponds to linear spectral phase over the filter's passband). A data rate of 10 Gbit/s has a spectral width of 6.25 GHz, using a spectral efficiency of 1.6 bit/s/Hz [2]. The ideal passband of a filter with a rectangular amplitude response for this data rate would therefore be 6.25 GHz. For bandpass filter applications, several factors influence the required passband width beyond the fundamental limit set by the bit rate. The passband width must accommodate fabrication tolerances on the filter and laser center wavelengths as well as their polarization, temperature and aging characteristics. For high bitrate long-distance systems, filter dispersion and broadening of the signal due to nonlinearities in the fiber can also become an issue. The requirement of filter characteristics for 40 Gbit/s-based DWDM systems are described in [3].

The description of some of the most common optical filters [4] is given:

a) plane grating

A typical reflective grating consists of a mirrored surface with tiny periodically located grooves. When illuminated, the light reflected from one groove interferes with the light reflected from other grooves, resulting in constructive and destructive interference. The wavelength dependence of the interference patterns are exploited to separate the different wavelengths which are detected for example by using a photodiode.

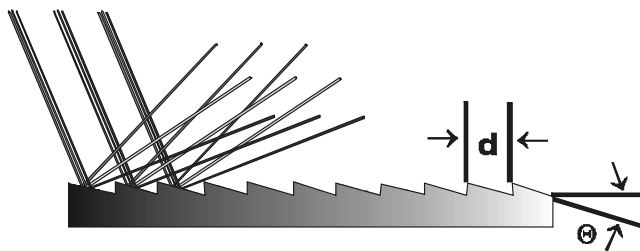


Fig. 3: Plane grating.

### b) Fabry-Perot interferometer

This principle of this filter was invented in 1898 by the French physicists Charles Fabry and Alfred Perot. The principle is still the same, two highly reflective parallel mirrors are separated by a small distance. Most of the light which encounters the first mirror is reflected, but some of it transmits, travels through the cavity [the space between the mirrors, often filled with some kind of dielectric e.g. liquid crystals (LCs)], and strikes the second mirror. At the second mirror most of the light is reflected, while some transmits. The reflected light travels backwards, hitting the first mirror, where some of it again reflects and some transmits. The result is that depending on the spacing and index of refraction between the mirrors, at some wavelengths the multiple reflections interfere constructively. At these wavelengths the cavity “resonates”, so that the light passes through. For other wavelengths the transmitted waves add out of phase and the reflected waves add in phase. At these wavelengths the interferometer’s overall transmission is low, and the overall reflectivity is high.

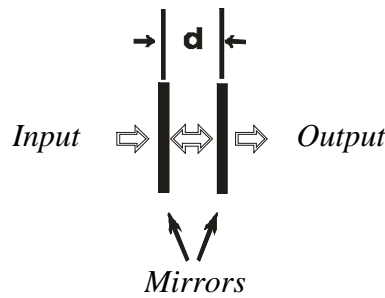


Fig. 4: Fabry-Perot interferometer.

### c) fiber Bragg grating

These types of filters consist of a region in which the index of the fiber varies periodically between high and low, and they are formed in optical fibers by exposing the fiber to interferometric patterns from an ultraviolet (UV) laser. As in the Fabry-Perot interferometer, multiple reflected and transmitted waves result. For a specific wavelength the reflected waves all add in phase, and at this wavelength the grating appears to be highly reflective, while transmitting all the others.

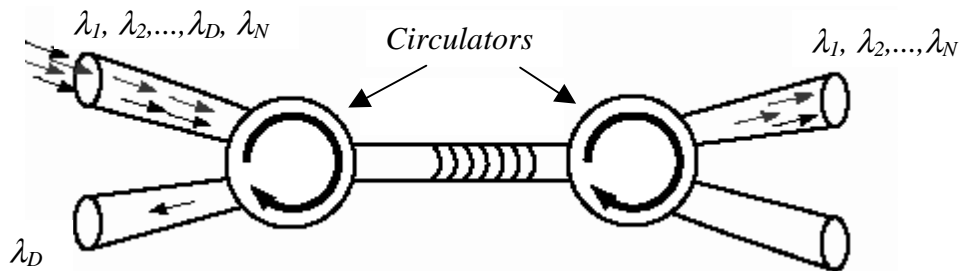


Fig. 5: Optical fiber Bragg grating [5].

d) arrayed waveguide grating (AWG)

The most common filter in optical telecommunications is this type of filter. The AWG uses an array of single mode waveguides in which the lengths of adjacent waveguides differ by a fixed amount. The input light from a single fiber illuminates all these waveguides. Because of the different lengths of the waveguides, the phase of the light (at the output end of the array of waveguides) varies by a fixed amount, from one waveguide to the next. This variation results in a wavelength dependent phase front that is similar to the one from a plane grating. This pattern is then arranged so that different wavelengths illuminate different output fibers. The AWG can serve as a wavelength multiplexer as well as a demultiplexer.

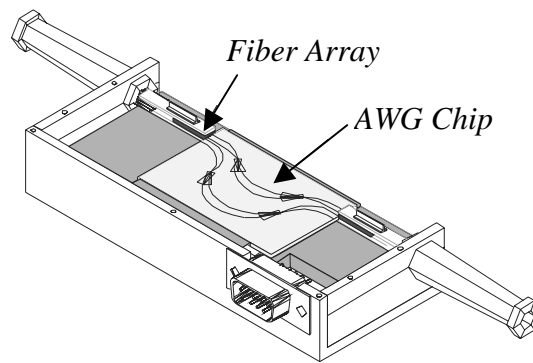


Fig. 6: Packaged arrayed waveguide grating [6].

e) Mach-Zehnder interferometer (MZI)

This filter consists of a pair of couplers connected by two paths of unequal length. Group velocity dispersion in the optical paths of different lengths results in some wavelengths being output to the top port, and other wavelengths being output to the bottom port.

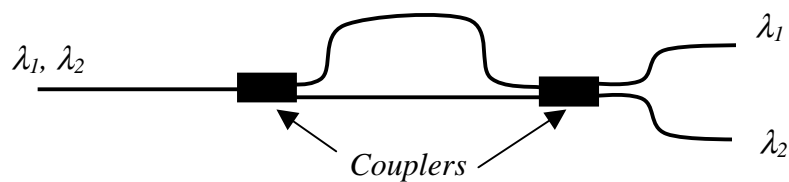


Fig. 7: Mach-Zehnder interferometer.

f) Thin film dielectric interference filter

This filter requires the deposition of many layers of coating to create narrow-band filters. A typical filter with a 3 dB bandwidth of 100 GHz requires more than a hundred layers of coating. With so many layers being deposited, errors caused by local film thickness variation and alternation in density increase, reducing the yield of useful filters. A transmitted beam that goes through a filter is composed of multiple sub-beams, each having a slightly different travel time, which adds dispersion to the data signal.

The characteristics of important optical filters are listed in Table 1.

Filter Type \ Properties	Technology / rating	Temperature stability	Wavelength selectivity	Insertion loss	Polarization dependence	Bandwidth	Tuneability	Comments
<b>Thin film dielectric interference</b>	Planar silica / Mature	Good	High	Low	Low	Difficult to produce narrow channel spaced filters <100 GHz	Low	Highly dispersive
<b>Planar arrayed waveguide</b>	Planar silica / Mature	Good but temp. controller required	High	Increases for a high channel count	Low	Channel spacing 100 GHz and 200 GHz	Not directly tunable	Integration of multiple functions on a single chip
<b>Fiber Bragg grating</b>	Fiber / Mature	Good	High	Low	Low	Difficult to produce narrow channel spaced filters < 50 GHz	Mechanic. stability problem	Short length of fiber exposed to ultraviolet radiation
<b>Mach-Zehnder interferometer</b>	Planar silica / Mature	Good	High	Medium	Low	Can produce narrow channel spaced devices	Medium	High channel count requires cascaded devices $\Rightarrow$ large size
<b>Diffraction grating</b>	3D assembly / Mature	Good	High	High	Low	Narrow channel spacing is achieved	High	Requires careful assembly technique
<b>Fabry-Perot interferometer</b>	3D assembly / Mature	Good	High	Medium	Low	Narrow	Poor stability / reliability	Fast tuning speed (e.g. piezos)
<b>Angle tuning interference filter</b>	3D assembly / Mature	Good	High	Medium	High	Narrow	High	Variable filter charact.
<b>"Linear-Sliding" filter</b>	3D assembly / Mature	Good	High	Medium	Low	Down to a channel spacing of < 50 GHz	High	Special deposition technique required

Table 1: Typical characteristics of common optical filters [7].

A filter which has emerged in the last few years in integrated optics is the ring resonator. This type of filter is studied intensively in this thesis.

## 1.2 The Ring Resonator - History

The proposal to use an integrated ring resonator for a bandpass filter has been made in 1969 by E. A. Marcatili [8]. The layout of the channel dropping filter is shown in Fig. 8. The transmission properties of the used guide consisting of a dielectric rod with rectangular cross section, surrounded by several dielectrics of smaller refractive indices has been described by E. A. Marcatili in [9].

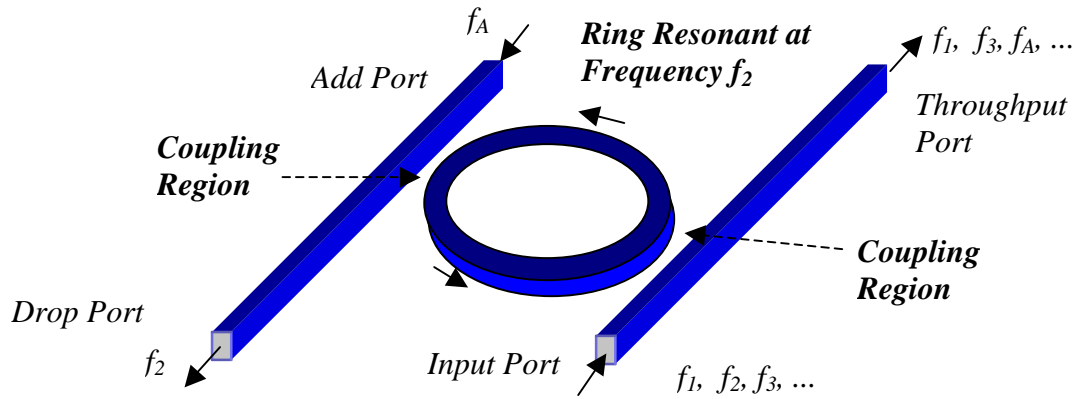


Fig. 8: Ring resonator channel dropping filter.

A general architecture for an autoregressive planar waveguide optical filter was demonstrated for the first time in 1996 [10]. The autoregressive lattice filters which were designed and fabricated consisted of one and two stages using Ge-doped silica waveguides.

A concept for photonic highway switches based on ring resonators used as frequency-selective components was presented in [11]. A signal flow chart transformation for evaluating the filter transfer functions was demonstrated. Purely passive single ring resonator filters as shown in Fig. 8 have been realized in the material system AlGaAs-GaAs [12], [13] and Si-SiO<sub>2</sub> [14] and Si<sub>3</sub>N<sub>4</sub>-SiO<sub>2</sub> [15]. The radius of the used ring resonators is between 5  $\mu\text{m}$  and 30  $\mu\text{m}$  and the free spectral range (FSR) achieved is between 20 nm and 30 nm. Passive ring resonators in the form of a racetrack have been realized in the material system GaInAsP [16] and AlGaAs-GaAs [17]. The filter performance is limited by bending and scattering losses in the resonator. These losses could be compensated for by using an active material instead or in addition. Purely active semiconductor ring lasers have recently received attention [18], [19], [20] because they are attractive as light sources in photonic integrated circuits. They can be positioned anywhere on a substrate and can easily be defined by a minimum of lithographic steps, since neither cleaved facets nor gratings are needed for feedback. An integration of semiconductor optical amplifiers in passive ring resonators has not been realized so far to the author's knowledge. It has only been demonstrated using fiber optics. Fiber optic ring resonator filters employing optical amplifiers were demonstrated in [21] and [22]. It is shown


that optical amplifiers (OA) can provide extra flexibility for unique fiber-optic filter designs, not available in passive configurations. Results are presented [21] for both amplified and unamplified fiber-optic recirculating delay lines (AFORDL and UFORDL) indicating that the AFORDL is capable of realizing filters not possible with the UFORDL. The work presented in [22] focuses on the finesse of an amplified ring resonator. This paper analyzes theoretically the performance of the optical filter, as a function of the coupling coefficients of the electro-optical directional coupler and the gain of the fiber amplifier.


The combination of a passive and active material enables the possibility to realize passive ring resonators with integrated semiconductor optical amplifier (SOA), similar to the mentioned fiber optic filters with erbium-doped fiber amplifiers (EDFA), for improved filter performance of single ring resonator devices as well as of multiple coupled ring resonator devices which has not yet been realized so far to the authors knowledge and is one of the main targets of this thesis. The ring resonator filters which are investigated in this thesis should be tunable and switchable using the integrated SOA. The on-off ratio of the filter should at least be 20 dB. Another challenge is to match the required channel spacing for example 50 GHz to the transmission characteristic of the ring resonator filter. The single ring resonator could be used as a building block in higher order ring resonator filters to achieve flat-top passbands.



### 1.2.1 Applications

There is a wide range of applications for the use of ring resonators. This section is a means of highlighting a few examples of the use of ring resonators.

 The first application which comes to mind after the last section is the use of these coupled ring resonators in *optical delay lines* [23], which provide a time delay for an optical signal. In *optical time division multiplexed* (OTDM) communication systems for example, this function is required for synchronization purposes. In OTDM demultiplexers and in optical logic gates for example, local control signals need to be overlapped in time with incoming data signals.

 Another important field is the use of ring resonators for flexible *dispersion compensation*. Chromatic dispersion is caused by a variation in the group velocity of light traveling within a fiber with changes in optical frequency. A data pulse always contains a spectrum of wavelengths. As the pulse travels along the fiber, the shorter wavelength components travel faster (negative dispersion) than the longer wavelength components (positive dispersion). This effect broadens the pulse and causes it to interfere with neighboring pulses and distort the transmission signal. Practical *dispersion compensators* should have limited tuneability, uniform insertion loss upon tuning of dispersion and multiple wavelength operation. Ring resonators can be used to enhance the physical length by forcing the light to traverse the physical distance many times. Resonant enhancement, however, comes at the price of finite bandwidth. The larger the enhancement, the narrower the bandwidth. Ring resonators allow large compensation for multiple wavelengths simultaneously in a so far limited frequency range [24], [25], [26]. The building block of a multistage dispersion compensator using ring resonators is shown in Fig. 9. The group delay of the ring resonator follows a periodic curve. Cascading multiple loops enables synthetization of various delay curves.

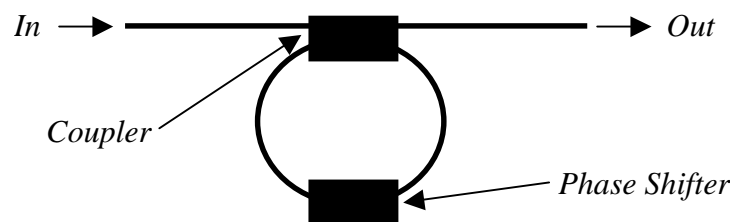


Fig. 9: Single ring resonator (SRR) as a building block for multistage dispersion compensators.

■ A single ring resonator (SRR) integrated with a photo diode (PD) could be used for example to *stabilize a laser diode* (LD) emitting at a specific wavelength (Fig. 10) or for definite switching in FSR channel spacing (e.g. 25 GHz). The PD is adjusted in such a way, that it is tuned to the resonance wavelength of the ring, which is in turn the emitted wavelength of the laser. If the PD detects more light, the laser is out of its wavelength and has to be retuned.

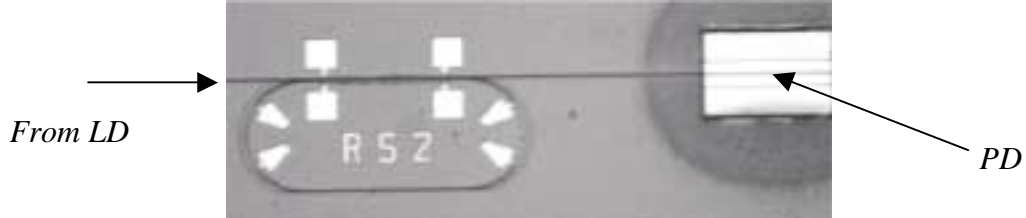


Fig. 10: Photograph of a fabricated passive SRR with integrated PD at the throughput port.

A setup for the wavelength stabilization of a laser diode is presented in Fig. 11.

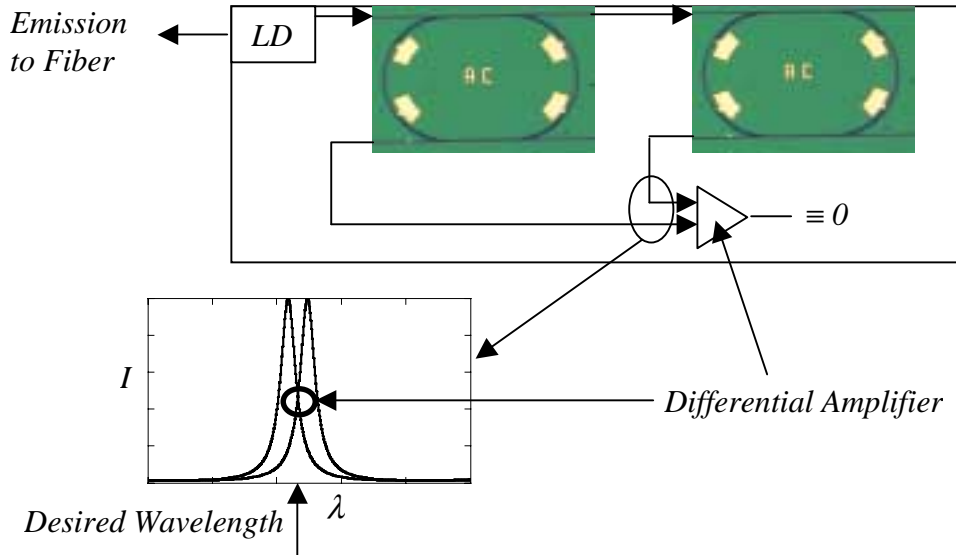


Fig. 11: Wavelength stabilization and switching setup using ring resonators.

The ring resonators have identical geometries. The transmission characteristic of the second ring resonator is slightly detuned as shown in the diagram. A differential amplifier subtracts both signals. The laser is at the desired wavelength as long as a zero is detected. The FSR of the ring resonators enables the switching on a desired wavelength grid. A similar configuration can also be used for the generation of mm – wave signals without the need of a high frequency photo diode [27]. A semiconductor laser structure integrated with a passive ring resonator is proposed in [28]. It is demonstrated that with the help of the Lorentzian-type filter characteristic of the single ring resonator, the side mode suppression ratio, the linewidth, and the frequency chirp of this ring resonator coupled laser will be improved.

The **integration** of a ring resonator with a **Mach-Zehnder Interferometer** (Fig. 12) has been realized recently for the use as a compact **notch filter** [29] and as a periodic **multi/demultiplexer** [30].

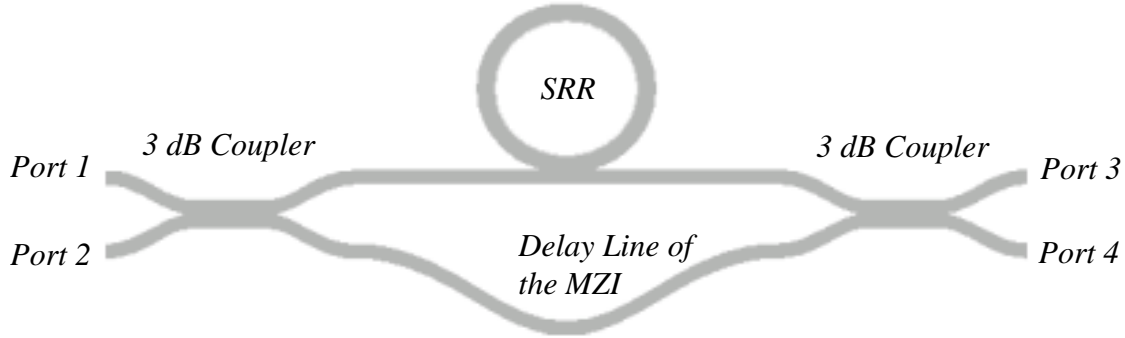


Fig. 12: Configuration of a MZI with a ring resonator.

In the case of the **notch filter**, the roundtrip loss in the ring is small compared to the waveguide coupling strength. The ring introduces a phase shift of  $\pi$  at resonance on the side-coupled waveguide. Single ring resonators coupled to one waveguide which are presented in this thesis can be used as **notch filters** with an on-off ratio larger than 20 dB.

Ring resonators with integrated SOAs could be used as programmable **add/drop modules** for the flexible use of WDM channels in wavelength division multiplexing networks. High performance **add/drop filters** can be realized using double ring resonators (DRRs) and triple ring resonators (TRRs) with the specific transmission characteristic (flat top and high on-off ratio  $> 20$  dB) presented theoretically and practically in this thesis. The layout of a possible four channel **add/drop module** is shown in Fig. 13.

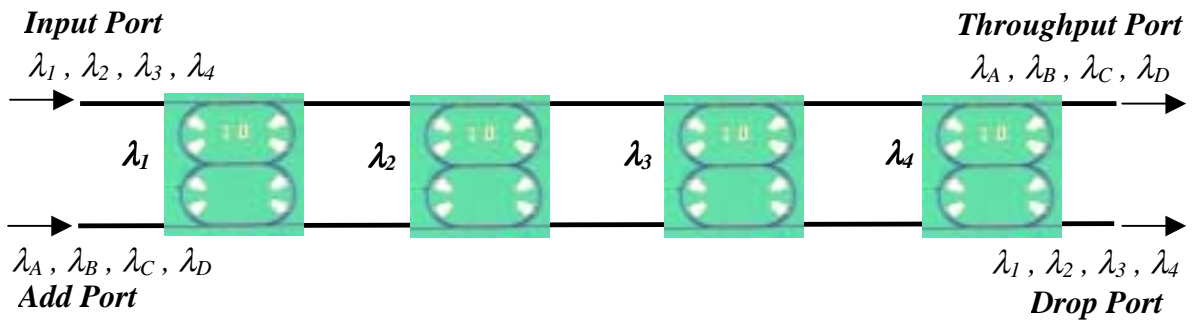


Fig. 13: Layout of a four channel add/drop filter using DRRs.

The input wavelengths have a channel spacing of e.g. 25 GHz. The DRRs used in this configuration should then have an FSR of at least 100 GHz. Each double ring resonator is tuned for each corresponding wavelength. This is a smart way of realizing an **add/drop module** using only two bus waveguides. A higher channel number can be used if ring resonators with a larger FSR are used. An eight channel **add/drop filter** using vertically

coupled ring resonators is demonstrated in [31]. An analytic theory governing the complete scattering response of two-dimensional ring resonator arrays is presented in [32].

Vertically coupled ring resonators are also possible candidates for the realization of **add/drop filters**. Devices based on lateral coupling require the use of advanced fabrication technologies to achieve reproducible filter bandwidths and high dropping efficiencies. Another way to couple from the ring resonator to the waveguide is by vertical coupling [33], [34], [35], [36], [37]. The sensitive separation between the ring resonator and the bus waveguides is controlled by material growth or deposition enabling the fabrication of gaps  $< 0.3 \mu\text{m}$ . The vertical coupling technology used so far is mainly for passive devices. The integration of active devices and their electric control has been investigated using the vertical coupling technology and a patent application has been submitted (c.f. publications: filed patent applications [2]).

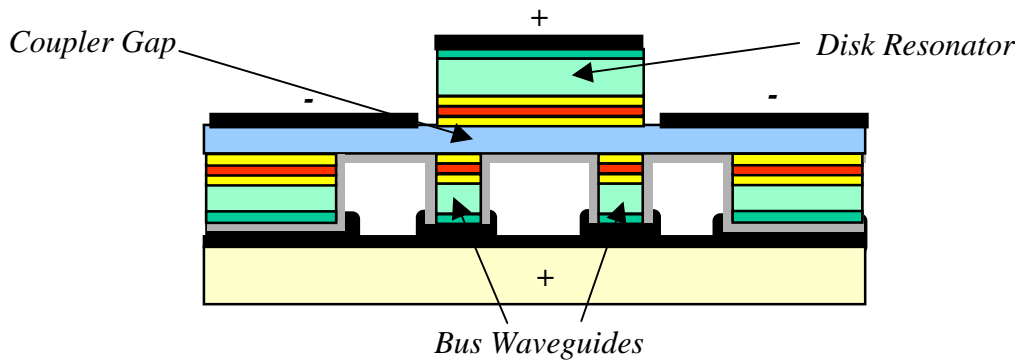


Fig. 14: Vertically coupled all-active microring resonator.

An **optical frequency division multiplexed** (FDM) transmission experiment using a DRR was presented in [38]. The experiment was performed using 8 channels at a data rate of 622 Mb/s with a channel spacing of 10 GHz. The used DRR had an FSR of approximately 100 GHz. This is to the authors knowledge one of the first transmission experiments using ring resonators. Recently a 5 Gbit/s **transmission experiment** using a microsphere as an add/drop device was reported [39].

The polarization dependency of the ring resonator configurations presented in this thesis could be used advantageously in **polarization division multiplexing** (PDM) systems. Alcatel has demonstrated [40] a 10.2 Tbit/s transmission experiment using polarization division multiplexing technology. In the current experiment each wavelength was split up into two polarizations and was encoded separately. Ring resonator filters can be designed as will be shown in this thesis for TE and for TM polarization enabling their use in this novel transmission technique.

The wavelength selective, switchable and tunable devices realized in this thesis are also candidates to be used as *interleavers* in DWDM systems for the spacial separation of the DWDM channels into two complementary sets at twice the original channel spacing. (e.g.: an incoming spectrum with a channel spacing of 50 GHz is transferred into two sets having a channel spacing of 100 GHz). This is an effective way to decrease channel spacing and increase the channel number and so increase network capacity and reduce transmission costs. A combination of *interleavers* for example enables the fabrication of a *demultiplexer* for 8 channels with a channel spacing of 25 GHz (Fig. 15).

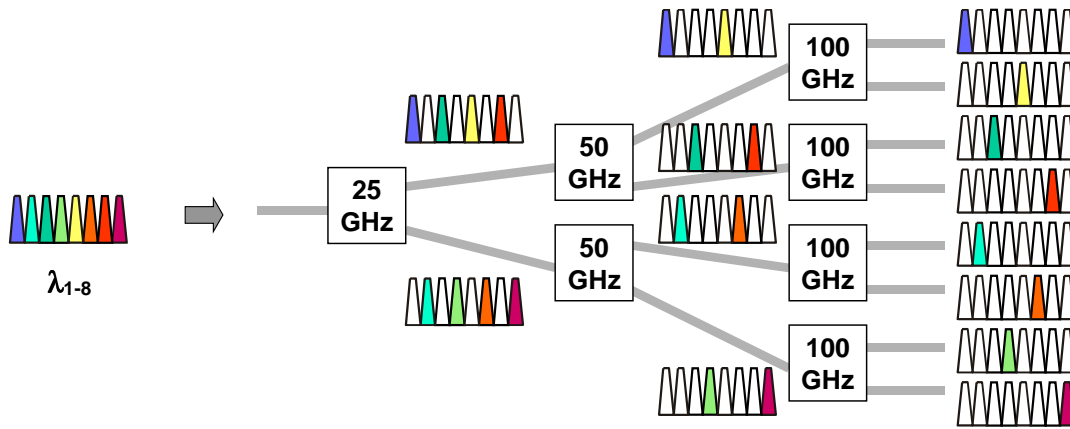


Fig. 15: DWDM demultiplexer on the basis of interleavers.

*Interleavers* are an easy way to make arrayed waveguide gratings work in ultra-dense networks. A combination of ring resonators used as *interleavers* for a channel spacing below 100 GHz and AWGs for the separation of individual channels at a channel spacing of 100 GHz could be used.

Ring resonators can even find application in biology, as sensitive biosensors [41]. The device operates by means of monitoring the change in transfer characteristics of the ring resonator when biological materials fall onto on to the resonator. High sensitivity can be achieved because the light wave interacts many times with each pathogen as a consequence of the resonant recirculation of light within the ring structure.

These are only some of the applications which could be realized with ring resonators.

The following section presents the basic functionalities of ring resonators. A simulation model describing the behavior of ring resonators is given.



## 2 Coupled ring resonators - theory and simulation model

### 2.1 Introduction

Active and passive ring resonator devices are promising candidates for wavelength filtering [42], routing [43], switching [44], modulation, conversion [45] and multiplexing/demultiplexing applications as was shown in the previous section. Ring resonators do not require facets or gratings for optical feedback and are particularly suited for monolithic integration with other components [46]. The passband shape of ring resonator filters can be designed by the use of multiple coupled resonators [47], [48], [49]. The filter characteristic (steep roll-off, flat top and high contrast  $> 20$  dB) depends on the energy flow in the resonators which defines the desired filter shape [50]. It is necessary to achieve smooth waveguide sidewalls for low waveguide losses [51], deep etched curvatures for low bending losses and precise waveguide dimensions for power splitting. Steeper roll-off and out-of-band rejection require cascaded micro ring resonators [52]. The implementation of SOAs within the ring resonator opens the possibility to adjust the energy flow for optimum response. The matching of the resonance frequency of each ring in multiple coupled ring resonators is inevitable to achieve the desired filter characteristic. The principal function of a single ring resonator (SRR) is shown in Fig. 16 and Fig. 17. The resonator (Fig. 16) is not in resonance with the wavelength inserted at the input port. The wavelength passes by and can be detected at the throughput port. The amount of light, which enters the ring resonator depends on the coupling factor of the used coupler. As can be seen there is a certain amount of intensity which reaches the drop port, this is also known as the crosstalk. The aim is to design a filter with low crosstalk.

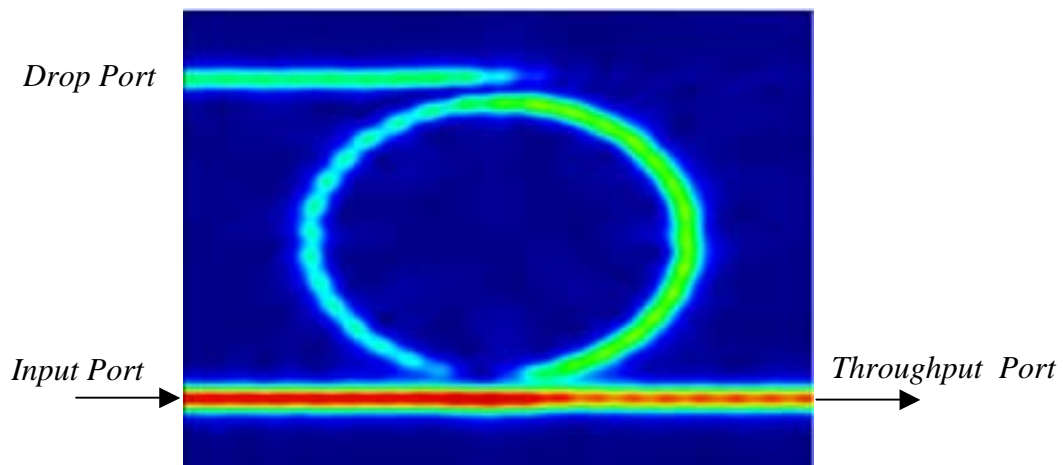


Fig. 16: Ring resonator at a wavelength of  $\lambda = 1.55 \mu\text{m}$ .

The wavelength inserted at the input port in Fig. 17 is in resonance with the ring resonator and is "dropped". The same principle applies for double ring resonators (DRR) and similar

arrangements using ring resonators. The use of DRRs and multiple coupled ring resonators enables the realization of various types of filter characteristics.

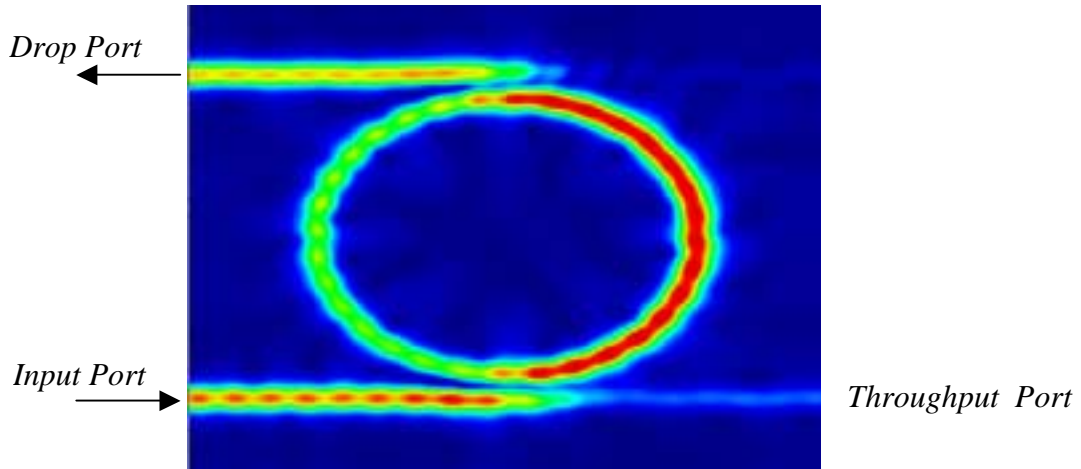


Fig. 17: Ring resonator at a wavelength of  $\lambda = 1.57 \mu\text{m}$ .

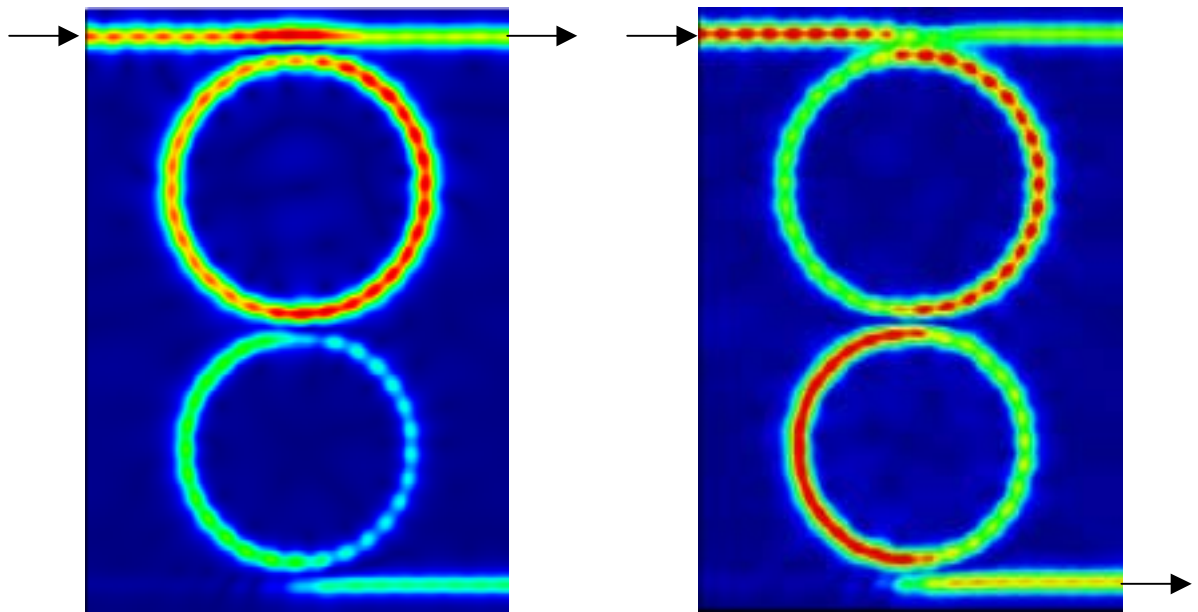


Fig. 18: Double ring resonator out of resonance (left) and in resonance (right).

The simulations shown in Fig. 16, Fig. 17, Fig. 18 have been calculated using a commercially available finite difference time domain (FDTD) program [53].



## 2.2 Synthesis of optical filters using ring resonators

The synthesis of ring resonator filters concatenated in series or parallel have already been described in 1988 [54] and realized using fiber optics. The synthesis of various types of optical filters using ring resonators has attracted attention recently [55], [56], [57]. The aim is the realization of a box-like filter shape and a high on-off ratio. Theoretically many desired filter shapes can be created using multiple (6 stages [48], 1-10 Stages [49]) coupled ring resonators. The described filter stages are assumed to be identical in their behavior, which is not the case in reality. The resonance frequency of fabricated multiple coupled ring resonators which are demonstrated in this thesis (maximum of 3 stages) has to be matched to overcome fabrication tolerances and achieve the desired filter shape. From the authors point of view a ring resonator filter consisting of more than three or four ring resonators fabricated using today's state-of-the-art technology is not practicable. The interaction among all involved resonators has to be assured to obtain the desired filter response, which is another challenge to be demonstrated in this thesis.

### 2.2.1 Z - transform analysis of a ring resonator optical filter

The basic autoregressive (AR) planar waveguide add/drop filter is a single ring with two couplers (Fig. 8). The filter has a single pole and no zeros as shown in its transfer function (2.1) which assumes that both couplers are identical with coupling factor  $\kappa$  [10].

$$H(z) = \frac{\text{Output}}{\text{Input}} = \frac{-\kappa\sqrt{z^{-1}}}{1 - (1 - \kappa)z^{-1}} \quad (2.1)$$

The transmission around one ring is represented by  $z^{-1} = \exp(-\alpha L/2 - jk_n L)$  where  $k_n$  is the propagation constant and  $\alpha L/2$  is the ring loss (roundtrip loss) which includes propagation loss, losses resulting from transitions in the curvature, and bending losses. The value of  $\alpha$  [unit length<sup>-1</sup>] depends on the properties of the material and the waveguide used and is referred to as the intensity attenuation coefficient,  $L$  is the circumference of the ring resonator. A detailed analysis of different types of ring resonator configurations can be found in [47]. The transfer function of a serially coupled ring resonator filter (Fig. 19) is derived using the matrix formalism described in [58]. It is an IIR filter consisting of  $N$  rings with equal perimeters connected by couplers with coupling factors  $\kappa_0, \dots, \kappa_N$ . Phase errors are included in the Z – transform analysis by multiplying  $z^{-1}$  by the term  $\exp(j\phi_n)$  for each stage. The input and output fields are denoted by  $E_{i1}, E_{i2}$  and  $E_{t1}, E_{t2}$  respectively as well as intermediate fields propagating in the forward  $T_0, \dots, T_N$  and reverse  $R_0, \dots, R_N$  directions. The frequency response of this structure is derived by starting with the transmission matrix for a single stage.

The coupling for the throughput path is referred to as  $y_n = \sqrt{I - \kappa_n}$  and for the cross path  $r_n = j\sqrt{\kappa_n}$  for each directional coupler. The directional coupler is assumed to be symmetric in its behavior for the remainder of this thesis.

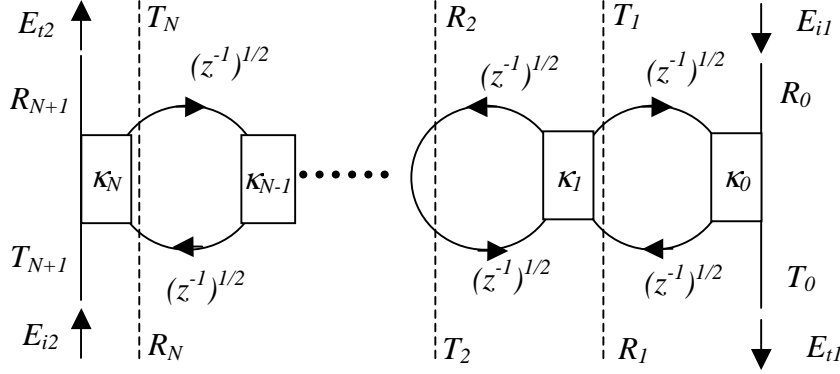


Fig. 19: Serially coupled ring resonator filter.

The transformation of inputs to outputs for each stage can be represented by the matrix  $\Phi_n$  as [10] :

$$T_{n-1} = r_n \sqrt{z^{-1}} T_n + y_{n-1} R_{n-1} \quad (2.2a)$$

$$R_n = \sqrt{z^{-1}} [y_{n-1} \sqrt{z^{-1}} T_n + r_{n-1} R_{n-1}] \quad (2.3b)$$

$$\begin{bmatrix} T_{n+1}(z) \\ R_{n+1}(z) \end{bmatrix} = \frac{I}{r_n \sqrt{e^{j\phi_{n+1}} z^{-1}}} \Phi_n \begin{bmatrix} T_n(z) \\ R_n(z) \end{bmatrix} \quad (2.4c)$$

$$\Phi_n = \begin{bmatrix} I & -y_n \\ y_n e^{j\phi_{n+1}} z^{-1} & -e^{j\phi_{n+1}} z^{-1} \end{bmatrix} \quad (2.5)$$

The relationship between the first and last stages is then expressed by concatenating  $\Phi_n$ 's as follows:

$$\begin{bmatrix} T_{N+1}(z) \\ R_{N+1}(z) \end{bmatrix} = \frac{I}{j^{N+1} \left\{ \sigma_N e^{j(\phi_{tot} + \phi_{N+1})} z^{-(N+1)} \right\}^{\frac{1}{2}}} \cdot \Phi_N \dots \Phi_0 \begin{bmatrix} T_0(z) \\ R_0(z) \end{bmatrix} \quad (2.6)$$

where  $\phi_{tot} = \sum_{n=1}^N \phi_n$  and  $\sigma_N = \prod_{n=0}^N \kappa_n$ .

Let  $\Phi_{N0}$  represent the product of matrices  $\Phi_{N0} = \prod_{n=0}^N \Phi_n$ , then the individual terms in the

Nth-order transmission matrix can be expressed in terms of two polynomials as follows [55]:

$$\Phi_{N0} = \begin{bmatrix} A_N(z) & B_N^R(z) \\ e^{j\phi_{N+1}} z^{-1} B_N(z) & e^{j\phi_{N+1}} z^{-1} A_N^R(z) \end{bmatrix} \quad (2.7)$$

where  $A_N(z)$  and  $B_N(z)$  are Nth-order polynomials in  $z^{-1}$ . The reverse polynomials are defined as follows:

$$A_N^R(z) = (-1)^{N-1} z^{-N} e^{j\phi_{tot}} A_N^* \left( \frac{1}{z^*} \right) \quad (2.8)$$

$$B_N^R(z) = (-1)^{N-1} z^{-N} e^{j\phi_{tot}} B_N^* \left( \frac{1}{z^*} \right) \quad (2.9)$$

Assuming no input on  $E_{i1}$ , the transfer functions for  $E_{i2}$  to each output are expressed as follows:

$$\begin{aligned} H_{11}(z) &= \frac{E_{t1}}{E_{i2}} = \frac{T_0(z)}{\sqrt{e^{j\phi_{N+1}} z^{-1} T_{N+1}(z)}} = \frac{j^{N+1} z^{-\frac{N}{2}} e^{\frac{j\phi_{tot}}{2}} \sqrt{\sigma_N}}{A_N(z)} \\ H_{21}(z) &= \frac{E_{t2}}{E_{i2}} = \frac{z R_{N+1}(z)}{e^{j\phi_{N+1}} T_{N+1}(z)} = \frac{B_N(z)}{A_N(z)} \end{aligned} \quad (2.10)$$

Similarly, assuming no input at  $E_{i2}$ , the remaining transfer functions are:

$$\begin{aligned} H_{22}(z) &= \frac{E_{t2}}{E_{i1}} = \frac{R_{N+1}(z)}{\sqrt{e^{j\phi_{N+1}} z^{-1} R_0(z)}} = H_{11}(z) \\ H_{12}(z) &= \frac{E_{t1}}{E_{i1}} = \frac{T_0(z)}{R_0(z)} = \frac{-B_N^R(z)}{A_N(z)} \end{aligned} \quad (2.11)$$

$H_{11}(z)$  is an autoregressive filter and  $H_{21}(z)$  is an autoregressive moving average filter (c.f. section 1.1.1). The location of the poles are a nonlinear function of the coupling factors as demonstrated by the  $A_N$  and  $B_N$  polynomials of first and second order given below. In particular, the zeros and poles are not independent of each other.

$$\begin{aligned} A_1 &= 1 - y_0 y_1 e^{j\phi_1} z^{-1} \\ B_1 &= y_1 - y_0 e^{j\phi_1} z^{-1} \\ A_2 &= 1 - y_1 (y_0 e^{j\phi_1} + y_2 e^{j\phi_2}) z^{-1} + y_0 y_2 e^{j(\phi_1 + \phi_2)} z^{-2} \\ B_2 &= y_2 - y_1 (y_0 y_2 e^{j\phi_1} + e^{j\phi_2}) z^{-1} + y_0 e^{j(\phi_1 + \phi_2)} z^{-2} \end{aligned} \quad (2.12)$$

Both the ring loss and the coupling factors contribute to the magnitude of the  $A_N$  and  $B_N$  polynomial coefficients since the magnitude of  $z^{-1}$  is less than unity. If there are no phase errors, then the coefficients are real valued. The total phase can be obtained from the Nth coefficient of  $A_N$  and  $B_N$  polynomials. Any variation in ring loss from one stage to another can be included as a separate term with the phase error, i.e.,  $\exp(j\phi_n - \Delta\alpha L/2)$ . Unlike the phase error terms, where conjugation of the polynomial coefficients allows the reverse polynomials to be defined without prior knowledge of the individual phase errors, the  $\Delta\alpha_n$  terms must be known before to define the reverse polynomials in (2.6) and (2.7).

A modified Levinson algorithm is described in [47] to solve the previously mentioned equations. The method can be used for both synthesizing and analyzing AR waveguide filters.

The basic recursion relations of this algorithm which are based on (2.3) and (2.5) are given by:

$$A_{N-1}(z) = \frac{I}{\kappa_N} [A_N(z) - y_N B_N(z)] \quad (2.13)$$

$$B_{N-1}(z) = \frac{z}{\kappa_N e^{j\phi_N}} [y_N A_N(z) - B_N(z)] \quad (2.14)$$

These equations are specialized for the ring resonator filter configuration (Fig. 19) and allow a uniform waveguide loss and independent phase terms for each stage to be included. The order reduction is satisfied when the following relationship for the coefficients of the  $A_N$  and  $B_N$  polynomials is met:

$$a_N(0)a_N(N) = b_N(0)b_N(N) \quad (2.15)$$

where  $a_N(\text{coefficient no.})$  and  $b_N(\text{coefficient no.})$  are the coefficients for the polynomials of order  $N$ . Both  $A_N(z)$  and  $B_N(z)$  are needed for the recursion relations as well as the ring loss and phase error  $\phi_N$ . The ring loss is assumed to be uniform across the stages, otherwise a unique solution for the coupling ratios cannot be obtained. The transfer function  $H(z)$  of a ring resonator filter is obtained using a desired filter transmission response. The polynomial  $A(z)$  is defined by the relationship  $H(z)A(z) = \Gamma$ , which is analogous to signal modeling. The signal model for  $H(z)$  is the response  $\Gamma/A(z)$ . The polynomial  $A(z)$  is restricted to a finite order polynomial,  $A_P(z) = 1 + a_{p1}z^{-1} + \dots + a_{pp}z^{-P}$  and  $\Gamma^2 = \sigma_N e^{-\alpha L N}$  [10]. An underlying assumption is that the  $A_N(z)$  polynomial is a valid one, i.e., all of its roots are within the unit circle. Given a desired filter transmission response,  $A_N(z)$  and  $\Gamma$  can be determined. The ring loss which has to be measured is needed to determine  $A_N^R$  as well as  $\sigma_N$ . The phase of the highest-order term of  $A_N(z)$  is  $\phi_{tot}$ . Knowing these parameters  $B_N(z)$  can be determined. After these steps, solutions for the coupling factors and the individual phase terms have to be evaluated which is not trivial. The final step of the algorithm is to check the solutions evaluated for the coupling factors and the individual phase terms against the input for consistency. An acceptable solution must satisfy two criteria beyond having physically realizable coupling ratios:

- a) the sum of the individual phase terms must equal  $\phi_{tot}$
- b) the product of the coupling ratios must equal  $\sigma_N$

Since  $A_N(z)$  is given,  $\phi_{tot}$  is known, however, it is known only to within an integer multiple of  $2\pi$ . If either criterion is not met, it is likely due to the nonunique  $\phi_{tot}$  in which case an integer multiple of  $2\pi$  is added and the algorithm is repeated with  $\phi_{tot\ new} = \phi_{tot} + 2\pi$ .

## 2.3 Ring resonators – the used model

The Lorentzian transmission characteristic of a single ring resonator is transferred into a box like filter shape using a double ring resonator or a triple ring resonator configuration. A calculation model is derived and all essential parameters describing the transmission characteristic are extracted. On the basis of this ring resonator model, configurations with a specific transmission behavior are designed and fabricated.

### 2.3.1 The single ring resonator (SRR)

The simple model [59] of a single ring resonator is shown in Fig. 20. The circumference of the ring is  $L$  ( $L = 2\pi R$ ; the radius is  $R$ ), the coupling factor is  $\kappa$ . The intensity attenuation coefficient of the ring is  $\alpha$ . The wave propagation constant is  $k_n$ .

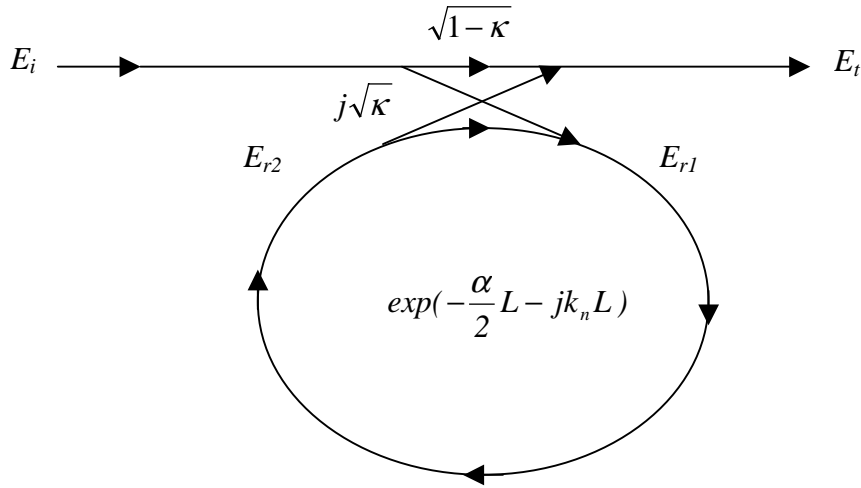


Fig. 20: The single ring resonator.

The transmitted and inserted electric field relations can be derived as follows:

$$E_t = (1 - \gamma)^{\frac{1}{2}} \cdot [E_i \cdot \sqrt{1 - \kappa} + j \cdot E_{r2} \sqrt{\kappa}] \quad (2.16)$$

$$E_{r1} = (1 - \gamma)^{\frac{1}{2}} \cdot [j \cdot E_i \cdot \sqrt{\kappa} + E_{r2} \cdot \sqrt{1 - \kappa}] \quad (2.17)$$

$$E_{r2} = E_{r1} \cdot \exp\left(-\frac{\alpha}{2} \cdot L - j \cdot k_n \cdot L\right) \quad (2.18)$$

where  $k_n = \frac{2\pi \cdot n_{eff}}{\lambda}$  and  $\gamma$  denotes the intensity insertion loss coefficient of the directional coupler and  $n_{eff}$  is the effective refractive index.

Using these equations,  $E_t/E_i$  can be calculated:

$$\frac{E_t}{E_i} = (1 - \gamma)^{\frac{1}{2}} \cdot \left[ \frac{\sqrt{1 - \kappa} - (1 - \gamma)^{\frac{1}{2}} \cdot \exp\left(-\frac{\alpha}{2} \cdot L - j \cdot k_n \cdot L\right)}{1 - (1 - \gamma)^{\frac{1}{2}} \cdot \sqrt{1 - \kappa} \cdot \exp\left(-\frac{\alpha}{2} \cdot L - j \cdot k_n \cdot L\right)} \right] \quad (2.19)$$

In the following, new parameters will be used for simplification:

$$D = (1 - \gamma)^{1/2}$$

$$x = D \cdot \exp\left(-\frac{\alpha}{2} \cdot L\right)$$

$$y = \sqrt{1 - \kappa} \quad (2.20)$$

$$\phi = k_n \cdot L$$

The intensity relation for the output port is given by [60]:

$$\frac{I_t(\phi)}{I_i} = \left| \frac{E_t}{E_i} \right|^2 = D^2 \cdot \left[ 1 - \frac{(1 - x^2) \cdot (1 - y^2)}{(1 - x \cdot y)^2 + 4 \cdot x \cdot y \cdot \sin^2\left(\frac{\phi}{2}\right)} \right] \quad (2.21)$$

The transmission spectrum of a single ring resonator is shown in Fig. 21. The maximum and minimum transmission is calculated, using:

$$T_{\max} = D^2 \cdot \frac{(x + y)^2}{(1 + x \cdot y)^2} \quad (2.22)$$

$$T_{\min} = D^2 \cdot \frac{(x - y)^2}{(1 - x \cdot y)^2} \quad (2.23)$$

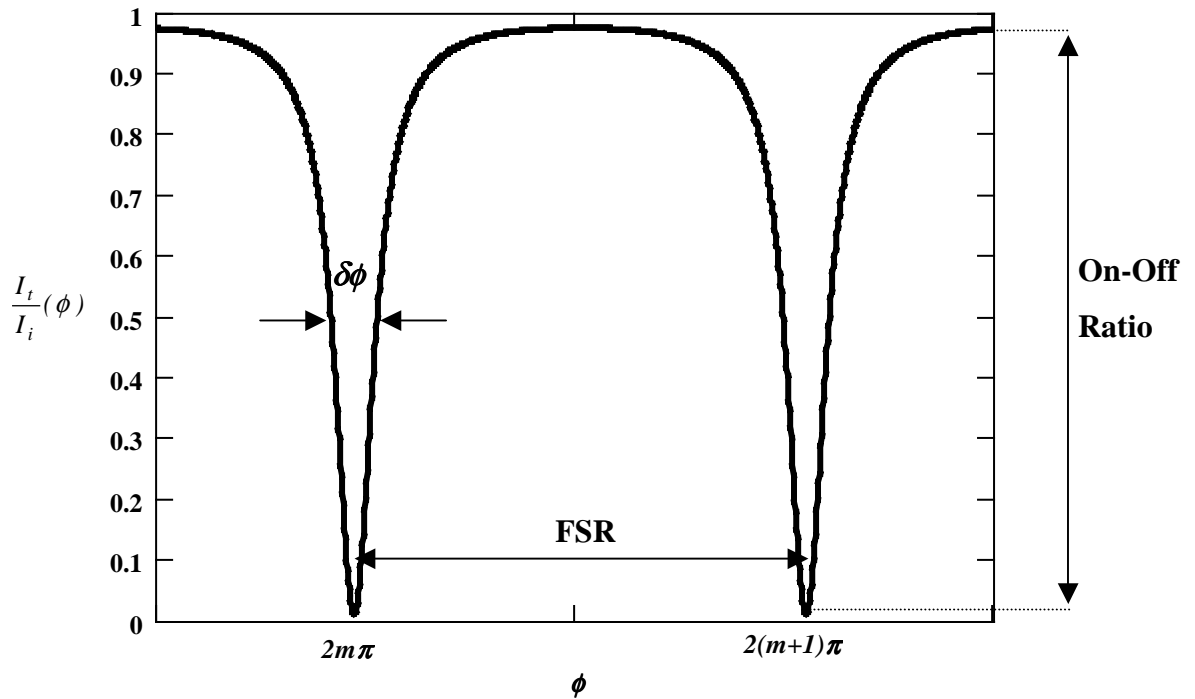


Fig. 21: Transmission characteristic of the single ring resonator.

The full-width at half-maximum (FWHM or 3 dB bandwidth)  $\delta\phi$   $\left[ \frac{I_t}{I_i}(\phi) = 0.5 \right]$  and the finesse  $F$  of the resonator are given by:

$$\delta\phi = \frac{2 \cdot (1 - x \cdot y)}{\sqrt{x \cdot y}} \quad (2.24)$$

$$F = \frac{2\pi}{\delta\phi} = \frac{\pi \cdot \sqrt{x \cdot y}}{(1 - x \cdot y)} \quad (2.25)$$

The finesse is a measure for the transmission characteristic of a filter. A resonance point of  $T_{min}$  in Eq. (2.21) is defined by:

$$\phi = k_n \cdot L = 2 \cdot m \cdot \pi \quad (2.26)$$

The on-off ratio will become maximum if:

$$T_{min} = 0 \Rightarrow x = y \Rightarrow \alpha = -\frac{1}{L} \cdot \ln\left(\frac{1 - \kappa}{D^2}\right) \quad (2.27)$$

This relationship is also referred to as the critical coupling. The maximum on-off ratio  $[I_t/I_i (2m\pi) = 0]$  can be achieved by varying the coupling factor  $\kappa$  or the intensity attenuation coefficient  $\alpha$  (Eq. (2.25)). The value of  $\alpha$  can only be changed severely by the implementation of an SOA within the ring resonator or using an all-active ring resonator.

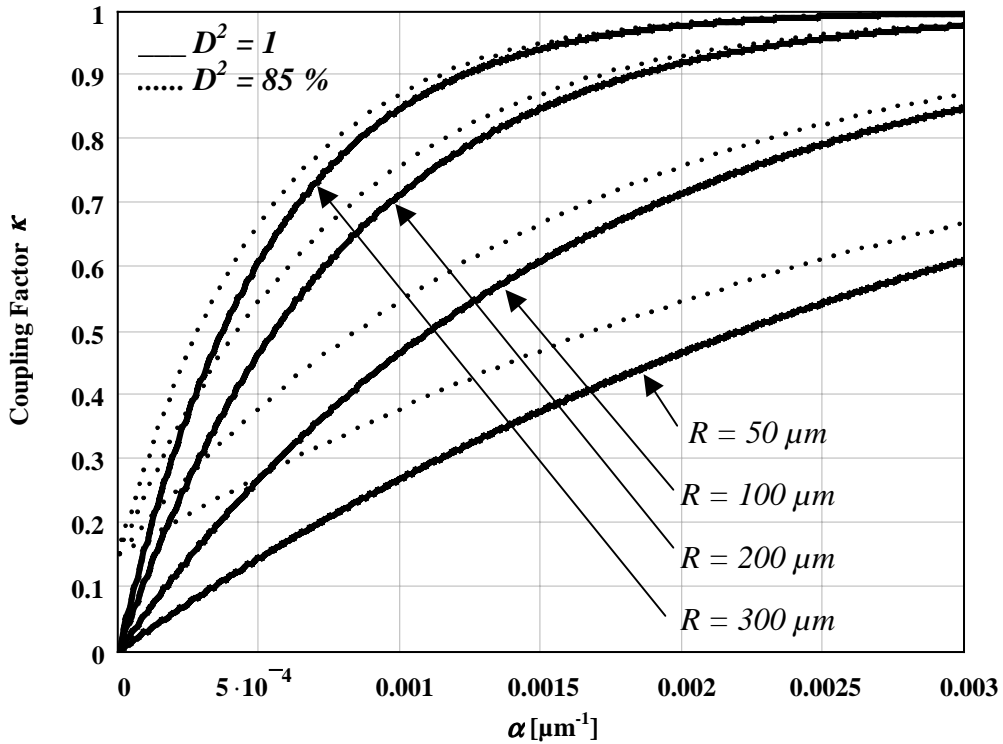


Fig. 22: Evaluation of the ideal coupling factor  $\kappa$  for a given intensity attenuation coefficient  $\alpha$ .

The ideal intensity attenuation coefficient  $\alpha$  for an SRR to achieve a maximum on-off ratio  $[I_t/I_i (2m\pi) = 0]$ , for example, with a radius of  $R = 100 \mu\text{m}$ , a power coupling factor of  $\kappa = 0.5$ , an intensity insertion loss of the coupler of  $D^2 = 85\%$  ( $\gamma = 15\%$ ) is taken from the diagram (Fig. 22) to be  $\alpha = 0.0008 \mu\text{m}^{-1}$ . The achieved finesse  $F$  for this configuration is

$F = 4.4$ . The value of the intensity attenuation coefficient  $\alpha$  is fixed if a purely passive material is used for the realization of the ring resonator filter.

The finesse  $F$  [Eq. (2.23)] is given for a maximum on-off ratio [ $x = y$ ; Eq. (2.25)]:

$$F_{x=y} = \frac{\pi y}{1 - y^2} = \frac{\pi \sqrt{1 - \kappa}}{\kappa} \quad (2.28)$$

$$F_{y=x} = \frac{\pi x}{1 - x^2} = \frac{\pi D e^{-\frac{\alpha}{2}L}}{1 - D^2 e^{-\alpha L}} \quad (2.29)$$

The finesse  $F$  depending on the coupling factor  $\kappa$  at the point of maximum on-off ratio [Eq. (2.26)] is shown in Fig. 23.

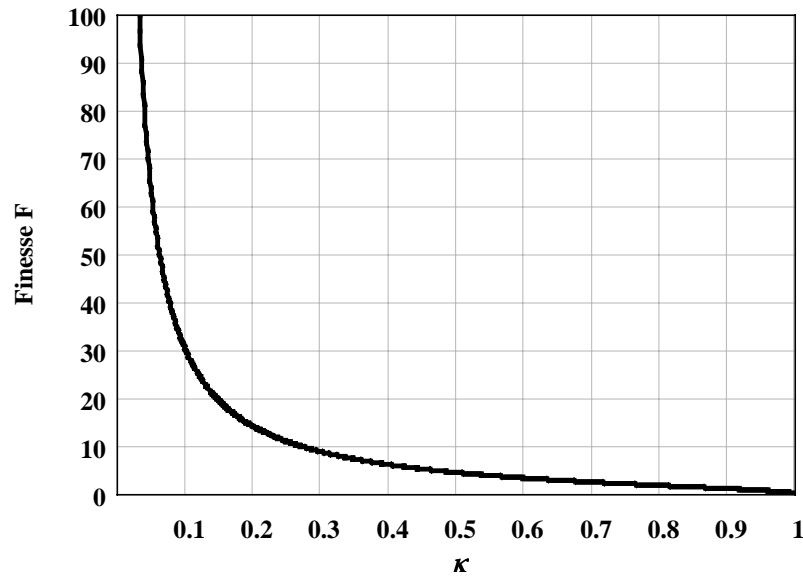


Fig. 23: Finesse depending on the coupling factor  $\kappa$  at the point of maximum on-off ratio.

The finesse depending on the intensity attenuation coefficient of the ring  $\alpha$  at the point of maximum on-off ratio [Eq. (2.27)] for a ring resonator with  $R = 100 \mu\text{m}$  is shown in Fig. 24.

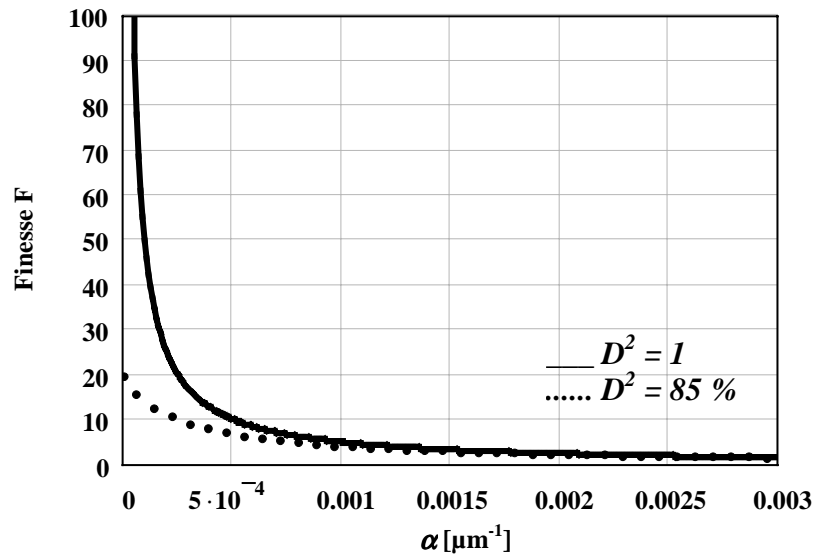


Fig. 24: Finesse depending on  $\alpha$  at the point of maximum on-off ratio.



A high finesse  $F$  ( $> 10$ ) can be realized using a coupling factor  $\kappa < 0.3$ , a coupler with  $\gamma < 15\%$  and an intensity attenuation coefficient of the ring  $\alpha < 0.0001 \mu\text{m}^{-1}$ .

The distance between two resonance peaks is calculated as follows: The phase constant which corresponds to  $\phi = 2 \cdot m \cdot \pi$  is defined as  $k$ . The phase constant which corresponds to  $\phi = 2 \cdot (m + 1) \cdot \pi$  is defined as  $k + \Delta k$ .

The frequency shift  $\Delta f$  and the wavelength shift  $\Delta \lambda$  are related to the variation of the phase constant  $\Delta k$  as  $\Delta f = \frac{c}{2\pi} \cdot \Delta k$  and  $\Delta \lambda = -\left(\frac{\lambda^2}{2\pi}\right) \cdot \Delta k$ . The resonance spacing in terms of the frequency  $f$  and wavelength  $\lambda$  are given by:

$$\Delta f = \frac{c}{n_{gr} \cdot L} \quad (2.30)$$

$$\Delta \lambda = \left| -\frac{\lambda^2}{n_{gr} \cdot L} \right| \quad (2.31)$$

where  $n_{gr}$  is the group refractive index, which is defined as:

$$n_{gr} \equiv n_{eff} - \lambda \frac{dn_{eff}}{d\lambda} \quad (2.32)$$

The frequency spacing between two resonance peaks is called the free spectral range (FSR).

Using  $\delta\phi = \delta(k_n \cdot L) = \frac{2\pi}{F}$ , the FWHM  $\delta\phi$  in terms of frequency and wavelength at the resonance peaks are given by:

$$\delta f = \frac{c}{F \cdot n_{gr} \cdot L} \quad (2.33)$$

$$\delta \lambda = \frac{\lambda^2}{F \cdot n_{gr} \cdot L} \quad (2.34)$$

The finesse can also be calculated using the FSR ( $\Delta f$  or  $\Delta \lambda$ ) and the FWHM ( $\delta f$  or  $\delta \lambda$ ) of a filter and is given by:

$$\text{in the frequency domain: } \frac{\Delta f}{\delta f} = \frac{\frac{c}{n_{gr} L}}{\frac{c}{F n_{gr} L}} = F \quad (2.35)$$

$$\text{in the wavelength domain: } \frac{\Delta \lambda}{\delta \lambda} = \frac{\frac{\lambda^2}{n_{gr} L}}{\frac{\lambda^2}{F n_{gr} L}} = F \quad (2.36)$$

Another value for the characterization of ring resonators is the  $Q$  factor, which is the stored energy divided by the power lost per optical cycle. It has the form:

$$Q = \frac{f_0}{\delta f} = \frac{\lambda_0}{\delta \lambda} \quad (2.37)$$

The  $Q$  factor is the ratio of the absolute frequency  $f_0$  or absolute wavelength  $\lambda_0$  to the 3 dB bandwidth ( $\delta f$  or  $\delta \lambda$ ). The shape and the bandwidth ( $\delta f$  or  $\delta \lambda$ ) of the filter response is determined by the  $Q$  factor.

The finesse and the  $Q$  factor are both important when one is interested in both the FSR ( $\Delta f$  or  $\Delta \lambda$ ) and the 3 dB bandwidth ( $\delta f$  or  $\delta \lambda$ ). They are related by:

$$\frac{Q}{F} = \frac{f_0}{\Delta f} = \frac{\lambda_0}{\Delta \lambda} \quad (2.38)$$

The  $Q$  factor depending on the finesse  $F$  for a ring resonator with a radius  $R = 100 \mu\text{m}$ ,  $50 \mu\text{m}$  and  $10 \mu\text{m}$ , a group refractive index  $n_{gr} = 3.44$  at a wavelength of  $\lambda = 1.55 \mu\text{m}$  is shown in Fig. 25.

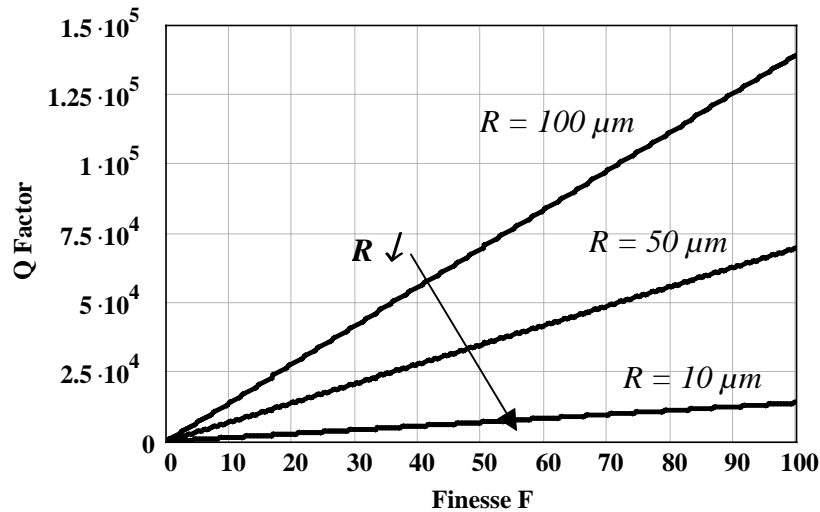


Fig. 25:  $Q$  factor depending on the finesse  $F$  for a specific radius  $R$ .

A high finesse  $F (> 100)$  and a low  $Q$  factor ( $< 2.5 \cdot 10^4$ ) is obtained, for example, for ring resonators with a low radius ( $R < 20 \mu\text{m}$ ). A ring resonator for a given specific bandwidth ( $\delta f$  or  $\delta \lambda$ ) can be designed using the following steps:

$$\delta f \text{ or } \delta \lambda \xrightarrow{\text{Eq. 2.35}} Q \xrightarrow{\text{Eq. 2.36}} F, R \xrightarrow{\text{Eq. 2.26, Eq. 2.27}} \kappa, \alpha \text{ (point of maximum on-off ratio)}$$

High  $Q$  cavities can serve for example as building blocks for optical signal processing applications or for laser applications where high quality factors are required. Ideal interleavers require a finesse  $F = 2$ . The basic figures for the description of a single ring resonator with one input waveguide have been presented. This model is extended to multiple coupled ring resonators in the following sections.

The single ring resonator (SRR), which has two adjacent waveguides for in- and out- coupling is shown in Fig. 26.

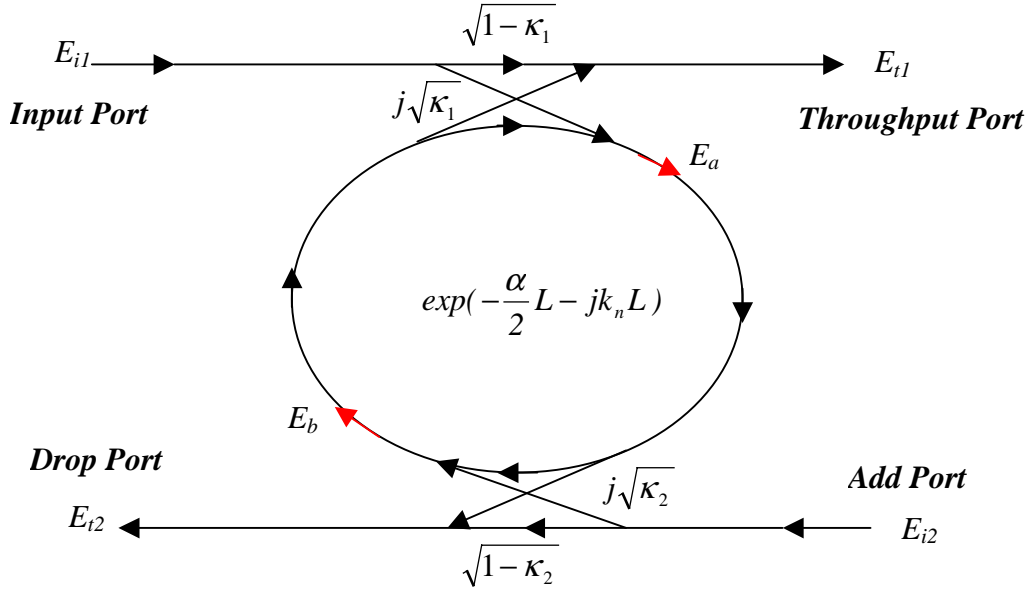


Fig. 26: The single ring resonator with two adjacent waveguides.

For simplification, the calculation of the intensity relation [61] does not take into account coupling losses ( $D^2 = 1$ ).

$$E_a = E_{il} j\sqrt{\kappa_1} + E_b \sqrt{1-\kappa_1} e^{-\frac{\alpha L}{2} - jk_n \frac{L}{2}} \quad (2.39)$$

$$E_b = E_a \sqrt{1-\kappa_2} e^{-\frac{\alpha L}{2} - jk_n \frac{L}{2}} \quad (2.40)$$

$$E_a = \frac{E_{il} j\sqrt{\kappa_1}}{1 - \sqrt{1-\kappa_1} \sqrt{1-\kappa_2} e^{-\frac{\alpha}{2} L - jk_n L}} \quad (2.41)$$

$$E_b = \frac{E_{il} j\sqrt{\kappa_1}}{1 - \sqrt{1-\kappa_1} \sqrt{1-\kappa_2} e^{-\frac{\alpha}{2} L - jk_n L}} \cdot \sqrt{1-\kappa_2} e^{-\frac{\alpha L}{2} - jk_n \frac{L}{2}} \quad (2.42)$$

$$E_{tl} = E_b e^{-\frac{\alpha L}{2} - jk_n \frac{L}{2}} j\sqrt{\kappa_1} + E_{il} \sqrt{1-\kappa_1} \quad (2.43)$$

$$E_{t2} = E_a e^{-\frac{\alpha L}{2} - jk_n \frac{L}{2}} j\sqrt{\kappa_2} \quad \text{at } E_{i2} = 0 \quad (2.44)$$

$$\frac{E_{tl}}{E_{il}} = \frac{-\kappa_1 \sqrt{1-\kappa_2} e^{-\frac{\alpha}{2} L - jk_n L} + \sqrt{1-\kappa_1} - (1-\kappa_1) \sqrt{1-\kappa_2} e^{-\frac{\alpha}{2} L - jk_n L}}{1 - \sqrt{1-\kappa_1} \sqrt{1-\kappa_2} e^{-\frac{\alpha}{2} L - jk_n L}} = \frac{-\sqrt{1-\kappa_2} e^{-\frac{\alpha}{2} L - jk_n L} + \sqrt{1-\kappa_1}}{1 - \sqrt{1-\kappa_1} \sqrt{1-\kappa_2} e^{-\frac{\alpha}{2} L - jk_n L}} \quad (2.45)$$

$$\frac{E_{t2}}{E_{il}} = \frac{-\sqrt{\kappa_1 \cdot \kappa_2} e^{-\frac{\alpha L}{2} - jk_n \frac{L}{2}}}{1 - \sqrt{1-\kappa_1} \sqrt{1-\kappa_2} e^{-\frac{\alpha}{2} L - jk_n L}} \quad (2.46)$$

$$\frac{I_{t1}}{I_{i1}} = \left| \frac{E_{t1}}{E_{i1}} \right|^2 = \frac{I - \kappa_1 - 2\sqrt{I - \kappa_1} \cdot \sqrt{I - \kappa_2} e^{-\frac{\alpha}{2}L} \cos(k_n L) + (I - \kappa_2) e^{-\alpha L}}{I + (I - \kappa_1)(I - \kappa_2) e^{-\alpha L} - 2\sqrt{I - \kappa_1} \cdot \sqrt{I - \kappa_2} e^{-\frac{\alpha}{2}L} \cos(k_n L)} \quad (2.47)$$

$$\frac{I_{t2}}{I_{i1}} = \left| \frac{E_{t2}}{E_{i1}} \right|^2 = \frac{\kappa_1 \cdot \kappa_2 e^{-\frac{\alpha}{2}L}}{I + (I - \kappa_1)(I - \kappa_2) e^{-\alpha L} - 2\sqrt{I - \kappa_1} \sqrt{I - \kappa_2} e^{-\frac{\alpha}{2}L} \cos(k_n L)} \quad (2.48)$$

Equations (2.45) and (2.46) will be rewritten using (2.18) and the following parameters:

$$\begin{aligned} y_1 &= \sqrt{I - \kappa_1} \\ y_2 &= \sqrt{I - \kappa_2} \end{aligned} \quad (2.49)$$

The intensity relations Eq. (2.45) and (2.46) are then given by:

$$\frac{I_{t1}}{I_{i1}}(\phi) = \left| \frac{E_{t1}}{E_{i1}} \right|^2 = I - \frac{(I - y_1^2) \cdot (I - y_2^2 x^2)}{(I - y_1 y_2 x)^2 + 4 y_1 y_2 x \sin^2\left(\frac{\phi}{2}\right)} \quad (2.50)$$

$$\frac{I_{t2}}{I_{i1}}(\phi) = \left| \frac{E_{t2}}{E_{i1}} \right|^2 = \frac{(I - y_1^2) \cdot (I - y_2^2) \cdot x}{(I - y_1 y_2 x)^2 + 4 y_1 y_2 x \sin^2\left(\frac{\phi}{2}\right)} \quad (2.51)$$

The full-width at half-maximum (FWHM) is given for this configuration by:

$$\delta\phi = 2 \frac{I - y_1 y_2 x}{\sqrt{y_1 y_2 x}} \quad (2.52)$$

The finesse F is given by:

$$F = \frac{2\pi}{\delta\phi} = \frac{\pi \sqrt{y_1 y_2 x}}{I - y_1 y_2 x} \quad (2.53)$$

The filter response of an SRR with two waveguides and coupling factors of  $\kappa_1 = \kappa_2 = 0.2$  in both symmetrical couplers is shown in Fig. 27. The internal ring losses are assumed to be fully compensated ( $\alpha = 0$ ).

The maximum and minimum transmission is calculated as follows.

For the throughput port:

$$T_{max} = \frac{(y_1 + y_2 x)^2}{(I + y_1 y_2 x)^2} \quad (2.54)$$

$$T_{min} = \frac{(y_1 - y_2 x)^2}{(I - y_1 y_2 x)^2} \quad (2.55)$$

For the drop port:

$$T_{max} = \frac{(I - y_1^2) \cdot (I - y_2^2) \cdot x}{(I - y_1 y_2 x)^2} \quad (2.56)$$

$$T_{min} = \frac{(1 - y_1^2) \cdot (1 - y_2^2) \cdot x}{(1 + y_1 y_2 x)^2} \quad (2.57)$$

The on-off ratio is calculated using equations (2.52) and (2.55) and is given by:

$$\frac{T_{max(ThroughputPort)}}{T_{min(DropPort)}} = \frac{(y_1 + y_2 x)^2}{(1 - y_1^2) \cdot (1 - y_2^2) \cdot x} \quad (2.58)$$

The on-off ratio for  $\kappa_1 = \kappa_2 = \kappa$  and  $\alpha = 0$  in dB is given by:

$$10 \log \left( \frac{4(1 - \kappa)}{\kappa^2} \right) [dB] \quad (2.59)$$

The value for the on-off ratio for coupling factors of  $\kappa_1 = \kappa_2 = 0.2$  for both couplers and compensated waveguide losses ( $\alpha = 0$ ) is calculated to be 19 dB.

The on-off ratio will be maximum ( $> 20$  dB) for coupling factors  $\kappa_1 = \kappa_2 < 0.2$  in both couplers and compensated waveguide losses ( $\alpha = 0$ ).

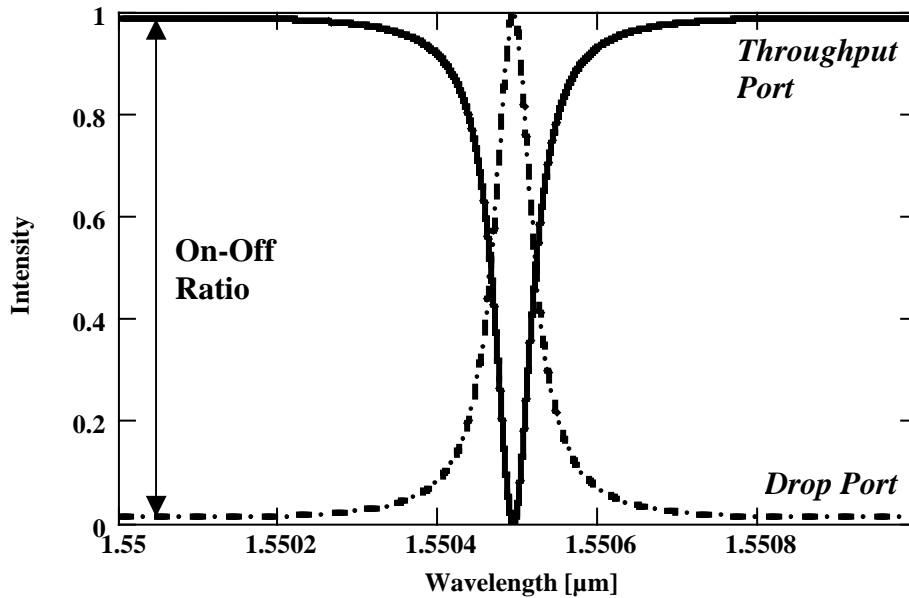


Fig. 27: Transmission characteristic of the ring resonator (Fig. 26) with  $R = 150 \mu m$ ,

$\kappa_1 = \kappa_2 = 0.2$ ,  $\alpha = 0$ .

The output intensity  $I_{tl}$  at the throughput port [Eq. (2.45)] will be zero at resonance ( $k_n L = 2m\pi$ ), which indicates that the resonance wavelength is fully extracted by the resonator, for identical symmetrical codirectional couplers  $\kappa_1 = \kappa_2$  if  $\alpha = 0$ . The value of  $\alpha = 0$  can only be achieved by the implementation of an SOA inside the ring resonator to compensate the waveguide losses. The value of the intensity attenuation coefficient  $\alpha$  is fixed in a purely passive ring resonator. A possibility of achieving minimum intensity ( $I_{tl}/I_{il} = 0$ ) at resonance of the output transmission  $I_{tl}$  at the throughput port is to adjust the coupling factors  $\kappa_1$ ,  $\kappa_2$  to the intensity attenuation coefficient  $\alpha$ . From equation (2.43) we obtain:

$$\frac{E_{t1}}{E_{i1}} = \frac{-\sqrt{1-\kappa_2}e^{-\frac{\alpha}{2}L} + \sqrt{1-\kappa_1}}{1 - \sqrt{1-\kappa_1}\sqrt{1-\kappa_2}e^{-\frac{\alpha}{2}L}} \equiv 0 \Rightarrow -\sqrt{1-\kappa_2}e^{-\frac{\alpha}{2}L} + \sqrt{1-\kappa_1} = 0$$

$$\Rightarrow e^{-\frac{\alpha}{2}L} = \sqrt{\frac{1-\kappa_1}{1-\kappa_2}} \quad (2.60)$$

The Eq. (2.58) will become one for identical couplers and  $\alpha = 0$ . Other configurations for  $\kappa_1$  and  $\kappa_2$  can be calculated from this expression. For example if the intensity attenuation coefficient  $\alpha$  for a ring resonator ( $R = 100 \mu\text{m}$ ) with the configuration shown in Fig. 26 is  $\alpha = 0.0005 \mu\text{m}^{-1}$  the coupling coefficients  $\kappa_1$  and  $\kappa_2$  have to obey the following equation:

$$\sqrt{\frac{1-\kappa_1}{1-\kappa_2}} = e^{-2\pi R \frac{\alpha}{2}} \quad (2.61)$$

As an example, the value for  $\kappa_2$  is chosen to be  $\kappa_2 = 0.2$ , the value for  $\kappa_1$  is calculated from Eq. (2.59) to be  $\kappa_1 = 0.42$ . Using different coupling factors  $\kappa_1$ ,  $\kappa_2$  either the throughput port can be minimized or the drop port can be maximized on resonance. It is essential for system applications, that the signal on resonance with the ring resonator is entirely extracted from the remaining signals off resonance with the ring resonator. Therefore the focus lies in minimizing the throughput port on resonance.

The practical realization is very difficult because the intensity attenuation coefficient  $\alpha$  and the coupling factors  $\kappa_1$ ,  $\kappa_2$  can not be determined with the demanded high accuracy to match the condition in (2.58). One possible solution would be to use tunable couplers.

A possible configuration of a ring resonator with two input / output waveguides (Fig. 26) should have symmetrical couplers with coupling factors  $\kappa_1 = \kappa_2 < 0.2$  for an on-off ratio  $> 20 \text{ dB}$  and an integrated SOA for realizing an intensity attenuation coefficient  $\alpha$  of the ring which is  $\alpha = 0$ .

In order to achieve a box like filter characteristic, double and triple ring resonator configurations will be discussed in the following sections.

### 2.3.2 The double ring resonator (DRR)

The schematic diagram of a double ring resonator (DRR) is shown below. The input field  $E_{i1}$  is coupled into port 1. The output field is obtained at the throughput port  $E_{t1}$  or at the drop port  $E_{t2}$ . Another input field  $E_{i2}$  can be inserted at the add port of the device.

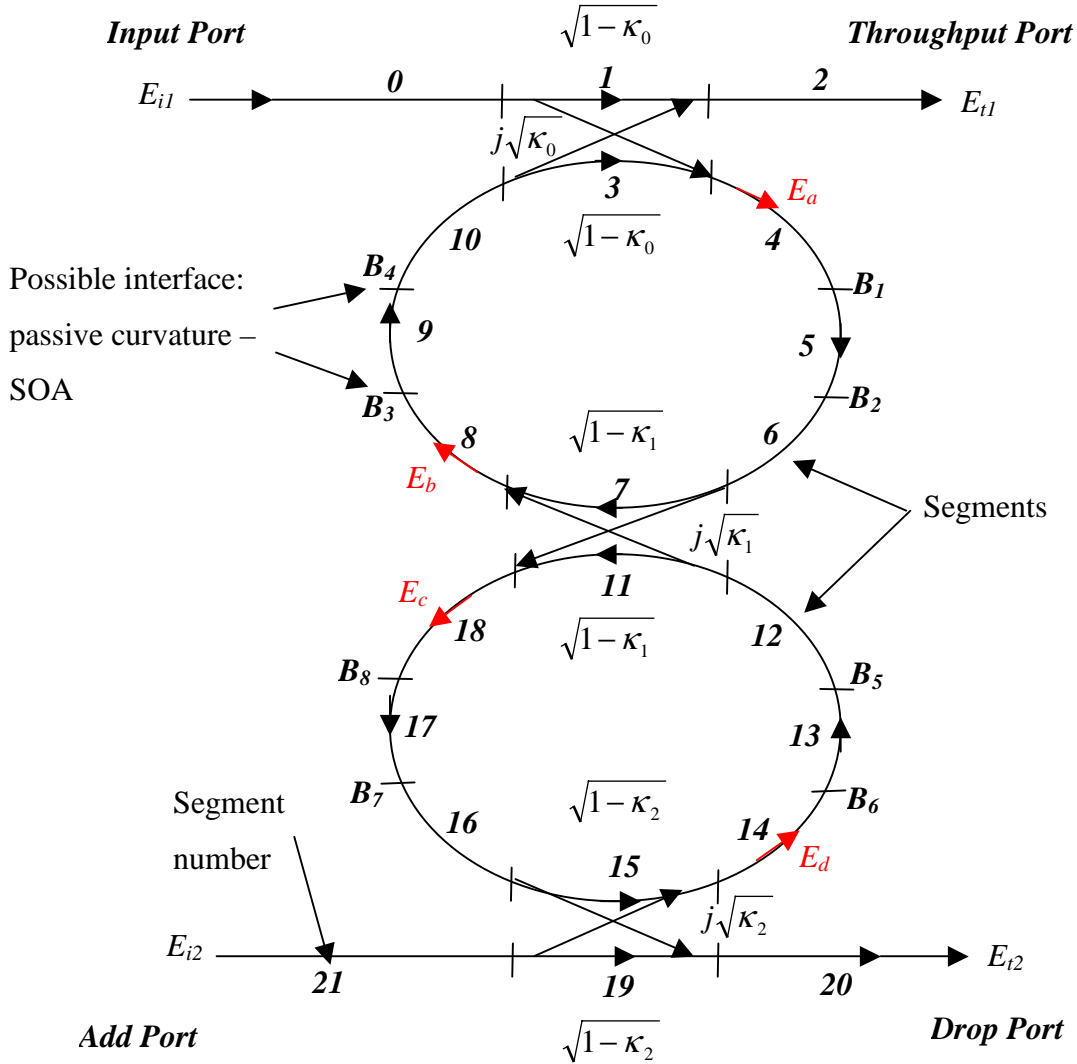


Fig. 28: The double ring resonator.

The calculation models described in the previous sections are well suited for devices with a homogenous refractive index in the resonator. The model has to be extended in such a way, that the implementation of active sections, changes of the refractive index in one part of the resonator due to local heating, transition losses for example at the active – passive interface, at the interface straight waveguide – curved section, coupling losses and material losses in each segment are considered. In order to account for these specific details, the ring resonator configuration is divided into different segments as shown for the DRR in Fig. 28. The electric field of the traveling wave in each segment is described by the following equation:

$$E_{\text{Segment}} = E_A \cdot \exp \left[ \frac{\alpha_{\text{Segment}}}{2} L_{\text{Segment}} - j k_{n \text{ Segment}} L_{\text{Segment}} \right] \quad (2.62)$$

where  $E_A$  is the amplitude of the electric field,  $\alpha_{Segment}$  is the intensity attenuation coefficient,  $L_{Segment}$  is the length and  $k_{n\ Segment}$  is the wave propagation constant of each segment. The inserted electric field at the upper port is  $E_{il}$ . The electric field  $E_{t1}$  and  $E_{t2}$  of the throughput port and drop port are obtained by determining the electric field at the specific points defined in Fig. 28 as  $E_a$ ,  $E_b$ ,  $E_c$  and  $E_d$ . The fraction of the electric field passing for e.g. the active – passive interface is denoted with  $B_{0.7}$ . The matrix is solved using the determinant method (see Appendix). An example of the transmission spectrum of a DRR is shown in Fig. 29.

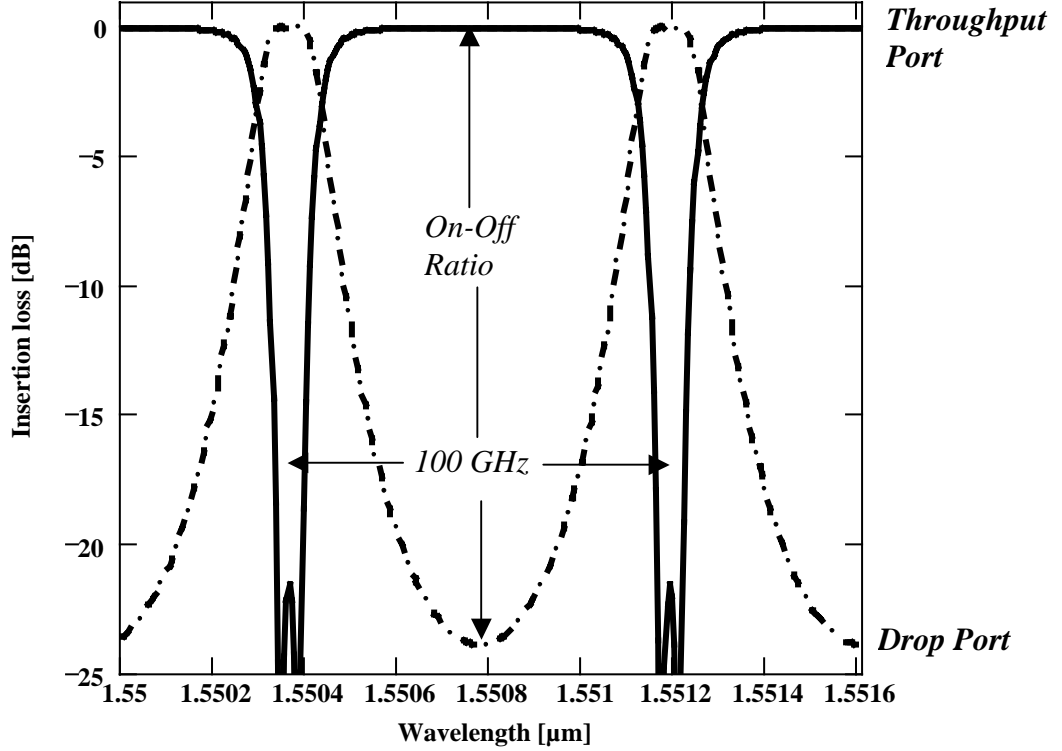


Fig. 29: Simulated box-like filter response of a DRR with  $\alpha_{Segment} = 0$ ,  $\kappa_0 = 0.5$ ,  $\kappa_l = 0.13$ ,  $\kappa_2 = 0.5$ ,  $n_{gr} = 3.46$ ,  $R_{l,2} = 134 \mu\text{m}$ .

The coupling coefficients are  $\kappa_0 = 0.5$ ,  $\kappa_l = 0.13$ ,  $\kappa_2 = 0.5$  from top to bottom. The ring radius  $R_{l,2} = 134 \mu\text{m}$  is chosen to achieve a channel spacing of 100 GHz. The group refractive index is assumed to be  $n_{gr} = 3.46$  and the internal losses are fully compensated ( $\alpha_{Segment} = 0$ ). Ring resonators coupled in series enable the realization of a box-like transmission characteristic.

The transfer function for the throughput port  $\frac{E_{t1}}{E_{il}}(\phi_1, \phi_2)$  and for the drop port  $\frac{E_{t2}}{E_{il}}(\phi_1, \phi_2)$  are derived for a uniform intensity attenuation coefficient in both rings which are denoted by  $\alpha_{Ring1}$ ,  $\alpha_{Ring2}$  respectively. The circumference of the rings are denoted by  $L_{Ring1}$  (radius  $R_1$ ) and  $L_{Ring2}$  (radius  $R_2$ ). The phase terms for the rings are  $\phi_1$ ,  $\phi_2$ . There is no input from the add port,



$E_{i2} = 0$ . This simplification can be extended incorporating all segments using the formulas presented in the appendix.

$$\frac{E_{t2}}{E_{i1}}(\phi_1, \phi_2) = \frac{\kappa_0 e^{-\frac{\alpha_{Ring1}}{2} L_{Ring1} - j\phi_1} \left[ \sqrt{1 - \kappa_2} e^{-\frac{\alpha_{Ring2}}{2} L_{Ring2} - j\phi_2} - \sqrt{1 - \kappa_1} \right]}{1 - e^{-\frac{\alpha_{Ring2}}{2} L_{Ring2} - j\phi_2} \sqrt{1 - \kappa_2} \sqrt{1 - \kappa_1} - e^{-\frac{\alpha_{Ring1}}{2} L_{Ring1} - j\phi_1} \sqrt{1 - \kappa_1} \sqrt{1 - \kappa_0} + e^{-\frac{\alpha_{Ring1}}{2} L_{Ring1} - j\phi_1} e^{-\frac{\alpha_{Ring2}}{2} L_{Ring2} - j\phi_2} \sqrt{1 - \kappa_2} \sqrt{1 - \kappa_0}} \quad (2.63)$$

$$\frac{E_{t2}}{E_{i1}}(\phi_1, \phi_2) = \frac{-j\sqrt{\kappa_2 \kappa_1 \kappa_0} e^{-\frac{\alpha_{Ring1}}{2} L_{Ring1} - j\phi_1} e^{-\frac{\alpha_{Ring2}}{2} L_{Ring2} - j\phi_2}}{1 - e^{-\frac{\alpha_{Ring2}}{2} L_{Ring2} - j\phi_2} \sqrt{1 - \kappa_2} \sqrt{1 - \kappa_1} - e^{-\frac{\alpha_{Ring1}}{2} L_{Ring1} - j\phi_1} \sqrt{1 - \kappa_1} \sqrt{1 - \kappa_0} + e^{-\frac{\alpha_{Ring1}}{2} L_{Ring1} - j\phi_1} e^{-\frac{\alpha_{Ring2}}{2} L_{Ring2} - j\phi_2} \sqrt{1 - \kappa_2} \sqrt{1 - \kappa_0}} \quad (2.64)$$

The flatness of the filter response for the drop port can be described by a shape factor [62] which is defined as:

$$\text{Shape factor} = \frac{-1 \text{ dB bandwidth}}{-10 \text{ dB bandwidth}} = \frac{\left| \frac{\phi_{E_{t2}=-1\text{dB}}}{E_{i1}} - 2\pi \right|}{\left| \frac{\phi_{E_{t2}=-10\text{dB}}}{E_{i1}} - 2\pi \right|} \quad (2.65)$$

Instead of using the - 10 dB bandwidth in Eq. (2.63), the - 20 dB bandwidth could be used, the definition of the shape factor is arbitrary. The shape factor and the on-off ratio are the two essential parameters describing the behavior of a multiple coupled ring resonator filter. The aim is to realize a box-like filter response. The filter response shape of a single ring resonator filter with two input / output waveguides (Fig. 27), for example, is expressed by the Lorentzian function, the shape factor for the drop port is as small as 0.18.

The on-off ratio is calculated for a lossless DRR ( $\alpha_{Ring1} = \alpha_{Ring2} = 0$ ) where  $\kappa_0 = \kappa_2$ ,  $L_{Ring1} = L_{Ring2}$  and  $\phi_1 = \phi_2 = (2m+1)\pi$ .

The on-off ratio is:

$$\begin{aligned} 10 \log \left( \frac{I_{t1}}{I_{i1} \phi_1 = \pi(2m+1)} \right) - 10 \log \left( \frac{I_{t2}}{I_{i1} \phi_1 = \pi(2m+1)} \right) &= 10 \log \left( \left| \frac{E_{t1}}{E_{i1}} \right|^2 \right) - 10 \log \left( \left| \frac{E_{t2}}{E_{i1}} \right|^2 \right) \\ &= 20 \log \left( \frac{2\sqrt{1 - \kappa_0} + \sqrt{1 - \kappa_1}(2 - \kappa_0)}{\kappa_0 \sqrt{\kappa_1}} \right) [dB] \end{aligned} \quad (2.66)$$

The minimum transmission on resonance for the throughput port is obtained for [Eq. (2.61)]:

$$\frac{E_{t1}}{E_{i1}}(\phi_1 = \phi_2 = 2m\pi) = 0 \quad (2.67)$$

The value for the coupler in the center  $\kappa_1$  is calculated using Eq. (2.65) and setting  $\alpha_{Ring1} = \alpha_{Ring2} = 0$ ,  $\kappa_0 = \kappa_2$  and  $L_{Ring1} = L_{Ring2}$ .

$$\kappa_1 = 1 - \left( \frac{2\sqrt{1 - \kappa_0}}{\kappa_0 - 2} \right)^2 = \frac{\kappa_0^2}{(\kappa_0 - 2)^2} \quad (2.68)$$

The transmission from the drop port on resonance for this configuration would be 1, as there are no internal losses ( $\alpha_{Ring1} = \alpha_{Ring2} = 0$ ):

$$\frac{E_{t2}}{E_{i1}}(\phi_1 = \phi_2 = 2m\pi) = 1$$

There are basically two types of filter responses which can be realized with a DRR, a Lorentzian filter response and a box-like filter response. For a Lorentzian filter response, the coupling coefficients can be calculated from Eq. (2.66), for achieving minimum transmission for the throughput port and maximum transmission for the drop port on resonance. The coupling coefficients for a box-like filter response with a specific shape factor and a specific on-off ratio are evaluated using Eqs. (2.63) and (2.64). There are several solutions. One solution for the coupling coefficients for a DRR coupled in series with  $\alpha_{Ring1} = \alpha_{Ring2} = 0$ ,  $\kappa_0 = \kappa_2$  and  $L_{Ring1} = L_{Ring2}$  is  $\kappa_0 = \kappa_2 = 0.5$  for the outer couplers and the coupling factor in the center is within the range  $\kappa_1 = 0.125 - 0.14$  in order to achieve a box-like passband shape. The shape factor for the drop port for this double ring resonator configuration is 0.42. The achievable on-off ratio for this configuration is more than 20 dB [Eq. (2.64)].

A double ring resonator opens the possibility of expanding the FSR to the least common multiple of the FSR of individual ring resonators. This is done by choosing different radii in the DRR. In the case of different radii, the light passing through the DRR is launched from the drop port when the resonant conditions of the two single ring resonators are satisfied. The FSR of the DRR with two different radii is expressed by:

$$\text{FSR} = N \cdot \text{FSR}_1 = M \cdot \text{FSR}_2 \quad (2.69)$$

which leads to:

$$\text{FSR} = |M - N| \frac{\text{FSR}_1 \cdot \text{FSR}_2}{|\text{FSR}_1 - \text{FSR}_2|} \quad (2.70)$$

where N and M are natural and coprime numbers. The transfer functions are critically dependent on the coupling coefficients. The coupling coefficients  $\kappa_0$  and  $\kappa_2$  characterize the crosstalk between resonant peaks and spurious resonant peaks.

The calculated transmission spectrum of a DRR with  $R_1 = 274 \mu\text{m}$ ,  $R_2 = 342 \mu\text{m}$ ,  $\alpha_{\text{Ring1}} = \alpha_{\text{Ring2}} = 0.1 \text{ dB cm}^{-1}$ ,  $\kappa_0 = \kappa_2 = 0.57$  and  $\kappa_1 = 0.2$  is shown in Fig. 30. The FSR of resonator 1 is 50 GHz and the FSR of resonator 2 is 40 GHz. The FSR of the DRR is calculated using Eq. (2.67) to be 200 GHz ( $N = 4$ ,  $M = 5$ ). The sidemode suppression of the throughput port is more than 20 dB, but it is only 4 dB for the drop port. The different coupling factors can be realized within the tolerance margins of fabrication, but the sidemode suppression is not enough for the separation of optical channels in, for example, DWDM systems.

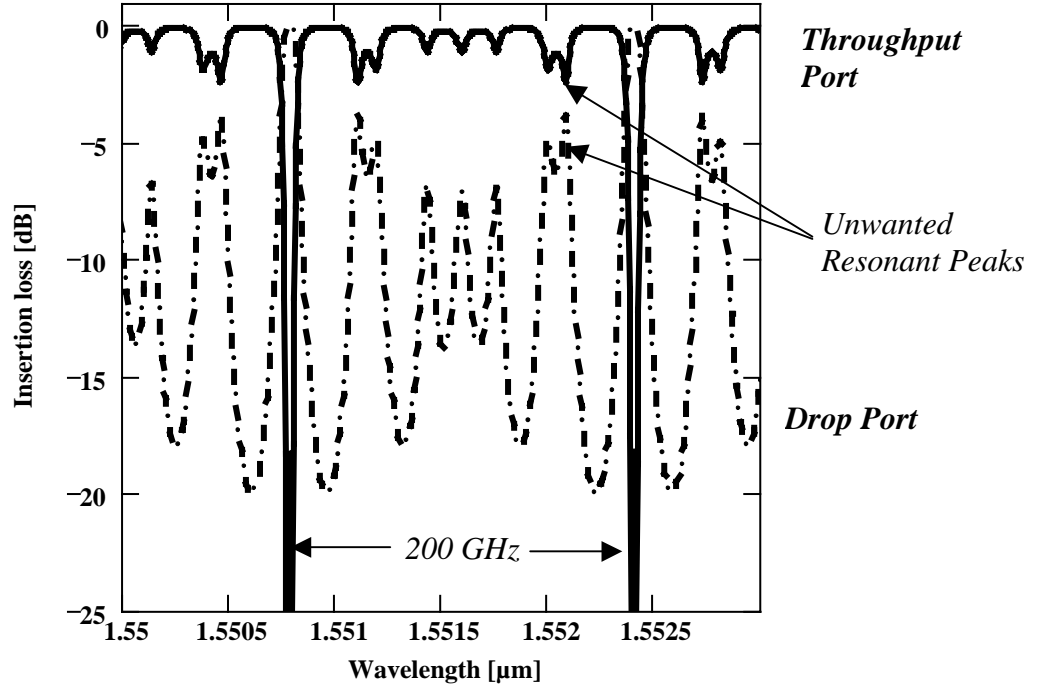


Fig. 30: DRR with  $R_1 = 274 \mu\text{m}$ ,  $R_2 = 342 \mu\text{m}$ ,  $\alpha_{\text{Ring1}} = \alpha_{\text{Ring2}} = 0.1 \text{ dB cm}^{-1}$ ,  $\kappa_0 = \kappa_2 = 0.57$ ,  $\kappa_1 = 0.2$  and an FSR of 200 GHz.

The use of two ring resonators with different radii opens the possibility to realize a larger FSR than would be achieved using only a single ring resonator. The transmission characteristic of the throughput port has mainly a Lorentzian shape. A box-like filter response could be realized using two parallel coupled DRRs ( $R_1 \neq R_2$ ). The use of such configurations as optical filters is limited by unwanted additional resonant peaks as shown in Fig. 30. Investigations on these types of filters have been performed in [63], [64] and [65].

### 2.3.3 The triple ring resonator (TRR)

The diagram of the calculation model of a triple ring resonator (TRR) is shown in Fig. 31. The transmission characteristic is derived as explained in the previous section 2.3.2. The equations for calculating the filter response are located in the appendix.

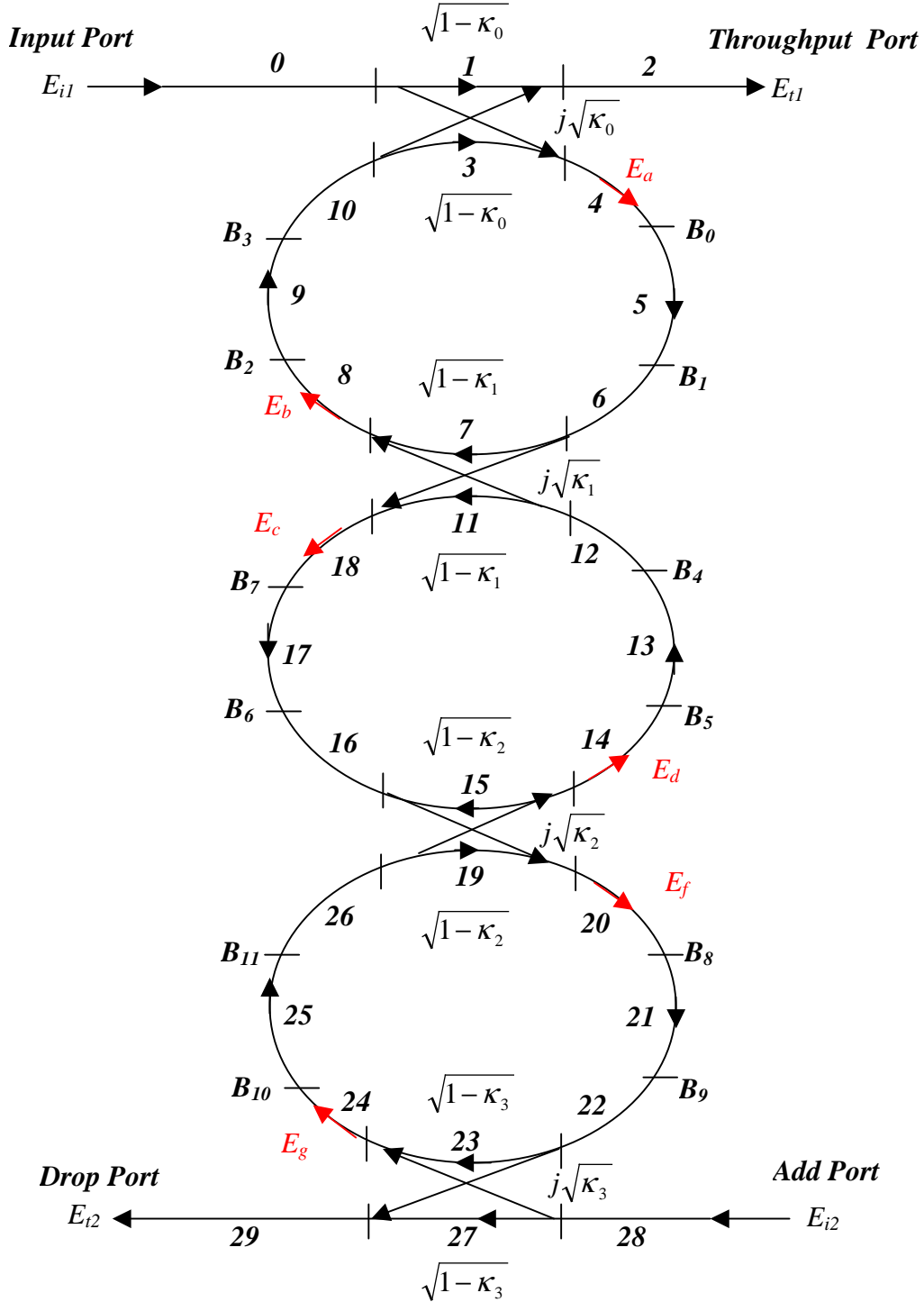


Fig. 31: The triple ring resonator.

To design a flat top filter response, the TRR is used to increase the shape factor and the on-off ratio of the throughput and the drop port. The filter design is performed in a similar way as

described in the previous section 2.3.2. The possible coupling coefficients  $\kappa_{0,3}$  are calculated for a certain on-off ratio and for a shape factor of 0.6 for the drop port. There are again various possible solutions. The calculation can be simplified by using symmetric coupling coefficients,  $\kappa_0 = \kappa_3$  and  $\kappa_1 = \kappa_2$ .

The transmission characteristic of a TRR configuration with coupling factors of  $\kappa_0 = \kappa_3 = 0.7$  for the outer couplers and  $\kappa_1 = \kappa_2 = 0.2$  for the couplers in the center with compensated losses ( $\alpha_{\text{Segment}} = 0$ ) is shown in Fig. 32.

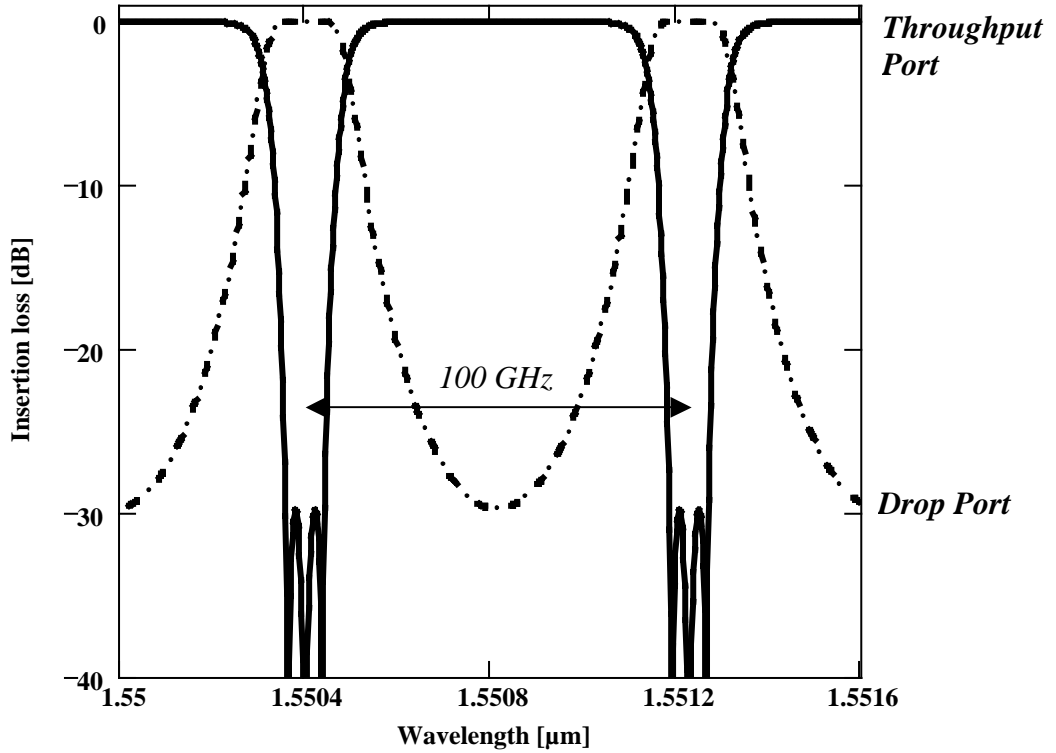


Fig. 32: Simulated box-like filter response for a TRR with coupling factors of  $\kappa_0 = 0.7$ ,  $\kappa_1 = 0.2$ ,  $\kappa_2 = 0.2$ ,  $\kappa_3 = 0.7$ , ( $\alpha_{\text{Segment}} = 0$ ),  $R = 134 \mu\text{m}$ .

The ring radius  $R = 134 \mu\text{m}$  is chosen to achieve a channel spacing of 100 GHz. The group refractive index is assumed to be 3.46. The on-off ratio is 30 dB. A steep roll-off and a high out of band rejection is achieved with this configuration. A possible solution for realizing a box-like filter shape and an on-off ratio of more than 30 dB is obtained for lossless resonators and for coupling factors within the tolerances of  $\kappa_0 = \kappa_3 = 0.65 - 0.7$  for the outer couplers and  $\kappa_1 = \kappa_2 = 0.18 - 0.26$  for the couplers in the center. Another possibility for realizing a box-like filter is using coupling factors of  $\kappa_0 = \kappa_3 = 0.5$  and  $\kappa_1 = \kappa_2 = 0.07 - 0.1$ . This configuration enables an on-off ratio of more than 30 dB and a shape factor for the drop port of 0.6.

A linear array of three SRRs is investigated and the calculation model which was described in section 2.3.1 is used to obtain the filter response. The simulation model of a parallel coupled TRR is shown in Fig. 33.

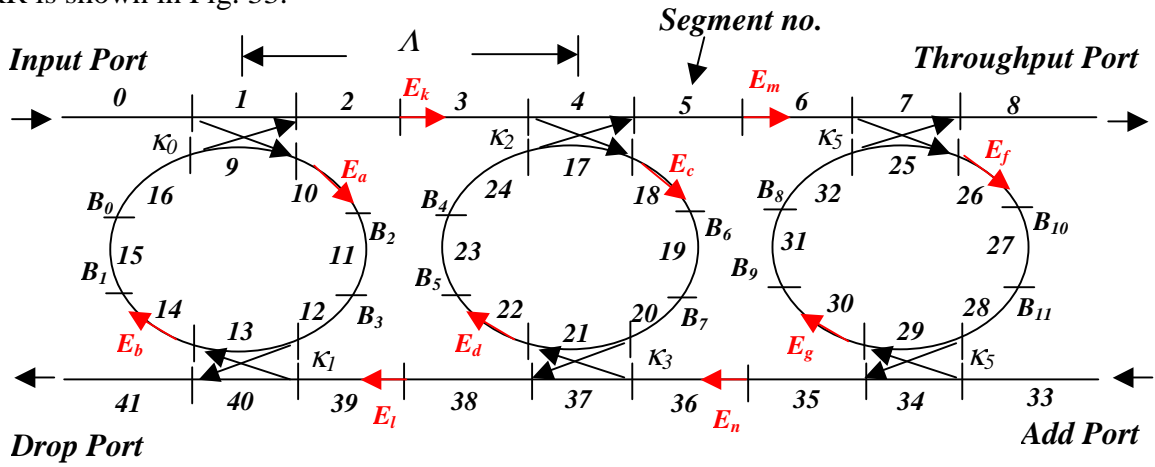


Fig. 33: The parallel coupled triple ring resonator.

The transmission characteristic is calculated for a linear array of identically spaced SRRs. The basic building block consists of an SRR with radius of curvature of the circular section  $R = 117 \mu\text{m}$ , and a length of  $200 \mu\text{m}$  for the coupling region and a length of  $300 \mu\text{m}$  for the straight sections 11 and 15. The SRR is assumed to be lossless and the refractive index which is subject to material and waveguide dispersion is the same for all segments. The distance between the resonators is  $\frac{1}{2}9 + 10 + 11 + 12 + \frac{1}{2}13$ , which is equal to half the circumference of the ring resonator. The response of the throughput and of the drop port is shown in Fig. 34. The ring resonators are phase matched.

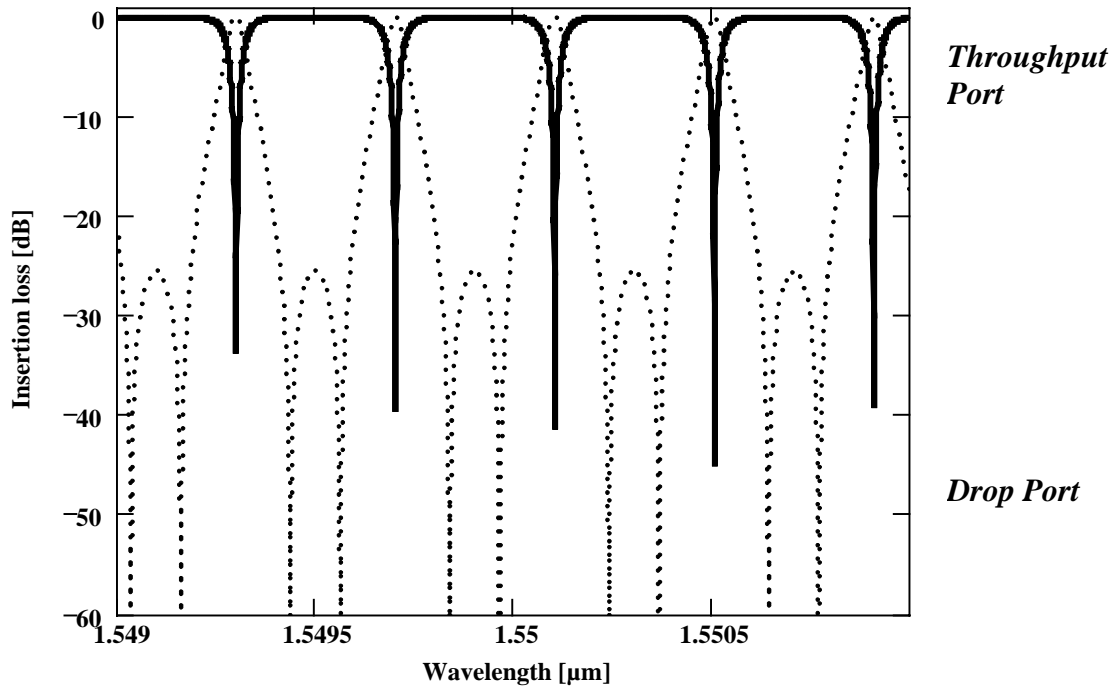


Fig. 34: Simulated parallel coupled TRR with  $\kappa_{0.5} = 0.1$  and an FSR of 50 GHz.

The shape factor for this arrangement is calculated to be 0.18. A flat passband characteristic can be achieved by a small shift of the resonance frequency of each used SRR. This controlled deviation from the resonance frequency enables the realization of optical filters with flat-top passbands, desirable for all-optical wavelength division multiplexed networks. A synthesis of an optical filter using a linear array of SRRs with two input / output waveguides is described in [49]. Here the transmission as a function of deviation from resonance of a symmetrically, equally spaced array of SRRs comprising one, two, and four elements is presented. The response from the drop port reveals that the Lorentzian characteristic of an SRR becomes flat with a stop band formed around the resonance center. The important feature to note is that a stop band is well defined for only a few elements in the array. This is due to the fact that, unlike the case of a periodical grating, here each element of the array is a high  $Q$  resonator with unity transmission at resonance, and therefore has a significant contribution to the overall transmission. If the ring resonators are lossless and symmetrical, then the transmission at resonance is unity. If an incoming signal is tuned exactly to one of the resonance frequencies, then the first ring of a linear array which consists of such rings will transmit the entire signal from the input to the output channel, leaving no signal power for the remaining rings in the chain. With loss, a similar situation occurs when the resonator is matched (section 2.3.1), with the exception that the transmission at resonance is less than unity due to dissipative loss in the first ring. If, on the other hand, the incoming signal is not exactly on a resonance frequency, or if the rings in the array are asymmetrical and unmatched, then the transmission of the first ring of the array is less than unity. In that case, the part of the signal not picked up by the first ring resonator continues to propagate down the input channel, where it is collected by the other elements of the array and added to the output signal. The collective contribution of all elements of the array enables augmentation of the transmitted signal, as well as flattening the transmission spectrum around resonance. However, all the contributions from the individual array elements add up coherently, if the phase difference between successive contributions is equal to an integer number of  $2\pi$  radians, that is,  $2k_n\Lambda = q2\pi$ , with  $q = 1, 2$ , etc where  $\Lambda$  is the spacing between the rings. This results in a resonant transmission spectrum of the array similar to the one obtained for a single element (2.28) but with an FSR given by:

$$\text{FSR}_B = \frac{c}{2n_{gr}\Lambda} \quad (2.71)$$

Only signals at frequencies fulfilling both resonance conditions (2.28) and (2.69) will be transmitted by the array. These frequencies are separated by integer numbers  $M$  and  $N$  of both FSRs. The free spectral range of the array is given by:

$$\Delta\nu_{array} = M \cdot \text{FSR}_B = N \cdot \text{FSR}_{SRR} \quad (2.72)$$

A proper choice of the integers M and N results in a Vernier effect and depression of all the resonance frequencies of either the ring resonators or the periodical array that do not fulfill both resonance conditions. This provides a means of synthesizing a transmission spectrum with an FSR much larger than that of the individual elements in the array. The condition for the ring spacing is evaluated from (2.28), (2.69) and (2.70) to:

$$\Lambda = \frac{M}{N} \pi \cdot R_{SRR} \quad (2.73)$$

where R is the ring radius. In a linear array  $\Lambda > 2R_{SRR}$ , where M and N should be selected that  $(M/N) > (2/\pi)$ . The Vernier effect will only be effective for intermodal suppression in situations where the elements in the array are strongly asymmetrical such that each is making a small contribution to the overall transmission. A calculated transmission spectrum of a nine-element array of lossless ring resonators is presented in [66]. The distance between parallel coupled SRRs and the influence on the filter shape is investigated theoretically in [56].

For the realization of a box-like filter response which implies a high shape factor (0.5 – 0.6), the serially coupled TRR configuration presented in the previous section is preferred. The filter response of the serially coupled TRR is mainly defined by the proper choice of the coupling factors. The phase has to be matched in both configurations. The advantage of the parallel coupled TRR is the possibility of increasing the FSR as was described before. This can only be done in the serially coupled configuration by choosing a smaller ring radius.

In this section, the mathematical tool for the description of the behavior of ring resonator configurations has been derived. The realization of these proposed "lossless" structures has to be performed in a semiconductor compound with a direct bandgap in order to fabricate active structures or integrate passive and active devices. The technology for the fabrication of the devices in the semiconductor compound GaInAsP / InP and its properties are described in the following sections.



### 3 The material system GaInAsP / InP

#### 3.1 The quaternary semiconductor compound GaInAsP

III/V semiconductors on the basis of InP with a direct bandgap are used for a variety of components in the all-optical network. The composition of the quaternary (III-V) semiconductor compound GaInAsP lattice matched to InP, can be changed, so that the bandgap can be adjusted in the range between 0.97  $\mu\text{m}$  und 1.65  $\mu\text{m}$ . The choice of the appropriate bandgap, which is smaller than the signal wavelength, enables the fabrication of passive, transparent waveguides with low loss ( $< 1 \text{ dB/cm}$ ). This material system is also used for the realization of lasers and optical amplifiers in the spectral window around 1.55  $\mu\text{m}$  and 1.3  $\mu\text{m}$ . Electronic components can also be fabricated with this material system, by incorporating Si, Be, Zn and realizing p- or n-doped areas. The properties of the semiconductor compound ( $\text{Ga}_x\text{In}_{1-x}\text{As}_y\text{P}_{1-y}$ ) can be described by Vegard's law. Using this law and the known semiconductor compounds GaAs, GaP, InAs and InP it is possible to determine the coefficients  $x$  and  $y$  [67].

$$B(\text{Ga}_x\text{In}_{1-x}\text{As}_y\text{P}_{1-y}) = x y B(\text{GaAs}) + x (1-y) B(\text{GaP}) + y (1-x) B(\text{InAs}) + (1-x) (1-y) B(\text{InP})$$

where  $B$  is the lattice constant. The composition of the semiconductor compound is displayed over the bandgap energy or the bandgap wavelength at room temperature in most diagrams and not  $x$  and  $y$ . The waveguide material used for the realization of the devices in the following has a bandgap wavelength of  $\lambda_g = 1.06 \mu\text{m}$  at room temperature and is written as Q(1.06). The bandgap of some semiconductors is displayed in Fig. 35.

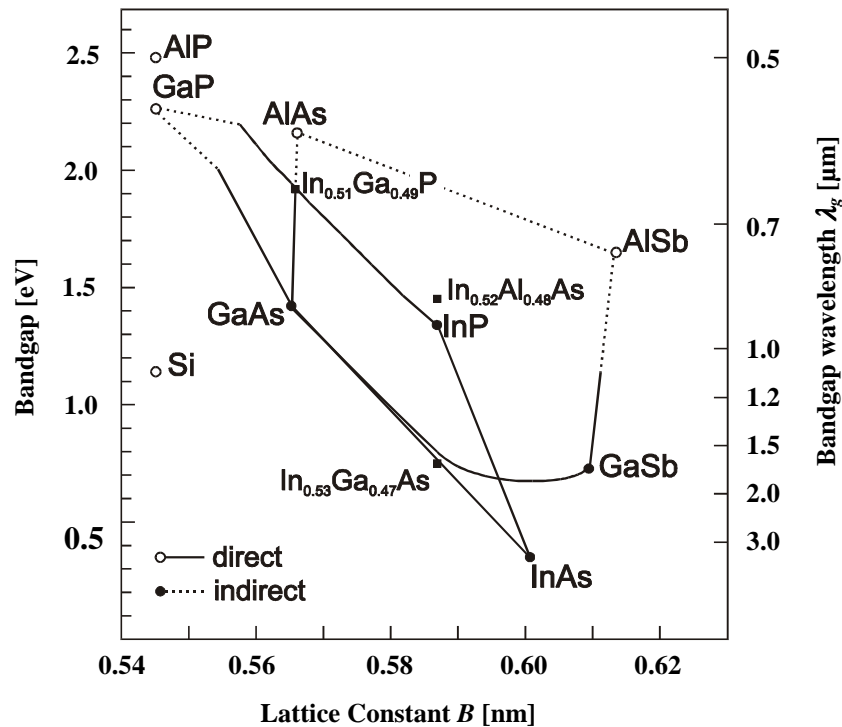


Fig. 35: Bandgap of some semiconductor compounds.

There have been good experiences at the Heinrich-Hertz-Institute with the quaternary Q(1.06) material regarding the fabrication and development of waveguides. This is one of the main reasons why the material was chosen to realize the ring resonators.

The basic material properties of InP and of the semiconductor compound GaInAsP are summarized in the table below.

	Symbol	Unit	InP	Ga <sub>x</sub> In <sub>1-x</sub> As <sub>y</sub> P <sub>1-y</sub>
Lattice constant	B	nm	0.58688	
Lattice match to InP				$y=2.202x/(1+0.0659y)$
Bandgap energy	$W_g$	eV	1.35	$1.35 - 0.72 y + 0.12 y^2$
Electron mass/ $m_0$	$m_e/m_0$		0.077	$0.07-0.0308 y$
Heavy hole mass/ $m_0$	$m_{hh}/m_0$		0.6	$0.6 - 0.218 y + 0.07 y^2$
Light hole mass/ $m_0$	$m_{lh}/m_0$		0.12	$0.12 - 0.078 y + 0.002 y^2$
Effective index ( $\lambda = 1.55 \mu\text{m}$ )	$n_{\text{eff}}$		3.169	
Dielectric constant (static)	$\epsilon_s$		12.35	$12.35 + 1.62 y - 0.055 y^2$
Dielectric constant (high Frequency)	$\epsilon_\infty$		9.52	$9.52 + 2.06 y - 0.205 y^2$
Density	$\rho$	$\text{g cm}^{-3}$	4.81	$4.81 + 0.74 y$
$\Delta W_g/\Delta T$		$10^{-4}$ eV/K	-2.67	$-2.67 + 0.102 y + 0.073 y^2$
Temperature dependence of the refractive index	$\frac{1}{n} \cdot \frac{dn}{dT}$	$\text{K}^{-1}$	$2.7 \cdot 10^{-5}$	
Length increase due to temperature	$\frac{1}{l} \cdot \frac{dl}{dT}$	$\text{K}^{-1}$	$0.475 \cdot 10^{-5}$	

Table 2: Physical properties of InP and of lattice matched Ga<sub>x</sub>In<sub>1-x</sub>As<sub>y</sub>P<sub>1-y</sub> at room temperature (300 K) [67], [68].

### 3.2 Dispersion

In classical optics, "dispersion" is used to denote the wavelength dependence of the refractive index in matter, ( $dn/d\lambda$  , where  $n$  is the refractive index and  $\lambda$  is the wavelength) caused by interaction between the matter and light. In communication technology, "dispersion" is used to describe any process by which an electromagnetic signal propagating in a physical medium is degraded because the various wave components (i.e., frequencies) of the signal have different propagation velocities within the physical medium.

Material dispersion causes different wavelengths to travel at different speeds due to the variation of the refractive index of the fiber core with wavelength. However, part of the light travels also in the cladding of the fiber, which has a different refractive index again and therefore propagates right through it at a different speed to the core – an effect known as waveguide dispersion. Material and waveguide dispersion are combined to give an overall effect called "chromatic dispersion."

The allowed chromatic dispersion in an optical network is inversely proportional to the square of the transmitted bit rate, so as data rates increase, dispersion tolerances decreases dramatically. While 2.5 Gbit/s networks can tolerate 16000 ps/nm of dispersion, 10 Gbit/s networks can tolerate only 1200 ps/nm and at 40 Gbit/s the tolerance drops to only 60 ps/nm of dispersion. In addition, 40 Gbit/s systems require a wider modulation spectrum. A 12 GHz wide spectrum is typical for 10 Gbit/s, for 40 Gbit/s, it can be as high as 50 GHz, which means the total dispersion per channel is higher. Chromatic dispersion has a fixed, stable component in addition to a dynamic one. Most of the fixed dispersion is caused by the fiber and is predictable as a function of the type of fiber and the distance. In addition, the component present on the optical path add a smaller, fixed contribution. A dynamic contribution must be added to the fixed one. Since many passive components do not have a simple flat or linear dispersion curve, laser drift (caused by aging or temperature change) can lead to dispersion fluctuations that are nonlinear and hard to predict. Another important type of dispersion is the polarization mode dispersion (PMD). PMD is caused by light traveling faster in one polarization plane compared to another. Fundamentally, it is caused by the core of the fiber not being perfectly round in cross section and by birefringence which is introduced by mechanical forces. As a result, the optical thickness is not absolutely identical on every possible axis.

The following section focuses on the wavelength dependence of the refractive index of the material used for fabricating the devices. The factor  $dn/d\lambda$  which is necessary for the simulation of the filter characteristic described in section 2.2 is derived for the wavelength range between 1.5  $\mu\text{m}$  and 1.6  $\mu\text{m}$ .

### 3.2.1 Dispersion in GaInAsP / InP

The wavelength dependence of the refractive index of the GaInAsP / InP material can be calculated using the method described in [69]. The effective refractive index of quaternary GaInAsP / InP material with a bandgap wavelength of 1.06  $\mu\text{m}$  is shown in Fig. 36.

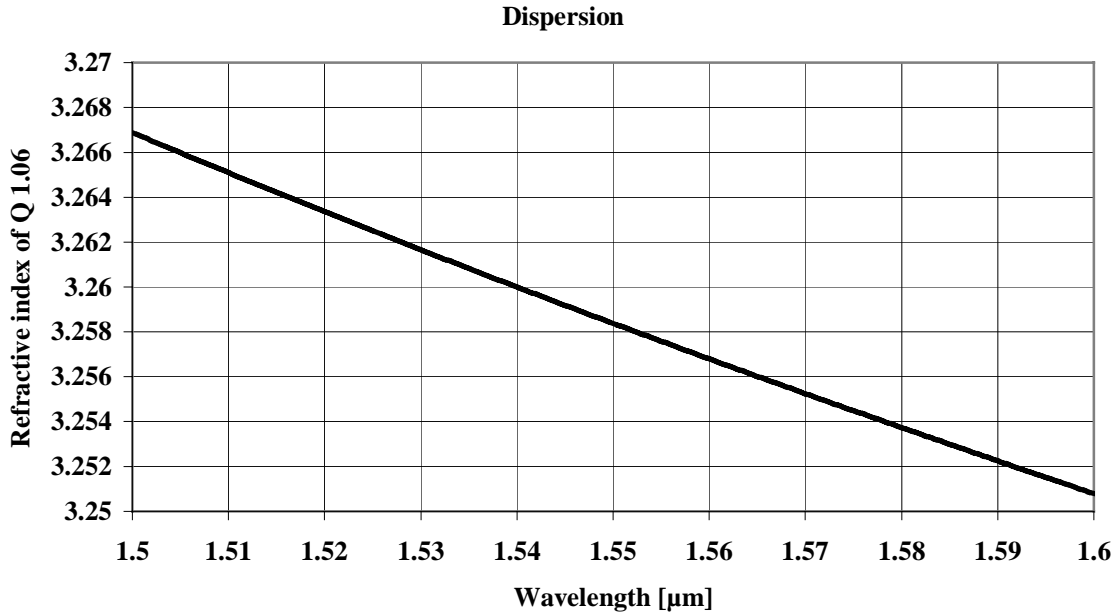


Fig. 36: Wavelength dependence of the refractive index of Q – 1.06 material [70].

The group refractive index is calculated using Eq. (2.30). The dispersion can be approximated linearly in the wavelength range between 1.5  $\mu\text{m}$  – 1.6  $\mu\text{m}$ . The slope  $\frac{dn}{d\lambda}$  is calculated to be  $-0.16 [\mu\text{m}^{-1}]$ . The group refractive index for the Q(1.06) material is shown in Fig. 37.

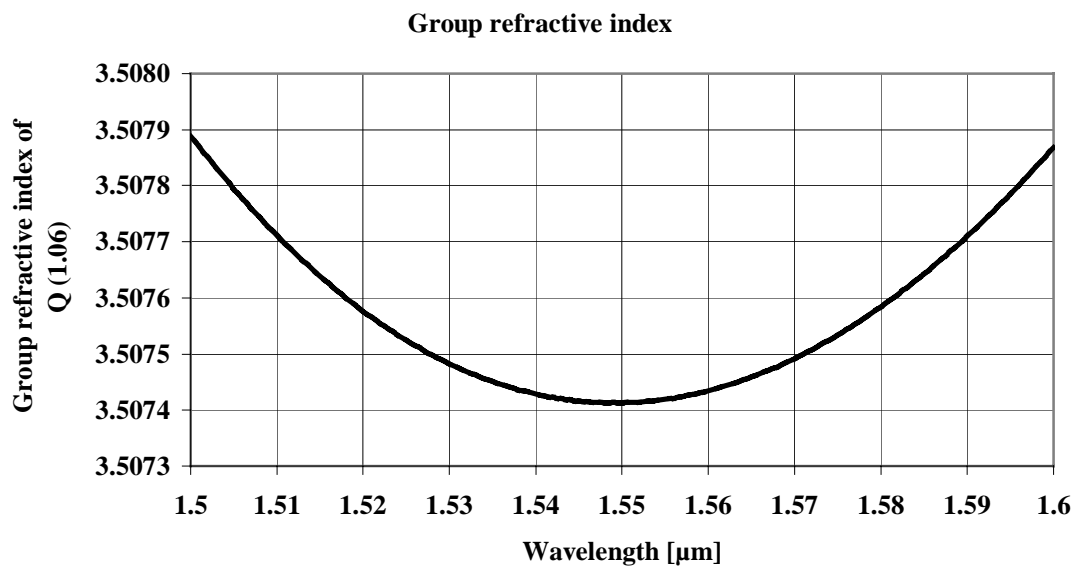


Fig. 37: Group refractive index of Q – 1.06 material.

## 4 The building blocks of the ring resonator

The basic tools for designing the ring resonators in the material system GaInAsP / InP have been described in the previous sections. This knowledge comes into use in the following section. The building blocks (straight and curved waveguides and couplers) of the ring resonators are designed and the method of fabrication is presented. In order to realize an FSR of 100 GHz, bending radii of as low as  $R \approx 100 \mu\text{m}$  are required [Eq. (2.29),  $\Delta\lambda = 100 \text{ GHz} = 0.8 \text{ nm}$  at  $\lambda = 1.55 \mu\text{m}$ ;  $\lambda = 1.55 \mu\text{m}$ ;  $n_{gr} \approx 3.5$ ;  $L = 2\pi R = 858 \mu\text{m}$ ;  $R = 137 \mu\text{m}$ ]. The following section starts with the design of the straight waveguide.

### 4.1 The waveguide

#### 4.1.1 Concept of a strong guiding waveguide

The waveguide which is to be used has to be single mode with a strong confinement in order to realize small bending radii in the order of  $R = 100 \mu\text{m}$ . The structure of the used rib waveguide is shown in Fig. 38. The layer sequence of the device is as follows (from bottom to top):

Substrate: InP -  $370 \mu\text{m}$

Buffer: InP -  $0.5 \mu\text{m}$

Waveguide: Q 1.06 -  $0.38 \mu\text{m}$

Etch stop: InP -  $0.02 \mu\text{m}$

Rib: Q 1.06 -  $0.84 \mu\text{m}$

Cap: InP -  $0.2 \mu\text{m}$

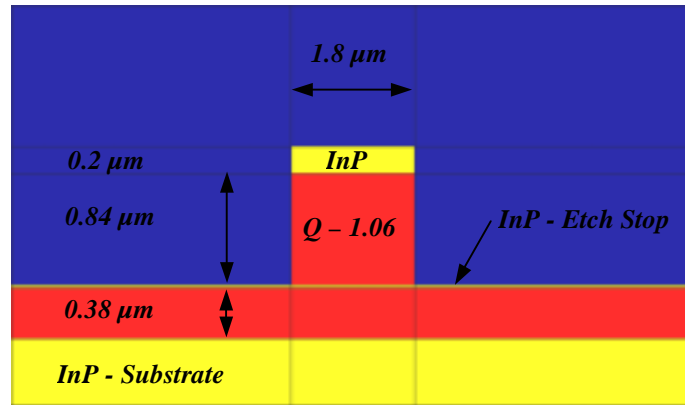
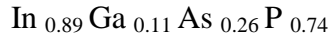


Fig. 38: The structure of the waveguide.

The composition of the quaternary  $1.06 \mu\text{m}$  semiconductor layer matched to InP is calculated as follows. Using the equation  $W_g = \frac{h \cdot c}{\lambda}$  with a value  $\lambda = 1.06 \mu\text{m}$  we obtain a bandgap energy  $W_g = 1.17 \text{ eV}$ . After solving the equation:  $W_g = 1.35 - 0.72y + 0.12y^2$  [71], the value

obtained for  $y$  is 0.26. The value for  $x$  can be derived from the equation  $x = 0.4y + 0.067y^2$  [71] and leads to  $x = 0.11$ . The composition of the quaternary Q(1.06) material can then be written as:



The waveguide width is  $1.8\ \mu\text{m}$ .

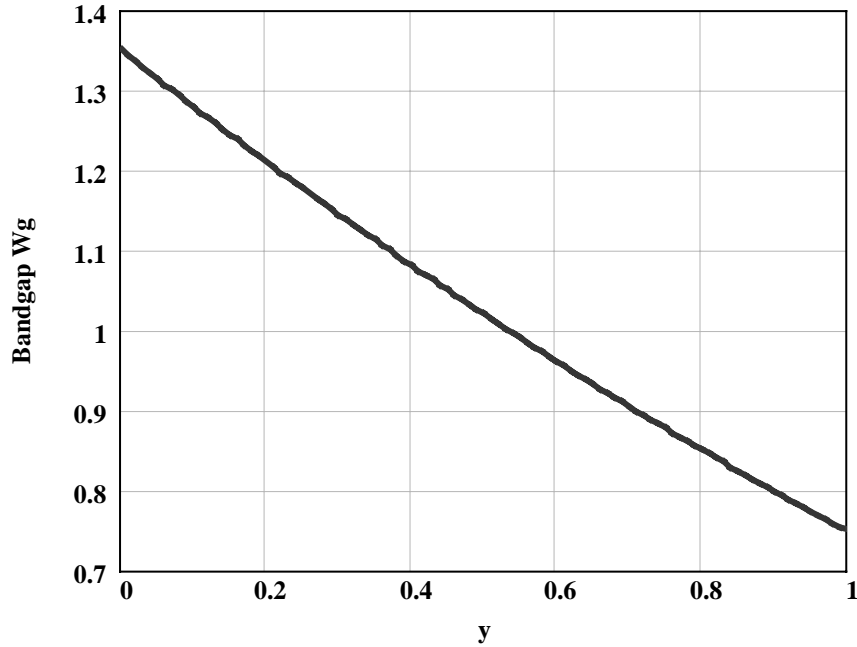


Fig. 39: Bandgap of  $\text{Ga}_x\text{In}_{1-x}\text{As}_y\text{P}_{1-y}$  at 300K.

The design assures both a monomodal propagation of the light in the waveguide and, due to a good confinement, low bending losses. The mode profile of the straight rib waveguide at  $\lambda = 1.55\ \mu\text{m}$  and using TE polarization is shown in Fig. 40. The calculations have been performed using a full vector waveguide mode solver [53].

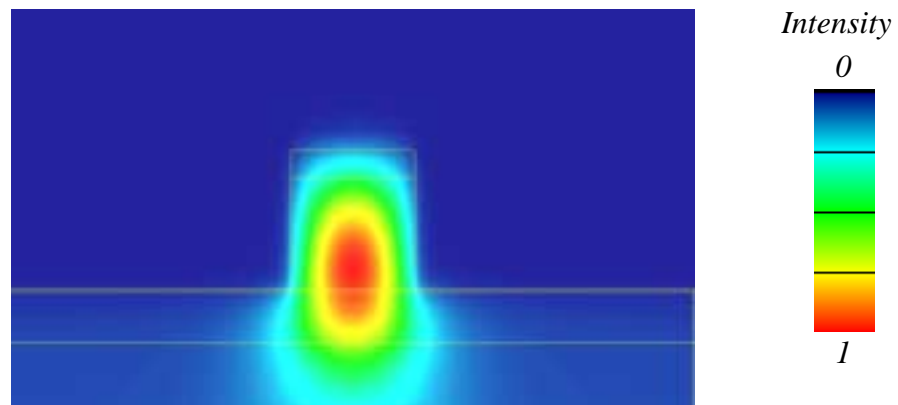


Fig. 40: Modeprofile of the waveguide at  $\lambda = 1.55\ \mu\text{m}$ .

The main portion of the energy is in the center of the waveguide (red). The effective index of the waveguide is calculated to be  $n_{\text{eff}} = 3.1985$ . The change in the effective refractive index

using TM polarization is  $\Delta n_{eff (TE-TM)} \approx 0.0014$ . The effective refractive index is lower for TM polarized light in the case of the straight waveguide. The simulations are carried out at a wavelength of  $\lambda = 1.55 \mu\text{m}$  and TE polarization with regard to a later integration with an SOA which favors TE polarization due to the used quantum well structure. The mode profile of the waveguide without InP – cap (200 nm) is shown in Fig. 41.

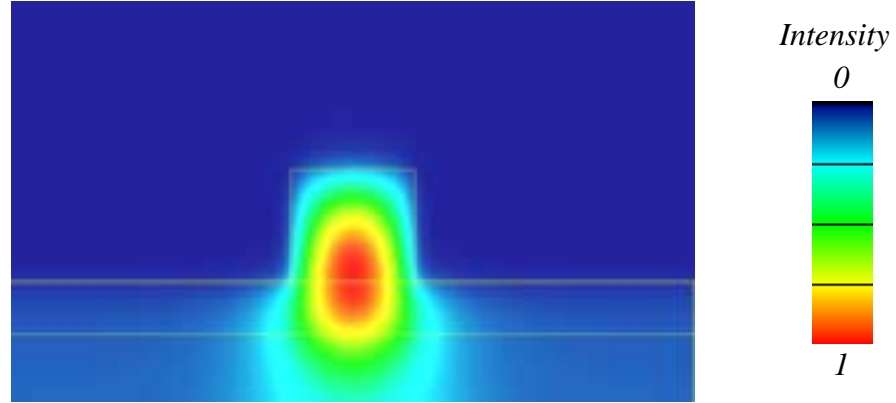


Fig. 41: Modeprofile of the waveguide without InP cap at  $\lambda = 1.55 \mu\text{m}$  [53].

The effective refractive index is calculated to be  $n_{eff} = 3.1984$ . The downward vertical mode shift due to the removal of the InP – cap is  $\approx 50 \text{ nm}$ .

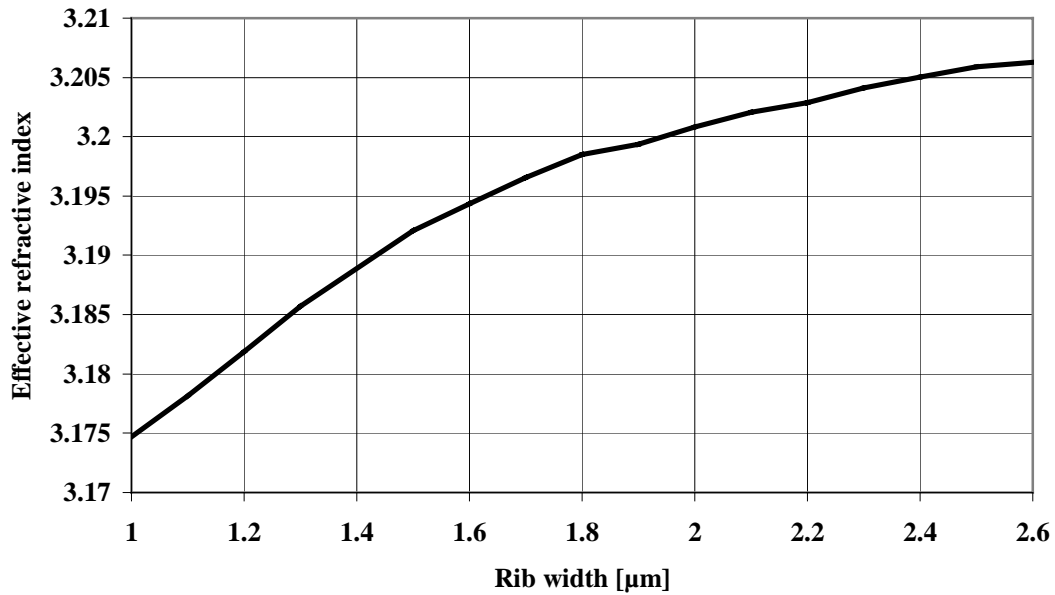


Fig. 42: Effective refractive index as a function of the ridge width at  $\lambda = 1.55 \mu\text{m}$ .

The effective refractive index changes with the width of the ridge (Fig. 42). Fabrication tolerances have to be considered when designing ring resonators. The optical path changes with the refractive index of the material. If the width is in the range between  $1.6 \mu\text{m}$  and  $2 \mu\text{m}$ , the maximum effective index change is approximately  $\Delta n_{eff} = 0.004$  (ridge width =  $2 \mu\text{m}$ ). The effective refractive index change due to the material bandgap wavelength is

shown in Fig. 43. The composition variation of the material bandgap wavelength is assumed to be  $\pm 5$  nm. The maximum effective refractive index change is approximately  $\Delta n_{eff} [Q(1.06) \pm 5 \text{ nm}] = 0.003$ . The etch depth of the waveguide is fabricated with an accuracy of approximately  $< \pm 50$  nm. It is controlled by the etch stop layer and therefore high exactness is realized were the change of the effective refractive index is negligible compared to the other influences. The worst case assumption of the change of the refractive index adds up to  $\Delta n_{eff} \approx 0.007$ .

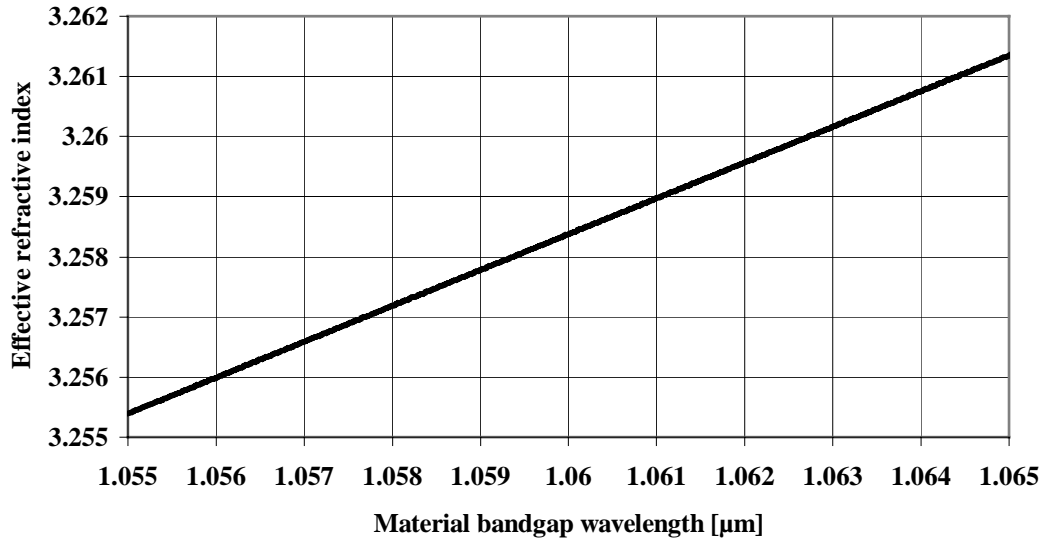


Fig. 43: Effective refractive index as a function of the material bandgap wavelength.

The maximum variation of the optical path  $L_{optical}$  ( $L_{optical} = L \cdot n_{eff} + L \cdot \Delta n_{eff}$ ) of a waveguide with a physical length  $L$  of  $100 \mu\text{m}$  due to fabrication tolerances is calculated to be  $L \cdot \Delta n_{eff} = 0.7 \mu\text{m}$ . It is essential for the design of special FSR values to know the optical length of the resonators. The change of the FSR for an SRR with a circumference of  $1736 \mu\text{m}$  and a designed FSR of  $50 \text{ GHz}$  is about  $100 \text{ MHz}$ . The ability to control the effective refractive index after fabrication is indispensable in order to achieve the targeted FSR. It is easier to increase the effective refractive index by thermal influences in the material system GaInAsP / InP. This advantage of the material system should be considered in the design of the resonators. The ring resonators will be polarization dependent due to the difference in the refractive index for TE and TM polarized light. With regard to a later integration of a semiconductor optical amplifier which prefers TE polarized light, all calculations will be performed using TE polarized light if not stated explicitly.

The following section presents the simulation of the waveguide in the curvatures.



### 4.1.2 The waveguide in the curvature

By using a cylindrical coordinate system  $(x, \rho, \phi)$ , propagation of light in circularly curved waveguides can be described in terms of modal propagation (Fig. 44a). A mode in such a structure is given by [72]:

$$E(R) = E_m(x, \rho) e^{-jk_n \phi} \quad (4.1)$$

This mode has as equi-phase front which propagates in the angular direction  $\phi$ . This implies that, for large  $\rho$ , modal power would propagate at a linear speed larger than the speed of light  $c$ , which is, of course, physically not possible. Therefore this part of the power will radiate away and be lost. Waveguide bends are inherently lossy, and sharper bends or weaker confinement will increase the loss. By good design, the loss can be kept small enough for practical applications.

Using a conformal mapping technique [73], the problem of solving the wave equation in cylindrical coordinates can be transformed to rectangular coordinates when the refractive index profile  $n(\rho)$  of the waveguide in the wave equation is replaced by  $n(\rho) e^{\frac{\rho}{R_T}}$  (with  $R_T$  a freely selectable reference radius).

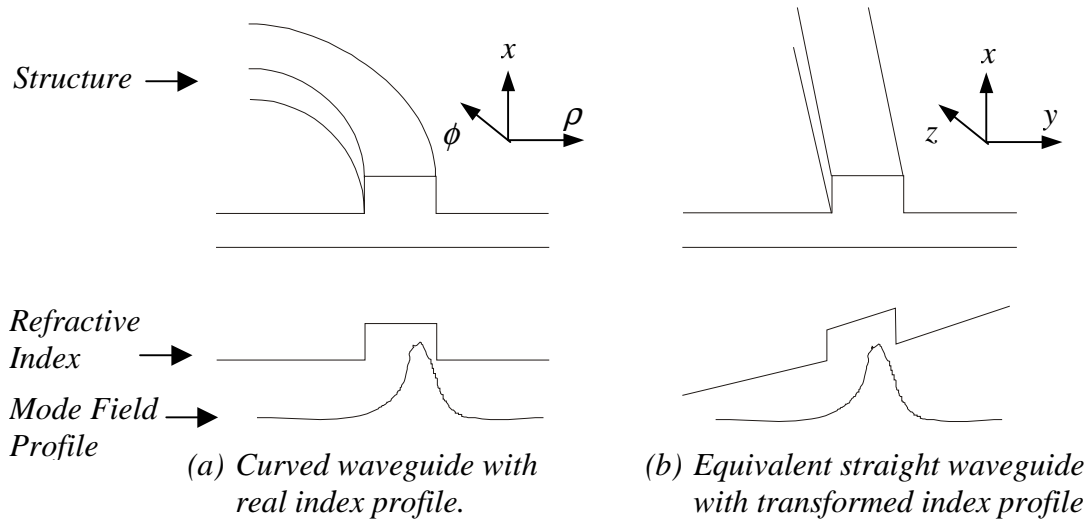


Fig. 44: Curved waveguide transferred to a straight waveguide using conformal mapping.

With this transformation an ordinary straight waveguide problem is obtained, which can be solved with the effective index method (e.g. [74]) by using a staircase approximation for the transformed index profile in the  $\rho$ -direction (Fig. 44b). The shape of the transformed profile can be qualitatively understood by considering that the longer path length of the light travelling in the outside bend has to turn up in the straight waveguide problem as a slower phase velocity, hence the higher index there. A typical solution is shown in Fig. 47 in which it can be seen that the centre of gravity of the mode profile in a curved waveguide moves outward, an effect that becomes larger the sharper the bend is.

For a bent slab waveguide, Marcuse [75] obtained an equation for the exponential power attenuation coefficient  $\alpha_{bend}$  due to bending losses using an analysis of the wave equation in cylindrical coordinates.

Using effective index notation, this attenuation coefficient  $\alpha_{bend}$  is given by [76]:

$$\alpha_{bend} = \frac{\alpha_y^2}{k_0^3 n_{eff} \left(1 + \alpha_y \frac{w}{2}\right)} \frac{k_y^2}{(n_{e2}^2 - n_{e1}^2)} \exp(\alpha_y w) \cdot \exp\left(\frac{-2\alpha_y^3}{3n_{eff}^2 k_0^2} R\right) \quad (4.2)$$

where

$$\alpha_y = k_0 \sqrt{n_{eff}^2 - n_{e1}^2}, \quad k_y = k_0 \sqrt{n_{e2}^2 - n_{eff}^2} \quad \text{and} \quad k_0 = \frac{2\pi}{\lambda_0} \quad (4.3)$$

$w$  is the width of the waveguide,  $n_{eff}$  is the effective refractive index of the waveguide,  $n_{e1}$  is the effective refractive index of the medium surrounding the slab,  $n_{e2}$  is the effective refractive index of the slab,  $R$  is the radius of curvature and  $\lambda_0$  is the used wavelength.

The transmission through a bend of radius of curvature  $R$  and included angle  $\theta$  is:

$$\eta_{bend} = \exp(-\alpha_{bend} \theta R) \quad (4.4)$$

The bending loss in dB for a  $90^\circ$  bend using the waveguide without InP cap described in section 4.1.1 is given in Fig. 45. The values for the effective indices were calculated using [53] where  $n_{eff} = 3.1984$ ,  $n_{e1} = 3.1645$ ,  $n_{e2} = 3.211$ . The wavelength used was  $\lambda_0 = 1.55 \mu\text{m}$ .

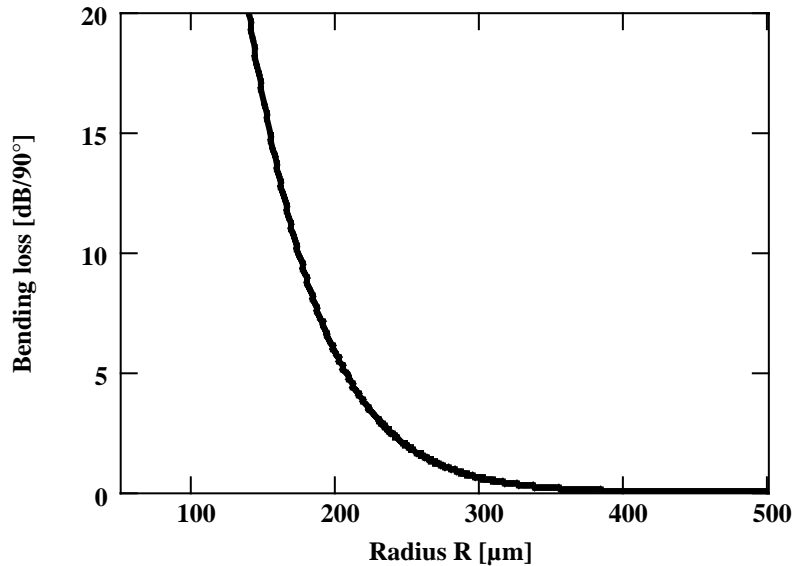


Fig. 45: Calculated bending losses of the waveguide without deep etching.

The waveguide described in section 4.1.1 can be used for radii above  $R = 200 \mu\text{m}$ . Below a radius of  $R = 200 \mu\text{m}$ , the centre of gravity of the mode profile moves outward resulting in a weak confinement and high bending losses ( $> 5 \text{ dB}/90^\circ$ ). The realization of radii below  $200 \mu\text{m}$  requires an additional change in the structure. The outer wall of the curved section is

removed, so that a higher refractive index contrast is achieved and thus a higher mode confinement in the waveguide. The idea of using a lower refractive index on the outer side of a waveguide in the curvature and thus reduce the bending losses was first demonstrated by E. G. Neumann in [77]. He proposed to replace the material on the outer side of the waveguide by another dielectric medium with an index which is smaller than the index of the waveguide. The layout of the asymmetric waveguide in the curvatures is shown in Fig. 46. In using this waveguide, it is possible to fabricate radii as small as  $100\text{ }\mu\text{m}$  with very low bending losses. The mode profile of the waveguide with a radius of  $100\text{ }\mu\text{m}$  is shown in Fig. 47. The effective index of the waveguide in the curvature is calculated using an optical waveguide mode solver [53] to be  $n_{eff} = 3.192$ .

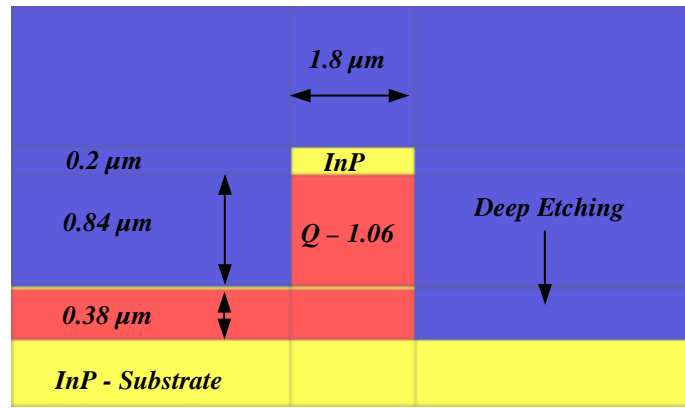


Fig. 46: The asymmetric structure of the waveguide in the curvature.

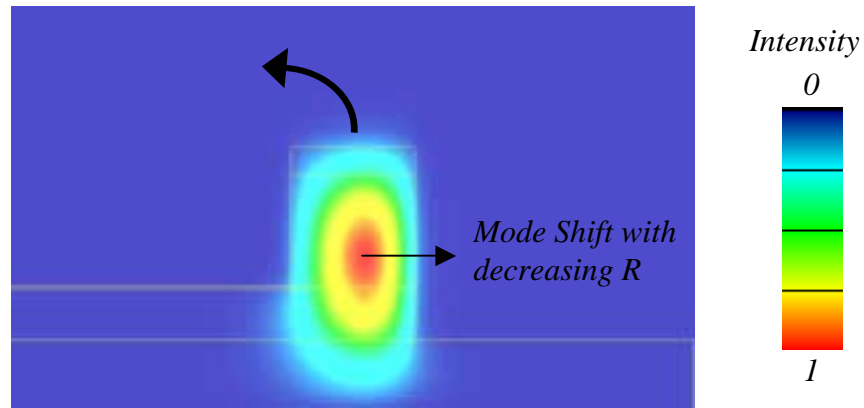


Fig. 47: Modeprofile of the waveguide at a radius of  $R = 100\text{ }\mu\text{m}$ .

The mode shift towards the outer side of the waveguide which is due to the deeply etching of the outer wall and the small bending (here  $R = 100\text{ }\mu\text{m}$ ) radius of the waveguide is about  $160\text{ nm}$ . The minimum bending radius is evaluated by calculating the overlap between the straight waveguide (section 4.1.1) and the waveguide with deep etching.

The overlap is calculated as follows:

$$\text{Overlap} = \frac{\text{Intensity of the mode field profile for a curved waveguide at a specific radius } R}{\text{Intensity of the mode field profile of a straight waveguide}}$$

The result is shown in Fig. 48. The theoretical minimum bending radius calculated with a finite difference simulation tool [70] is about 80  $\mu\text{m}$  with negligible bending loss ( $< 1 \text{ dB}/90^\circ$ ).

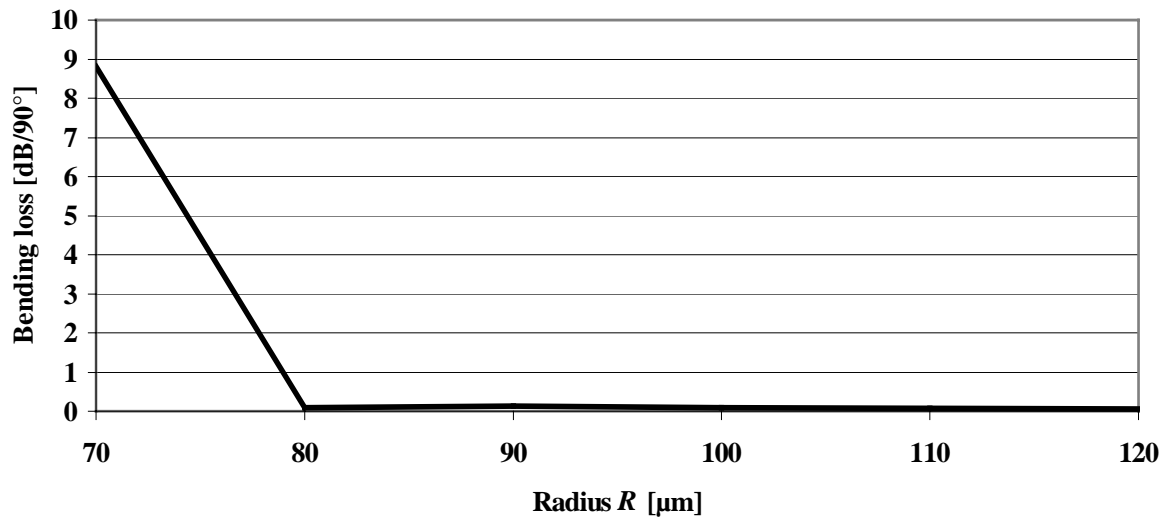


Fig. 48: Waveguide bending loss at different radii.

The mode field profile of a deeply etched waveguide at a radius of  $R = 50 \mu\text{m}$  is shown in Fig. 49. It can be clearly seen, that the mode is not guided any more and radiates into the substrate.

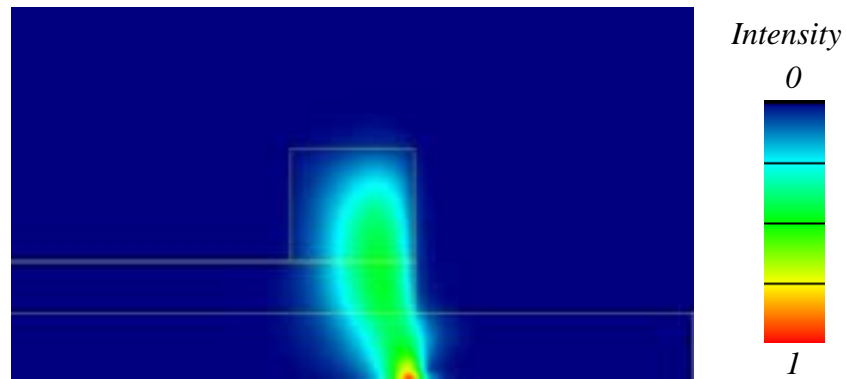


Fig. 49: Mode profile of the waveguide at a radius of  $R = 50 \mu\text{m}$ .

The loss which occurs when the light transmits from a straight waveguide into a waveguide with deep etching at a radius of  $R = 100 \mu\text{m}$  is  $\approx 0.4 \text{ dB}$ .

The following section presents the fabrication process of the simulated waveguides.

### 4.1.3 Fabrication of the waveguide

The layer sequence of the device is given again in Fig. 50.

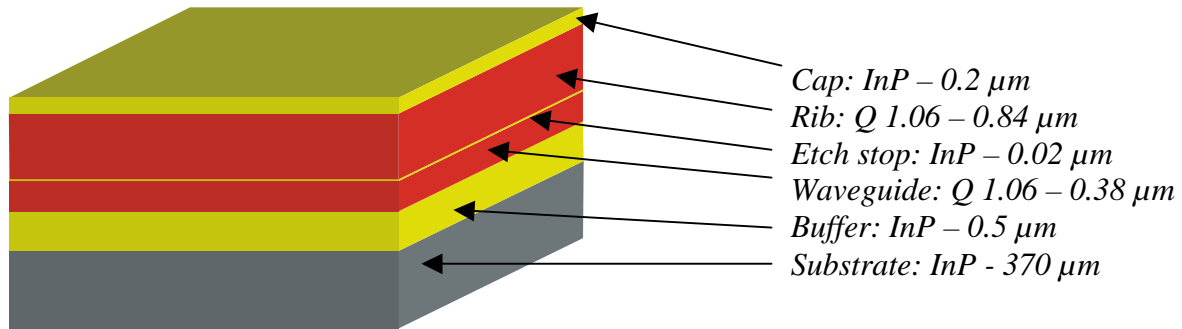


Fig. 50: Layer sequence.

The InP cap is grown for the protection of the quaternary Q(1.06) layers and can be removed in the following step, but is not necessary. If the InP cap is removed, the center of the optical field is shifting to a different level (see section 4.1.1) and this has to be taken into consideration for further processing. The InP – cap is not removed in the following fabrication step.

The first step is the deposition of silicon nitride ( $\text{SiN}_x$ ) by PECVD (Plasma enhanced chemical vapor deposition), which serves as the etching mask for the waveguides (Fig. 51). The thickness of the  $\text{SiN}_x$  is  $\approx 200\ \text{nm}$  and is deposited at a temperature of  $370\ ^\circ\text{C}$ .

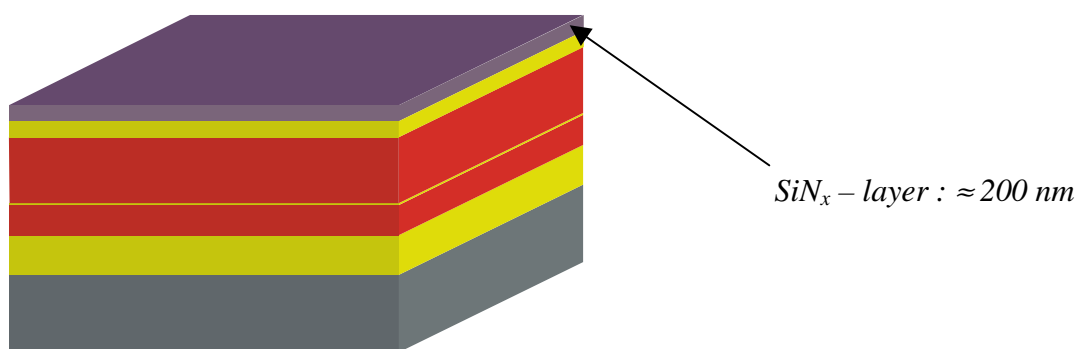


Fig. 51: Deposition of the  $\text{SiN}_x$  layer.

The next processing step is the structuring of the  $\text{SiN}_x$  layer, which is performed using standard photolithography. The photoresist which is used is AZ5214 (Fig. 52). The intensity of the light used is  $12 \text{ mW/cm}^2$ . The exposing time is 24 s and the developing time is between 40 s – 50 s for a positive exposure. The developer used is MIF724.

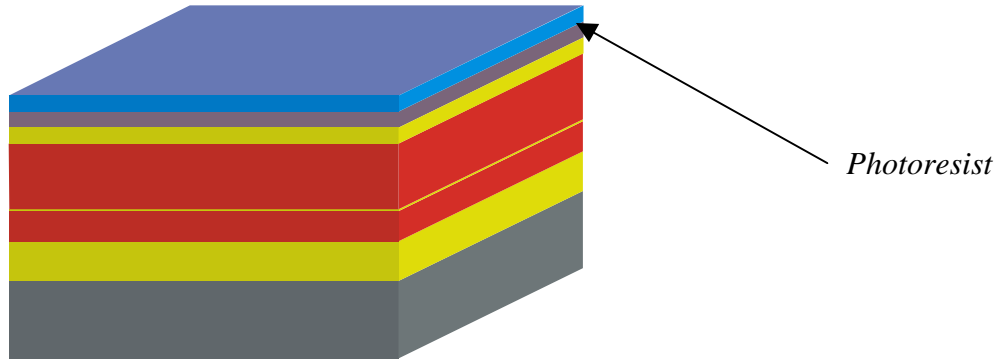


Fig. 52: Deposition of the photoresist.

The developed photoresist serves as the etching mask for the reactive ion etching step (RIE). The etching is done with the gases  $\text{CHF}_3$  (22 sccm) and  $\text{O}_2$  (2.2 sccm) at a pressure of  $12 \mu\text{bar}$  and 50 W. The result is illustrated in Fig. 53.

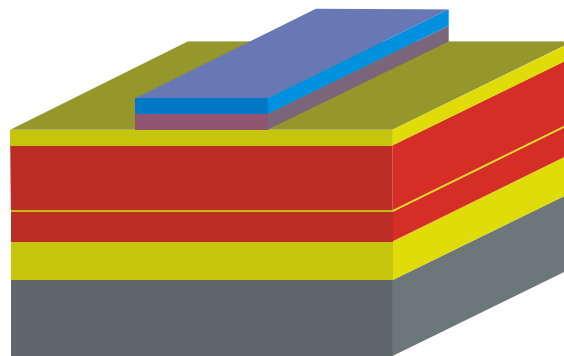


Fig. 53: Structuring of the  $\text{SiN}_x$  layer.

The photoresist is removed and the previously structured  $\text{SiN}_x$  layer serves as the mask for the following RIE step. The used etching gases are  $\text{CH}_4$ ,  $\text{H}_2$  (6 ml/min, 40 ml/min). In order to reduce the formation of polymers during dry etching and so to minimize the sidewall roughness a small fraction of  $\text{O}_2$  (0.3 ml/min) is added. The power used is 150 W at a pressure of 0.02 mbar. The etching is controlled by an ellipsometer and a mass spectrometer. The etching is stopped when the InP etch stop layer is detected.

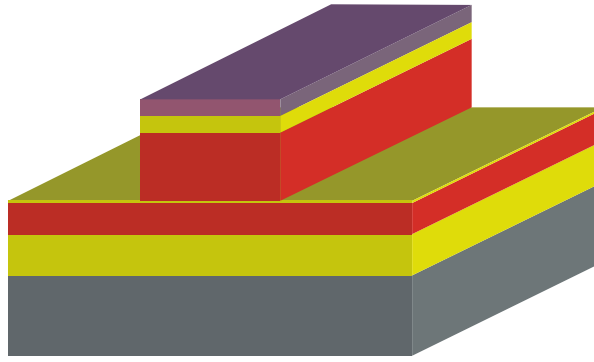


Fig. 54: Etching of the waveguide.

The next dry etching step is the realization of the deeply etched section on the outer wall of the waveguides in the curvatures. The  $\text{SiN}_x$  layer from the previous step and the photoresist serve as the etching mask for this process. The fabrication procedure is illustrated in Fig. 55.

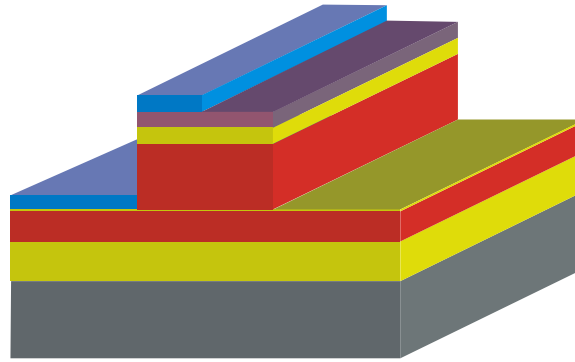


Fig. 55: Preparation of the waveguide for the deep etch process.

The photoresist covers only a part of the waveguide. The  $\text{SiN}_x$  layer from the previous processing step serves as the etching mask. This self aligning process assures that the width of the waveguide is not changed by this processing step. The etching is performed again using RIE, but this time without the portion of oxygen which could partly remove the photoresist mask and cause errors. The photoresist is removed after the dry etching by the use of an oxygen plasma (15 min, power = 500 W,  $T \leq 200^\circ\text{C}$ ). The diagram of a fabricated waveguide with deep etching is shown in Fig. 56.

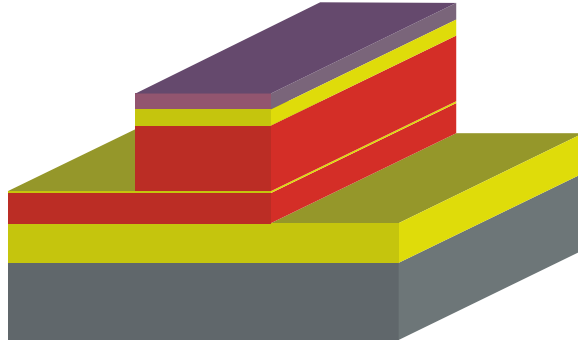


Fig. 56: Waveguide in the curvature with deep etching.

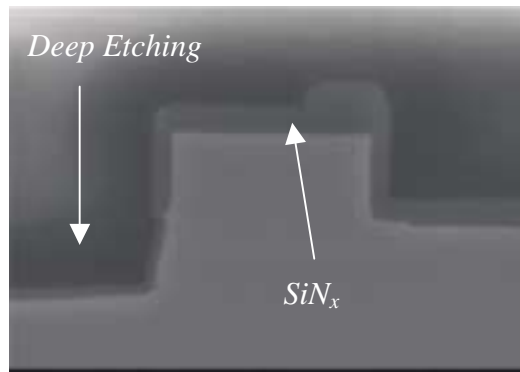


Fig. 57: Scanning electron microscope (SEM) photograph of the waveguide with deep etching.

The  $\text{SiN}_x$  layer is used as an insulating layer between the waveguide material (Q-1.06) and the platinum layer which is deposited at the end for the realization of the wavelength tuneability of the devices. A solution of  $\text{H}_2\text{SO}_4$ ,  $\text{H}_2\text{O}_2$  and  $\text{H}_2\text{O}$  can be used for the improvement of the sidewall smoothness for the reduction of the bending losses [78]. The final structure of the waveguide is illustrated in Fig. 58.

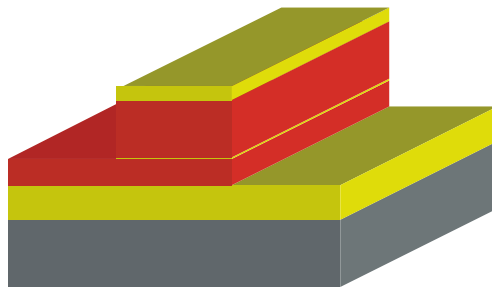


Fig. 58: The structure of the waveguide in the curvature.



The scanning electron microscope (SEM) picture of the facet of a straight waveguide without deep etching is shown in Fig. 59. The SEM pictures of the waveguide in the curvatures are shown in Fig. 60 and Fig. 61.



Fig. 59: SEM – photograph of a waveguide.



Fig. 60: SEM – photograph of an asymmetric waveguide in the curvature.



Fig. 61: SEM – photograph of the deeply etched curvature.

The described fabrication processes are available at the Heinrich-Hertz-Institute. The existing recipes (etch gases, temperature, pressure) for the processes have been used to realize the passive ring resonators.

The used  $\text{CH}_4$  – based dry etching process for realizing the deeply etched waveguides with vertical facet-quality sidewalls has also attracted attention recently [79], [80].



## 4.2 The measurement method

The characterization of the devices was mainly done by using the measurement method described in section 4.2.1. A new approach for the determination of essential parameters (e.g. coupling factor, round trip loss, FSR) of ring resonators was performed using the OLCR (optical low coherence reflectometry) method. This measurement was done in cooperation with France Telecom, the Centre National de la Recherche Scientifique (CNRS), Laboratoire de Photonique et de Nanostructures (LPN).

### 4.2.1 The standard measurement setup for the characterization of the devices

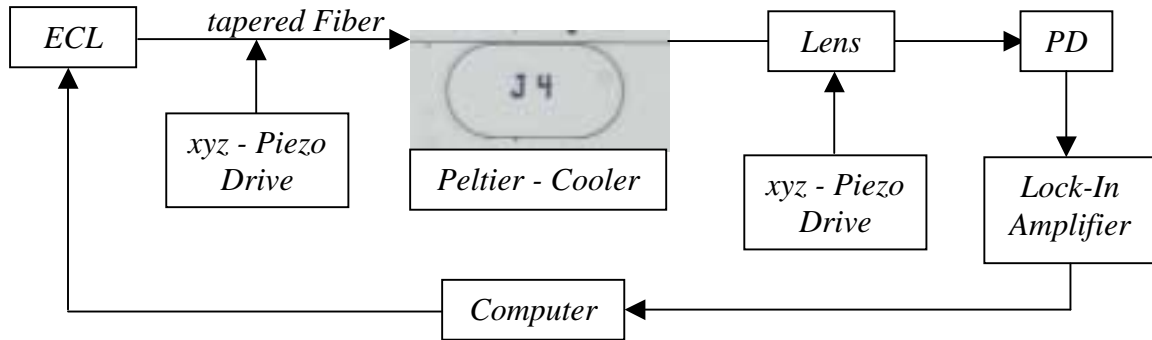


Fig. 62: Measurement setup for the characterization of the devices.

The measurement of the devices is done connecting an external cavity laser (ECL) and a polarization controller at the input waveguide. The transmitted signal is detected in a photo diode and a lock-in amplifier. The ECL signal is coupled to the input waveguide by using a tapered fiber, which can be adjusted by a three axis piezo drive. The near field of the output waveguide is focused on the photo diode by using a microscope lens which has a sufficient aperture to guarantee correct power measurement. The specimen is placed on a Peltier – cooler so that all measurements are performed at a definite temperature. The passive devices are measured at 20 °C and the devices with integrated SOA at 15 °C. All measurements are performed using TE polarized light, if not stated explicitly.

#### 4.2.2 The OLCR measurement setup

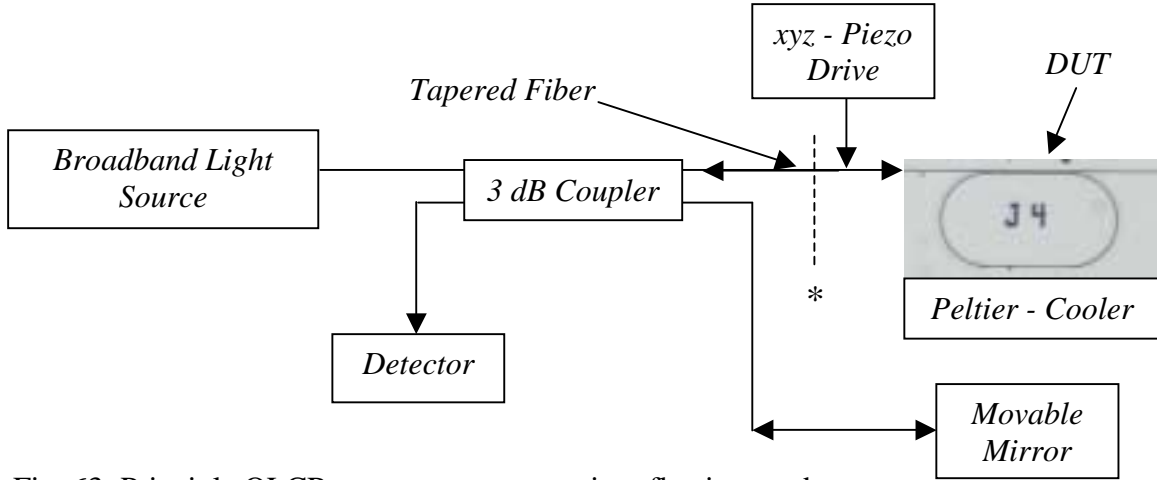


Fig. 63: Principle OLCR measurement setup in reflection mode.

A methodology wherein the broadband source of OLCR (optical low coherence reflectometry) is simultaneously employed precisely in the usual reflection (Fig. 63) and also in the transmission modes is used for the characterization of the devices [81], [82]. The OLCR setup employed here is basically a Michelson interferometer coupled to a broadband light source, which is nearly Gaussian-like and is centered at a wavelength of  $\lambda \approx 1.565 \mu\text{m}$  with a half-width of 50 nm. When the optical path length of the arm with the moveable reference mirror is equal to that in the one that contains the device under test (DUT), an interference signal is detected with a spatial resolution that depends on the coherence length of the probe ( $< 10 \mu\text{m}$ ). Refractive index discontinuities less than  $10^{-4}$  (dynamic range of  $\approx -80 \text{ dB}$ ) in the device can be detected. To achieve precise control of the probe light input coupling and also to record the transmission data, the output end of the setup can be coupled to an infrared-sensitive camera and an optical spectrum analyzer (OSA), respectively.

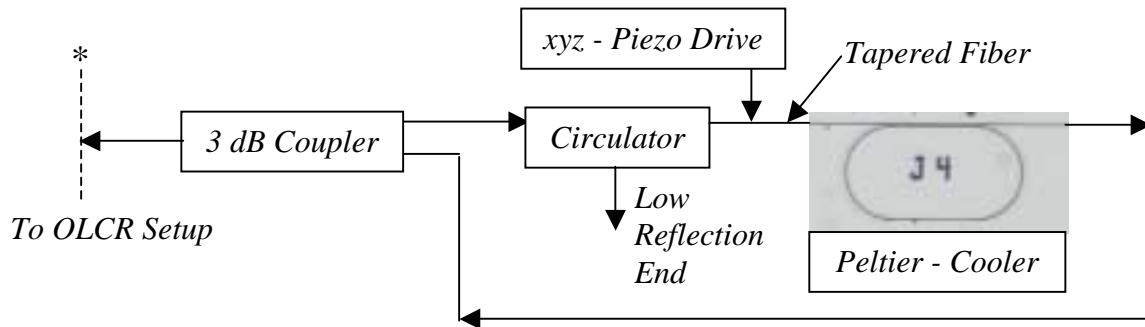


Fig. 64: Principle OLCR measurement setup in transmission mode.

The reflection mode setup is used to characterize the active-passive transition. Due to the anti reflection (AR) coating of the facets of the ring resonators the transmission mode setup (Fig. 64) is used for the characterization of these devices. A similar method for the characterization of optical resonators is the optical time-domain reflectometry which is presented in [83].

### 4.2.3 Specifications of optical performance

The **insertion loss**  $\alpha_{insertion}$  of the device is the minimum transmission for a specific wavelength range for all polarization states. It represents the worst possible loss through the device. The **insertion loss uniformity** of a device is the difference between the **insertion loss** of the best-case and worst-case channels.

The **insertion loss**  $\alpha_{insertion}$  is defined for an input intensity  $I_{in}$  and an output intensity  $I_{out}$  as:

$$\alpha_{insertion} = -10 \cdot \log \frac{I_{out}}{I_{in}} \quad (4.5)$$

The total **insertion losses**  $\alpha_{insertion}$  include the intrinsic losses  $\alpha_{propagation}$  and the fiber – chip coupling losses  $\alpha_{coupling}$ .

$$\alpha_{insertion} = \alpha_{propagation} + \alpha_{coupling} \left[ \frac{dB}{cm} \right] \quad (4.6)$$

The intrinsic losses can be described by the following equation:

$$\alpha_{propagation} = -\frac{1}{L} \left\{ 10 \cdot \log \frac{I_{out}}{I_{in}} + \alpha_{coupling} \right\} \left[ \frac{dB}{cm} \right] \quad (4.7)$$

where  $L$  is the total length of the measured waveguide.

#### 4.2.4 Experimental results

The insertion losses can be determined using the measurement setup described in Fig. 62. The coupling losses can be calculated from different measurements of different device lengths. This internationally recognized reference test method is known as the cut-back technique [84]. The slope of the curve in Fig. 65 is determined by the propagation losses of the waveguide. The coupling losses are taken from the value extrapolated to a device length of zero cm, here 4.84 dB.

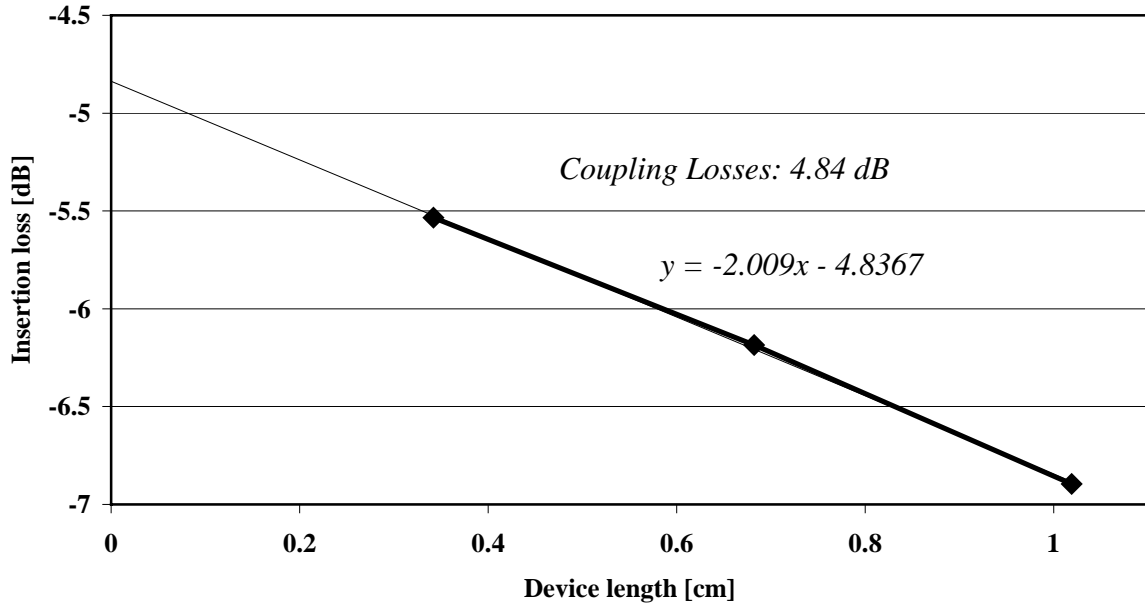


Fig. 65: Determination of the coupling losses of the fabricated straight waveguide using the cut-back-method.

The coupling losses can be evaluated with this measurement method for a specific type of waveguide for reproducible input and output coupling conditions. This method is used to determine waveguide losses of about 1 dB/cm and beyond. Losses below 1 dB/cm are difficult to detect due to scattering losses. Tolerances of  $\pm 0.5$  dB/cm are obtained with this method for good facets of the chip.

Another measurement method for the determination of the propagation losses of the waveguide is the so called Fabry-Perot resonance method [85].

The chip is regarded as a Fabry-Perot Resonator for waveguide losses  $< 1$  dB/cm, where the facets of the chip serve as the mirrors of the resonator. The optical wave is reflected back and forth within the chip waveguide depending on the intrinsic losses and the reflection factor of the facets. The optical length is changed by varying the temperature of the whole chip or the wavelength exploiting the group velocity dispersion. The result is a transmission spectrum of

a Fabry-Perot resonator, where the transmitted maximum and minimum intensities can be described by:

$$I_{min} = \frac{(1-R)^2 \cdot e^{-2\alpha_{insertion}L}}{(1+R \cdot e^{-2\alpha_{insertion}L})^2} \quad (4.8)$$

$$I_{max} = \frac{(1-R)^2 \cdot e^{-2\alpha_{insertion}L}}{(1-R \cdot e^{-2\alpha_{insertion}L})^2} \quad (4.9)$$

where  $R$  is the reflection factor,  $L$  the length of the resonator and  $\alpha_{insertion}$  the insertion losses of the waveguide. This is another way of evaluating the insertion losses, which are given by:

$$\alpha_{insertion} = \frac{1}{L} \left\{ \ln \frac{1+\sqrt{u}}{1-\sqrt{u}} + \ln R \right\} [cm^{-1}] \quad (4.10)$$

where  $u = \frac{I_{min}}{I_{max}}$ .

When the reflection factor of the chip is unknown, it can be calculated from the measurements at different device lengths. A typical result of a measurement is shown in Fig. 66.

The measurement is approximated by a straight line from which the reflection factor is directly taken. The slope of the curve is again the value for the intrinsic losses of the waveguide. The waveguide losses  $\alpha_{propagation}$  are calculated to be:

$$\ln \left( \frac{1+\sqrt{u}}{1-\sqrt{u}} \right) = 0.293 \Rightarrow \alpha_{propagation} = 1.27 \text{ dB/cm}$$

When the reflection factor is known, the intrinsic losses of the chip are easily determined without the necessity to cut the waveguide several times for characterization.

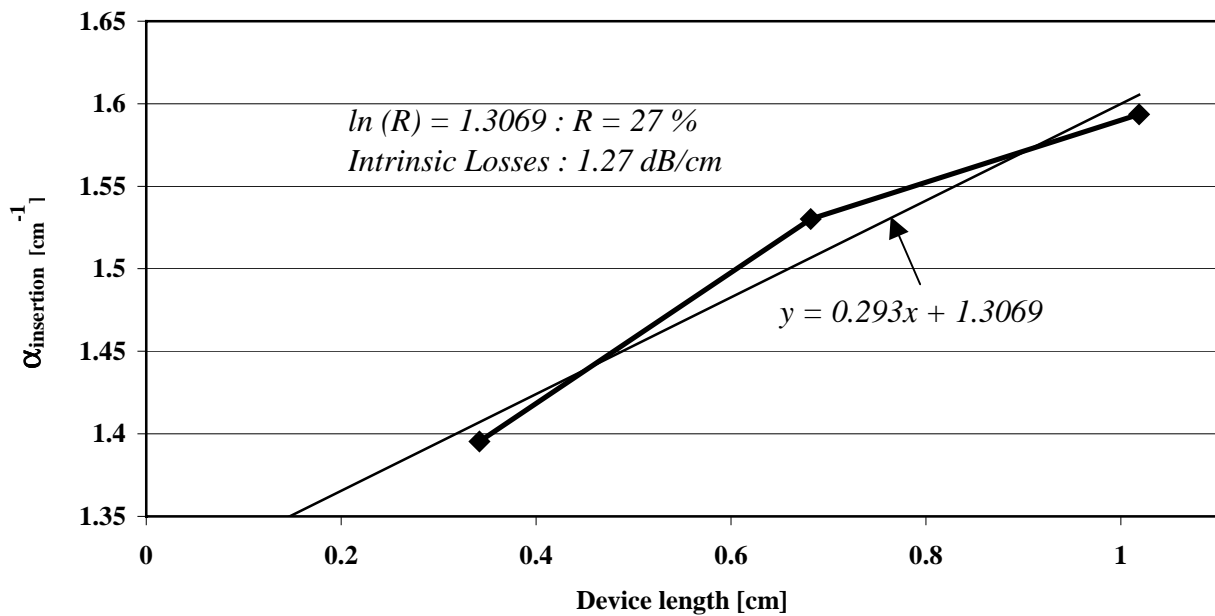


Fig. 66: Determination of the intrinsic losses.

The result of bend waveguides with and without deep etching on the outer side in the curvatures is shown in Fig. 67. The value for a straight waveguide is shown for comparison. Minimum bending radii of 200  $\mu\text{m}$  can be realized with negligible bending losses without deeply etched curvatures. The minimum bending radius for deep etched bend waveguides is as low as 100  $\mu\text{m}$  without significant loss. The experimental results obtained correspond very well to the predicted simulated values in Fig. 45 and Fig. 48.

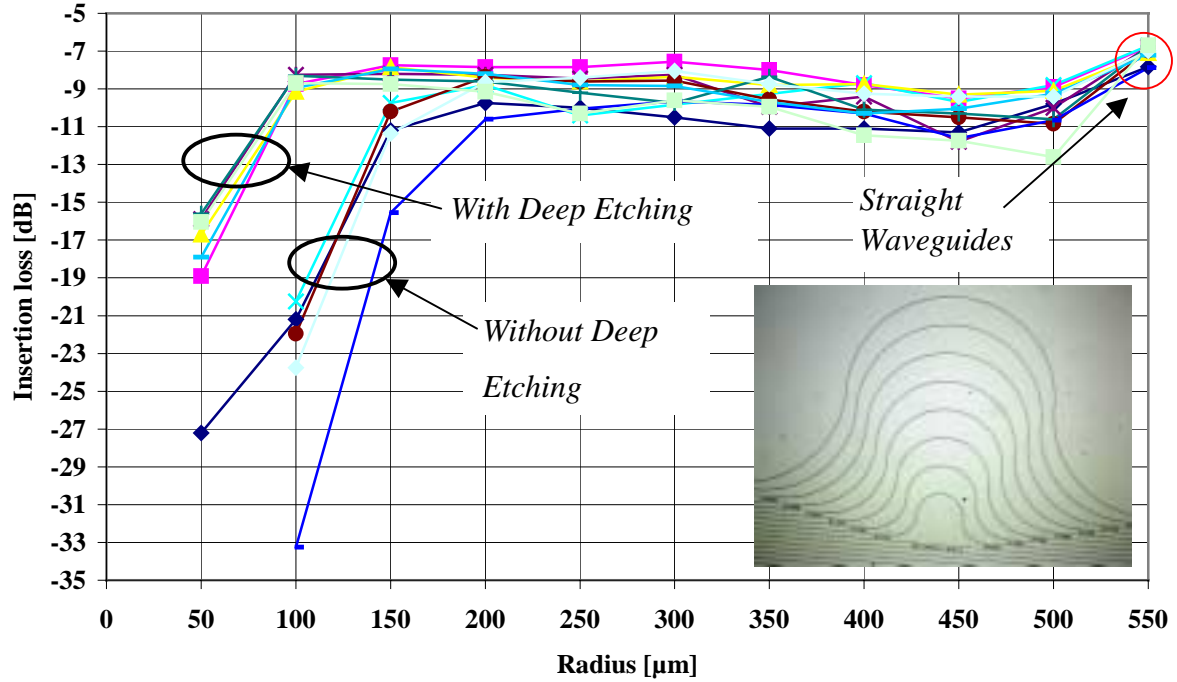


Fig. 67: Measurement of the waveguides with and without deep etching in the curvatures.

The designed waveguide with deep etching on the outer side of the waveguide in the curvature is used for the realization of the ring resonators.

The following section describes the design of the couplers using the waveguide structure described in the previous sections.



### 4.3 Couplers

#### 4.3.1 Multimode – interference – coupler (MMI)

A multimode interference (MMI) coupler (Fig. 68) consists of a broad center waveguide which supports several modes depending on the width and the layer sequence of the waveguide [86].

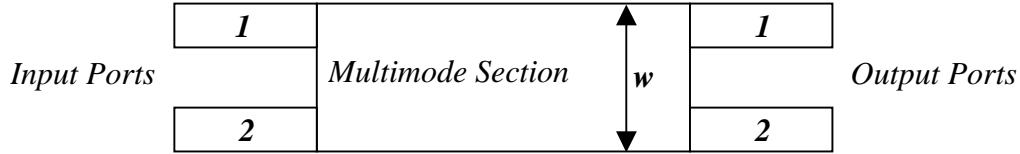


Fig. 68: Top view of a MMI coupler.

This type of waveguide has the property of self-imaging, which means that an arbitrary input field which is inserted at the input waveguide of the device is periodically reproduced in the transmission direction of the center waveguide. Between these positions, the input field is reproduced with only a fraction of the input intensity, divided symmetrically in the multimode section. The main advantage of MMI couplers compared to codirectional couplers is the fabrication tolerance with respect to the 3-dB splitting ratio. If other coupling ratios are required, codirectional couplers are favored. Due to the layer sequence which was already developed in the previous sections and the geometry of the straight waveguide, the MMI coupler is practically already designed. A MMI coupler with two in- and output ports and a splitting ratio of 3-dB is required. The multimode section should support more than three modes to assure an appropriate interference signal of the input mode. The multimode section is simulated with an optical waveguide mode solver [53]. The result is shown in Fig. 69.

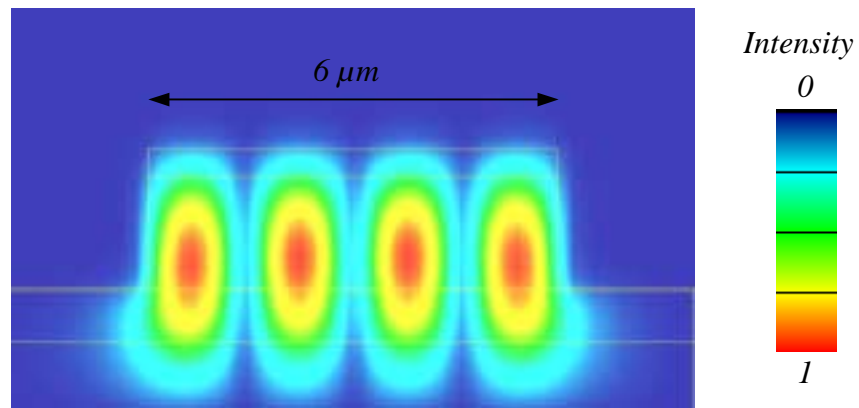


Fig. 69: Modeprofile of a MMI coupler (TE polarization).

The designed and simulated MMI has a width of 6  $\mu\text{m}$ . As can be seen in Fig. 69 there are four modes which are supported in the broad section and the effective index is  $n_{\text{eff}} = 3.2115$ . The interference of the four modes in transmission direction can be simulated with a time-

frequency domain solver [53]. The ideal length for the 3-dB splitting ratio is evaluated from the interference simulation in Fig. 70 for a Gaussian shaped input signal at a wavelength of  $1.55 \mu\text{m}$  coupled in the upper left input of the MMI. The 3-dB splitting ratio is achieved after a length of  $150 \mu\text{m}$ . At this point, the intensity at the input of the MMI coupler is divided equally at both of the output ports.

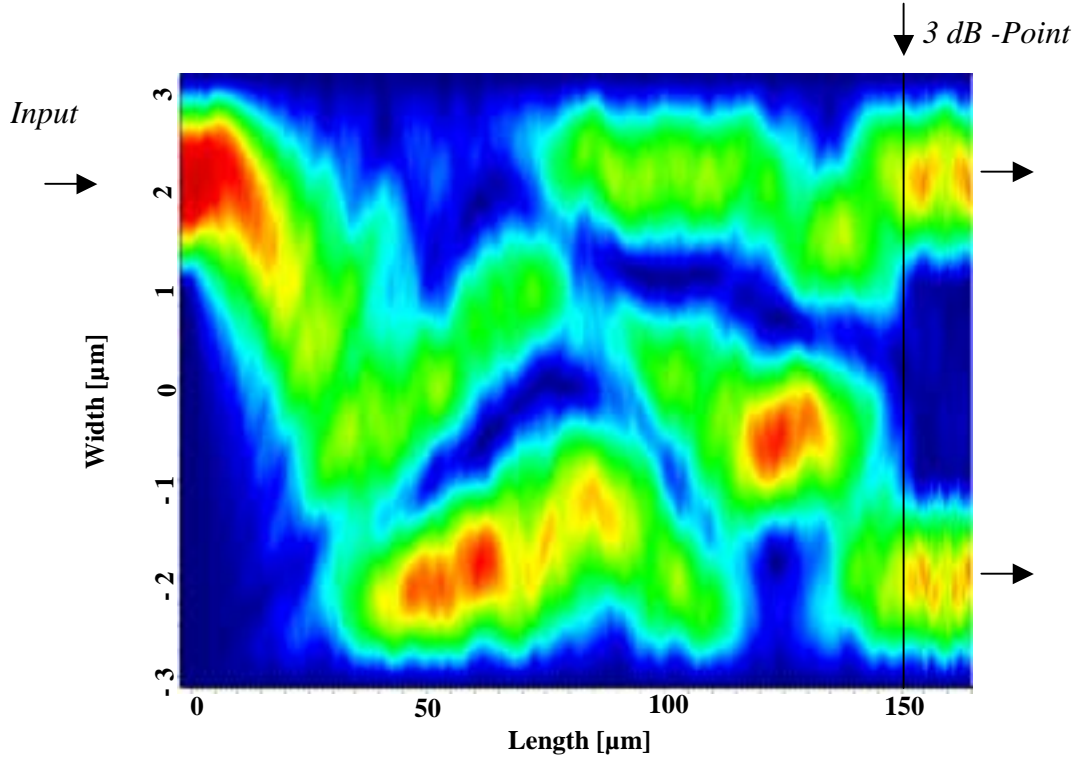


Fig. 70: Simulation of the multimode section at  $\lambda = 1.55 \mu\text{m}$  (TE polarization).

The 3-dB splitting ratio is calculated from the overlap result between the input port and the two output ports at this specific point. The result is shown in Fig. 71.

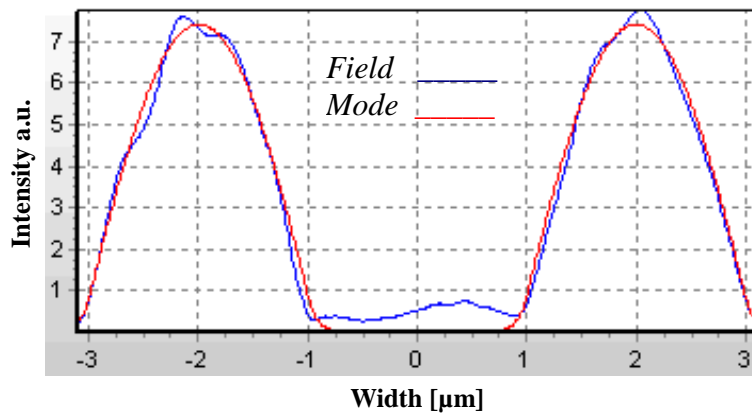


Fig. 71: Overlap result of the input – output relation.

The intensity at one of the output ports is about 0.49. This is not exactly 0.5. The difference ( $\approx 0.1 \text{ dB}$ ) is due to scattering losses which occur at the center of the two output ports. The 3-dB length can also be approximated by the formula given in [18]:

$$L_{3dB} = \frac{3}{4} \frac{\lambda_0}{n_{eff0} - n_{eff1}} \approx 2 \frac{n_{eff} \cdot w^2}{\lambda_0} \quad (4.11)$$

where  $\lambda_0$  is the wavelength,  $n_{eff0}$  and  $n_{eff1}$  are the effective indices of the fundamental and first order mode,  $n_{eff}$  is the effective index of the waveguide,  $w$  is the width of the multimode section. The effective index of the waveguide was calculated to be  $n_{eff} = 3.1985$ , the width of the MMI is  $6 \mu\text{m}$ , the used wavelength is  $1.55 \mu\text{m}$ . This leads to a length  $L_{3dB}$  of  $148.58 \mu\text{m}$ . The MMI is also investigated under TM polarization at a wavelength of  $\lambda = 1.55 \mu\text{m}$ . The change in the refractive index is  $\Delta n_{eff(T\bar{E}-TM)} \approx 0.003$ . The result from the simulation is shown in Fig. 72.

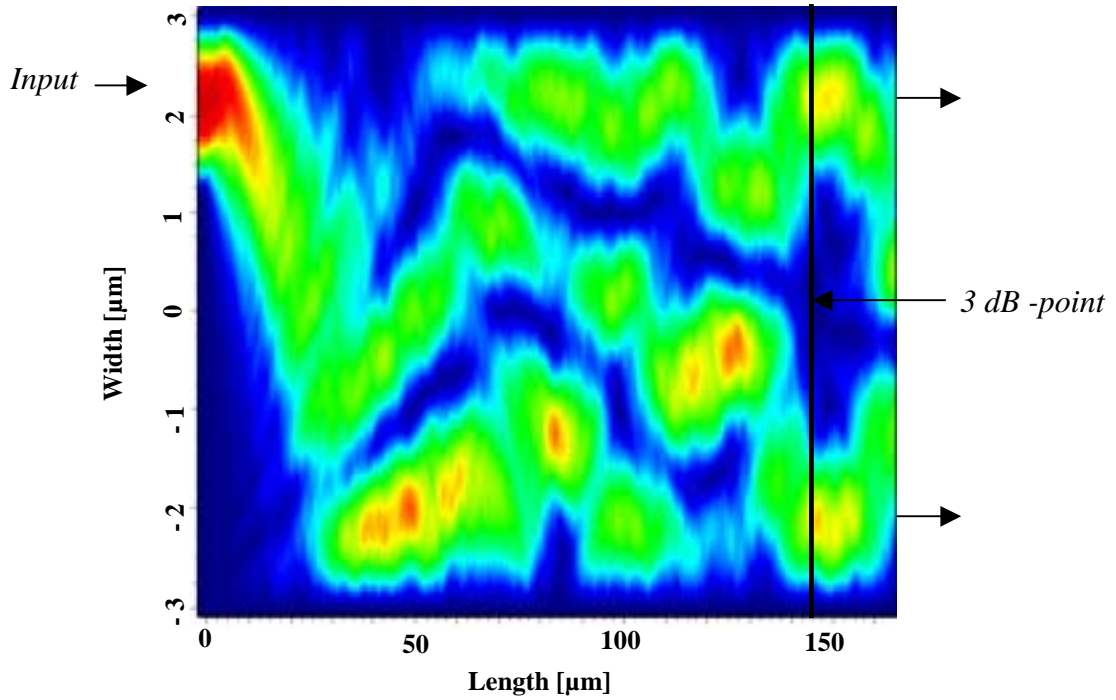


Fig. 72: Simulation of the MMI inserting TM polarized light at  $\lambda = 1.55 \mu\text{m}$ .

The 3-dB length is calculated to be  $146 \mu\text{m}$ . The MMI is nearly polarization independent with respect to the 3 dB point. This is an advantage compared to the codirectional coupler which will be described later.

The intensities at both output ports subject to the length of the multimode section have been calculated with a finite difference simulation tool [70] and are shown in Fig. 73. The light at the wavelength  $\lambda = 1.55 \mu\text{m}$  is inserted into input port 1. At a length of about  $160 \mu\text{m}$ , 50 % of the intensity from input port 1 is transferred to output port 2 and only 35 % is transferred to output port 1. The difference of 25 % is lost in the multimode section. The length for realizing a splitting ratio of  $\approx 3 \text{ dB}$  is obtained at  $L_{3 \text{ dB}} = 170 \mu\text{m}$  with low insertion losses. This

calculation is based on a three-dimensional finite difference method [87] for weakly guided waveguides which results in a lower accuracy of calculating the 3 dB length.

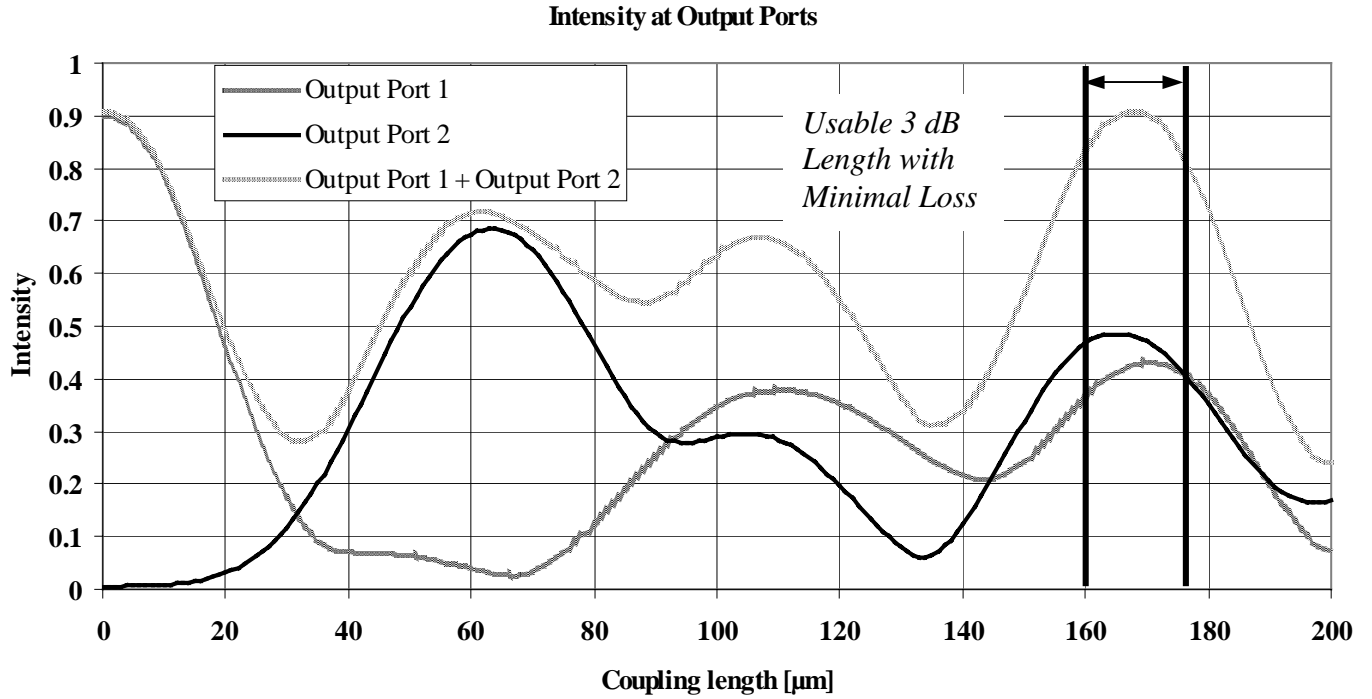


Fig. 73: Simulation of the intensities at the output ports of the used MMI coupler (TE - polarization) [87].

The time-frequency domain solver [53] used for the simulation shown in Fig. 70 performs the calculation of the mode interference in the multimode section in one entire step for a specific length. The 3 dB length is taken from the intensity diagram as demonstrated. The time-frequency domain solver has a higher accuracy than the calculation method used in Fig. 73 for calculating the mode interference in the MMI coupler. If both calculations are taken into account, the 3 dB length of the MMI coupler is in the range of 150  $\mu\text{m}$  – 175  $\mu\text{m}$ .

The following section presents the experimental results obtained for the simulated MMI structure.

### 4.3.2 Experimental results

The atomic force microscope (AFM) photograph of the input region of a MMI coupler is shown in Fig. 74. The deep etching on the outer side of the waveguide coming from the ring resonator can be clearly seen. The gap between the two input waveguides is  $2.4\ \mu\text{m}$ .

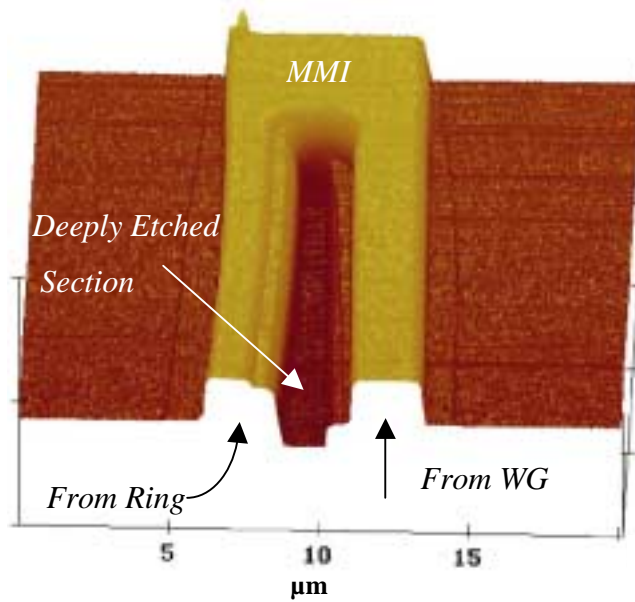


Fig. 74: AFM picture of the input region of the MMI coupler.

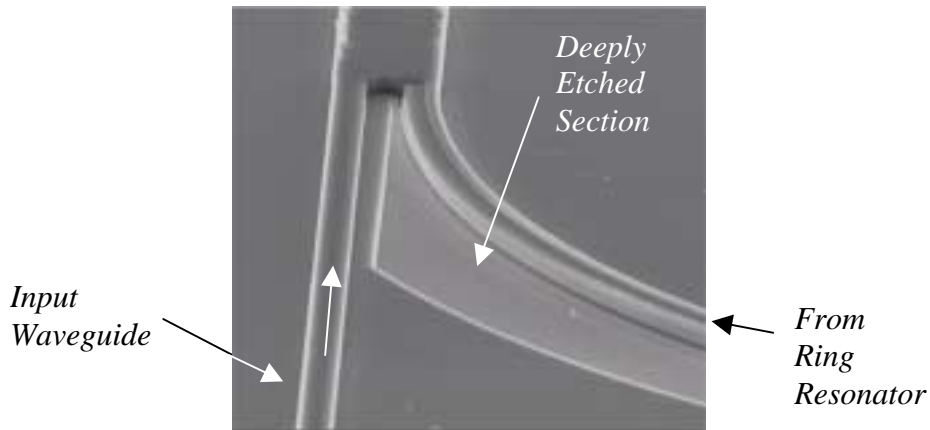


Fig. 75: SEM photograph of the input region of a MMI coupler integrated into an SRR.

The measurement results of MMI couplers with different lengths are shown in Fig. 76. The intensity of both outputs of the MMI coupler have been added and normalized to the output intensity of a straight reference waveguide in order to eliminate the coupling losses and intrinsic waveguide losses. The splitting ratio is tolerant with respect to the length of the MMI from a length of  $148\ \mu\text{m}$  onward. The ideal MMI coupler with a low loss ( $D^2 \approx 14\%$ ) is obtained at a length of  $150\ \mu\text{m}$  as was predicted by the simulations in the previous section. This is a very compact MMI coupler which is used for realizing a 3 dB splitting ratio in the ring resonators. MMI couplers with a length of  $184 - 233\ \mu\text{m}$  have previously been used in

ring lasers [18]. Extremely short 3 dB MMI couplers with a length of 15 – 50  $\mu\text{m}$  are demonstrated in [88].

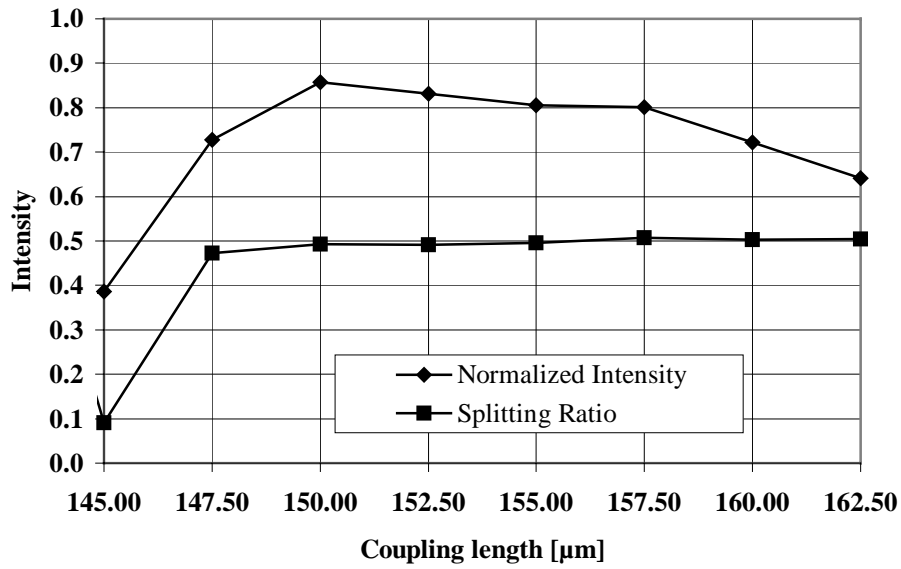


Fig. 76: Measurement results of the MMI couplers at different lengths.

The usage of short couplers with defined splitting ratio is essential in ring resonators for achieving a high FSR. Ring resonators ideally require a tunable coupler in order to adjust the coupling factor to the roundtrip loss in the case of passive resonators and to realize specific filter characteristics in the case of multiple coupled ring resonators. An MMI coupler with a tunable splitting ratio was demonstrated in [89].

The following section describes the simulated and fabricated results of the used codirectional couplers.

### 4.3.3 The codirectional coupler

Another important device which is used to couple light into the ring resonator is the codirectional coupler (CC). This type of coupler is used to realize splitting ratios other than 3 dB (c.f. Fig. 77).

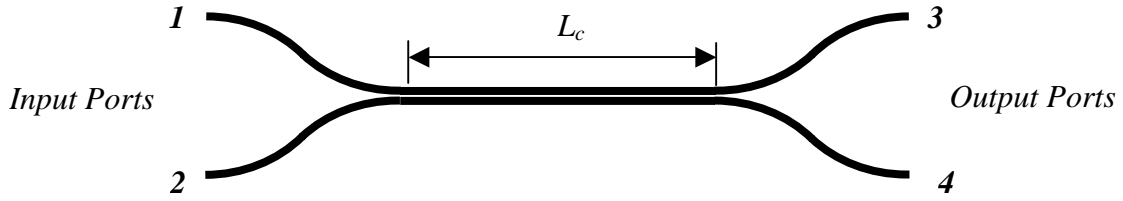


Fig. 77: The codirectional coupler.

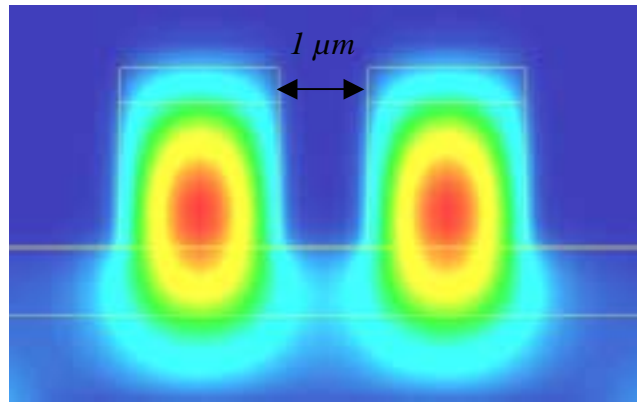


Fig. 78: Modeprofile of the codirectional coupler with a coupling gap of 1  $\mu\text{m}$ .

The effective refractive index for TE polarization for the used coupler with gaps of 0.8  $\mu\text{m}$  – 1  $\mu\text{m}$  is  $n_{\text{eff}} \approx 3.1923$ . The difference in the refractive index due to polarization is  $\Delta n_{\text{eff}}(\text{TE-TM}) \approx 0.006$ . The coupler which is used for the input and output coupling is a symmetrical coupler (identical waveguide geometries) with uniform coupling losses  $D^2$ . The equations which describe the input and output field of the coupler are given by [90]:

$$\begin{bmatrix} E_3 \\ E_4 \end{bmatrix} = (1 - \gamma)^{\frac{1}{2}} \begin{bmatrix} \sqrt{1 - \kappa} & -j\sqrt{\kappa} \\ -j\sqrt{\kappa} & \sqrt{1 - \kappa} \end{bmatrix} \cdot \begin{bmatrix} E_1 \\ E_2 \end{bmatrix} \quad (4.12)$$

The relation between the in- and output intensity of a symmetrical codirectional coupler is given using:

$$\begin{bmatrix} I_3 \\ I_4 \end{bmatrix} = (1 - \gamma) \begin{bmatrix} 1 - \kappa & \kappa \\ \kappa & 1 - \kappa \end{bmatrix} \cdot \begin{bmatrix} I_1 \\ I_2 \end{bmatrix} \quad (4.13)$$

where  $\gamma$  is the intensity loss coefficient,  $\kappa$  is the intensity coupling factor.

If both waveguides have the same propagation constant which is the case in this configuration and the light is inserted into input port 1, then after a length  $L_c$  the energy will have coupled into the other waveguide and can be detected at output port 4.

The coupling behavior dependent on  $L_c$  for light inserted at input port 1 is expressed by [71]:

$$E_3(x) = E_1(1-\gamma)^{\frac{1}{2}} \cos\left(\frac{\pi}{2L_c}x\right) \quad (4.14)$$

$$E_4(x) = jE_1(1-\gamma)^{\frac{1}{2}} \sin\left(\frac{\pi}{2L_c}x\right) \quad (4.15)$$

$$I_3(x) = E_3(x) \cdot \overline{E_3(x)} \text{ and } I_4(x) = E_4(x) \cdot \overline{E_4(x)} \quad (4.16)$$

The coupling behavior for a coupler with  $L_c = 450 \mu\text{m}$ ,  $E_1 = 1$ ,  $E_2 = 0$  is shown in Fig. 79. The intensity at both output ports is normalized to the sum of the output intensities:

$$\text{Intensity at output port 3} = \frac{I_3}{I_3 + I_4} \quad (4.17)$$

$$\text{Intensity at output port 4} = \frac{I_4}{I_3 + I_4} \quad (4.18)$$

The power coupling factor  $\kappa$  is taken from the diagram (Fig. 79) for a specific coupling length  $x$ . For example, the power coupling factor  $\kappa$  is equal to  $\kappa = 0.9$  for a coupler with a length of  $360 \mu\text{m}$ .

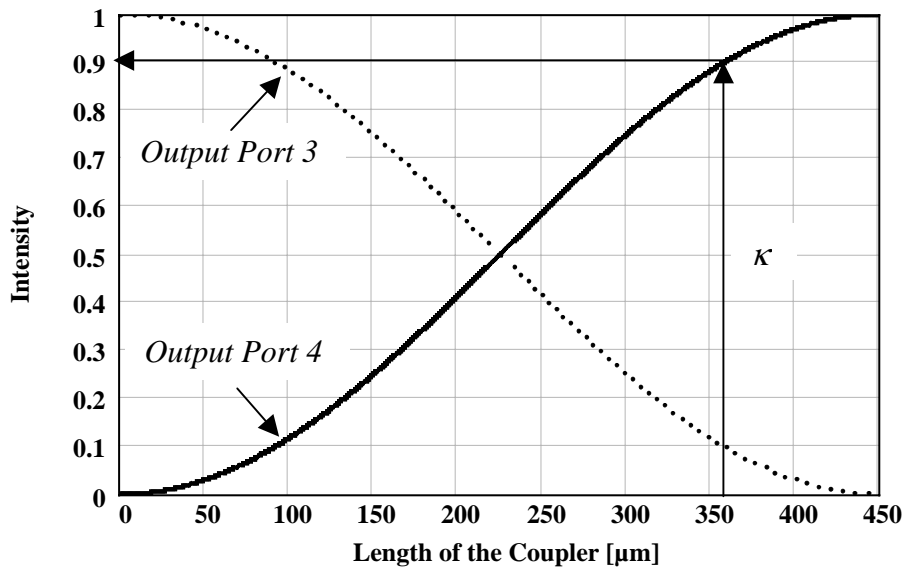


Fig. 79: Coupling behavior of a symmetrical codirectional coupler.

The experimental results for fabricated codirectional couplers are described in the following section.



#### 4.3.4 Experimental results

The following results are obtained from codirectional couplers fabricated by using standard photolithography. The splitting ratio is very sensitive with respect to the length of the couplers. For this reason MMI couplers are chosen to realize 3 dB splitting ratios. The measurement results for codirectional couplers with a coupling gap of  $0.8 \mu\text{m}$  are shown in Fig. 80. The simulation was carried out using relation (4.18) with  $L_c = 500 \mu\text{m}$ .

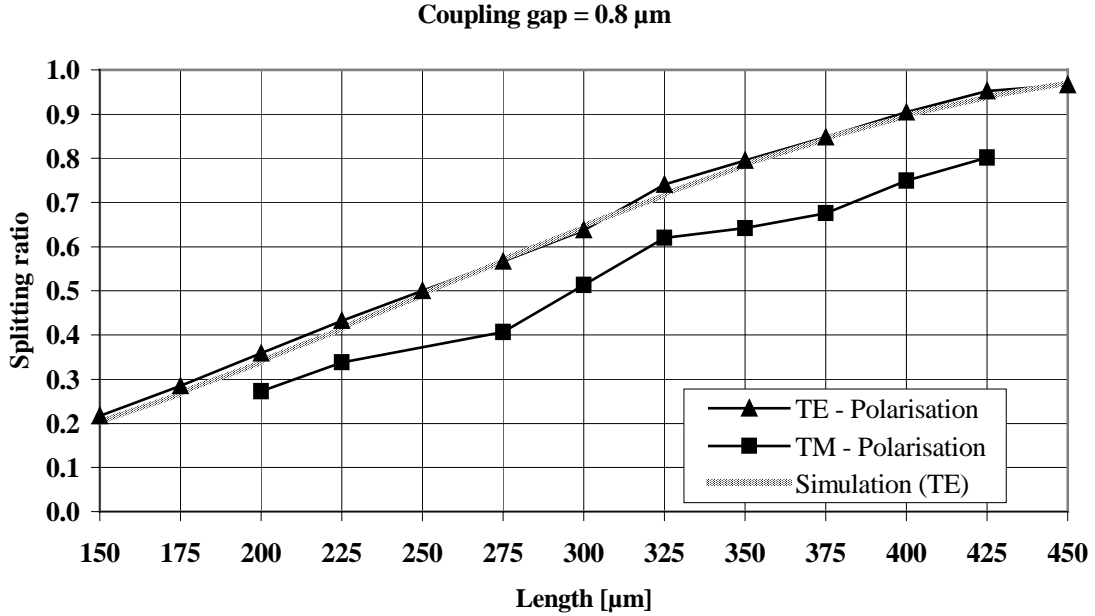


Fig. 80: Measurement results of a coupler with a gap of  $0.8 \mu\text{m}$ .

Using conventional photolithography speeds up the fabrication process and enables an easier transfer for large scale manufacturing later on. Here, coupling gaps of  $0.8 \mu\text{m}$ ,  $0.9 \mu\text{m}$ ,  $1 \mu\text{m}$  were realized. The measurement for the couplers with a gap of  $0.8 \mu\text{m}$  and  $0.9 \mu\text{m}$  was performed using TE and TM polarized light, which revealed a difference in the splitting ratio between 0.08 - 0.1. The coupler losses are less than 10 %. Finally, a coupling gap of  $0.8 \mu\text{m}$  is used in the resonators where high splitting ratios are needed (e.g.  $\kappa = 0.7$ ). Low splitting ratios are achieved using couplers with gaps of  $1 \mu\text{m}$  ( $\kappa < 0.1$ ).

The measurement results for codirectional couplers with a coupling gap of  $0.9 \mu\text{m}$  are shown in Fig. 81. The simulation was carried out using relation (4.18) with  $L_c = 770 \mu\text{m}$ .

The measurement results for codirectional couplers with a coupling gap of  $1 \mu\text{m}$  are shown in Fig. 82. The simulation was carried out using relation (4.18) with  $L_c = 1000 \mu\text{m}$ .

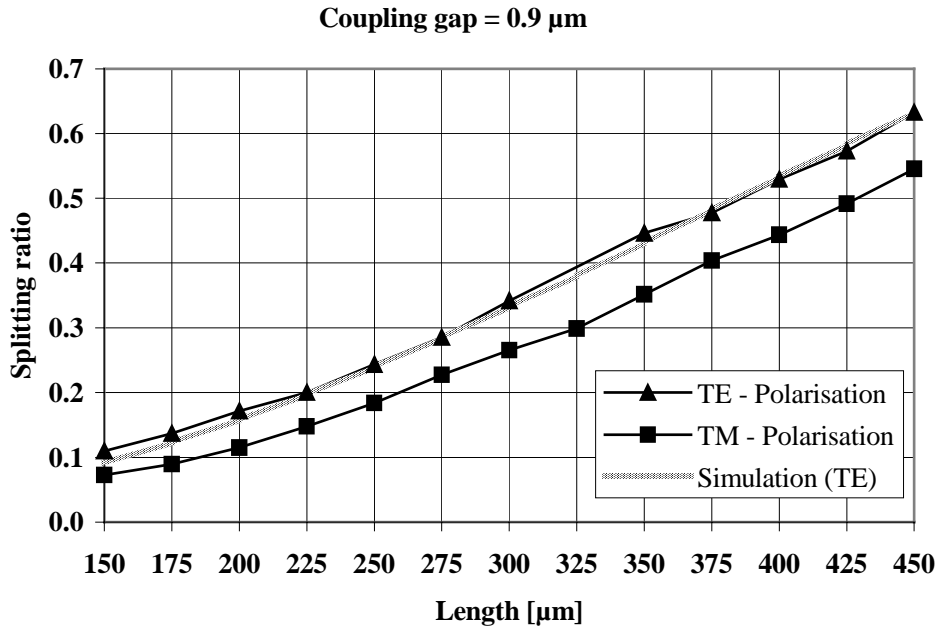


Fig. 81: Measurement results of a coupler with a gap of 0.9  $\mu\text{m}$ .

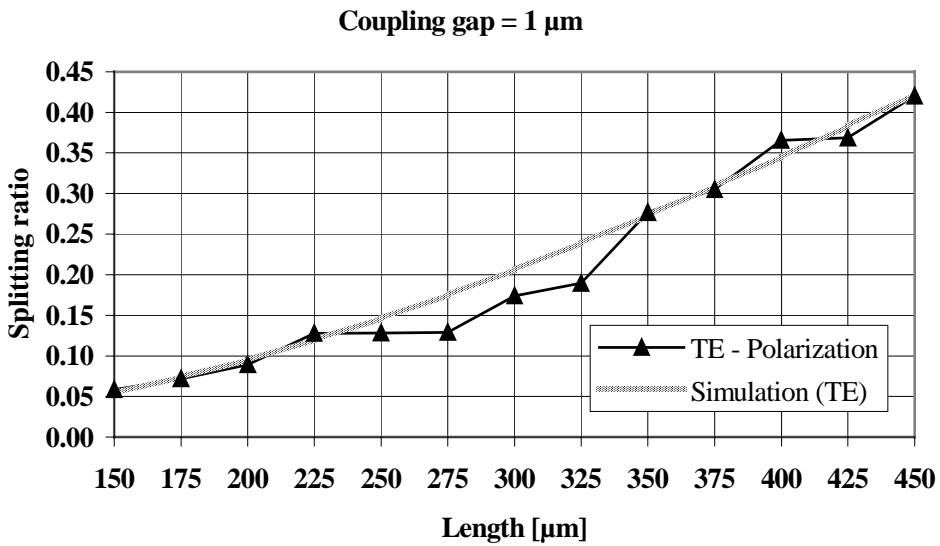


Fig. 82: Measurement results of a coupler with a gap of 1  $\mu\text{m}$ .

The separation between the waveguides in the codirectional coupler is the critical element regarding the fabrication. The resolution of the photolithography defines the minimum coupling gap, which is 0.8  $\mu\text{m}$  in our case. The fabrication of the gap depends mainly on the waveguide width and the etch depth in gap. The etch depth in the gap is lower (Fig. 83) than on the outer side of the coupler waveguides, which is due to the lower etch rate in the gap. The dry etching process is strongly dependent on the etch gases and conditions used and has to be modified if performed with other RIE systems to achieve similar results.

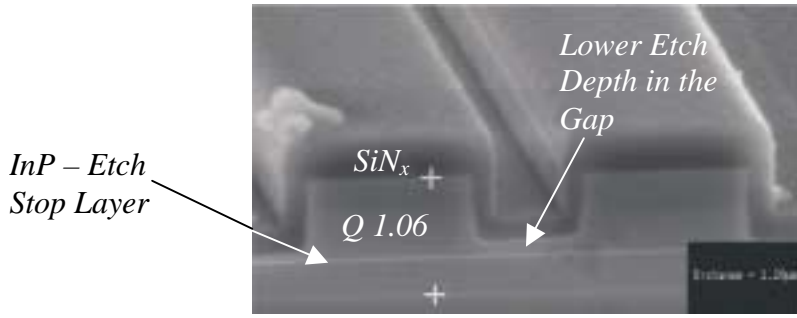


Fig. 83: SEM photograph of the input region of a directional coupler, Gap = 0.8  $\mu\text{m}$ .

The coupling length at a splitting ratio of  $\kappa = 1$  depending on the height of the material in the gap has been calculated using a finite difference method simulation tool [70] (TE polarization, Fig. 84). The obtained results are verified using the fabricated codirectional coupler with a gap of 0.8  $\mu\text{m}$  (Fig. 80) and the SEM photograph in Fig. 83. The measured coupling length for a splitting ratio of  $\kappa = 1$  is  $\approx 500 \mu\text{m}$  (TE polarization). The measured height of the material in the center is  $\approx 120 \text{ nm}$ .

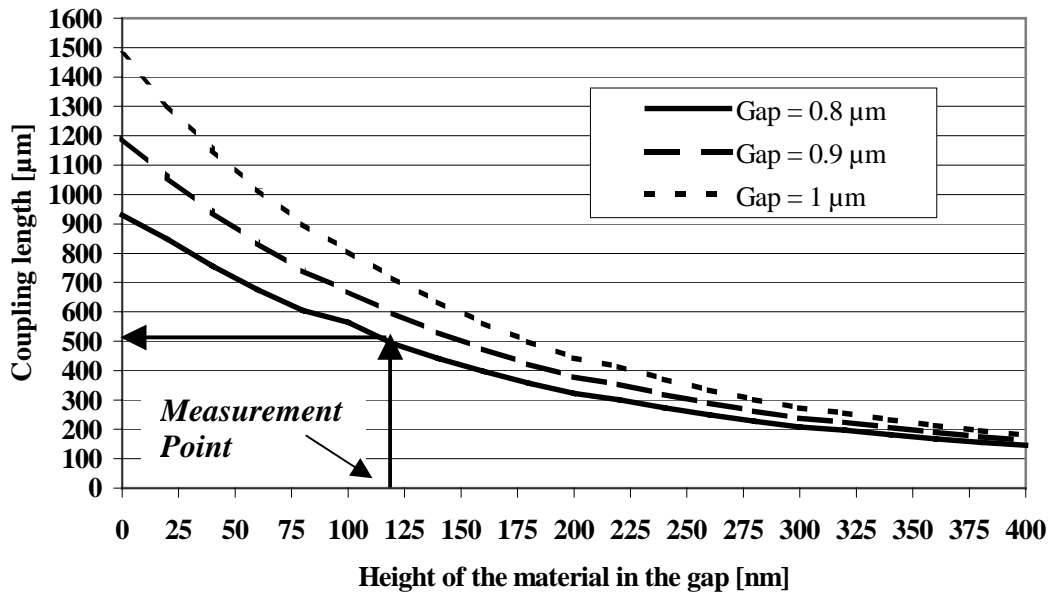


Fig. 84: Calculated coupling length depending on the etch depth in the gap.

These values are confirmed by the simulation. These presented codirectional couplers with the specific coupling factors depending mainly on the coupling length and the etch depth in the gap have been fabricated reproducibly.



## 5 Ring resonators

### 5.1 Passive ring resonators

#### 5.1.1 Integration of the elements

The elements described in the previous sections are integrated in the ring resonators. The challenging technological task is to realize the deep etching of the waveguide in the outer section, without deep etching of the coupling region. The gap in between the coupling waveguides should remain as described in the previous section to realize short coupling lengths and reproducible coupling factors. The platinum layer which enables the local heating of waveguide segments of the ring resonators is deposited in a final step. Before the platinum is deposited, the entire devices are covered with a  $\text{SiN}_x$  layer. This layer assures that no metal will diffuse into the waveguide material and no waveguide mode couples to the metal and increases the propagation losses.

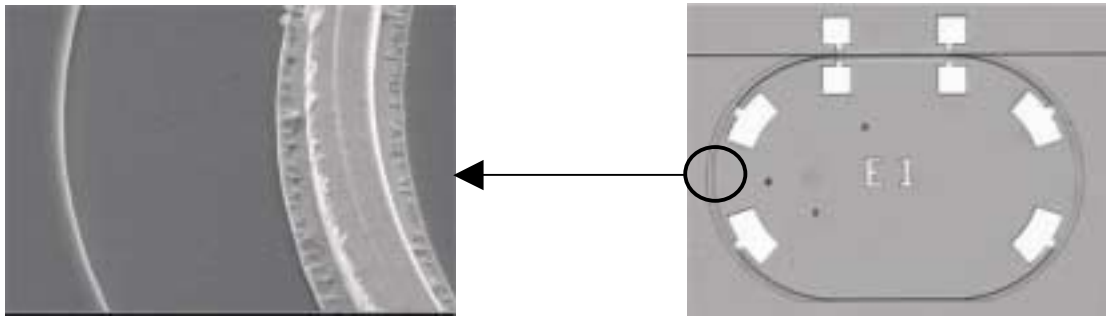


Fig. 85: SEM picture of the waveguide section with Pt heater.

A photograph of a part of a Pt-resistor integrated in an SRR is shown in Fig. 85. The pads for contacting the Pt-resistor are composed of Ti-Pt-Au. A DRR with integrated Pt-resistors is shown in Fig. 86.

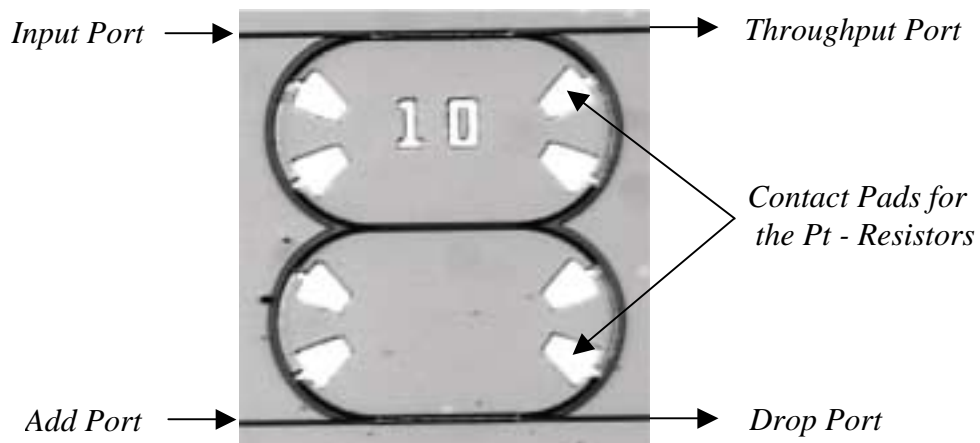


Fig. 86: Fabricated passive DRR.

The devices have cleaved end facets which are anti reflection coated in order to avoid Fabry-Perot resonances in the straight waveguides.

### 5.1.2 Experimental results

The measurement result shown in Fig. 87 is from an SRR ( $R = 100 \mu\text{m}$ ) with one input/output waveguide including a 3 dB MMI coupler with a length of  $150 \mu\text{m}$ . The insertion loss of the device is 6 dB. From the simulation, the effective index for the curved section ( $\lambda = 1.55 \mu\text{m}$ ) is calculated to be 3.192. The group index ( $\lambda = 1.55 \mu\text{m}$ ) for the curved waveguide section is calculated using Eq. (2.30) to be 3.44. The roundtrip loss ( $\alpha L$ ) is evaluated to be 1.9 dB. The FSR achieved is 94 GHz. The FWHM is 0.137 nm resulting in a finesse of  $F = 5.5$  and a  $Q$  factor of  $Q \approx 11300$ . The on-off ratio is 13 dB.

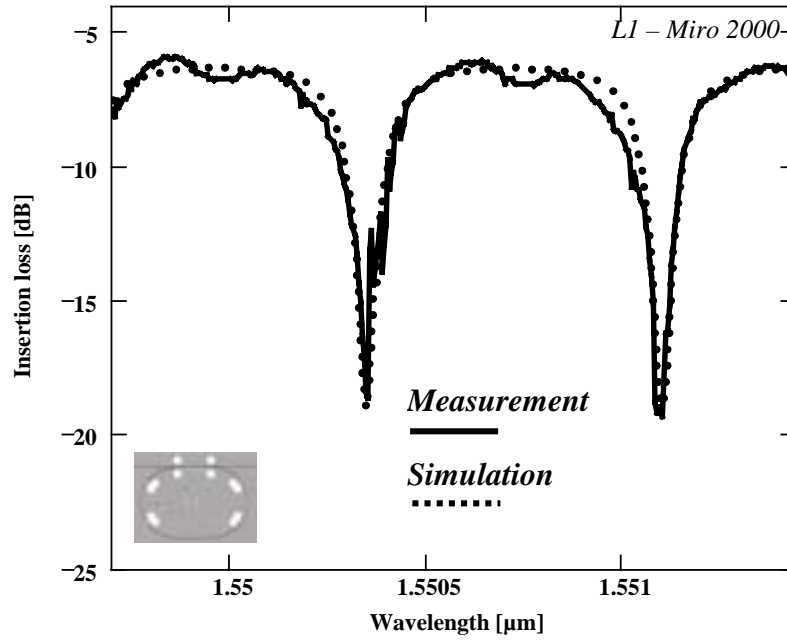


Fig. 87: SRR with one input/output waveguide, 3 dB MMI coupler (length =  $150 \mu\text{m}$ ),  $R = 100 \mu\text{m}$ , FSR = 94 GHz.

The transmission characteristic shown in Fig. 88 was achieved using a similar SRR as mentioned before but with a different length of the MMI, which is  $160 \mu\text{m}$ , resulting in a higher coupler loss. This leads to a slightly higher on-off ratio (14 dB). As all other parameters are unchanged, the resonator is better matched than the one before. Whereas many other integrated optical devices are limited by loss, ring resonators can use loss advantageously by fitting the loss into the overall configuration. Due to the increased length of the resonator, the FSR is now only 91.4 GHz. The roundtrip losses have been calculated to be 2.1 dB, which is slightly higher than before. This is only because of the additional losses in the coupler. The radius is still the same. The FWHM is 0.12 nm resulting in a finesse of  $F = 6.1$  and a  $Q$  factor of  $Q \approx 12900$ .

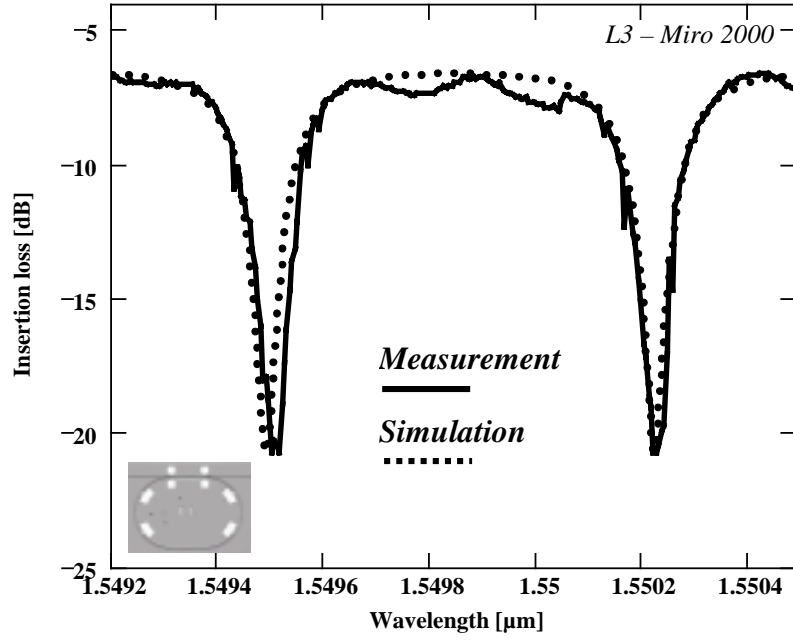


Fig. 88: SRR with one input/output waveguide, 3 dB MMI (length = 160  $\mu\text{m}$ ),  $R = 100 \mu\text{m}$ , FSR = 91.4 GHz.

The measurement in Fig. 89 was performed for the same ring resonator with the 160  $\mu\text{m}$  long MMI coupler using TM polarized light. The coupling factor  $\kappa$  was determined from the simulation to be  $\kappa = 0.5$ . This shows, that this MMI coupler is insensitive to polarization with respect to the splitting ratio. The ring losses have decreased by about 0.7 dB per roundtrip, which leads to an on-off ratio of only  $\approx 8$  dB. The lower bending loss is due to the better confinement of the mode in TM polarization.

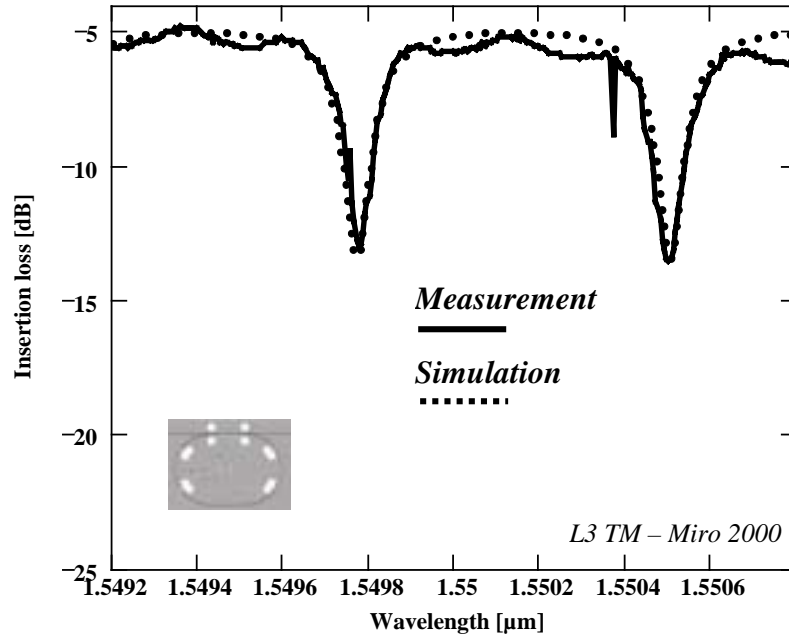


Fig. 89: SRR as in Fig. 88 but measured in TM polarization.

The field is more concentrated in the center of the waveguide and does not "see" as much of the sidewall roughness in the curvature as in TE polarization. The FWHM is measured to be 0.09 nm leading to a finesse of  $F = 8$ . The on-off ratio is measured to be 8.5 dB. The Q factor is evaluated to be  $Q \approx 17200$ . The lower bending loss for TM polarized light compared to the TE polarized light is responsible for this high Q value. The wavelength shift due to TM polarization is 0.28 nm = 35 GHz ( $\lambda = 1.55 \mu\text{m}$ ). The effective index in the curvature is higher for TM polarized light than for TE polarized light. The effective refractive index difference between TE and TM polarization for the entire ring resonator including the straight waveguide and the MMI coupler is evaluated from the simulation to be  $\Delta n_{\text{eff} \text{ TE-TM}} = 9.5 \times 10^{-4}$ .

The transmission characteristic of a single ring resonator with a 3 dB MMI (length = 150  $\mu\text{m}$ ) and a radius of  $R = 200 \mu\text{m}$  is shown in Fig. 90. The FSR achieved is 56 GHz at  $\lambda = 1.55 \mu\text{m}$ . The roundtrip loss is 2 dB. The on-off ratio is measured to be 14 dB. The FWHM is 0.08 nm, resulting in a finesse of  $F = 5.4$  and a Q factor of  $Q \approx 19400$ .

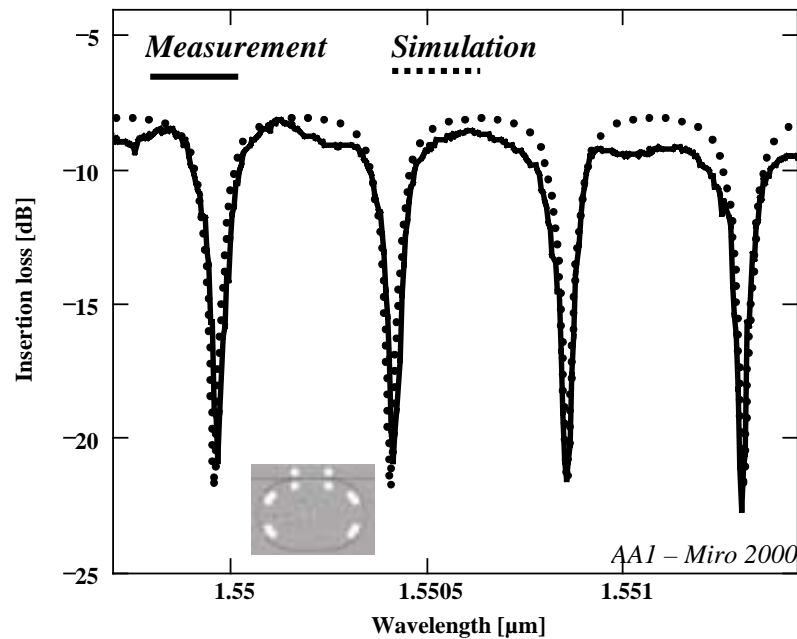


Fig. 90: SRR with one input/output waveguide, 3 dB MMI (length = 150  $\mu\text{m}$ ),  $R = 200 \mu\text{m}$ , FSR = 56 GHz.

The filter response of an SRR with a codirectional coupler measured in TE and TM polarization is shown in Fig. 91 and Fig. 92, respectively. The SRR has a radius of  $R = 200 \mu\text{m}$  and a coupler length of 260  $\mu\text{m}$  with a gap of 0.9  $\mu\text{m}$ . The FSR is 49 GHz and the FWHM is 0.04, resulting in a finesse of  $F = 10$  and a Q factor of  $Q \approx 39000$ . The on-off ratio is more than 20 dB. The roundtrip loss is 1.6 dB which is better than the SRR with the same radius and MMI coupler.



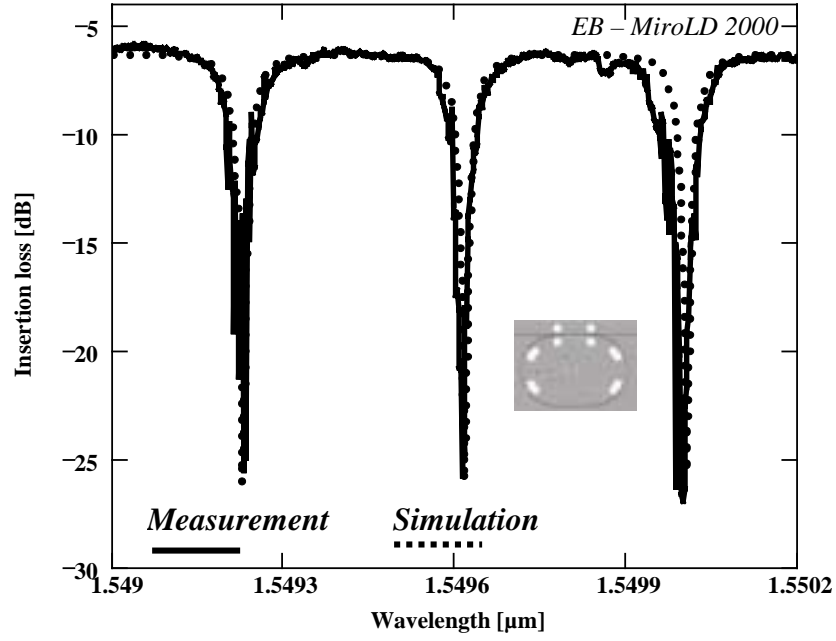


Fig. 91: SRR with one input/output waveguide, codirectional coupler (length = 260  $\mu\text{m}$ , gap = 0.9  $\mu\text{m}$ ),  $R = 200 \mu\text{m}$ , FSR = 49 GHz.

This is because the coupler loss of a directional coupler is lower than that of a MMI coupler. The simulation fits extremely well to the experimental data. The coupling factor  $\kappa$  is taken from the measurement in section 4.3.4, Fig. 81 and is  $\kappa = 0.26$ . The same resonator is investigated by using TM polarized light. The parameters which have changed are the coupling factor  $\kappa$ , which is  $\kappa = 0.195$  and the roundtrip loss, which is 1.4 dB.

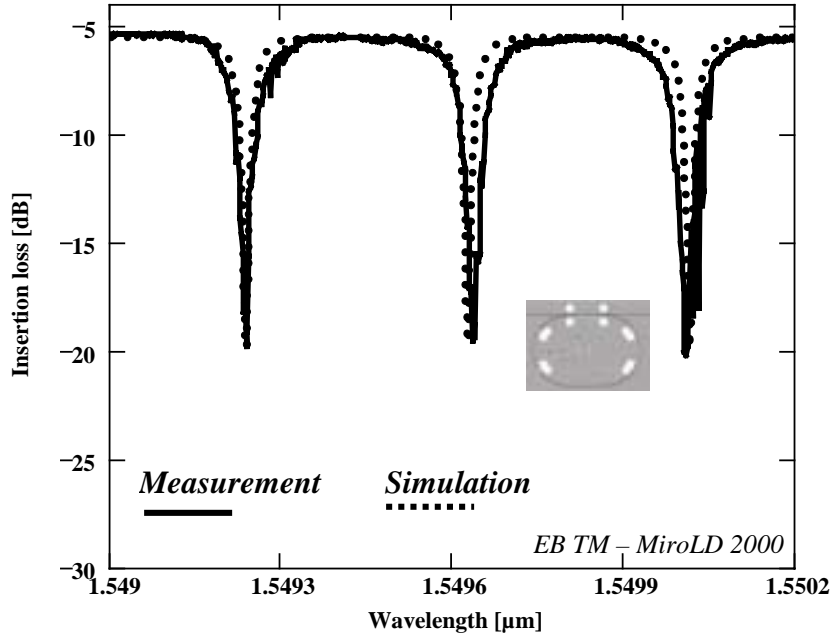


Fig. 92: SRR as in Fig. 91 but measured in TM polarization.

The effective index in the curves is higher for TM polarized light. The effective refractive index difference between TE and TM polarization for the entire ring resonator including the straight waveguide and the coupler is evaluated from the simulation to be  $\Delta n_{eff\ TE-TM} = 3 \times 10^{-5}$ . The position of the transmission minima changes only by 0.01 nm which is equal to 1.25 GHz. The FSR has only decreased by  $\approx 300$  kHz ( $\lambda = 1.55 \mu\text{m}$ ). This means that the wavelength accuracy of the minima due to different polarizations is 1.25 GHz. The on-off ratio has decreased to 15 dB. This lower value is caused by the coupling factor  $\kappa$ . If the coupling factor  $\kappa$  is matched to the lower roundtrip loss, an SRR for TM polarization with an on-off ratio of more than 20 dB can be realized. The FWHM is 0.034 nm, leading to a finesse of  $F = 11.5$  and a Q factor of  $Q = 45600$ .

The filter shape can be changed by using multiple coupled ring resonators. The following device is designed to include two ring resonators with a radius of  $100 \mu\text{m}$ . The upper and lower couplers  $\kappa_0, \kappa_2$  are MMI couplers with a length of  $150 \mu\text{m}$  and coupling ratios of  $\kappa_0, \kappa_2 = 0.5$ . A codirectional coupler (CC) with a coupling gap of  $1 \mu\text{m}$  and a length of  $150 \mu\text{m}$  is used in the center of the DRR. The coupling factor of  $\kappa_1 = 0.055$  is taken from the measurements in Fig. 82. The filter characteristic of the device is shown in Fig. 93.

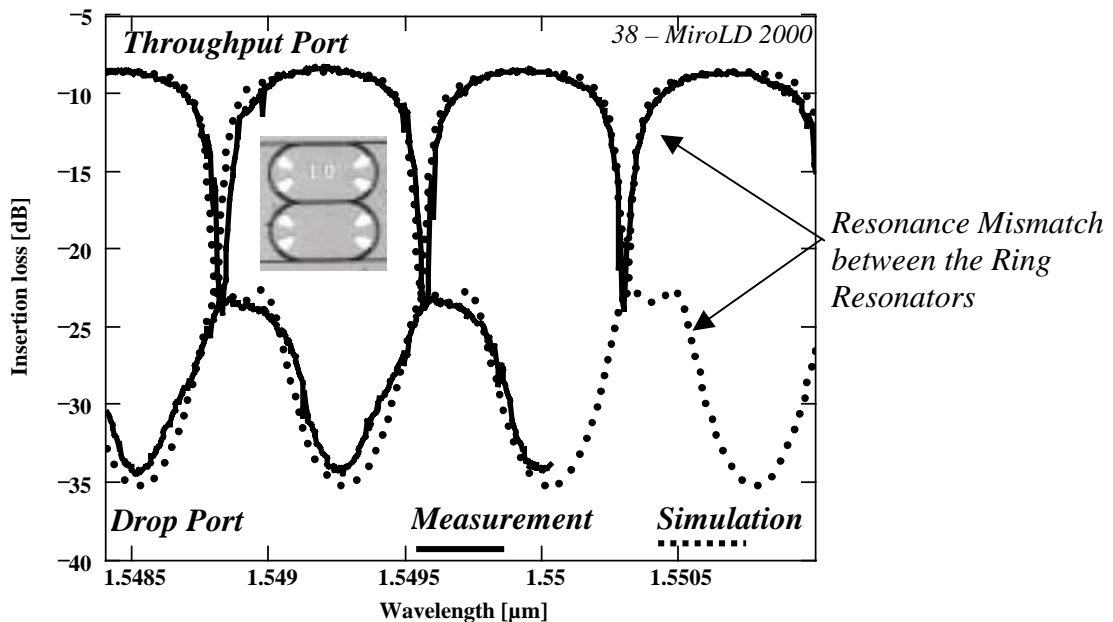


Fig. 93: DRR with two MMI couplers (length =  $150 \mu\text{m}$ ) and a codirectional coupler (length =  $150 \mu\text{m}$ , gap =  $1 \mu\text{m}$ ),  $\kappa_0, \kappa_2 = 0.5$ ,  $\kappa_1 = 0.055$ ,  $R = 100 \mu\text{m}$ , FSR = 94 GHz.

The FSR (94 GHz) of the DRR is equal to the previously mentioned SRR with the same parameters. The FWHM of the throughput and of the drop port is 0.12 and 0.28 nm, respectively. The finesse for the throughput and for the drop port is calculated to be  $F = 6$  and

$F = 3$ . The broadening of the FWHM of the drop port is due to a difference in the refractive index between the upper and lower resonator of  $\approx 0.00035$ . This index difference causes a resonance mismatch between the upper and lower resonator, which results in an asymmetrical filter characteristic. The resonance matching of the DRR is performed by activating the integrated Pt – resistors. This is described in detail in section 5.1.4. The resonance mismatch leads also to different on-off ratios which are about 16 dB and 12 dB for the throughput port and for the drop port, respectively.

The measured filter characteristic could be simulated very well with the used method in which all necessary data was extracted. The ring resonators were designed for an FSR of 50 GHz and 100 GHz. This was realized with an accuracy of about 6 GHz. The FSR can now be adjusted more efficiently to the desired values (12.5 GHz, 25 GHz, 50 GHz, 100 GHz) as all parameters have been extracted. This will be demonstrated later in section 5.2.4.

Another well known measurement method known as the OLCR (4.2.2) is used for the first time to the authors knowledge in the following section to extract all necessary parameters describing the transmission characteristic of a ring resonator from a so called reflectogram. The OLCR measurements of single ring resonators with one input/output waveguide and a codirectional coupler are presented.

### 5.1.3 Results from the OLCR measurement

The OLCR measurement in reflection mode in Fig. 94 is obtained from an SRR without anti reflection coating with a codirectional coupler (length = 150  $\mu\text{m}$ , gap = 0.9  $\mu\text{m}$ ) and  $R = 100$   $\mu\text{m}$ . Where  $P_0$  denotes the input intensity,  $\kappa$  is the power coupling coefficient,  $D^2$  is the intensity loss coefficient of the coupler,  $R$  is the reflection factor of the facets which is assumed to be identical for both facets and  $A$  is the roundtrip loss of the ring resonator.

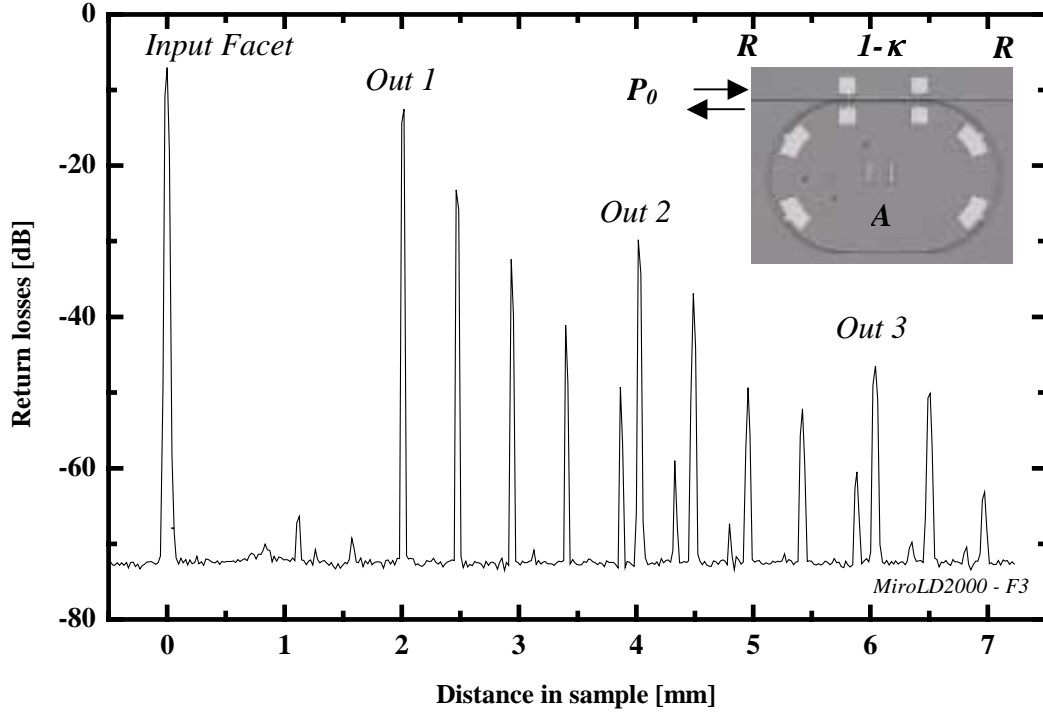


Fig. 94: SRR ( $R = 100$   $\mu\text{m}$ ) without AR, measured in reflection mode.

The first peak is measured at the input facet of the device. The second peak ( $\text{out}_1$ ) is measured at the output facet. There are no significant reflection peaks in between those peaks coming from the ring resonator, which shows that the input signal has passed the resonator undisturbed. The peaks in between peak  $\text{out}_1$ , peak  $\text{out}_2$  and peak  $\text{out}_3$  result from multiple roundtrips in the ring resonator. The distance between the peaks  $\text{out}_{1-2}$  is 2 mm which corresponds to the chip length. The distance between two peaks coming from the ring resonator is equal to half of the cavity length which is measured to be  $\approx 466$   $\mu\text{m}$  (physical value 464  $\mu\text{m}$ ). The coupling factor  $\kappa$  can be calculated from the values obtained for peak 1 and 2.

The intensity  $I$  of the peaks can be described as follows:

$$I_{\text{Peak1}} = P_0 \bar{R} \quad (5.1)$$

$$I_{\text{Peak2}} = P_0 \bar{R}^2 (1 - \kappa)^2 \bar{R} D^4 \quad (5.2)$$

$$I_{\text{Peak3}} = 2P_0 \bar{R}^2 \kappa^2 A (1 - \kappa) \bar{R} D^6 \quad (5.3)$$

$$I_{Peak4} = 2P_0 \overrightarrow{R^2} \kappa^2 A^2 (1 - \kappa)^2 \overrightarrow{RD}^8 \quad (5.4)$$

The peaks obtained from  $n$  roundtrips in the ring can be described by:

$$I_{Peak\ n} = 2P_0 \overrightarrow{R^2} \kappa^2 A^n (1 - \kappa)^n \overrightarrow{RD}^{4+2n} \quad (5.5)$$

The input intensity  $P_0$  is calculated from peak 1, assuming a reflection factor of  $R \approx 27\%$  (section 4.2.4), to be  $-1.4$  dB. The inserted light passes the input facet, passes the coupler, is reflected at the other facet, passes the coupler again and is emitted at the input facet. Assuming that the coupler has a loss of  $\approx 10\%$  and the straight waveguide is lossless, a power coupling factor of  $\kappa \approx 0.1$  is derived from the value of peak 2. The loss of the coupler and the reflection factor of the facets have to be known to be able to calculate the power coupling factor. The roundtrip loss  $A$  is estimated from these values to be  $A \approx 4$  dB.

A reflectogram of an SRR measured in transmission mode which has been mentioned already in section 5.1.2 (Fig. 91) is shown in Fig. 95. Where  $P_I$  is the intensity obtained at the throughput port of the ring resonator.

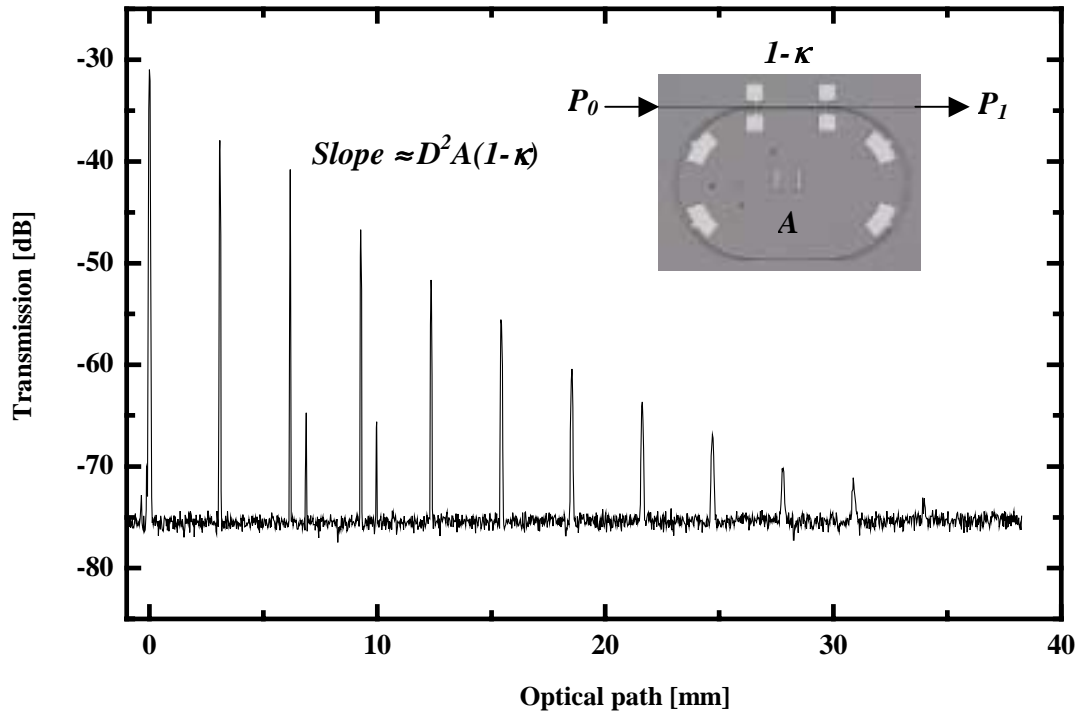


Fig. 95: Reflectogram of an SRR with one waveguide.

The first peak is the transmission passing the coupler without entering the ring. The second peak is the transmission from one roundtrip in the ring. The third peak is the transmission from two roundtrips and so on. The roundtrip loss is evaluated from the transmission data beginning from the second peak. In this calculation the loss in the straight waveguide is not considered and is contained in the coupling factor and the roundtrip loss. The length between the peaks is equal to half of the optical length of the ring resonator. The average optical length

(in the ring) is taken from the measurement (e. g. distance between peak 2 and 3) and is equal to 6171.86  $\mu\text{m}$ . The measured SRR has a resonator length of 1776.64  $\mu\text{m}$ . The group index is calculated to be  $n_{gr}=3.47$ . This is the average group index which the traveling light wave experiences when it passes the coupling region, the curved sections and the straight section in the resonator.

The output intensity  $P_I$  can be described as follows:

$$\text{Peak 1: } P_1 = P_0 D^2 (1 - \kappa) \quad (5.6)$$

$$\text{Peak 2: } P_1 = P_0 A D^4 \kappa^2 \quad (5.7)$$

$$\text{Peak 3: } P_1 = P_0 A^2 D^6 (1 - \kappa) \kappa^2 \quad (5.8)$$

The peaks obtained from  $n$  roundtrips in the ring can be described by:

$$\text{Peak } n: P_1 = P_0 A^n D^{2n} (1 - \kappa)^{n-1} \kappa^2 \quad (5.9)$$

The slope from the measurement peaks resulting from  $n$  roundtrips in the ring is given by:

$$\text{slope} = A(1 - \kappa) D^2 \quad (5.10)$$

The intensity difference between the first and the second peak  $P_{2-1}$  corresponds to:

$$P_{2-1} = D^2 \frac{\kappa^2 A}{1 - \kappa} \quad (5.11)$$

The slope from the second peak onward is evaluated to be - 3.7 dB/(roundtrip), leading to an estimated roundtrip loss of  $A \approx 2$  dB. The coupler loss is again assumed to be  $\approx 10$  % and the coupling factor is taken from section 5.1.2 (Fig. 91) to be  $\kappa = 0.26$ . The accuracy of the measured peaks is within a tolerance margin of  $\pm 1$  dB.

The OLCR measurement method enables an insight study of the quality of the ring cavity and has the potential to efficiently extract all necessary ring parameters to describe the spectral behavior of the ring resonator configuration.

The following section describes the tuneability and resonance matching using the integrated Pt – resistors.

### 5.1.4 Tuneability and resonance trimming

Tuneability is essential for the system application of optical filters. In the case of periodic filters, in this case ring resonators, it is important to fit the transmission curve to the defined channel spacing (e.g. ITU-Grid). The tuneability is realized with the help of the integrated Pt-resistors (5.1.1). The Pt-resistors have two functions. The first function is the tuning to a specific wavelength, the second function is the resonance matching of multiple coupled ring resonators to each other.

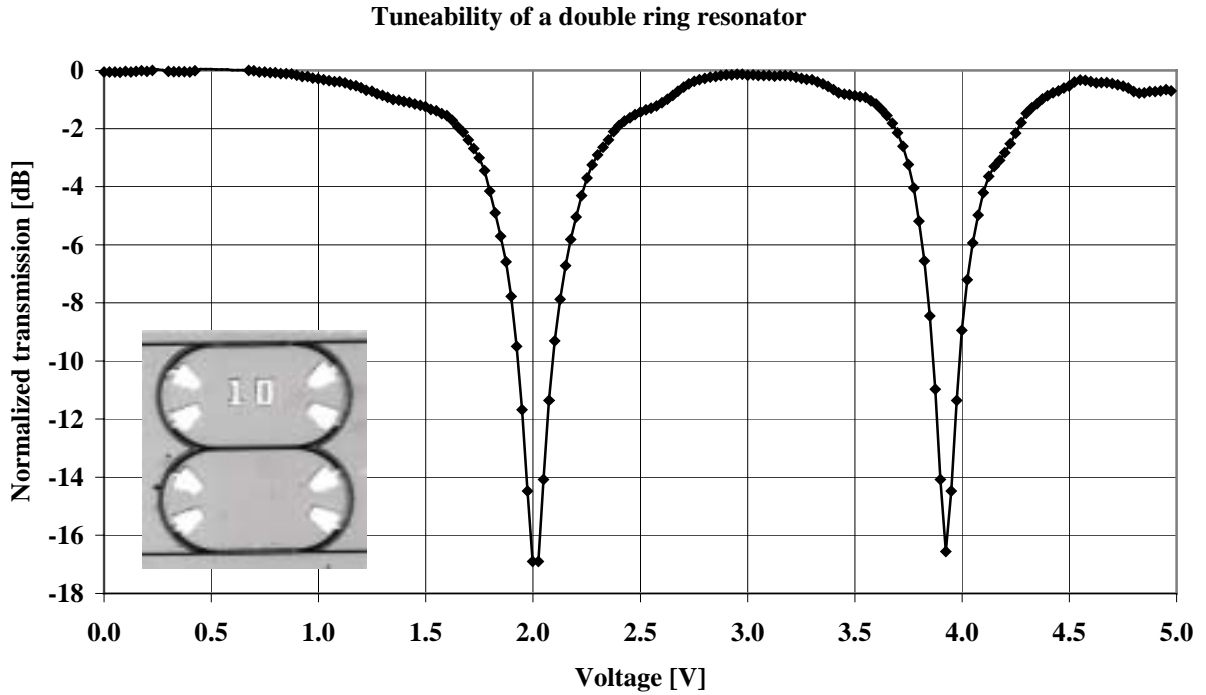


Fig. 96: Tuneability of a DRR with two MMI couplers (length = 150  $\mu\text{m}$ ) and a codirectional coupler (length = 150  $\mu\text{m}$ , gap = 1  $\mu\text{m}$ ),  $R = 100 \mu\text{m}$ , FSR = 94 GHz.

The measurement result in Fig. 96 shows the tuning to a specific wavelength. The output intensity was normalized to the insertion loss. The measurement was performed by adjusting the throughput port to maximum transmission at the corresponding wavelength. The platinum resistors in the upper and lower ring resonators were used simultaneously. By detection of the response of the throughput (drop) port the voltage was continuously increased. At a voltage of 2 V and 4 V, the signal is “dropped” with a crosstalk better than 16 dB. The second minimum at 4 V is due to the fact that the  $n+1$  wavenumber fits into the resonator. The tuning was performed using a DRR with a radius of  $R = 100 \mu\text{m}$  and an FSR of 94 GHz. The Pt – resistors assure the tuneability over the whole 94 GHz range and enable the realization of a wavelength selectable switch.

The tuning of an SRR is shown in Fig. 97. Here the on-off ratio is more than 20 dB. The transmission characteristic of the measured SRR is shown in Fig. 91. The use of the Pt –

resistors reveals a larger on-off ratio than obtained by sweeping the ECL wavelength. The Pt - resistors enable a finer tuning to the specified wavelength and so an improved on-off ratio is realized.

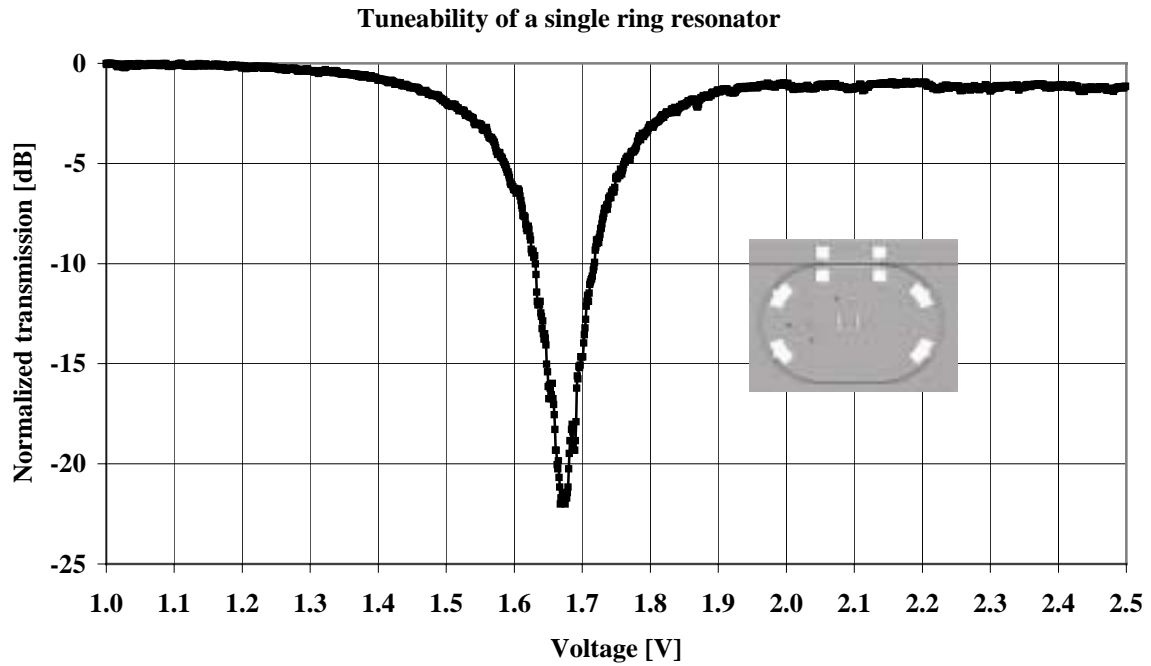


Fig. 97: Tuneability of an SRR with one input/output waveguide and a codirectional coupler.

The second feature of the Pt – resistors, the resonance matching, is demonstrated with a DRR ( $R = 200 \mu\text{m}$ , upper and lower coupling factors  $\kappa_{0,2} = 0.5$ , middle coupling factor  $\kappa_I = 0.055$ , coupler lengths =  $150 \mu\text{m}$ ). The upper curve (Fig. 98) shows the response of the throughput port and the lower curve that of the drop port.

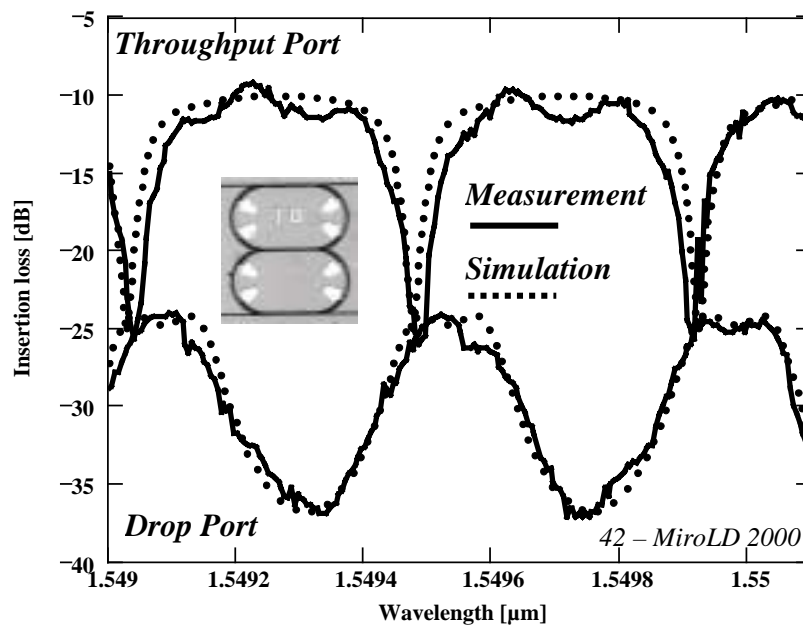


Fig. 98: DRR with two MMI couplers and a codirectional coupler (gap =  $1 \mu\text{m}$ ),  $R = 200 \mu\text{m}$ .



This device has not been anti reflection coated, which leads to Fabry-Perot resonances in the straight waveguides. The resonances are visible in the transmission spectrum of the throughput port. The typical filter characteristic of the DRR is not disturbed despite the Fabry-Perot resonances. It depends on the application, if anti reflection coating is required. The contrast of the throughput port is 16 dB and that of the drop port 13 dB. The simulated filter response reveals a difference of the effective refractive index of about 0.0003, which is also the origin of the different contrast values. According to the calculation, the refractive index is lower in the upper ring. This is mainly due to fabrication tolerances which occur during the deep etching on the outer side of the waveguide in the curvatures. The physical lengths of the resonators are the same. In order to match the resonance frequency in both rings in the resonator, the upper Pt-resistors have been used. A voltage of 0.5 V was applied to match the resonance frequency.

The temperature coefficient of InP can be approximated in our case to (see section 3.1):

$$\frac{dn}{dT} \approx 0.0001 \text{ K}^{-1} \quad (5.12)$$

The local temperature increased by approximately 3 K. The result is shown in Fig. 99.

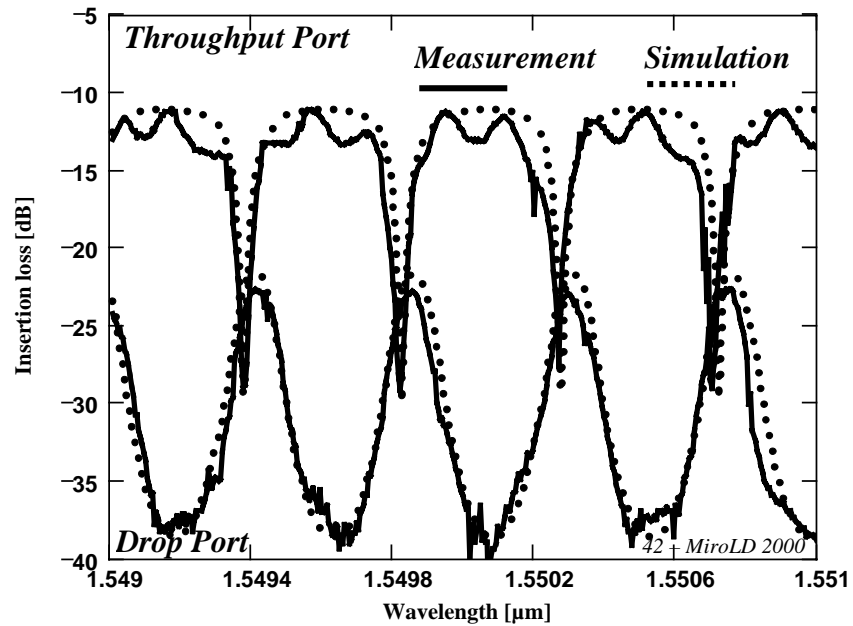


Fig. 99: DRR as in Fig. 98 with resonance matching.

The simulation model predicted a difference in the refractive index between the two rings. The shape of the transmission characteristic of the drop port in Fig. 99 has derogated and the on-off ratio of the throughput and of the drop port has increased by about 3 dB, leading to a contrast of more than 18 dB for both ports. A symmetrical behavior of the throughput port and of the drop port are thus demonstrated. The FSR achieved is 55 GHz. The FWHM for the throughput port is 0.08 nm, leading to a finesse of  $F = 5.5$  and a Q factor of  $Q \approx 19400$ . The

FWHM of the drop port is 0.1 nm, leading to a finesse of  $F = 4.4$  and a Q factor of  $Q \approx 15500$ . The shape factor of the drop port in Fig. 99 is evaluated to be 0.34.

The tuning to a specific wavelength can be performed after the frequency matching in such a way, that both of the Pt – heaters in the two rings are used. The driving voltage of the Pt – heaters is different in both of the rings due to the previous frequency matching but has to be increased by the same amount in order to shift to the specified wavelength.

Tuneable purely passive single and double ring resonators with multimode interference couplers and codirectional couplers have been realized. An on-off ratio of more than 20 dB could be demonstrated. The analysis of the filter shape and the extraction of all necessary data (coupling factor, FSR, FWHM, Finesse, Q factor, roundtrip loss, group index, on-off ratio) was performed by using the developed simulation model. On the basis of these obtained results, single and triple ring resonator configurations with SOAs are described in the following sections.

The presentation of the used semiconductor optical amplifier is described in the following section.

## 5.2 Ring resonators with integrated SOA

The SOA which is used in the ring resonators has already been developed at HHI and was tested in various elements and integration processes e.g. [91]. Due to the multi quantum well structure, the SOA was designed for favoring TE polarization. A new integration process was developed for the integration of this element with the passive ring resonator structures.

### 5.2.1 The structure of the SOA

The cross section of the used ridge waveguide (RW) semiconductor optical amplifier (SOA) structure is shown in Fig. 100. The layer sequence is given in table 3. The width of the RW SOA is  $2.2\ \mu\text{m}$ , which has to be considered for the fabrication of the low loss butt coupling interface with the  $1.8\ \mu\text{m}$  wide passive waveguide.

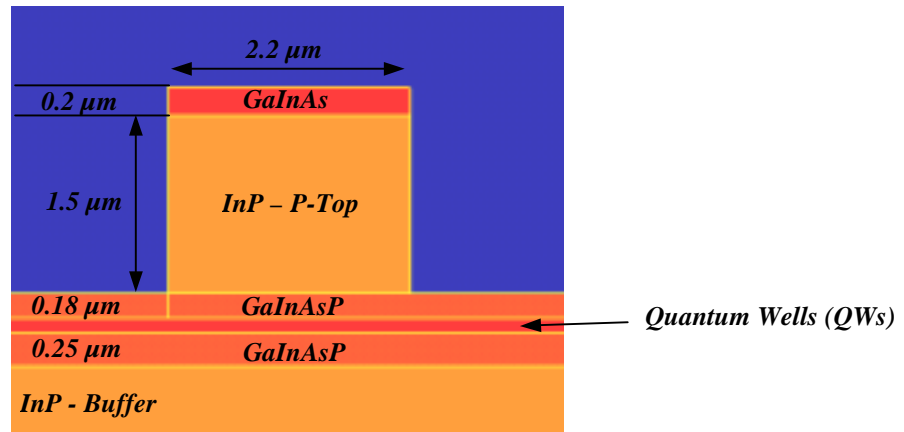


Fig. 100: Structure of the used active SOA.

The layer sequence and composition of the used SOA is as follows (from bottom to top):

Nr.	Material	$\lambda_g$ (nm)	Thickness	Dopand [ $\text{cm}^{-3}$ ]	Function
1.	InP-Sn-sub.		$360\ \mu\text{m}$		Substrate
2.	InP-buffer		500 nm	$\text{Si}:3 \cdot 10^{18}$	Buffer
3.	n-GaInAsP	1150	250 nm	$\text{Si}:3 \cdot 10^{18}$	n-Contact
4.	n-GaInAsP	1290	10 nm	Undoped	1. Barrier
5.	Q 1% compressive strained		6 nm	Undoped	6* QW
6.	Q-1.29	1290	10 nm	Undoped	6*Barrier
7.	GaInAsP	1150	180 nm	Undoped	LD-WG
8.	InP		1500 nm	$\text{Zn}:5 \cdot 10^{17}$	p-Top
9.	InGaAsP	1300	50 nm	$\text{Zn}:1 \cdot 10^{18}$	2. p-Top
10.	InGaAs		200 nm	$\text{Zn}:1 \cdot 10^{19}$	p-Contact

Table 3: Layer stack of the used SOA.

The calculated mode field profile of the RW structure is given in Fig. 101. The quantum wells (QWs) and the barrier layers have been considered as one layer with an effective refractive index of  $n_{eff} = 3.4$  [78]. The effective index of the SOA is determined to be  $n_{eff} = 3.238$ . The center of the guided mode in the RW structure (Fig. 101) is located lower compared with the passive waveguide structure. Thus, it is necessary for the integration process to adjust the height of the active – passive transition to assure minimal coupling losses.

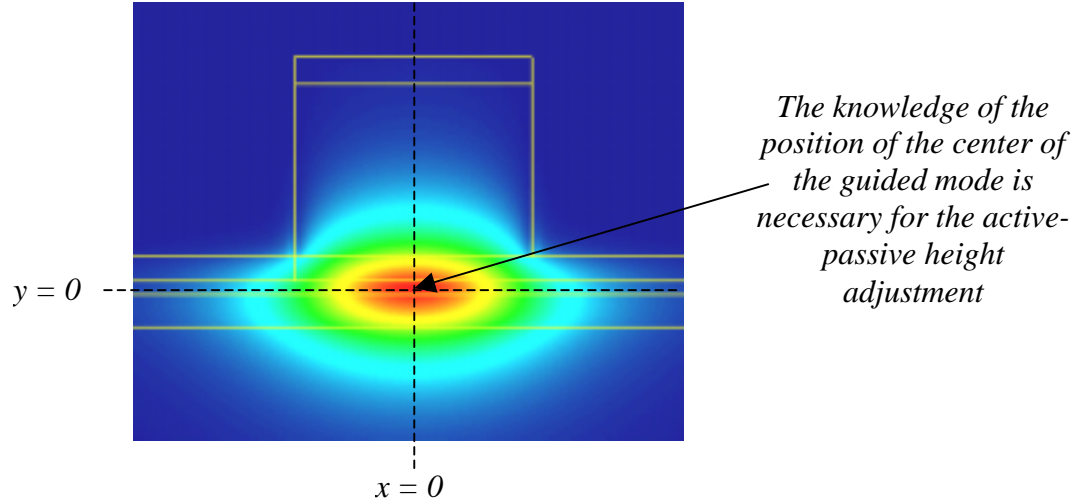


Fig. 101: Mode profile of the SOA (TE polarization).

The butt coupling losses at the passive - active waveguide interface have been calculated by the finite difference method (Fig. 102). The calculated vertical and lateral offset between the active and passive waveguide results in a minimum theoretical coupling loss of  $< 1$  dB.

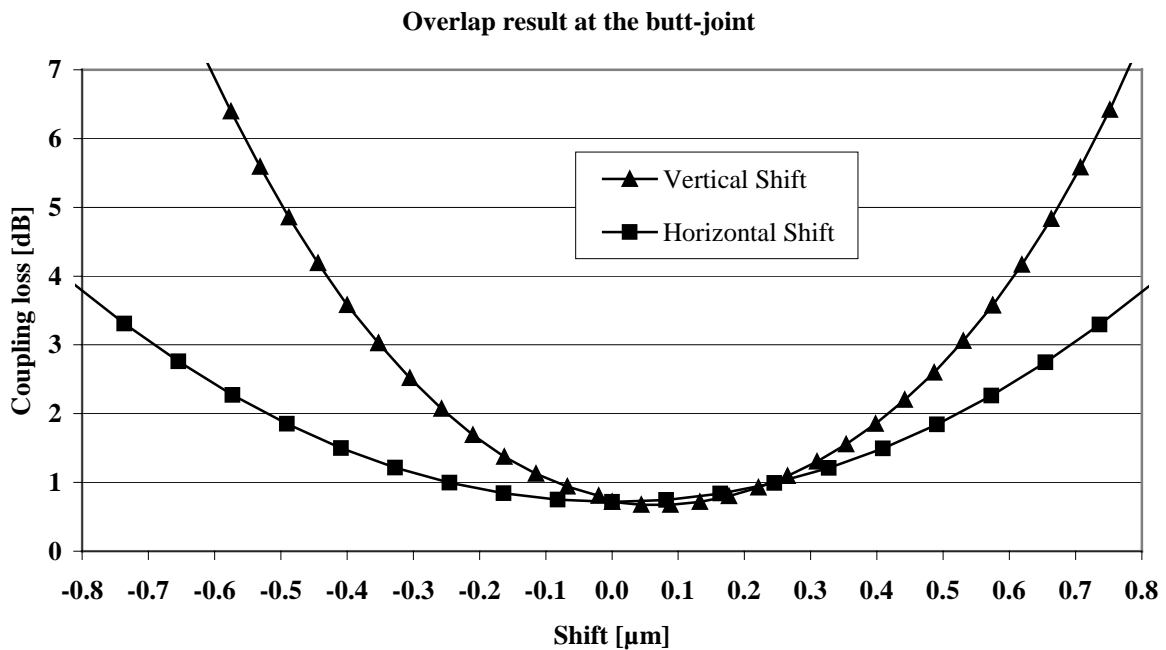


Fig. 102: Calculated butt-joint losses.

The starting point for the calculation of the horizontal shift has been chosen so that the passive structure is located symmetrical in the center of the active section. The calculation of the vertical shift starts with the passive – active section, butt coupled at the position where the rib starts for the passive structure and in the middle of the active layers ( $x, y = 0$ ; Fig. 101) for the SOA section. The practical realization of the active- passive transition is done in using a special taper structure at the interface. The lateral design is shown in Fig. 103.

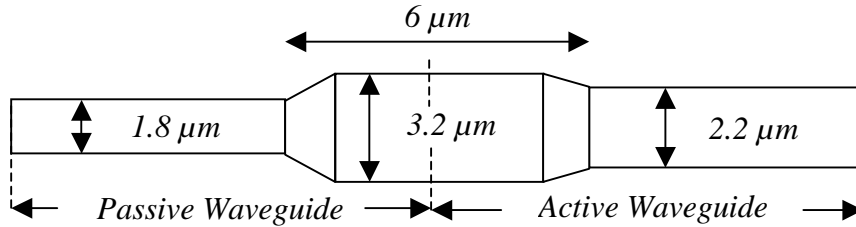


Fig. 103: Lateral dimensions of the active – passive waveguide interface.

The use of the tapered structure enables the propagating wave coming from the passive waveguide to laterally broaden, interfere, propagate into the active waveguide with a different refractive index and scale down to the dimension of the active waveguide. Active – passive transitions have been developed at the Heinrich-Hertz-Institute for various types of waveguide structures e.g. [92]. The type of tapered structure used in this thesis was found out to be technologically practicable to realize butt-joint losses between 2 – 3 dB [78].

Another technological challenge is the fabrication of a low resistance contact of the active section. As directly contacting the SOA on the ridge with a metal needle would destroy the SOA in the worst case, "support mesa" are designed at a distance of a few micrometer away from the SOA ridge on either side. The p – contact of the SOA is then located on these mesa for securely placing a measurement needle and for later bonding. The support mesa have the same active material layer stack as the SOA. The technological challenge lies in creating a low metal-semiconductor p – contact on the SOA. The isolation of the metal layer on top of the support mesa is performed with a  $\text{SiN}_x$  layer, which is removed only on top of the SOA waveguide.

The cross section of the SOA with support mesa is sketched in Fig. 104.

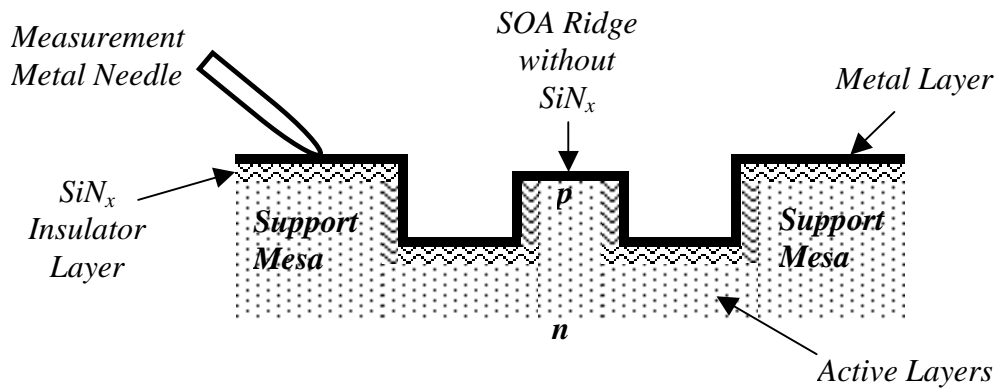


Fig. 104: Cross section of the SOA section with the support mesa.

The n – contact is realized on the metal coated backside of the wafer. A reliable process had to be developed to assure metal contacting from the p – contact via the grooves with perpendicular sidewalls to the bond pads (support mesa).

The following section describes the entire fabrication process of the integration of all previously described components. In depth coverage is given on the realization of this metal – semiconductor p - contact.

### 5.2.2 The integration process

The fabrication starts with the epitaxial growth of the layers of the SOA by using metal organic vapor phase epitaxy (MOVPE) (Fig. 105). The quantum wells and the upper p – top layer have been left out for simplification.. The first chemical vapor deposition (CVD) processing step is the deposition of  $\approx 230$  nm  $\text{SiN}_x$  at a temperature of  $370^\circ\text{C}$  for the fabrication of the etching mask (Fig. 106). The lateral active mesa structures are defined in a resist pattern by using standard photolithography (positive process, photoresist AZ5214, exposing time  $\approx 24$  s, developer MFI724, developing time  $\approx 50$  s). The resist pattern serves as an etching mask for the following reactive ion etching step ( $\text{CHF}_3$  – 22 sccm and  $\text{O}_2$  – 2.2 sccm, pressure = 0.012 mbar, power = 50 W). The photoresist is removed with an  $\text{O}_2$  plasma (10 min, power = 500 W,  $T < 250^\circ\text{C}$ ) after this process. The p – top mesa are etched in the following step by using RIE ( $\text{CH}_4$  – 8 ml/min and  $\text{H}_2$  – 20 ml/min, pressure = 0.006 mbar, power = 200 W). In order to remove the polymer which is build up during reactive ion etching, an  $\text{O}_2$  plasma (20 min, power = 550 W,  $T < 250^\circ\text{C}$ ) and a solution of KOH (20%) are used. The p – top is etched down to a distance of about  $1.1 - 1.2\ \mu\text{m}$  (Fig. 107) followed by a wet etching step by using a solution of  $20\ \text{H}_2\text{O} : 5\ \text{HBr} : \text{H}_2\text{O}_2$ . This wet etching process is the “undercut” etching. In this step, part of the sidewall is removed as sketched in Fig. 108. A layer of InP protects the active sections underneath. The etching of the undercut is indispensable for the second epitaxial growth step of the passive waveguide. The undercut reduces the formation of high “rabbit ears” during selective area MOVPE (SAMOVPE) at the vicinity of the mask and enables adequate control of the layer thickness in order to achieve the necessary vertical alignment within the active – passive transition. For further improvement of the SAMOVPE growth step, the “undercut” is covered by a layer of  $\text{SiN}_x$  which is realised by depositing the entire wafer with  $\text{SiN}_x$  and removing the material on the “ground” of the wafer by reactive ion etching. The result is shown in Fig. 109. The next step is the final etching of the p – top and the active layers using RIE ( $\text{CH}_4$  – 8 ml/min and  $\text{H}_2$  – 20 ml/min, pressure = 0.006 mbar, power = 200 W, Fig. 110). The control of the etch depth is very important in order to adjust the regrowth of the passive material. The following step is the regrowth of the passive material using selective area MOVPE (SAMOVPE). The correct hight of the passive material is defined by the thickness of an InP buffer layer. A sketch of the structure after the regrowth process is shown in Fig. 111. The regrowth process is followed by the removal of the entire  $\text{SiN}_x$  at the "undercut" using hydrofluoric acid ( $\text{HF}$  – 5%). After this step, the entire wafer is again covered with  $\approx 190$  nm  $\text{SiN}_x$  at a temperature of  $370^\circ\text{C}$  (Fig. 112).

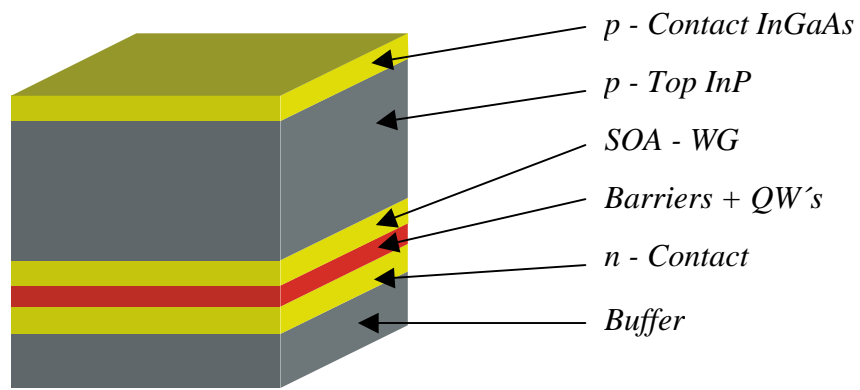


Fig. 105: Layer sequence of the active section.

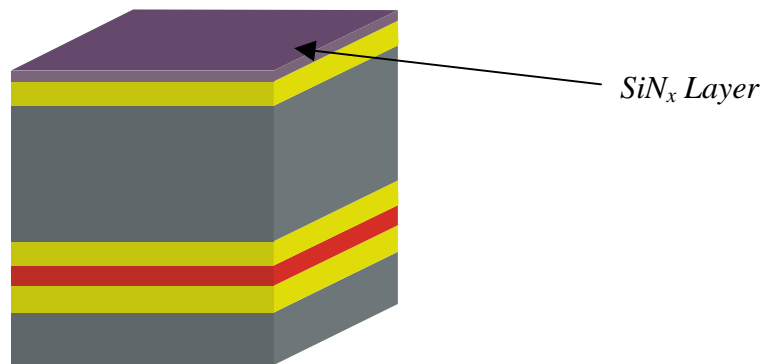


Fig. 106: Deposition of  $\text{SiN}_x$ .

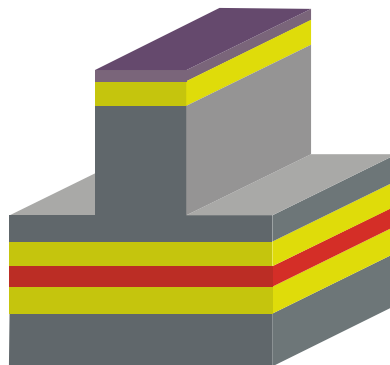


Fig. 107: The first etching of the p – top.

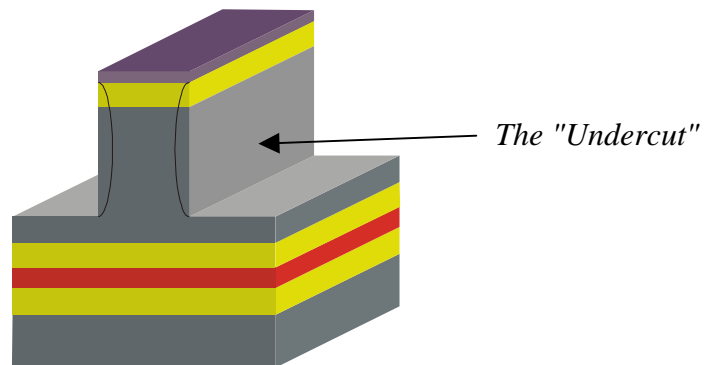


Fig. 108: Etching of the “undercut”



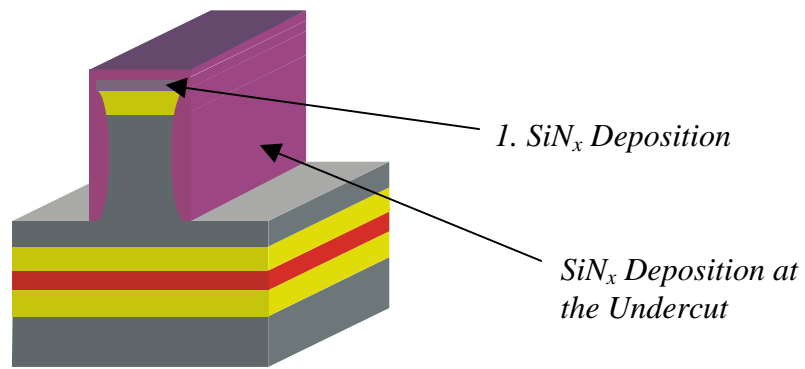


Fig. 109: Deposition of SiN<sub>x</sub> at the “undercut”.

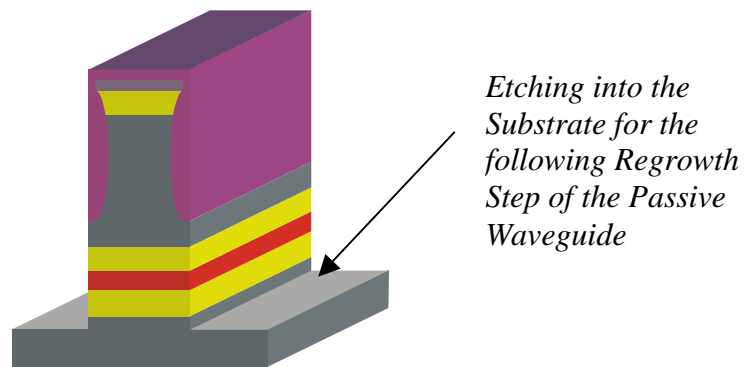


Fig. 110: The final etching of the p-top and the active layers.

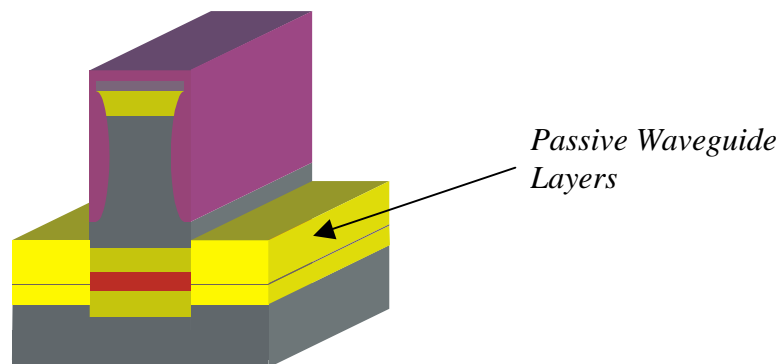


Fig. 111: Regrowth process.

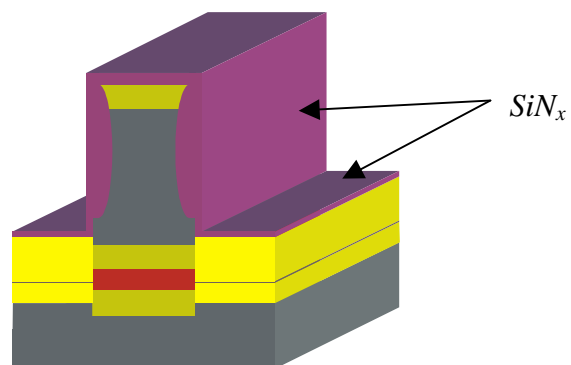


Fig. 112: SiN<sub>x</sub> deposition for the diffusion process.

The  $\text{SiN}_x$  is removed at the top of the active mesa using a photolithographic step, followed by a dry etching step ( $\text{CHF}_3$  – 22 sccm and  $\text{O}_2$  – 2.2 sccm, pressure = 0.012 mbar, power = 50 W). The photoresist is removed after the dry etching step using KOH (20%). The following diffusion process ( $T = 575^\circ\text{C}$ , 18 s) is carried out using zinc arsenide as the dopant. The process is illustrated in Fig. 113. In the next step, the waveguide is etched together with the laser ridge in a so called self aligning process, where the active – passive interface is generated using RIE ( $\text{CH}_4$  – 6 ml/min,  $\text{H}_2$  – 40 ml/min,  $\text{O}_2$  – 0.3 ml/min, pressure = 0.02 mbar, power = 150 W). Due to the higher laser ridge, the remaining material is etched by selective wet chemical etching using a solution of HCl and  $\text{H}_3\text{PO}_4$  (1:4). The wet etching is automatically stopped, when the quaternary layers are reached. The result of this step is shown in Fig. 114. The deep etching of the passive waveguide, which is necessary in order to achieve sufficient optical confinement in small bent waveguides (radii  $< 200\ \mu\text{m}$ ), is the next processing step. The etching mask material is again a  $\text{SiN}_x$  layer structured in a photolithographic and dry etching step. The  $\text{SiN}_x$  layer serves also as a protection layer for the laser ridge. This step is illustrated in Fig. 115. The deep etching of the passive waveguide is done by reactive ion etching using  $\text{CH}_4$  (8 ml/min) and  $\text{H}_2$  (20 ml/min) with a pressure of 0.006 mbar and a power of 200 W (Fig. 116). The following step is a critical one and has been developed especially for this fabrication process. The  $\text{SiN}_x$  which was deposited for the protection of the SOA ridge has to be removed only at the very top, to be able to place a metal layer for realizing an electric contact (5.2.1). Therefore, the entire wafer is covered with photoresist and is exposed a few seconds ( $\approx 14\ \text{s}$ ) at the areas of the SOA ridge which results in opening the tip of the laser ridge. The photograph of the top view of an SOA ridge with the structured photoresist is shown in Fig. 117. In this process the exposing time of the photoresist is the key figure. If the time is too high, the photoresist will become very thin between the SOA ridge and the support mesa and might uncover the insulating  $\text{SiN}_x$  layer which will be etched in the next fabrication step and so cause unwanted short cuts. On the other hand, if the exposing time is too less, only part of the photoresist on top of the SOA ridge is removed and the  $\text{SiN}_x$  layer can not entirely be etched away in the following process. The SEM photograph of the cross section of a developed SOA ridge is shown in Fig. 118. The  $\text{SiN}_x$  layer at the top of the SOA ridge is completely freed from the photoresist. The area in between the SOA ridge and the support mesa and also the entire wafer are covered by photoresist with a thickness of about 800 nm which is a sufficient amount for protecting the  $\text{SiN}_x$  layer from being etched in the next step.

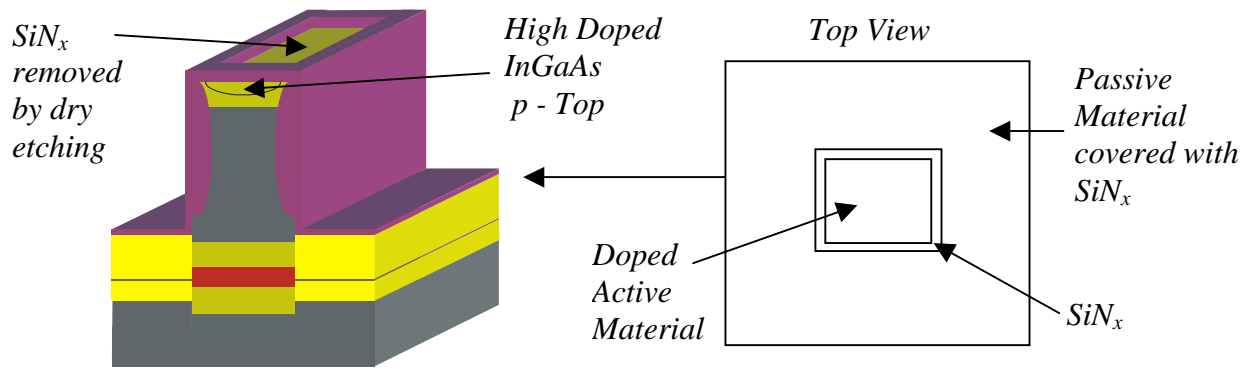


Fig. 113: Diffusion process.

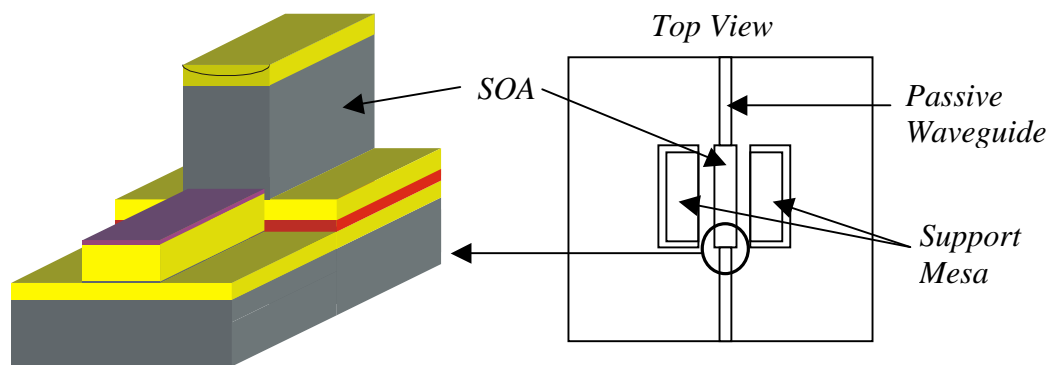


Fig. 114: Etching of the waveguide and the SOA.

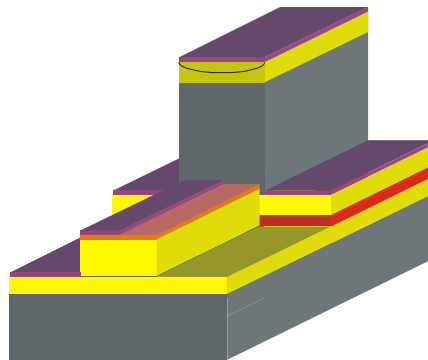


Fig. 115: Definition of the deep etching of the passive waveguide.

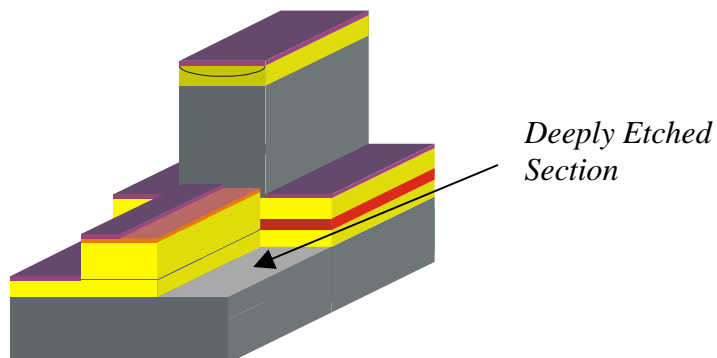


Fig. 116: Deep etching of the passive waveguide curvatures.

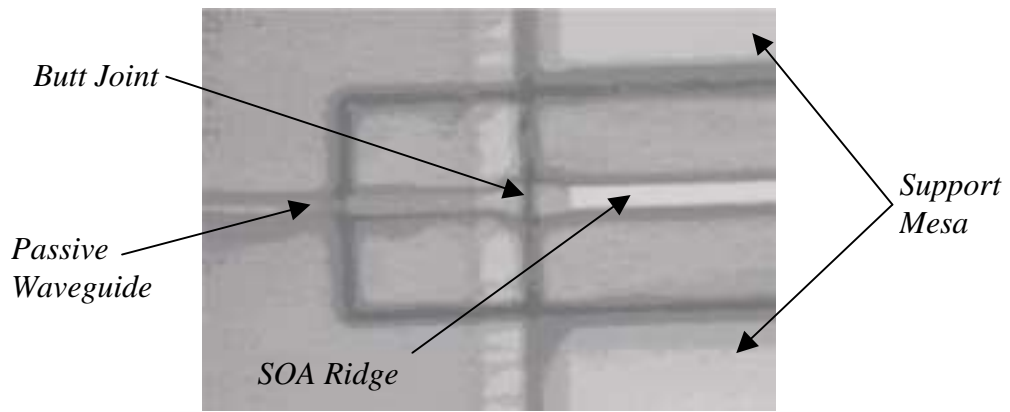


Fig. 117: Photograph of the removal of the photoresist at the top of the SOA ridge.

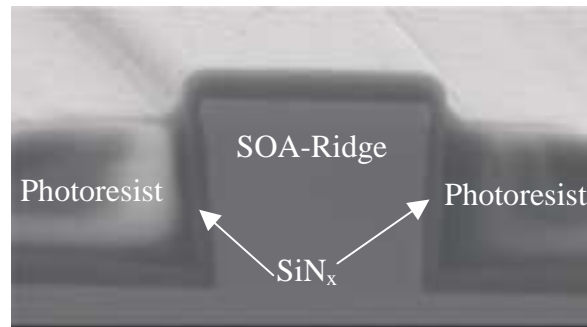


Fig. 118: SEM picture of the front view of an SOA-ridge.

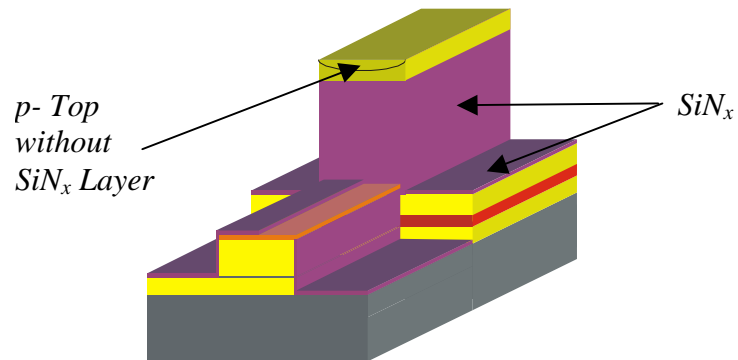


Fig. 119: Removal of the SiN<sub>x</sub> layer from the p – top of the SOA – ridge.

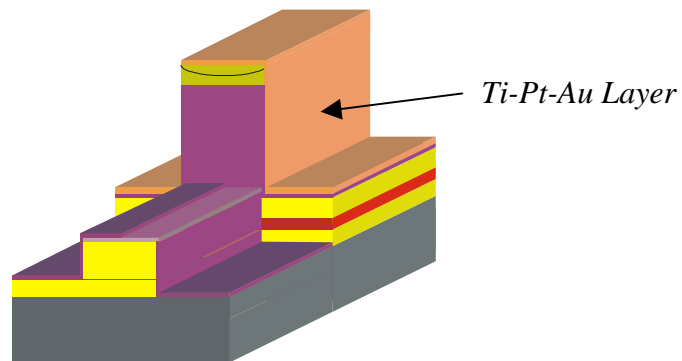


Fig. 120: The contacted SOA with passive waveguide.

The  $\text{SiN}_x$  is removed from the p – top in a dry etching process ( $\text{CHF}_3$  – 24 sccm,  $\text{H}_2$  – 1 sccm, pressure = 0.012 mbar, power = 50 W). Now, the metal contacts are fabricated starting with a photolithographic step for the definition of the contacts. The p - top of the SOA, the area in between the ridge and the support mesa and the top of the support mesa is deposited with titanium, platinum and gold and the remaining metal is removed in a “lift – off” process using NMP (n-methyl-2-pyrrolidon,  $\text{C}_5\text{H}_9\text{NO}$ ). The final result is sketched in Fig. 120. After the fabrication of the contacts for the SOA, the platinum heaters are realized starting with a photolithographic step for the definition of the heaters, followed by the deposition of platinum and the removal of the remaining platinum in a "lift-off" process.

The photographs of a fabricated ring resonator with integrated SOA is shown in Fig. 121.

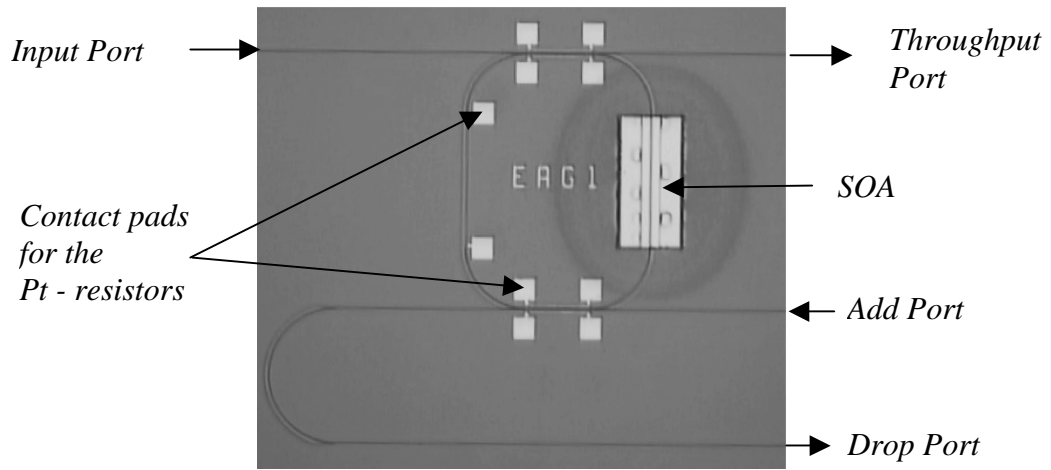


Fig. 121: Photograph of an SRR with integrated SOA.

The SOA with the additional support mesa on both sides is shown in the photograph. The drop port of the SRR has been placed on the same side as the throughput port for practical measurement reasons. The additional bending losses for the drop port have to be accounted for and are considered in the simulation of the devices. The SRR with SOA section is the main building block for the realization of various multiple coupled ring resonator circuits.

The fabricated active – passive transition is characterized in the next section in order to determine the butt joint losses and the gain of the SOA. These parameters are necessary for the simulation of the devices.

### 5.2.3 The active – passive transition

Test structures which consist of straight passive waveguides with integrated SOA sections of different length variations have been fabricated in order to extract the butt coupling losses and the gain per length. This knowledge is required for the realization of loss compensated ring resonators. The photograph of fabricated straight passive waveguides with integrated SOA of different lengths is shown in Fig. 122.

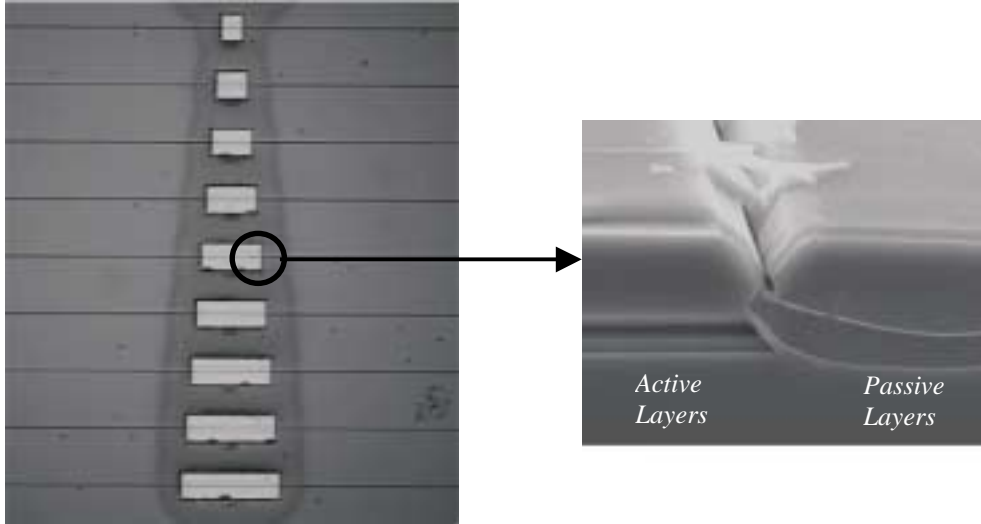


Fig. 122: Anti reflection coated straight waveguides with integrated SOAs.

The measurement of the amplification of the anti reflection coated active section has been performed using an ECL at the fixed wavelength of  $\lambda = 1.55 \mu\text{m}$  and inserting a gradually increased current  $I$ . The result is shown in Fig. 123.

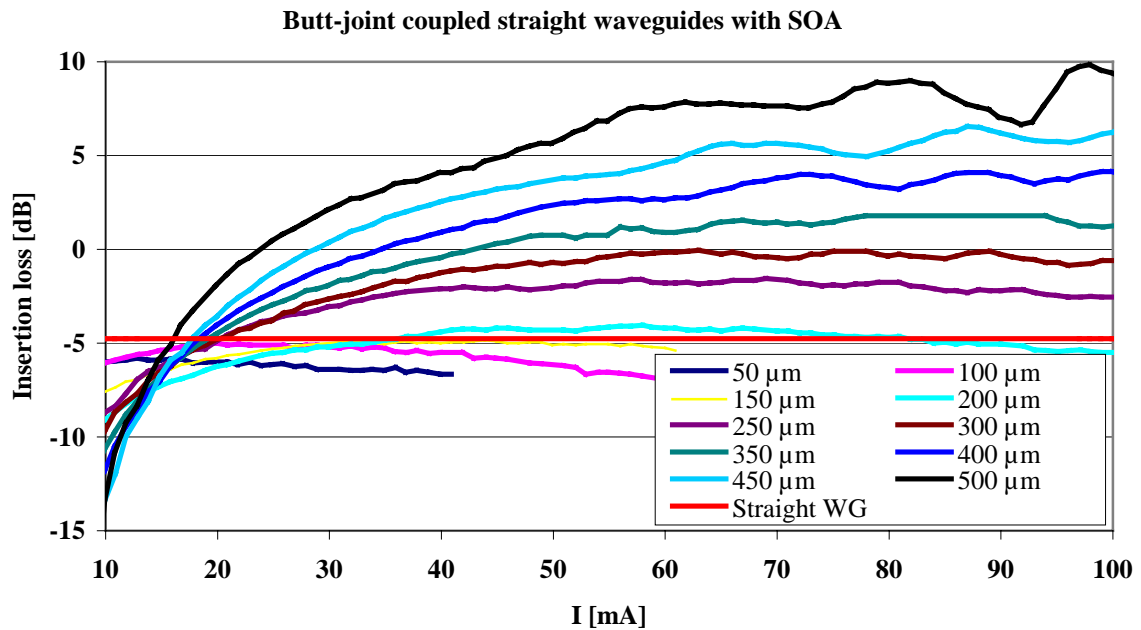


Fig. 123: Result of straight passive waveguides with integrated SOAs at  $\lambda = 1.55 \mu\text{m}$ .

The insertion loss of a straight waveguide is displayed as reference. The SOA with a length of  $150\ \mu\text{m}$  is the minimum SOA length to compensate the butt-joint losses. The implementation of SOAs above a length of  $150\ \mu\text{m}$  enables net gain of the incoming light. For the determination of the gain per length and the butt joint losses, it is important to determine the transparency current density  $J_0$  of the SOA section. The transparency current of the devices in Fig. 122 is measured via detection of the  $\pi$  - phase switching [93]. The input light used for this measurement is a modulated signal of an ECL at a fixed wavelength of  $\lambda = 1.55\ \mu\text{m}$ . Due to the quasi digital step function, the algebraic sign of the phase is directly proportional to the absorption / gain of the measured device. At the saturation of the active material the phase shifts from negative to positive (Fig. 124) due to a change in the current flow direction. This is a very effective method to determine the transparency current. After measuring various SOAs of different lengths, the transparency current density  $J_0$  is evaluated to be  $9\ \text{mA}/\mu\text{m}^2$ . This result is used to determine the butt-joint losses of the devices. The ECL signal is modulated at the wavelength of  $\lambda = 1.55\ \mu\text{m}$  and the output intensity is measured using the lock-in amplifier technique. The response of SOAs of different length are measured. The result is shown in Fig. 125.

The internal loss (gain) of the active section at the transparency current can be determined using the formalism described in section 2.3.1.

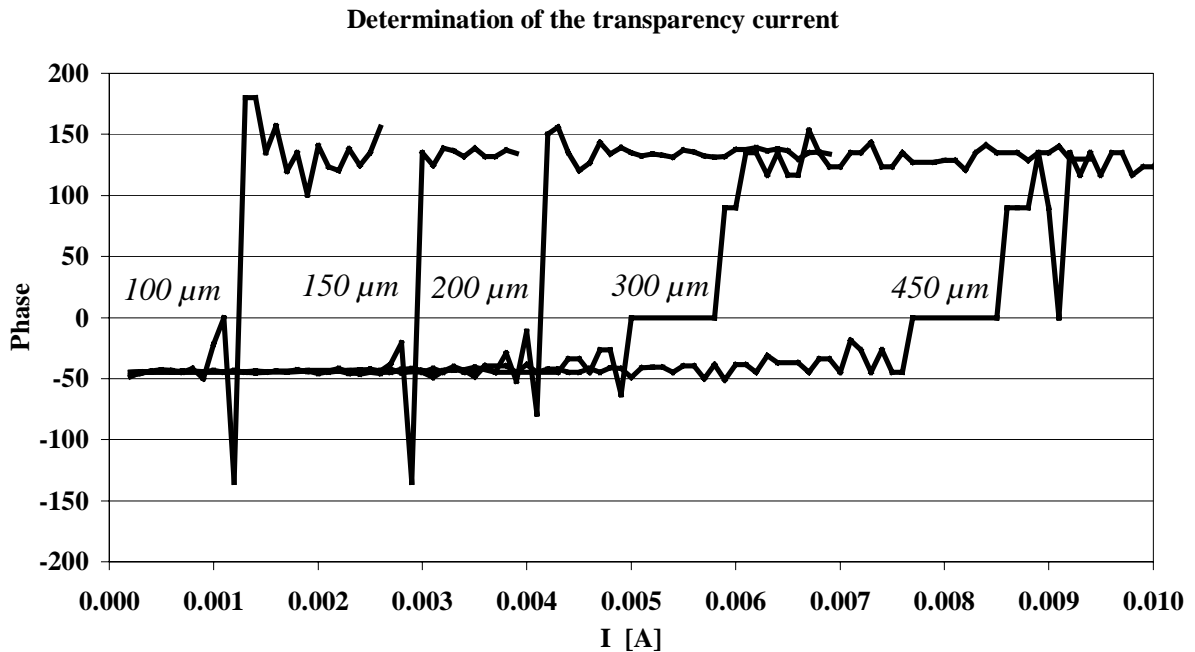


Fig. 124: Determination of the transparency current of SOA sections of different length.

The waveguide with SOA section is divided into three segments: two passive waveguides and the active section. The internal loss (gain) coefficient can then be calculated from the experimental fit shown in Fig. 125. The value obtained for the internal loss coefficient of the

SOA at the transparency current is  $\alpha_{SOA} = 0.0121 \text{ dB}\mu\text{m}^{-1} = 28 \text{ cm}^{-1}$ . The gain factor at  $J/J_0 = 10$  is  $\alpha_{SOA} = 78 \text{ cm}^{-1}$ . The butt-joint losses are obtained from the same calculation and are calculated to be approximately  $< 3 \text{ dB}$  each. The passive waveguide losses together with the fiber-chip coupling losses are  $5 \text{ dB}$  as was determined in section 4.2.4.

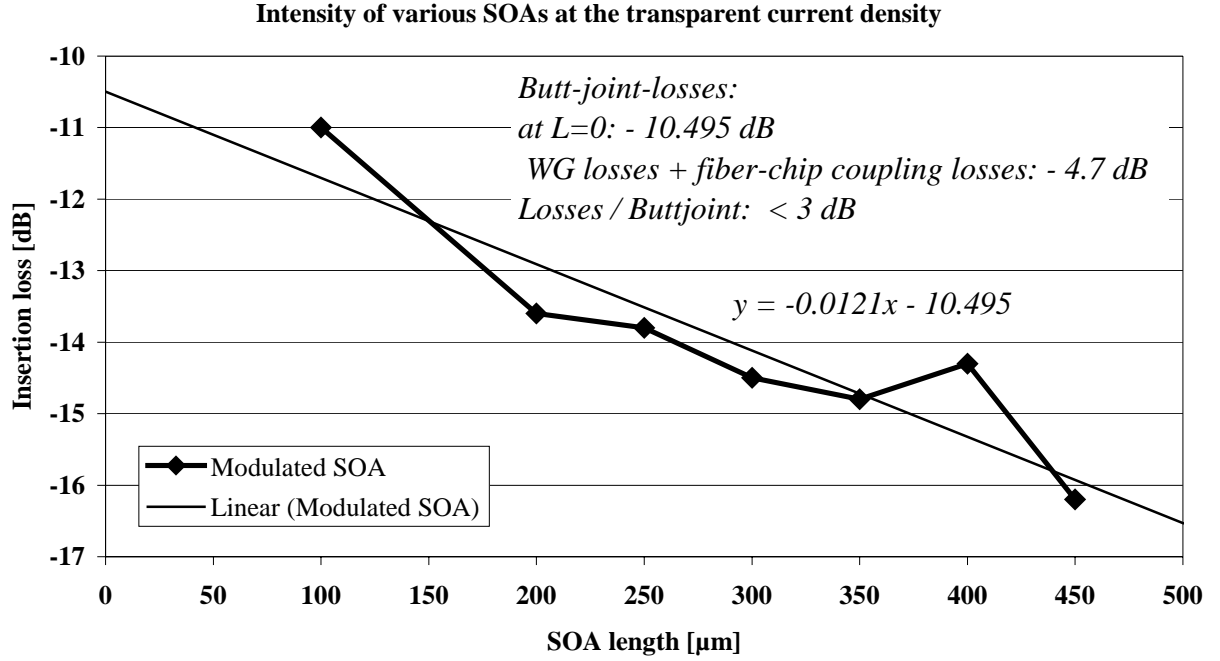


Fig. 125: Estimation of the butt-joint losses.

The active – passive transition can also be analyzed using the OLCR measurement. The result for a straight waveguide with a  $500 \mu\text{m}$  long SOA section, measured in reflection mode is shown in Fig. 126.



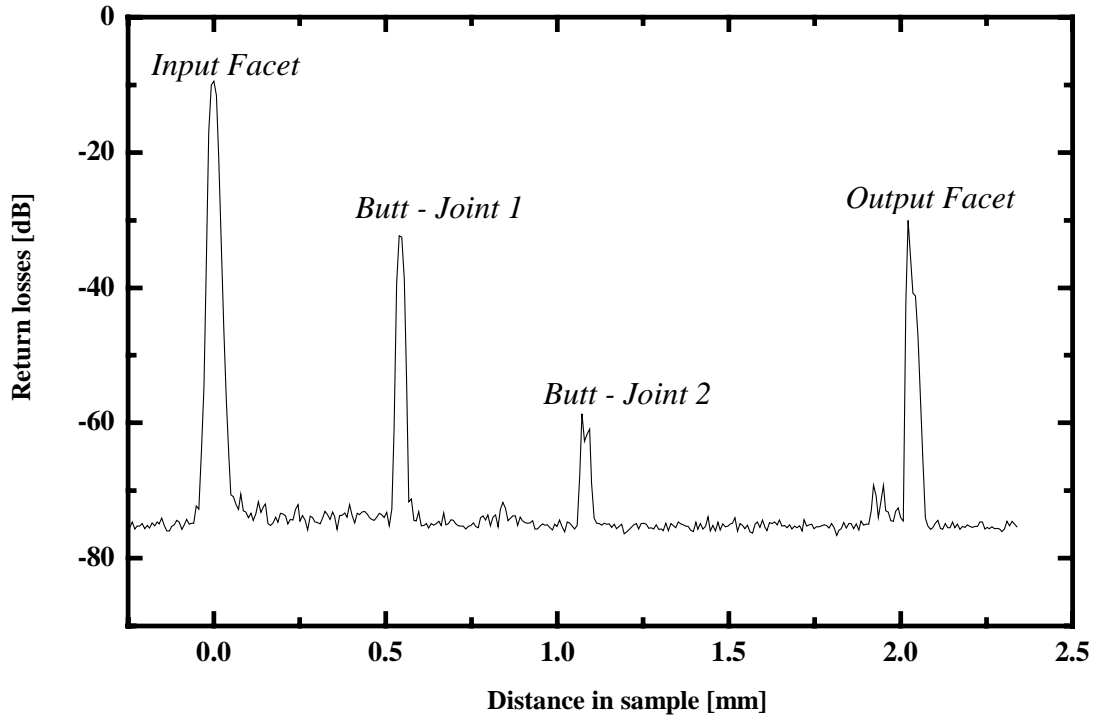


Fig. 126: Reflectogram of a straight waveguide with SOA section (gain length = 500  $\mu\text{m}$ ).

The facets are not anti reflection coated which is shown in the high reflection losses at the input and output facets. The return loss from butt joint 1 is about -32 dB. The length of the SOA section can also be taken from the OLCR measurement and is proven to be 500  $\mu\text{m}$ . The minimization of the reflection at butt joints has been investigated in [94]. It should be possible to reduce these return losses with these methods to more than -50 dB.

The reflectogram of a single ring resonator with an SOA (see inset) is shown in Fig. 127. The ring resonator has a radius of  $R = 200 \mu\text{m}$ , a coupler length of 150  $\mu\text{m}$  (gap = 1  $\mu\text{m}$ ) and a gain length of 100  $\mu\text{m}$ . The return loss resulting from the butt joint is only -50 dB which indicates a lower reflection than from the straight waveguide with SOA. This is due to the bending loss in the ring resonator, where part of the reflected intensity from the butt joint is lost, leading to a lower value for the return loss. This means that the amount of the optical wave which is reflected at the butt joints can be neglected in the simulation of the transmission characteristic of the ring resonator structures. There are again no reflection peaks due to imperfections in the resonator or straight waveguide for example which indicates a high quality cavity.

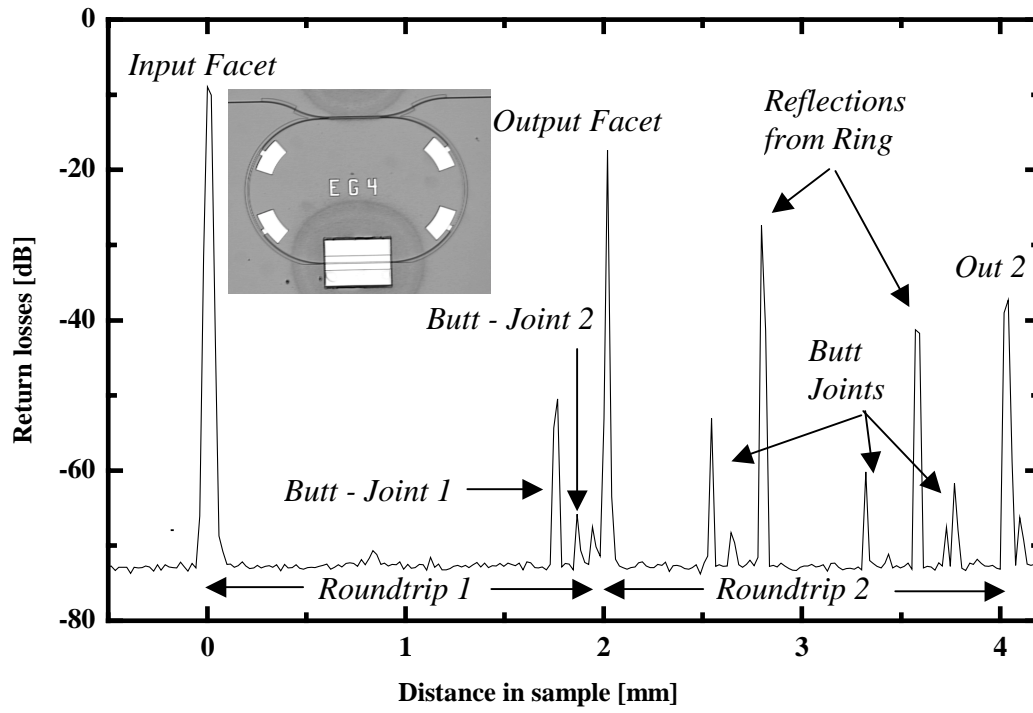


Fig. 127: Reflectogram of a single ring resonator with SOA ( $R = 200 \mu\text{m}$ , coupler length =  $150 \mu\text{m}$ , gap =  $1 \mu\text{m}$ , gain length =  $100 \mu\text{m}$ ).

All essential parameters of the active sections have been extracted in this section using various measurement methods.

The following section summarizes the transmission characteristics of ring resonators with integrated SOA.

### 5.2.4 Experimental results

The preliminary results of the fabricated ring resonators with integrated SOA are shown in Fig. 128 and Fig. 130. The ring resonators have gain lengths of 100  $\mu\text{m}$ . These ring resonators were fabricated before the detailed analysis of the butt joint losses and before the determination of the gain per length, where it was found out that the SOA length of 100  $\mu\text{m}$  is too short to compensate for the butt joint losses and the intrinsic waveguide losses of the ring resonator.

The transmission characteristic in Fig. 128 shows the measurement of the throughput port of an SRR with two input/output waveguides. The SRR has a radius of  $R = 200 \mu\text{m}$ , a coupler length of 250  $\mu\text{m}$  (gap = 0.8  $\mu\text{m}$ ), leading to a coupling factor of  $\kappa = 0.46$ . The SOA was operated at 40 mA. An on-off ratio of more than 11 dB and an FSR of 44 GHz have been achieved. The FWHM was determined to be 0.07 nm, leading to a finesse of  $F = 5$ . The Q factor is calculated to be  $Q \approx 22100$ . The butt joint losses were determined to be  $\approx 2.5$  dB each.

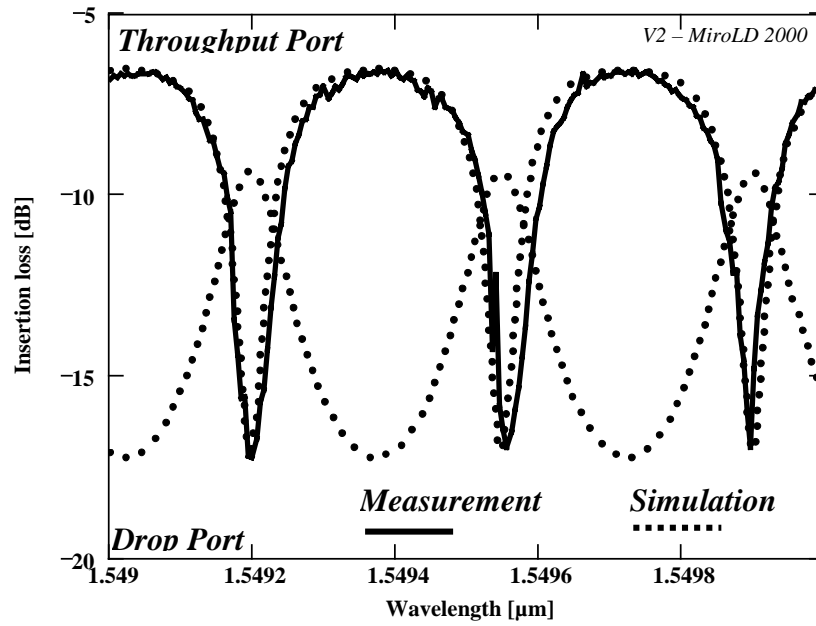


Fig. 128: SRR with two input/output waveguides and codirectional couplers (length = 250  $\mu\text{m}$ , gap = 0.8  $\mu\text{m}$ ),  $R = 200 \mu\text{m}$ , gain length = 100  $\mu\text{m}$ , FSR = 44 GHz.

The photograph of the SRR whose transmission characteristic is given in Fig. 130 is shown in Fig. 129.

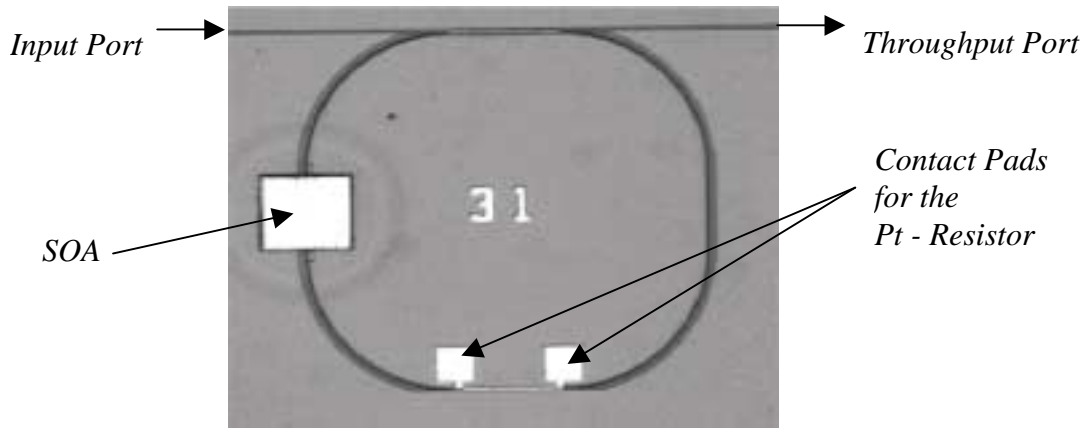


Fig. 129: Photograph of an SRR with one straight input/output waveguide and integrated SOA.

The SRR has a radius of  $R = 100 \mu\text{m}$ , a 3 dB MMI coupler (length  $150 \mu\text{m}$ ) and also a gain length of  $100 \mu\text{m}$ . The achieved FSR is 74 GHz. The FWHM is 0.13 nm. The finesse of the SRR is  $F = 4$ . The Q factor achieved is  $Q \approx 12000$ . Even when the SOA is switched off, a typical transmission characteristic from the resonator is visible. This is mainly due to the small length of the SOA, where only part of the incoming light is absorbed. The on-off ratio is about 12 dB which was also realized with the same passive SRR with the same dimension. This shows again, that the SOA does not add enough gain to the incoming signal to compensate the bending losses. The gain length has been increased in the following devices.

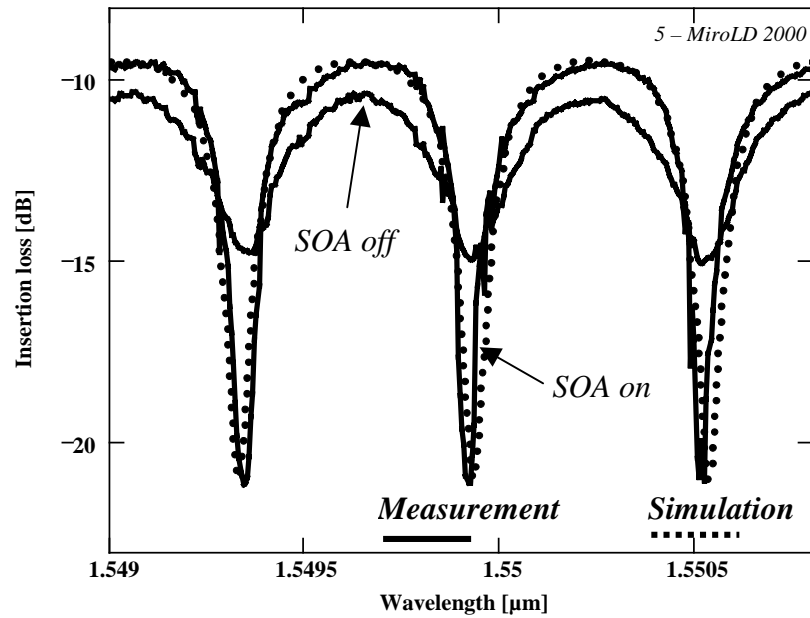


Fig. 130: SRR with one straight input/output waveguide and MMI coupler (length =  $150 \mu\text{m}$ ),  $R = 100 \mu\text{m}$ , gain length =  $100 \mu\text{m}$ , FSR = 74 GHz.

In order to assure a precise FSR, high on-off ratio and compensated bending losses, the following ring resonator configurations have been calculated using the simulation technique described in section 2.3. The data which have been extracted from the previously measured and characterized passive and active ring resonators have been used in designing the following ring resonator configurations with a targeted FSR of 12.5 GHz, 25 GHz and 50 GHz. The photograph of an SRR with two input/output waveguides is shown in Fig. 131.

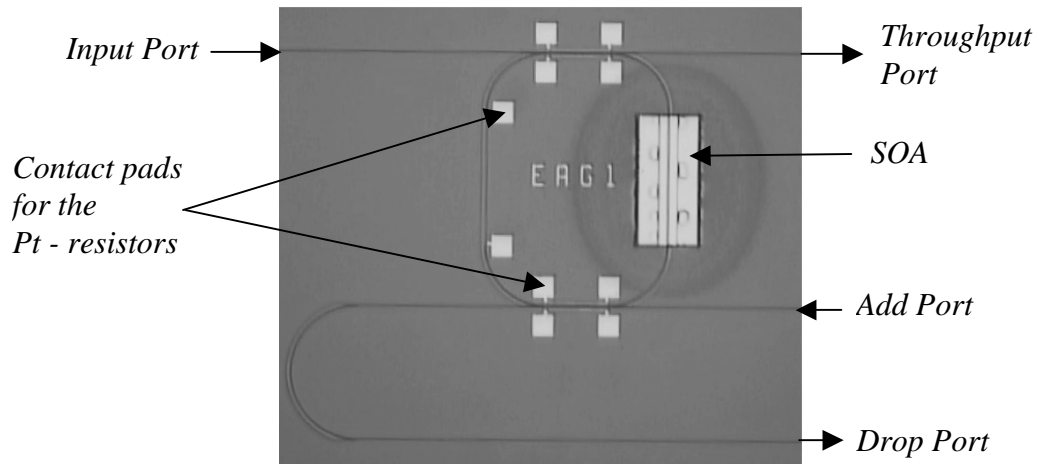


Fig. 131: Photograph of a fabricated SRR with two input/output waveguides and SOA.

The measurement of an SRR with two input/output waveguides, a radius of 780  $\mu\text{m}$ , a gain length of 800  $\mu\text{m}$ , coupler lengths of 225  $\mu\text{m}$  (gap = 0.9  $\mu\text{m}$ ) is shown in Fig. 132. The SOA was operated at a current of 100 mA. The achieved on-off ratio is more than 20 dB. The coupling factors have been determined from the simulation to be  $\kappa_{1,2} = 0.19$ . The FSR is 12.5 GHz as designed. The FWHM is determined to be 0.0067 nm leading to a Q factor for this device of  $Q \approx 232500$ . The shape factor of the drop port is approximately 0.16. The finesse of the ring resonator is  $F \approx 15$ . This is the highest finesse which can be achieved for this configuration. Using equation (2.51) and setting  $x = 1$  for total loss compensation and  $y_1 = y_2$  we obtain:

$$F = \frac{2\pi}{\delta\phi} = \frac{\pi\sqrt{y_1 y_2 x}}{1 - y_1 y_2 x} \underset{x=1, y_1=y_2=y}{=} \frac{\pi y}{1 - y^2} \underset{\kappa_{1,2}=0.19}{=} 14.88$$

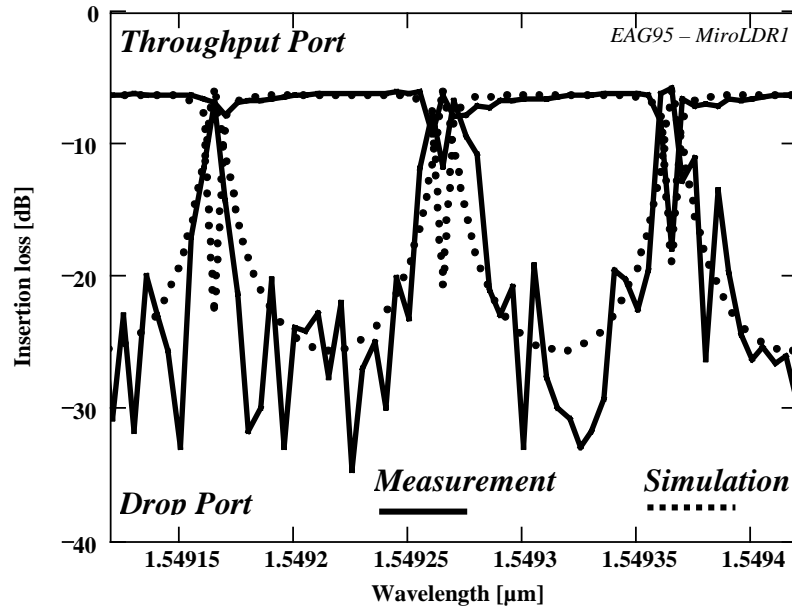


Fig. 132: SRR with two straight input/output waveguides and codirectional couplers (length = 225  $\mu\text{m}$ , gap = 0.9  $\mu\text{m}$ ),  $R = 780 \mu\text{m}$ , gain length = 800  $\mu\text{m}$ , FSR = 12.5 GHz.

The realization of the designed FSR shows the reproducibility of the technology in fabricating these devices and the extraction of the parameters with the used measurement and simulation tools.

The filter characteristic of an SRR with two input/output waveguides and an FSR of 25 GHz is shown in Fig. 133. The SRR has a radius of  $R = 403 \text{ } \mu\text{m}$ , a gain length of  $300 \text{ } \mu\text{m}$  and the coupler length of the codirectional couplers is  $175 \text{ } \mu\text{m}$  (gap =  $0.9 \text{ } \mu\text{m}$ ), leading to a coupling factor of  $\kappa_{1,2} = 0.165$ . The SOA was operated at a current of 70 mA. The FWHM is  $0.012 \text{ nm}$ , leading to a Q factor of  $Q \approx 130000$ . The finesse of the ring resonator is calculated from the measurement to be  $F = 17$ . The high finesse signifies very sharp resonances for the throughput port, which are visible in the simulation of the transmission characteristic. The simulation reveals a higher on-off ratio for the throughput port than measured. A distance of  $5 \text{ pm}$  between the wavelengths was used as the measurement and simulation resolution, which is still too high to detect the deep minima.

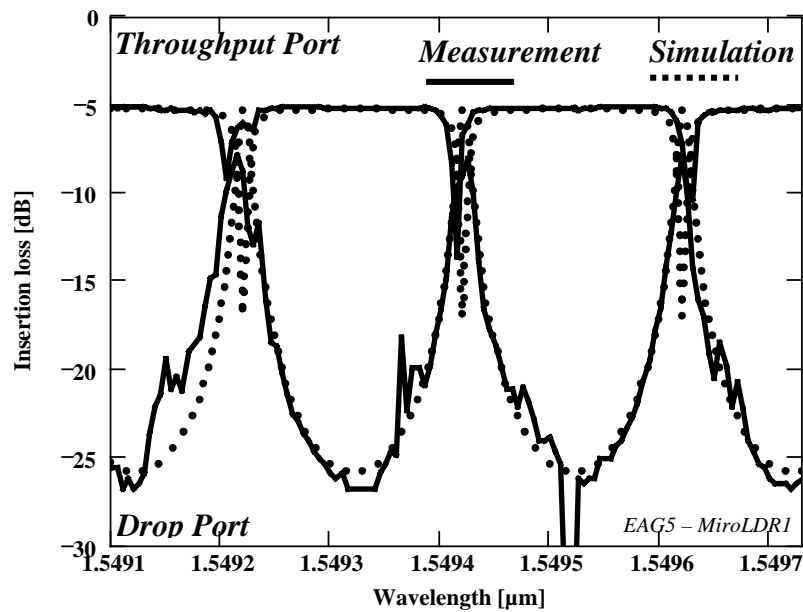


Fig. 133: SRR with two straight input/output waveguides and codirectional couplers (length =  $175 \text{ } \mu\text{m}$ , gap =  $0.9 \text{ } \mu\text{m}$ ),  $R = 403 \text{ } \mu\text{m}$ , gain length =  $300 \text{ } \mu\text{m}$ , FSR = 25 GHz.

The deep minima are definitely detected when a higher resolution of the ECL signal is chosen, because the transmission from the drop port is fully loss compensated. The deep minima can also be measured using the Pt – resistors, which was proven in section 5.1.4. Here the use of the Pt – resistors revealed a higher on-off ratio than the one measured by sweeping the ECL signal with an accuracy of  $1 \text{ pm}$ .

The transmission characteristic of an SRR with a radius of  $R = 363 \mu\text{m}$  and a gain length of  $400 \mu\text{m}$  is shown in Fig. 134. The FSR is 25 GHz. The length of the couplers is  $200 \mu\text{m}$  (gap =  $0.9 \mu\text{m}$ ), which results in coupling factors of  $\kappa_{1,2} = 0.17$ . The y-axis has been normalized to the insertion loss. The on-off ratio is measured to be more than 22 dB. The FWHM is determined to be  $0.012 \text{ nm}$ . The finesse of the ring resonator is  $F = 17$ , leading to a Q factor of  $Q = 130000$ . The filter response was measured by sweeping the ECL signal with a resolution of  $4 \text{ pm}$ . The SOA was operated at a current of  $90 \text{ mA}$ .

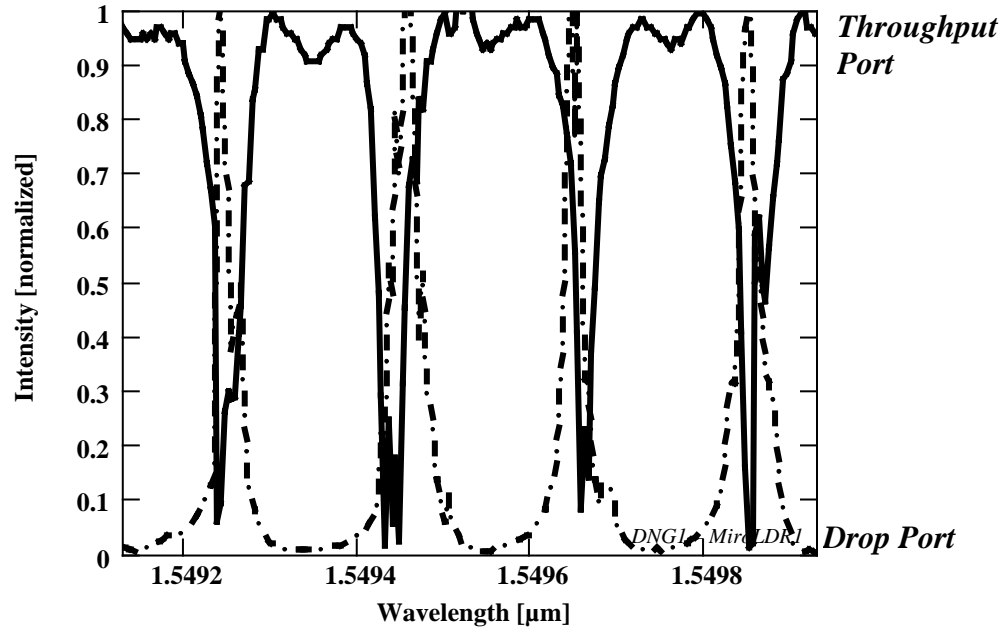


Fig. 134: SRR with two straight input/output waveguides and codirectional couplers (length =  $200 \mu\text{m}$ , gap =  $0.9 \mu\text{m}$ ),  $R = 363 \mu\text{m}$ , gain length =  $400 \mu\text{m}$ , FSR = 25 GHz.

The measurement result can be compared with the simulation in Fig. 27. The filter characteristic of a completely loss compensated filter is visible again and the fabricated device shows the calculated filter response.



The filter characteristic of an SRR with an FSR of 50 GHz is presented in Fig. 135. The radius is  $R = 125 \mu\text{m}$ , the gain length is  $300 \mu\text{m}$  and the length of the codirectional couplers is  $175 \mu\text{m}$  (gap =  $0.9 \mu\text{m}$ ). The coupling factor is determined to be again  $\kappa_{1,2} = 0.165$ . The FWHM is  $0.024 \text{ nm}$ , leading to a finesse of  $F = 17$  and a Q factor of  $Q \approx 65000$ . The on-off ratio is as was expected more than 20 dB. The measurement is performed when the SOA is operated at a current of 70 mA and 0 mA. The difference in the insertion loss of the two measurements is due to the coupling factor  $\kappa_l$ , neglecting the losses resulting from the straight waveguide and the coupler losses. Due to the coupling factor of  $\kappa_l = 0.165$  only  $\approx 84\%$  (- 0.8 dB) of the inserted intensity are transmitted and detected at the output port. This is also approximately the difference which can be measured when comparing the insertion loss of the two transmission curves of the throughput port.

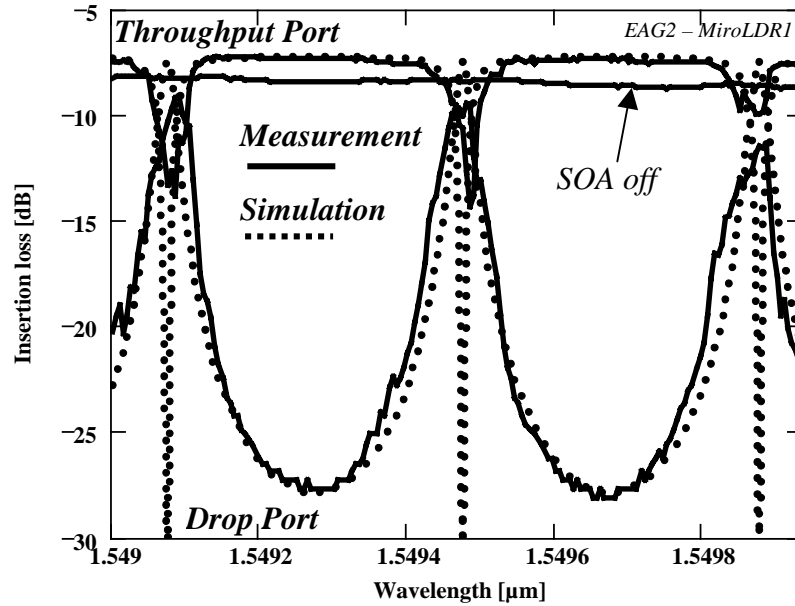


Fig. 135: SRR with two straight input/output waveguides and codirectional couplers (length =  $175 \mu\text{m}$ , gap =  $0.9 \mu\text{m}$ ),  $R = 125 \mu\text{m}$ , gain length =  $300 \mu\text{m}$ , FSR = 50 GHz.

The SOA absorbs the light coupled into the ring resonator, which can be seen in the transmission of the throughput port. If the SOA had not absorbed all the light, the transmission characteristic of the ring resonator would have been visible and not a “straight line”. By using a ring resonator with a low coupling factor ( $\kappa < 0.2$ ) and an integrated SOA, switchable wavelength selective devices with a high on-off ratio ( $> 20 \text{ dB}$ ) can be realized.

The following photograph (Fig. 136) is taken of a triple ring resonator with integrated SOAs. The characterization of the device was mainly focused on the filter response of the drop port (Fig. 137).

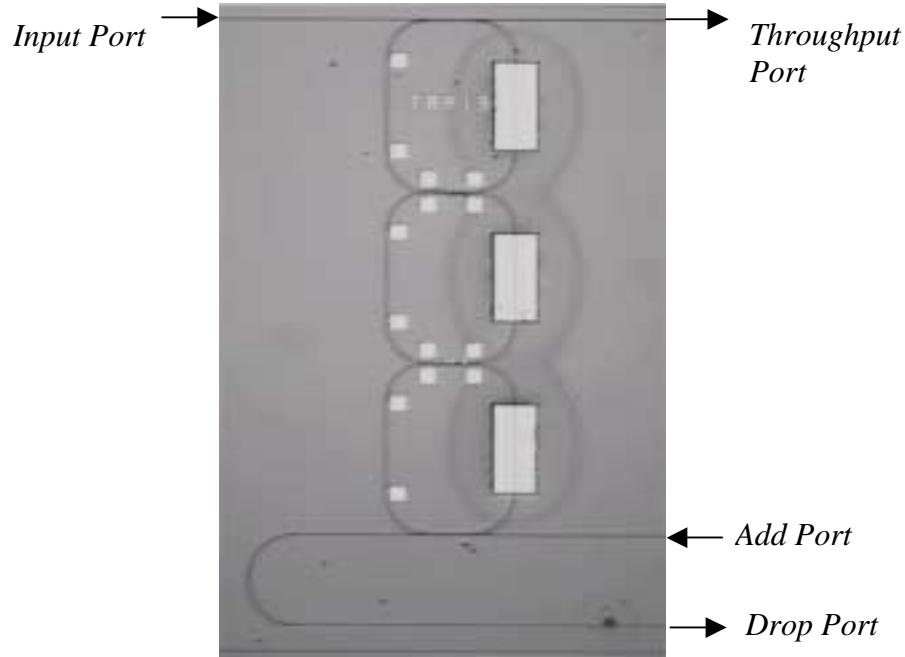


Fig. 136: Photograph of a fabricated TRR with three SOAs.

The measured TRR has a radius of  $R = 323 \mu\text{m}$ . The length of each SOA is  $400 \mu\text{m}$ . The length of the couplers is  $325 \mu\text{m}$  with a gap of  $0.8 \mu\text{m}$  for the outer couplers and  $1 \mu\text{m}$  for the couplers in the center. The achieved FSR is  $25 \text{ GHz}$ . The driving current for each of the three SOAs is  $50 \text{ mA}$ . Using this triple ring resonator configuration, a shape factor for the drop port of  $0.52$  has been realized. The steep roll-off can be seen from the measurement. The two ripples result from a slight resonance mismatch between the three ring resonators. In order to realize the transmission characteristic described in section 2.3.3, the coupling factors have to be within the tolerance margin to achieve on-off ratios greater than  $18 \text{ dB}$ , as explained. The on-off ratio for the fabricated TRR is more than  $18 \text{ dB}$  including the ripples.

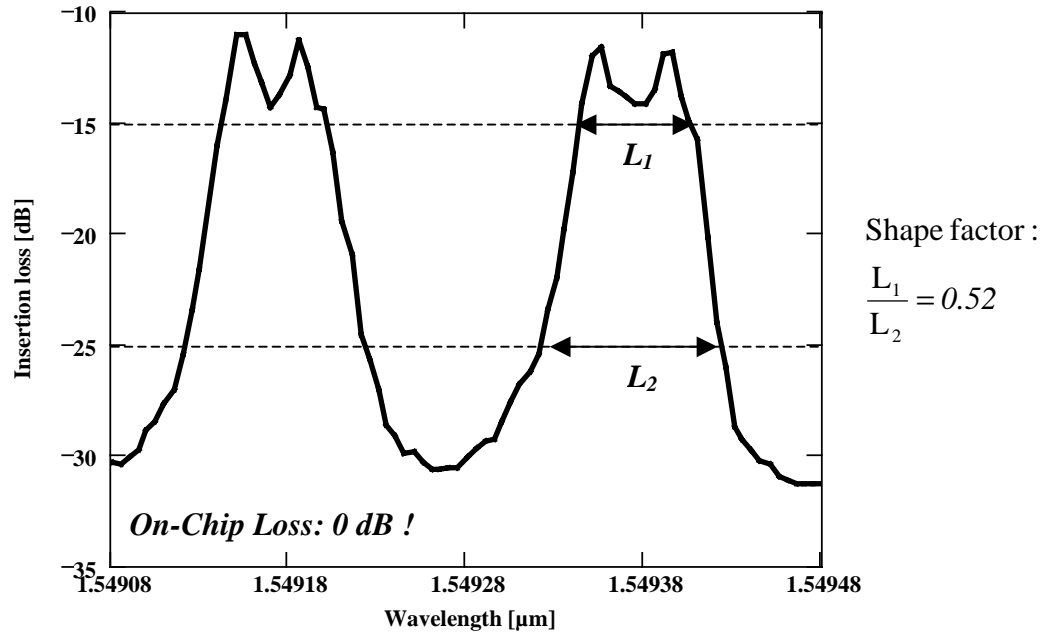


Fig. 137: Filter response of the drop port of a TRR with  $R = 323 \mu\text{m}$ , length of the couplers =  $325 \mu\text{m}$ , gain length =  $400 \mu\text{m}$ , FSR =  $25 \text{ GHz}$ .

Another triple ring resonator configuration is shown in Fig. 138. Here the ring resonators are placed in a parallel configuration.

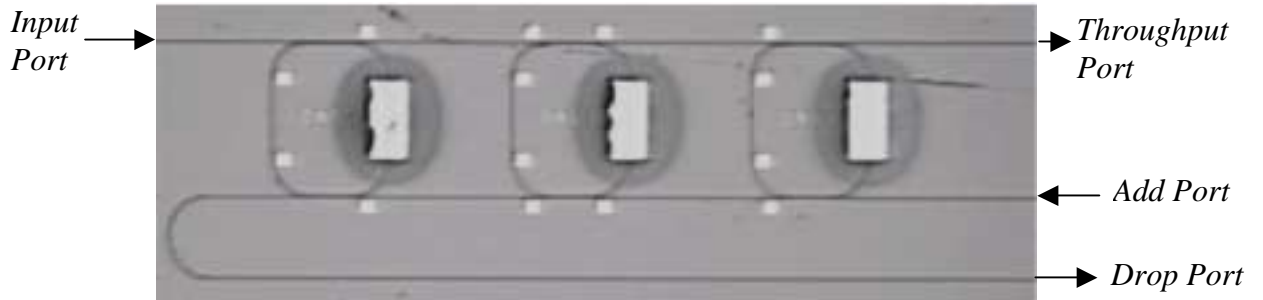


Fig. 138: Photograph of a fabricated triple coupled ring resonator in parallel configuration.

The ring resonators have a radius of  $117 \mu\text{m}$ , a coupler length of  $200 \mu\text{m}$  (gap =  $0.9 \mu\text{m}$ ) and a gain length of  $300 \mu\text{m}$ . A FSR of  $50 \text{ GHz}$  is realized. The driving current for each SOA is  $50 \text{ mA}$ . The distance between the resonators was chosen to be equal to half of the circumference of an SRR. The filter characteristic is shown in Fig. 139.

A measure of the on-chip loss of the filter can be obtained by comparing the maximum drop port power on resonance to the maximum throughput port power off resonance. For the parallel TRR configuration this ratio is  $-1.7 \text{ dB}$ . The on-chip losses of the serially coupled resonators were fully compensated by the SOAs.

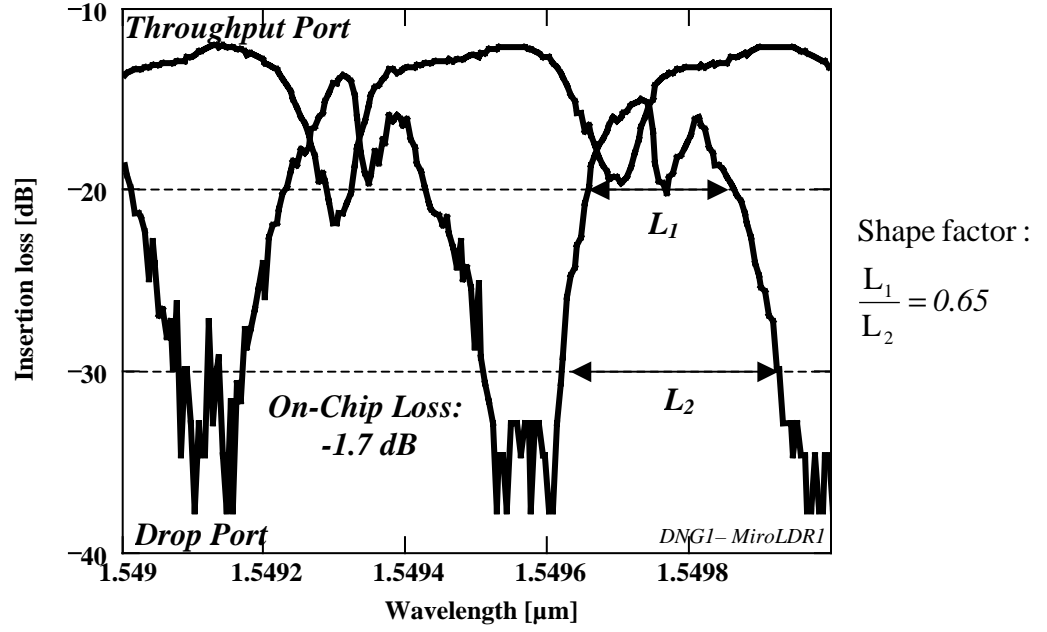


Fig. 139: Result of a parallel coupled TRR, length of the couplers = 200  $\mu\text{m}$ ,  $R = 117 \mu\text{m}$ , gain length = 300  $\mu\text{m}$ , FSR = 50 GHz.

The drop shape factor is determined to be 0.65, measured from below the ripples. One reason why the ripples are visible in the spectrum is the slight deviation from resonance of each involved SRR. A solution to minimize the ripples is by using the Pt – resistors, as was described in section 5.1.4.

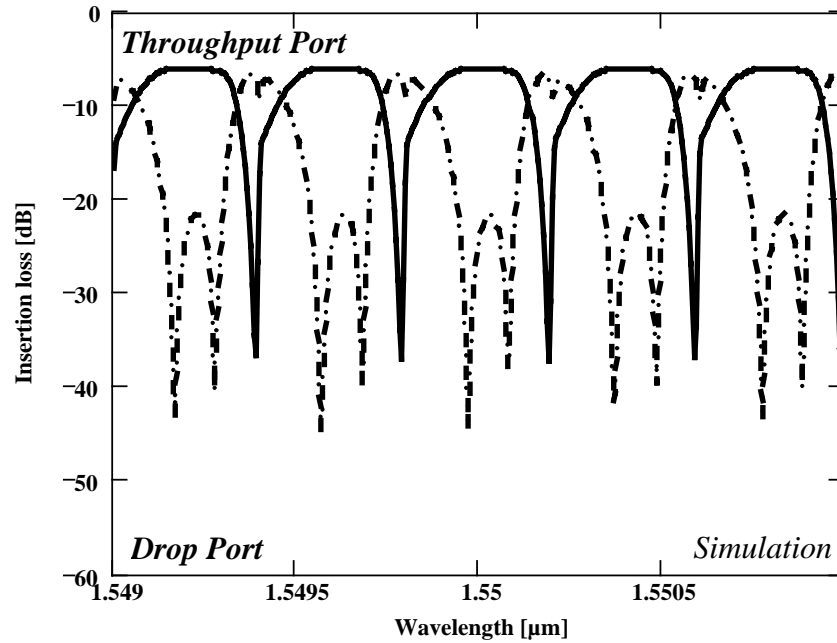


Fig. 140: Simulation of the measurement shown in Fig. 139.

Small ripples are seen due to the fact that the optical path in the ring resonators is not exactly a multiple of the optical path in between the resonators. A simulation of the filter

characteristic with the used configuration can be seen in Fig. 140. The ripples in the simulation result from the difference in the effective refractive index between a straight passive waveguide and an SOA section. The ring resonators are in resonance in the simulation. In order to achieve the resonance matching for all involved "resonators" the optical path has to be identical. In our case the slight resonance mismatch leads to the designed broadening and steep roll-off of the filter curve and so to a high shape factor.

*Passive single and double ring resonators with an FSR of 50 GHz and 100 GHz, on-off ratios of more than 20 dB and a finesse of 10 have been successfully fabricated and characterized. Single ring resonators with SOAs have been realized with an FSR of 12.5 GHz, 25 GHz and 50 GHz and have been used in triple ring resonator serial and parallel configurations to demonstrate their function as a building block for the development of optical filters using ring resonators. A design instruction for the development of ring resonator filters for the realization of box-like filter responses with on-off ratios of more than 20 dB was presented. The simulation model which has been developed was proven to be extremely accurate in predicting the filter characteristic of the fabricated devices.*

The following section gives an estimation of the system performance of these devices.



### 5.3 System operation – perspectives

As these ring resonator circuits with integrated SOA have been fabricated for the first time, the system performance has to be investigated for each desired optical transmission system to determine the limiting factors of these devices. This section provides only a simple estimation which does not claim for integrity of discussing all aspects for the calculation of the transmission performance of the ring resonator filters. A tradeoff between the optical bandwidth (FWHM) and the required datarate has to be found, which leads to a certain spectral width of the signal and the response time of the ring resonator filter. The response time is the time a system or functional unit takes to react to a given input. In a ring resonator filter the cavity response time is the time required to achieve steady-state finesse and is given by the product  $n\tau$ , where  $n$  is the number of circulations, which are required for the ring to be regarded as in resonance, and  $\tau$  is the delay time in the resonator [95]. The response time is equal to the minimum time a pulse should have in order to be loaded by the ring resonator. The maximum datarate which can be transmitted for a non-return to zero modulated signal is

approximated by  $\frac{1}{2 \times \text{response time}} \left[ \frac{\text{bit}}{\text{s}} \right]$  (Fig. 141) assuming a spectral efficiency of

0.5 bit/s/Hz. As the spectral efficiency continues to rise as was already mentioned in section 1.1.1, the limiting factor for the demonstrated ring resonators is the cavity response time. The cavity response time of a triple coupled parallel ring resonator filter (Fig. 139) is estimated to be about 300 ps, regarding the filter as in resonance after 5 roundtrips. The maximum datarate is calculated to be 1.6 Gbit/s.

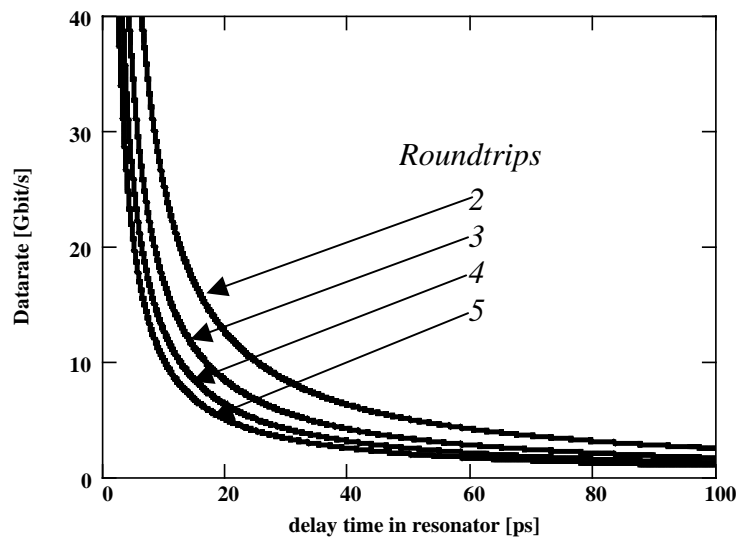


Fig. 141: Datarate for a specific delay time in the resonator.

This approach briefly describes the relations which have to be considered when designing ring resonator filters for various types of optical networks.





## 6 Summary

Optical *ring resonator filters* on the basis of GaInAsP / InP with and without integrated semiconductor optical amplifiers have been developed, fabricated and characterized in this thesis.

➤ *Passive single and double ring resonators* in the material system GaInAsP / InP in the form of racetracks, coupled to a multimode interference (MMI) coupler or a codirectional coupler (CC) with radii of  $R = 100 \mu\text{m} - 200 \mu\text{m}$  and free spectral ranges (FSRs) of 50 GHz and 100 GHz and on-off ratios of more than 20 dB have been realized.

➤ *Single and triple ring resonators* with integrated *SOAs* (length =  $100 \mu\text{m} - 800 \mu\text{m}$ ), coupled to two input/output waveguides using codirectional couplers with radii of  $R = 100 \mu\text{m} - 800 \mu\text{m}$  have been demonstrated. The ring losses are fully compensated by the SOA and an on-off ratio for the throughput and drop port of more than 20 dB has been realized. The achieved free spectral range is 12.5 GHz, 25 GHz and 50 GHz.

■ The *tuning* to a specific wavelength and the *resonance matching* of the double and triple ring resonators has been demonstrated by using integrated *Pt – resistors*.

■ The passband shape depends sensitively on the relative interactions between all resonators and the used couplers. In order to achieve a *box-like filter response*, a general design rule has been developed for engineering definite filter shapes using *double* and *triple coupled ring resonators*.

➤ The architecture of a *single ring resonator* with integrated SOA:

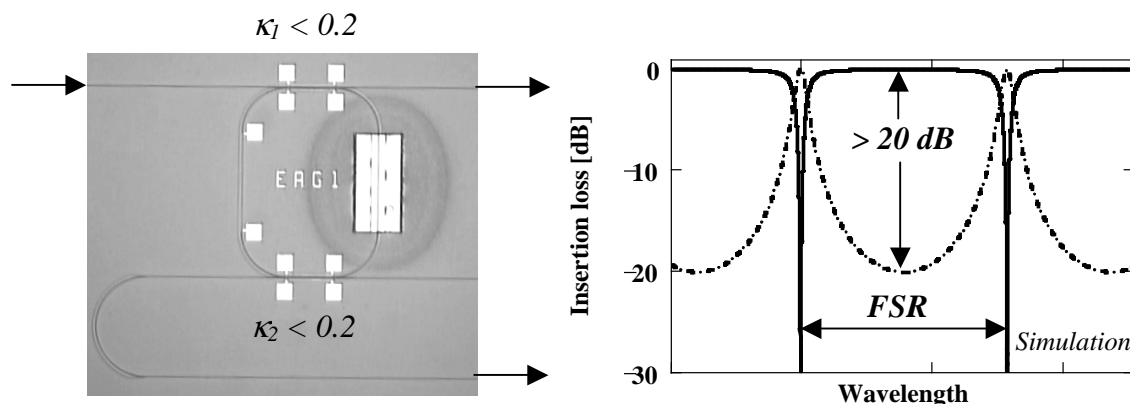


Fig. 142: Single ring resonator with codirectional couplers and integrated SOA.

- The architecture of a passive *double ring resonator*:

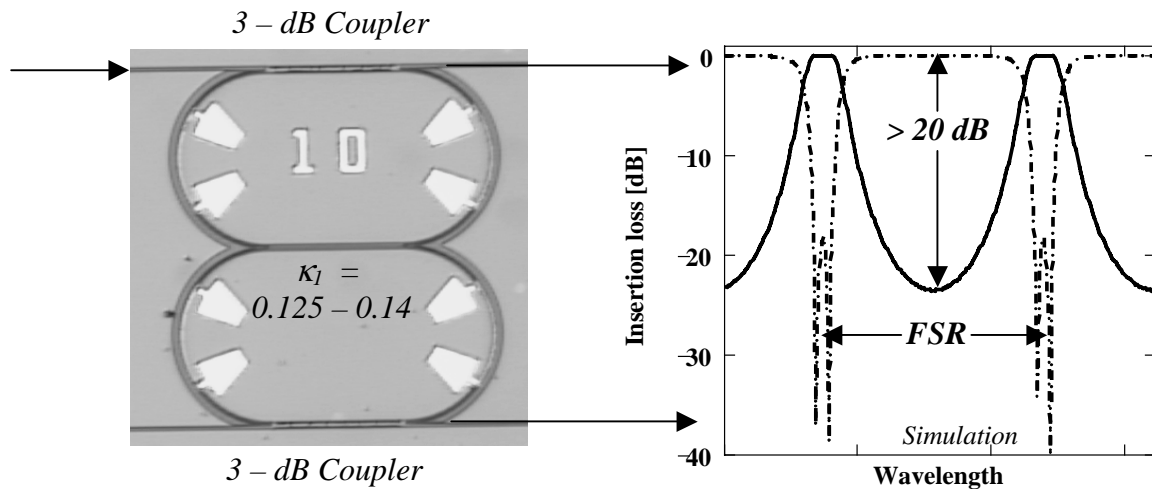


Fig. 143: Double ring resonator with two MMI couplers and a codirectional coupler.

- The architecture of a serially coupled *triple ring resonator* with integrated SOAs:

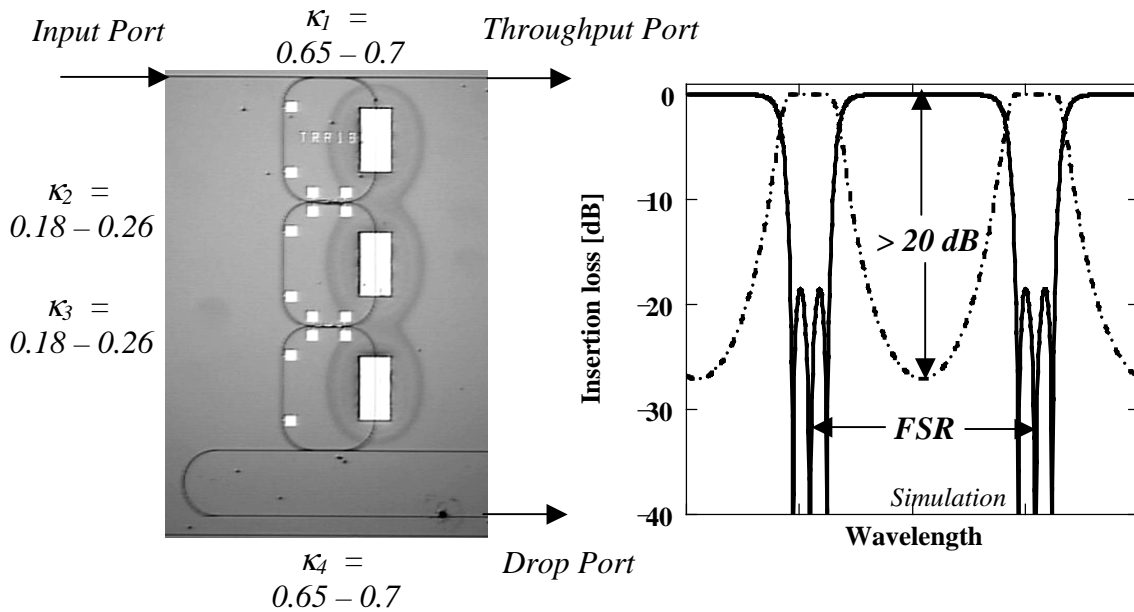


Fig. 144: Serially coupled triple ring resonator with codirectional couplers and SOAs.

A summary of the obtained results of the fabricated ring resonators with and without integrated SOAs is given in table 4 on the following page.

Ring resonator	Figure	FSR [GHz]	On-off ratio [dB]	FWHM [nm]	Finesse $F$	Q factor	Drop shape factor
<i>PASSIVE RING RESONATORS</i>							
<b>SRR</b>	Fig. 87	94	13	0.137	5.5	11300	-
<b>SRR</b>	Fig. 88	91.4	14	0.12	6.1	12900	-
<b>SRR</b>	Fig. 90	56	14	0.08	5.4	19400	-
<b>SRR</b>	Fig. 91	49	> 20	0.04	10	39000	-
<b>DRR</b>	Fig. 93	94	16 / 12	0.12 / 0.28	6 / 3	12900 / 5500	-
<b>DRR</b>	Fig. 99	55	> 18	0.08 / 0.1	5.5 / 4.4	19400 / 15500	0.34
<i>RING RESONATORS WITH INTEGRATED SOAS</i>							
<b>SRR</b>	Fig. 128	44	11	0.07	5	22100	-
<b>SRR</b>	Fig. 130	74	12	0.13	4	12000	-
<b>SRR</b>	Fig. 132	12.5	> 20	0.0067	15	232500	0.18
<b>SRR</b>	Fig. 133	25	> 20	0.012	17	130000	0.18
<b>SRR</b>	Fig. 134	25	> 20	0.012	17	130000	0.18
<b>SRR</b>	Fig. 135	50	> 20	0.024	17	65000	0.18
<b>TRR</b>	Fig. 137	25	18	0.06	3.3	25800	0.52
<b>TRR</b>	Fig. 139	50	18	0.16	2.5	9690	0.65

Table 4: Summary of the results obtained for the fabricated ring resonator filters.

The presented ring resonator filters have been shown to be polarization dependent which could be used advantageously, for example, in polarization division multiplexing. The tuneability and the resonance matching between multiply coupled ring resonators is realized by increasing the local temperature of a waveguide segment in the ring resonator. The resonance matching is a limiting factor for the realization of multiple coupled ring resonators which limits the number of coupled rings using today's state-of-the-art technology to a maximum of four rings. As these demonstrated ring resonator filters are temperature dependent which is used advantageously as shown, these ring resonator filters have to be temperature stabilized by using for example, a peltier cooler. The temperature stabilization is also required for the operation of the semiconductor optical amplifier.

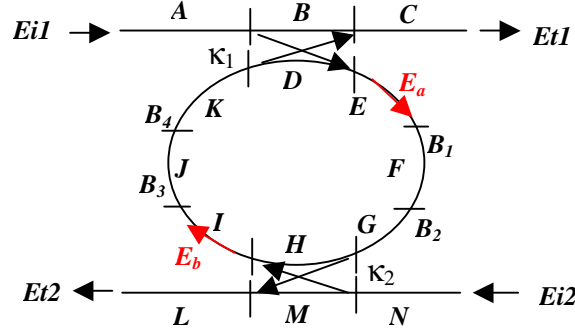
In conclusion, a simulation model was developed to determine the characteristic response of various **ring resonator architectures**. On the basis of this model, ring resonators with and without integrated semiconductor optical amplifiers in GaInAsP / InP were designed and fabricated. A design rule for the realization of box-like filter shapes using double and triple coupled ring resonators was presented. The realized single ring resonator with integrated semiconductor optical amplifier was demonstrated to be fully loss compensated, wavelength tunable and switchable. A combination of this single ring resonator enables the realization of various types of filters with a tailored passband characteristic. This single ring resonator could be the **building block** for different kinds of ring resonator configurations for various types of applications in the field of optical signal processing.

The properties of integrated ring resonator filters are at the beginning of exploration. The use of ring resonators is not limited to optical filter applications as was described. Future work could be the investigation of nonlinear effects in the ring resonators with integrated semiconductor optical amplifier and their system performance in optical systems using various transmission formats. As there is a lot of research going on in the field of ring resonators, future work will show the potential applications of all-active ring resonators (publications: conferences [4]), [96], vertically coupled ring resonators [97] and the ring resonators presented in this thesis in comparison to other filter concepts like gratings or thin film filters.

Ring resonators are emerging optical filters for different applications in the all optical network with a strong outlook for the future with a large potential for growth.

## Appendix

### Calculation of the intensity relations of an SRR with two input/output waveguides



$$A_{Segment} = \exp \left[ -\frac{\alpha_{Segment}}{2} L_{Segment} - j k_{Segment} L_{Segment} \right]$$

$B_x$  : remaining fraction of the electric field when passing an interface (e.g. active-passive)

$$E_a(\lambda) := (E_{i1} \cdot A(\lambda) \cdot B(\lambda) \cdot j \cdot \sqrt{\kappa_1}) + E_b(\lambda) \cdot I(\lambda) \cdot J(\lambda) \cdot K(\lambda) \cdot D(\lambda) \cdot \sqrt{1 - \kappa_1} \cdot B_3 \cdot B_4$$

$$E_b(\lambda) := B_1 \cdot B_2 \cdot E_a(\lambda) \cdot E(\lambda) \cdot F(\lambda) \cdot G(\lambda) \cdot H(\lambda) \cdot \sqrt{1 - \kappa_2} + E_{i2} \cdot N(\lambda) \cdot M(\lambda) \cdot j \cdot \sqrt{\kappa_2}$$

$$\text{MatrixA}(\lambda) := \begin{pmatrix} 1 & -I(\lambda) \cdot J(\lambda) \cdot K(\lambda) \cdot D(\lambda) \cdot \sqrt{1 - \kappa_1} \cdot B_3 \cdot B_4 \\ E(\lambda) \cdot F(\lambda) \cdot G(\lambda) \cdot H(\lambda) \cdot \sqrt{1 - \kappa_2} \cdot B_1 \cdot B_2 & -1 \end{pmatrix}$$

$$\text{MatrixB}(\lambda) := \begin{pmatrix} E_{i1} \cdot A(\lambda) \cdot B(\lambda) \cdot j \cdot \sqrt{\kappa_1} \\ -E_{i2} \cdot N(\lambda) \cdot M(\lambda) \cdot j \cdot \sqrt{\kappa_2} \end{pmatrix}$$

$$E_a(\lambda) := \frac{\left| \begin{pmatrix} E_{i1} \cdot A(\lambda) \cdot B(\lambda) \cdot j \cdot \sqrt{\kappa_1} & -I(\lambda) \cdot J(\lambda) \cdot K(\lambda) \cdot D(\lambda) \cdot \sqrt{1 - \kappa_1} \cdot B_3 \cdot B_4 \\ -E_{i2} \cdot N(\lambda) \cdot M(\lambda) \cdot j \cdot \sqrt{\kappa_2} & -1 \end{pmatrix} \right|}{|\text{MatrixA}(\lambda)|}$$

$$E_b(\lambda) := \frac{\left| \begin{pmatrix} 1 & E_{i1} \cdot A(\lambda) \cdot B(\lambda) \cdot j \cdot \sqrt{\kappa_1} \\ E(\lambda) \cdot F(\lambda) \cdot G(\lambda) \cdot H(\lambda) \cdot \sqrt{1 - \kappa_2} \cdot B_1 \cdot B_2 & -E_{i2} \cdot N(\lambda) \cdot M(\lambda) \cdot j \cdot \sqrt{\kappa_2} \end{pmatrix} \right|}{|\text{MatrixA}(\lambda)|}$$

$$E_{t1}(\lambda) := E_{i1} \cdot A(\lambda) \cdot B(\lambda) \cdot \sqrt{1 - \kappa_1} \cdot C(\lambda) + E_b(\lambda) \cdot I(\lambda) \cdot J(\lambda) \cdot K(\lambda) \cdot D(\lambda) \cdot j \cdot \sqrt{\kappa_1} \cdot C(\lambda) \cdot B_3 \cdot B_4$$

$$E_{t2}(\lambda) := (E_{i2} \cdot N(\lambda) \cdot M(\lambda) \cdot \sqrt{1 - \kappa_2} \cdot L(\lambda) + E_a(\lambda) \cdot E(\lambda) \cdot F(\lambda) \cdot G(\lambda) \cdot H(\lambda) \cdot j \cdot \sqrt{\kappa_2} \cdot L(\lambda) \cdot B_1 \cdot B_2) \cdot R(\lambda) \cdot R(\lambda) \cdot L(\lambda)$$

$$I_{t1}(\lambda) := E_{t1}(\lambda) \cdot \overline{E_{t1}(\lambda)}$$

$$I_{t2}(\lambda) := E_{t2}(\lambda) \cdot \overline{E_{t2}(\lambda)}$$

## Calculation of the intensity relations of a DRR

$$A_{Segment} = \exp \left[ -\frac{\alpha_{Segment}}{2} L_{Segment} - j k_{Segment} L_{Segment} \right]$$

$B_x$  : remaining fraction of the electric field when passing an interface (e.g. active-passive)

$$Ea(\lambda) := Ei1 \cdot A(\lambda)_0 \cdot A(\lambda)_1 \cdot j \cdot \sqrt{\kappa_0} + Eb(\lambda) \cdot A(\lambda)_8 \cdot A(\lambda)_9 \cdot A(\lambda)_{10} \cdot A(\lambda)_3 \cdot \sqrt{1 - \kappa_0} \cdot B_3 \cdot B_2$$

$$Eb(\lambda) := B_0 \cdot B_1 \cdot Ea(\lambda) \cdot A(\lambda)_4 \cdot A(\lambda)_5 \cdot A(\lambda)_6 \cdot A(\lambda)_7 \cdot \sqrt{1 - \kappa_1} + Ed(\lambda) \cdot A(\lambda)_{14} \cdot A(\lambda)_{13} \cdot A(\lambda)_{12} \cdot A(\lambda)_{11} \cdot j \cdot \sqrt{\kappa_1} \cdot B_4 \cdot B_5$$

$$Ec(\lambda) := B_0 \cdot B_1 \cdot Ea(\lambda) \cdot A(\lambda)_4 \cdot A(\lambda)_5 \cdot A(\lambda)_6 \cdot A(\lambda)_7 \cdot j \cdot \sqrt{\kappa_1} + Ed(\lambda) \cdot A(\lambda)_{14} \cdot A(\lambda)_{13} \cdot A(\lambda)_{12} \cdot A(\lambda)_{11} \cdot \sqrt{1 - \kappa_1} \cdot B_4 \cdot B_5$$

$$Ed(\lambda) := Ei2 \cdot A(\lambda)_{21} \cdot A(\lambda)_{19} \cdot j \cdot \sqrt{\kappa_2} + Ec(\lambda) \cdot A(\lambda)_{18} \cdot A(\lambda)_{17} \cdot A(\lambda)_{16} \cdot A(\lambda)_{15} \cdot \sqrt{1 - \kappa_2} \cdot B_7 \cdot B_6$$

$$Et1(\lambda) := Ei1 \cdot A(\lambda)_0 \cdot A(\lambda)_1 \cdot \sqrt{1 - \kappa_0} \cdot A(\lambda)_2 + Eb(\lambda) \cdot A(\lambda)_8 \cdot A(\lambda)_9 \cdot A(\lambda)_{10} \cdot A(\lambda)_3 \cdot j \cdot \sqrt{\kappa_0} \cdot A(\lambda)_2 \cdot B_3 \cdot B_2$$

$$Et2(\lambda) := Ei2 \cdot A(\lambda)_{21} \cdot A(\lambda)_{19} \cdot \sqrt{1 - \kappa_2} \cdot A(\lambda)_{20} + Ec(\lambda) \cdot A(\lambda)_{18} \cdot A(\lambda)_{17} \cdot A(\lambda)_{16} \cdot A(\lambda)_{15} \cdot j \cdot \sqrt{\kappa_2} \cdot A(\lambda)_{20} \cdot B_7 \cdot B_6$$

$$It1(\lambda) := Et1(\lambda) \cdot \overline{Et1(\lambda)}$$

$$It2(\lambda) := Et2(\lambda) \cdot \overline{Et2(\lambda)}$$

## Calculation of the intensity relations of a serially coupled TRR

$$A_{Segment} = \exp \left[ -\frac{\alpha_{Segment}}{2} L_{Segment} - j k_{Segment} L_{Segment} \right]$$

$B_x$  : remaining fraction of the electric field when passing an interface (e.g. active-passive)

$$Ea(\lambda) := Ei1 \cdot A(\lambda)_0 \cdot A(\lambda)_1 \cdot j \cdot \sqrt{\kappa_0} + Eb(\lambda) \cdot A(\lambda)_8 \cdot A(\lambda)_9 \cdot A(\lambda)_{10} \cdot A(\lambda)_3 \cdot \sqrt{1 - \kappa_0} \cdot B_3 \cdot B_2$$

$$Eb(\lambda) := B_0 \cdot B_1 \cdot Ea(\lambda) \cdot A(\lambda)_4 \cdot A(\lambda)_5 \cdot A(\lambda)_6 \cdot A(\lambda)_7 \cdot \sqrt{1 - \kappa_1} + Ed(\lambda) \cdot A(\lambda)_{14} \cdot A(\lambda)_{13} \cdot A(\lambda)_{12} \cdot A(\lambda)_{11} \cdot j \cdot \sqrt{\kappa_1} \cdot B_4 \cdot B_5$$

$$Ec(\lambda) := B_0 \cdot B_1 \cdot Ea(\lambda) \cdot A(\lambda)_4 \cdot A(\lambda)_5 \cdot A(\lambda)_6 \cdot A(\lambda)_7 \cdot j \cdot \sqrt{\kappa_1} + Ed(\lambda) \cdot A(\lambda)_{14} \cdot A(\lambda)_{13} \cdot A(\lambda)_{12} \cdot A(\lambda)_{11} \cdot \sqrt{1 - \kappa_1} \cdot B_4 \cdot B_5$$

$$Ed(\lambda) := Eg(\lambda) \cdot A(\lambda)_{24} \cdot A(\lambda)_{25} \cdot A(\lambda)_{26} \cdot A(\lambda)_{19} \cdot j \cdot \sqrt{\kappa_2} \cdot B_{10} \cdot B_{11} + Ec(\lambda) \cdot A(\lambda)_{18} \cdot A(\lambda)_{17} \cdot A(\lambda)_{16} \cdot A(\lambda)_{15} \cdot \sqrt{1 - \kappa_2} \cdot B_7 \cdot B_6$$

$$Ef(\lambda) := Ec(\lambda) \cdot A(\lambda)_{18} \cdot A(\lambda)_{17} \cdot A(\lambda)_{16} \cdot A(\lambda)_{15} \cdot j \cdot \sqrt{\kappa_2} \cdot B_7 \cdot B_6 + Eg(\lambda) \cdot A(\lambda)_{24} \cdot A(\lambda)_{25} \cdot A(\lambda)_{26} \cdot A(\lambda)_{19} \cdot \sqrt{1 - \kappa_2} \cdot B_{10} \cdot B_{11}$$

$$Eg(\lambda) := Ef(\lambda) \cdot A(\lambda)_{20} \cdot A(\lambda)_{21} \cdot A(\lambda)_{22} \cdot A(\lambda)_{23} \cdot \sqrt{1 - \kappa_3} \cdot B_8 \cdot B_9 + Ei2 \cdot A(\lambda)_{28} \cdot A(\lambda)_{27} \cdot j \cdot \sqrt{\kappa_3}$$

$$Et1(\lambda) := Ei1 \cdot A(\lambda)_0 \cdot A(\lambda)_1 \cdot \sqrt{1 - \kappa_0} \cdot A(\lambda)_2 + Eb(\lambda) \cdot A(\lambda)_8 \cdot A(\lambda)_9 \cdot A(\lambda)_{10} \cdot A(\lambda)_3 \cdot j \cdot \sqrt{\kappa_0} \cdot A(\lambda)_2 \cdot B_3 \cdot B_2$$

$$Et2(\lambda) := Ei2 \cdot A(\lambda)_{28} \cdot A(\lambda)_{27} \cdot \sqrt{1 - \kappa_3} \cdot A(\lambda)_{29} + Ef(\lambda) \cdot A(\lambda)_{20} \cdot A(\lambda)_{21} \cdot A(\lambda)_{22} \cdot A(\lambda)_{23} \cdot j \cdot \sqrt{\kappa_3} \cdot A(\lambda)_{29} \cdot B_8 \cdot B_9$$

## Calculation of the intensity relations of a parallel coupled TRR

$$A_{Segment} = \exp \left[ -\frac{\alpha_{Segment}}{2} L_{Segment} - j k_{Segment} L_{Segment} \right]$$

$B_x$  : remaining fraction of the electric field when passing an interface (e.g. active-passive)

$$\begin{aligned} Ea(\lambda) &:= (Ei1 \cdot A(\lambda)_0 \cdot A(\lambda)_1 \cdot j \cdot \sqrt{\kappa_0}) + Eb(\lambda) \cdot A(\lambda)_{14} \cdot A(\lambda)_{15} \cdot A(\lambda)_{16} \cdot A(\lambda)_9 \cdot \sqrt{1 - \kappa_0} \cdot B_0 \cdot B_1 \\ Eb(\lambda) &:= (Ea(\lambda) \cdot A(\lambda)_{10} \cdot A(\lambda)_{11} \cdot A(\lambda)_{12} \cdot A(\lambda)_{13} \cdot \sqrt{1 - \kappa_1} \cdot B_2 \cdot B_3) + El(\lambda) \cdot A(\lambda)_{39} \cdot A(\lambda)_{40} \cdot j \cdot \sqrt{\kappa_1} \\ Ek(\lambda) &:= (Ei1 \cdot A(\lambda)_0 \cdot A(\lambda)_1 \cdot A(\lambda)_2 \cdot \sqrt{1 - \kappa_0}) + Eb(\lambda) \cdot A(\lambda)_{14} \cdot A(\lambda)_{15} \cdot A(\lambda)_{16} \cdot A(\lambda)_9 \cdot j \cdot \sqrt{\kappa_0} \cdot B_0 \cdot B_1 \cdot A(\lambda)_2 \\ Ec(\lambda) &:= (Ek(\lambda) \cdot A(\lambda)_3 \cdot A(\lambda)_4 \cdot j \cdot \sqrt{\kappa_2}) + Ed(\lambda) \cdot A(\lambda)_{22} \cdot A(\lambda)_{23} \cdot A(\lambda)_{24} \cdot A(\lambda)_{17} \cdot \sqrt{1 - \kappa_2} \cdot B_4 \cdot B_5 \\ Ed(\lambda) &:= (Ec(\lambda) \cdot A(\lambda)_{18} \cdot A(\lambda)_{19} \cdot A(\lambda)_{20} \cdot A(\lambda)_{21} \cdot \sqrt{1 - \kappa_3} \cdot B_6 \cdot B_7) + En(\lambda) \cdot A(\lambda)_{36} \cdot A(\lambda)_{37} \cdot j \cdot \sqrt{\kappa_3} \\ El(\lambda) &:= (En(\lambda) \cdot A(\lambda)_{36} \cdot A(\lambda)_{37} \cdot A(\lambda)_{38} \cdot \sqrt{1 - \kappa_3}) + Ec(\lambda) \cdot A(\lambda)_{18} \cdot A(\lambda)_{19} \cdot A(\lambda)_{20} \cdot A(\lambda)_{21} \cdot j \cdot \sqrt{\kappa_3} \cdot A(\lambda)_{38} \cdot B_6 \cdot B_7 \\ Em(\lambda) &:= (Ek(\lambda) \cdot A(\lambda)_3 \cdot A(\lambda)_4 \cdot A(\lambda)_5 \cdot \sqrt{1 - \kappa_2}) + Ed(\lambda) \cdot A(\lambda)_{22} \cdot A(\lambda)_{23} \cdot A(\lambda)_{24} \cdot A(\lambda)_{17} \cdot j \cdot \sqrt{\kappa_2} \cdot B_4 \cdot B_5 \cdot A(\lambda)_5 \\ En(\lambda) &:= (Ei2 \cdot A(\lambda)_{33} \cdot A(\lambda)_{34} \cdot A(\lambda)_{35} \cdot \sqrt{1 - \kappa_5}) + Ef(\lambda) \cdot A(\lambda)_{26} \cdot A(\lambda)_{27} \cdot A(\lambda)_{28} \cdot A(\lambda)_{29} \cdot j \cdot \sqrt{\kappa_5} \cdot A(\lambda)_{35} \cdot B_{10} \cdot B_{11} \\ Ef(\lambda) &:= (Em(\lambda) \cdot A(\lambda)_6 \cdot A(\lambda)_7 \cdot j \cdot \sqrt{\kappa_4}) + Eg(\lambda) \cdot A(\lambda)_{30} \cdot A(\lambda)_{31} \cdot A(\lambda)_{32} \cdot A(\lambda)_{25} \cdot \sqrt{1 - \kappa_4} \cdot B_8 \cdot B_9 \\ Eg(\lambda) &:= (Ef(\lambda) \cdot A(\lambda)_{26} \cdot A(\lambda)_{27} \cdot A(\lambda)_{28} \cdot A(\lambda)_{29} \cdot \sqrt{1 - \kappa_5} \cdot B_{10} \cdot B_{11}) + Ei2 \cdot A(\lambda)_{33} \cdot A(\lambda)_{34} \cdot j \cdot \sqrt{\kappa_5} \\ \\ Et1(\lambda) &:= (Em(\lambda) \cdot A(\lambda)_6 \cdot A(\lambda)_7 \cdot A(\lambda)_8 \cdot \sqrt{1 - \kappa_4}) + Eg(\lambda) \cdot A(\lambda)_{30} \cdot A(\lambda)_{31} \cdot A(\lambda)_{32} \cdot A(\lambda)_{25} \cdot j \cdot \sqrt{\kappa_4} \cdot B_8 \cdot B_9 \cdot A(\lambda)_8 \\ Et2(\lambda) &:= (El(\lambda) \cdot A(\lambda)_{39} \cdot A(\lambda)_{40} \cdot A(\lambda)_{41} \cdot \sqrt{1 - \kappa_1}) + Ea(\lambda) \cdot A(\lambda)_{10} \cdot A(\lambda)_{11} \cdot A(\lambda)_{12} \cdot A(\lambda)_{13} \cdot j \cdot \sqrt{\kappa_1} \cdot B_2 \cdot B_3 \cdot A(\lambda)_{41} \end{aligned}$$



## Symbols and abbreviations

$\tau$	Delay Time
$\gamma$	Intensity Insertion Loss Coefficient of the CC
$\theta$	Angle
$\kappa$	Coupling Factor
$\rho$	Density
$\alpha$	Intensity Attenuation Coefficient
$\phi$	Phase
$\Lambda$	Spacing between Rings in a Parallel Configuration
$\lambda$	Wavelength
$\lambda_g$	Bandgap wavelength
$\delta\phi$	3 dB Bandwidth / FWHM
$\epsilon_\infty$	Dielectric Constant (High Frequency)
$\delta\lambda$	FWHM in Terms of Wavelength
$\Delta\lambda$	Wavelength Spacing / FSR
$\eta_{bend}$	Transmission through a Bend
$\Delta f$	Frequency spacing / FSR
$\delta f$	FWHM in Terms of Frequency
$\Delta n_{eff\ TE-TM}$	Effective refractive index difference between the TE and TM polarization
$\epsilon_s$	Dielectric Constant (Static)
$A$	Roundtrip Loss
AFM	Atomic Force Microscope
AFORDL	Amplified Fiber-Optic Recirculating Delay Lines
Al	Aluminum
APF	Optical All-Pass Filter
AR	Anti Reflection
AR	Autoregressive
As	Arsenate
Au	Gold
AWG	Arrayed Waveguide Grating
$B$	Fraction of the Electric Field passing an Interface
B	Lattice Constant

Be	Beryllium
c	Speed of Light in Vacuum
CC	Codirectional Coupler
CH <sub>4</sub>	Methane
CHF <sub>3</sub>	Hydrofluorocarbon
CVD	Chemical Vapor Deposition
$D^2$	Intensity Loss Coefficient of the CC
DRR	Double Ring Resonator
DUT	Device Under Test
DWDM	Dense Wavelength Division Multiplexing
$E$	Field Coefficient
$E_A$	Amplitude of the Electric Field
ECL	External Cavity Laser
EDFA	Erbium-Doped Fiber Amplifier
$F$	Finesse
$f$	Frequency
FBG	Fiber Bragg Grating
FDM	Frequency Division Multiplexing
FDTD	Finite Difference Time Domain
FIR	Finite Impulse Response
FSR	Free Spectral Range
FWHM	Full Width at Half Maximum
Ga	Gallium
Ge	Germanium
$h$	Planck's Constant
H <sub>2</sub>	Hydrogen
H <sub>2</sub> O	Water
H <sub>2</sub> O <sub>2</sub>	Hydrogen Peroxide
H <sub>3</sub> PO <sub>4</sub>	Phosphoric Acid
HBr	Hydrogen Bromide
HCl	Hydrochloric Acid
HF	Hydrofluoric Acid
$I$	Intensity
IC	Integrated Circuit
IIR	Infinite impulse response

In	Indium
ITU	International Telecommunication Union
$J_0$	Transparency Current Density
$k$	Phase Constant
$k_n$	Propagation Constant
KOH	Potassium hydroxide
$L$	Circumference of the Ring, Length of a Waveguide
LC	Liquid Crystal
LD	Laser Diode
$m_0$	Electron Effective Mass
MA	Moving Average
$m_e$	Electron Mass
$m_{hh}$	Heavy Hole Mass
$m_{lh}$	Light Hole Mass
MMI	Multimode Interference Coupler
MOVPE	Metal Organic Vapor Phase Epitaxy
MZI	Mach-Zehnder interferometer
$n$	refractive index
$n_{eff}$	Effective Refractive Index
$n_{gr}$	Group Refractive Index
NMP	n-Methyl-2-Pyrrolidon ( $C_5H_9NO$ )
$O_2$	Oxygen
OA	Optical Amplifier
OLCR	Optical Low Coherence Reflectometry
OSA	Optical Spectrum Analyzer
OTDM	Optical Time Division Multiplexing
P	Phosphorous
$P_0$	Input Intensity
PD	Photo Diode
PDM	Polarization Division Multiplexing
PECVD	Plasma Enhanced Chemical Vapor Deposition
PMD	Polarization Mode Dispersion
Pt	Platinum
$Q$	Quality Factor
QW	Quantum Well

$R$	Radius, Reflection Factor
RIE	Reactive Ion Etching
$R_n$	Intermediate Field in Reverse Direction
$R_T$	Reference Radius
RW	Ridge Waveguide
SAMOVPE	Selective Area Metal Organic Vapor Phase Epitaxy
SEM	Scanning Electron Microscope
Si	Silicon
SiN <sub>x</sub>	Silicon Nitride
SOA	Semiconductor Optical Amplifier
SRR	Single Ring Resonator
T	Temperature
TDM	Time Division Multiplexing
TE	Transversal Electric
TFF	Thin Film Filter
Ti	Titanium
TM	Transversal Magnetic
$T_n$	Intermediate Field in Forward Direction
TRR	Triple Ring Resonator
UFORDL	Unamplified Fiber-Optic Recirculating Delay Lines
UV	Ultraviolet
$w$	Width of Waveguide
WDM	Wavelength Division Multiplexing
$W_g$	Bandgap Energy
WG	Waveguide
WGR	Waveguide Grating Router
Zn	Zinc

## **Publications**

Part of this work has been published already:

### ***Journals and Letters***

- [1] D. G. Rabus and M. Hamacher, "Optical Filter and Laser Applications using Micro Ring Resonators," July 2001, Second Online Symposium for Electronic Engineers (OSEE), [www.techonline.com](http://www.techonline.com).
- [2] D. G. Rabus, M. Hamacher, "MMI-Coupled Ring Resonators in GaInAsP-InP," IEEE Photon. Technol. Lett., vol. 13, no. 8, pp. 812-814, August 2001.
- [3] D. G. Rabus, M. Hamacher, H. Heidrich, "Resonance Frequency Tuning of a Double Ring Resonator on GaInAsP / InP: Experiment and Simulation," Jpn. J. Appl. Phys. (JJAP), vol. 41, part 1, no. 2B, pp. 1186-1189, February 2002.
- [4] D. G. Rabus, M. Hamacher, H. Heidrich, U. Troppenz, "High Q Channel Dropping Filters using Ring Resonators with Integrated SOAs," submitted February 2002, revised May 7, 2002, for publication in IEEE Photon. Technol. Lett.

### ***Conferences***

- [1] D. G. Rabus, M. Hamacher, H. Heidrich, "Active and Passive Microring Resonator Filter Applications on GaInAsP / InP," in Proceed. Internat. Conf. On Indium Phosphide and Related Materials (IPRM'01), Nara, Japan, 14.-18.05.2001, pp. 477-480, paper ThA1-3, ISBN 0-7803-67006.
- [2] M. Hamacher, H. Heidrich, D. G. Rabus, U. Troppenz, "InP-based high index waveguides on GaInAsP / InP for applications in active/passive ring resonators," Invited Paper, no. 4640-63, Photonics West, San Jose, USA, January 2002.
- [3] D. G. Rabus, M. Hamacher, H. Heidrich, U. Troppenz, "Box-like filter response of triple ring resonators with integrated SOA sections based on GaInAsP / InP," in Proceed. Internat. Conf. On Indium Phosphide and Related Materials (IPRM'02), Stockholm, Sweden, 12.-16.05.2002, pp. 479-482, paper A7-5, ISBN 0-7803-7320-0.
- [4] U. Troppenz, M. Hamacher, D. G. Rabus, H. Heidrich, "All-active GaInAsP / InP ring cavities for widespread functionalities in the wavelength domain," in Proceed. Internat. Conf. On Indium Phosphide and Related Materials (IPRM'02), Stockholm, Sweden, 12.-16.05.2002, pp. 475-478, paper A7-4, ISBN 0-7803-7320-0.

### ***Filed patent applications***

- [1] H. Heidrich, D. G. Rabus, M. Hamacher, M. Hentschel, K. Richter, “Monolithisch integrierter Mikrolaser mit einem nur eine Spiegelebene aufweisenden Zirkularresonator,“ patent pending, official file number DE 101 32 479.0.
- [2] H. Heidrich, M. Hamacher, D. G. Rabus, U. Troppenz, “Verfahren zur kraftschlüssigen Ganzwaferverbindung mit Flip-Wafer-Bonding,“ patent pending, official file number DE 101 53 054.4.
- [3] D. G. Rabus, “Designregel zur Herstellung optischer Filter unter Verwendung von Ring Resonatoren,“ patent pending, official file number DE 102 19 244.8.

## Literature

- [1] International Telecommunication Union, ITU-T, G.692, October 1998.
- [2] H. Sotobayashi et al., "1.6 bit/s/Hz, 6.4 Tbit/s OCDM/WDM (4 OCDM x 40 WDM x 40 Gbit/s) transmission experiment," Proc. ECOC'01, Postdeadline Paper PD.M.1.3, pp. 6-7, October 2001.
- [3] G. Castanon et al., "Requirement of filter characteristics for 40 Gbit/s-based DWDM systems," Proc. ECOC'01, Paper Mo.F.3.5, pp. 60-61, October 2001.
- [4] D. Anderson, "Optical filters fill many roles," WDM Solutions, pp. 97-99, June 2001.
- [5] S. Kempainen, "Optical networking lightens carrier-backbone burden," EDN, [www.ednmag.com](http://www.ednmag.com), vol. 8, pp. 63-72, October 1998.
- [6] E. Pawlowski et al., "Fabrication of a multichannel Wavelength-division multiplexing-passive optical net demultiplexer with arrayed-waveguide gratings and diffractive optical elements," Appl. Optics, vol. 38, no. 14, pp. 3039-3045, 1999.
- [7] D. Heard, "Tunable Filter Technology Improves Fibre Optics and DWDMs," Europhotonics, pp. 44-45, June/July 2000.
- [8] E. A. J. Marcatili, "Bends in Optical Dielectric Guides," Bell Syst. Techn. J., vol. 48, pp. 2103-2132, 1969.
- [9] E. A. J. Marcatili, "Dielectric Rectangular Waveguide and Directional Coupler for Integrated Optics," Bell Syst. Techn. J., vol. 48, pp. 2071-2101, 1969.
- [10] C. K. Madsen and J. H. Zhao, "A General Planar Waveguide Autoregressive Optical Filter," IEEE J. Lightwave Technol., vol. 14, no. 3, pp. 437-447, March 1996.
- [11] W. Weiershausen and R. Zengerle, "Photonic highway switches based on ring resonators used as frequency-selective components," Appl. Opt., vol. 35, no. 30, pp. 5967-5978, October 1996.
- [12] S. C. Hagness et al., "FDTD Microcavity Simulations: Design and Experimental Realization of Waveguide-Coupled Single-Mode Ring and Whispering-Gallery-Mode Disk Resonators," IEEE J. Lightwave Technol. vol. 15, no. 11, pp. 2154-2165, November 1997.
- [13] D. Rafizadeh et al., "Waveguide-coupled AlGaAs/GaAs microcavity ring and disk resonators with high finesse and 21.6 nm free spectral range," Opt. Lett., vol. 22, no.16, pp. 1244-1246, August 1997.
- [14] B. E. Little et al., "Ultra-Compact Si-SiO<sub>2</sub> Microring Resonator Optical Channel Dropping Filters," IEEE Photon. Technol. Lett., vol. 10, no. 4, pp. 549-551, April 1998.

- [15] D. J. W. Klunder et al., "Vertically and laterally waveguide-coupled cylindrical microresonators in  $\text{Si}_3\text{N}_4$  on  $\text{SiO}_2$  technology," Appl. Phys. B 73, pp. 603-608, November 2001.
- [16] B. Vanderhaegen et al., "High Q InGaAsP ring resonator filters," ECIO'99, Torino, Italy, pp. 381-384, April 1999.
- [17] M. K. Chin et al., "GaAs Microcavity Channel-Dropping Filter Based on a Race-Track Resonator," IEEE Photon. Technol. Lett., vol. 11, no. 12, pp. 1620-1622, December 1999.
- [18] R. van Roijen et al., "Compact InP-based ring lasers employing multimode interference couplers and combiners," Appl. Phys. Lett., vol. 64, no. 14, pp. 1753-1755, April 1994.
- [19] S. Yu et al., "Mode locking in large monolithic semiconductor ring lasers," Opt. Eng., vol. 37, no. 4, pp. 1164-1168, April 1998.
- [20] G. Griffel et al., "Low-Threshold InGaAsP Ring Lasers Fabricated Using Bi-Level Dry Etching," IEEE Photon. Technol. Lett., vol. 12, no. 2, pp. 146-148, February 2000.
- [21] B. Moslehi, "Fibre-Optic Filters Employing Optical Amplifiers to Provide Design Flexibility," Electron. Lett., vol. 28, no. 3, pp. 226-228, January 1992.
- [22] Y. H. Chew et al., "An Optical Filter of Adjustable Finesse Using an Amplified Fiber Ring Resonator," IEEE J. Lightwave Technol., vol. 15, no. 2, pp. 364-370, February 1997.
- [23] G. Lenz et al., "Optical Delay Lines Based on Optical Filters," IEEE J. Quantum Electron., vol. 37, no. 4, pp. 525-532, April 2001.
- [24] C. K. Madsen et al., "Multistage dispersion compensator using ring resonators," Opt. Lett., vol. 24, no. 22, pp. 1555-1557, November 1999.
- [25] F. Horst et al., "Tunable Ring Resonator Dispersion Compensators Realized in High-Refractive-Index Contrast SiON Technology," in Proc. ECOC'2000, Post Deadline Paper, October 2000.
- [26] G. Lenz and C. K. Madsen, "General Optical All-Pass Filter Structures for Dispersion Control in WDM Systems," IEEE J. Lightwave Technol., vol. 17, no. 7, pp. 1248-1254, July 1999.
- [27] H. Heidrich et al., "Monolithischer Photonik-IC zur schmalbandigen Erzeugung optischer Signale bei Frequenzen im Millimeter-Wellenband," patent application DE 198 20 166, date of registration 29.04.1998.
- [28] B. Liu et al., "Passive microring-resonator-coupled lasers," Appl. Phys. Lett., vol. 79, no. 22, pp. 3561-3563, November 2001.



- [29] P. P. Absil et al., "Compact Microring Notch Filters," *IEEE Photon. Technol. Lett.*, vol. 12, no. 4, pp. 398-400, April 2000.
- [30] M. Kohtoku et al., "200-GHz FSR Periodic Multi/Demultiplexer with Flattened Transmission and Rejection Band by Using a Mach-Zehnder Interferometer with a Ring Resonator," *IEEE Photon. Technol. Lett.*, vol. 12, no. 9, pp. 1174-1176, September 2000.
- [31] S. T. Chu et al., "An Eight-Channel Add-Drop Filter Using Vertically Coupled Microring Resonators over a Cross Grid," *IEEE Photon. Technol. Lett.*, vol. 11, no. 6, pp. 691-693, June 1999.
- [32] B. E. Little et al., "Microring Resonator Arrays for VLSI Photonics," *IEEE Photon. Technol. Lett.*, vol. 12, no. 3, pp. 323-325, March 2000.
- [33] B. E. Little et al., "Vertically Coupled Glass Microring Resonator Channel Dropping Filters," *IEEE Photon. Technol. Lett.*, vol. 11, no. 2, pp. 215-217, February 1999.
- [34] D. V. Tishinin et al., "Vertical Resonant Couplers with Precise Coupling Efficiency Control Fabricated by Wafer Bonding," *IEEE Photon. Technol. Lett.*, vol. 11, no. 8, pp. 1003-1005, August 1999.
- [35] P. P. Absil et al., "Vertically Coupled Microring Resonators Using Polymer Wafer Bonding," *IEEE Photon. Technol. Lett.*, vol. 13, no. 1, pp. 49-51, January 2001.
- [36] R. Grover et al., "Vertically coupled GaInAsP-InP microring resonators," *Opt. Lett.*, vol. 26, no. 8, pp. 506-508, April 2001.
- [37] Y. Kokubun et al., "Polarization-independent vertically coupled microring resonator filter," *Electron. Lett.*, vol. 37, no. 2, pp. 90-92, January 2001.
- [38] K. Oda et al., "An Optical FDM Distribution Experiment Using a High Finesse Waveguide-Type Double Ring Resonator," *IEEE Photon. Technol. Lett.*, vol. 6, no. 8, pp. 1031-1034, August 1994.
- [39] M. Cai et al., "5 Gbit/s BER Performance on an All Fiber-Optic Add/Drop Device Based on a Taper-Resonator-Taper Structure," *IEEE Photon. Technol. Lett.*, vol. 12, no. 9, pp. 1177-1179, September 2000.
- [40] S. Bigo et al., "10.2 Tbit/s (256x42.7 Gbit/s PDM/WDM) transmission over 100 km TeraLight™ fiber with 1.28bit/s/Hz spectral efficiency," *Proc. OFC'01*, Postdeadline paper PD 25-1, March 2001.
- [41] R. W. Boyd and J. E. Heebner, "Sensitive disk resonator photonic biosensor," *Appl. Opt.*, vol. 40, no. 31, pp. 5742-5747, November 2001.

- [42] Y. Ma et al., "InGaAsP Thin-Film Microdisk Resonators Fabricated by Polymer Wafer Bonding for Wavelength Add-Drop Filters," *IEEE Photon. Technol. Lett.*, vol. 12, no. 11, pp. 1495-1497, November 2000.
- [43] B. E. Little et al., "Wavelength Switching and Routing Using Absorption and Resonance," *IEEE Photon. Technol. Lett.*, vol. 10, no. 6, pp. 816-818, June 1998.
- [44] V. Van et al., "All-Optical Nonlinear Switching in GaAs-AlGaAs Microring Resonators," *IEEE Photon. Technol. Lett.*, vol. 14, no. 1, pp. 74-76, January 2002.
- [45] P. P. Absil et al., "Wavelength conversion in GaAs micro-ring resonators," *Opt. Lett.*, vol. 25, no. 8, pp. 554-556, April 2000.
- [46] G. Allen et al., "All Optical Millimeter-Wave Electrical Signal Generation Using an Integrated Mode-Locked Semiconductor Ring Laser and Photodiode," *IEEE Photon. Technol. Lett.*, vol. 9, no. 12, pp. 1634-1636, December 1997.
- [47] C. K. Madsen and J. H. Zhao: *Optical Filter Design and Analysis*, John Wiley & Sons, Inc., ISBN 0-471-18373-3, New York, 1999.
- [48] R. Orta et al., "Synthesis of Multiple-Ring-Resonator Filters for Optical Systems," *IEEE Photon. Technol. Lett.*, vol. 7, no. 12, pp. 1447-1449, December 1995.
- [49] G. Griffel, "Synthesis of Optical Filters Using Ring Resonator Arrays," *IEEE Photon. Technol. Lett.*, vol. 12, no. 7, pp. 810-812, July 2000.
- [50] B. E. Little and S. T. Chu, "Theory of Loss and Gain Trimming of Resonator-Type Filters," *IEEE Photon. Technol. Lett.*, vol. 12, no. 6, pp. 636-638, June 2000.
- [51] B. E. Little and S. T. Chu, "Estimating surface-roughness loss and output coupling in microdisk resonators," *Opt. Lett.*, vol. 21, no. 17, pp. 1390-1392, September 1996.
- [52] J. V. Hryniewicz et al., "Higher Order Filter Response in Coupled Microring Resonators," *IEEE Photon. Technol. Lett.*, vol. 12, no. 3, pp. 320-322, March 2000.
- [53] Apollo Photonics Inc., Software OWMS and TFDS, 5-145 Columbia Street West, Waterloo, Ontario N2L3L2, Canada.
- [54] P. Urquhart, "Compound optical-fiber-based resonators," *J. Opt. Soc. Am. A*, vol. 5, no. 6, pp. 803-811, June 1988.
- [55] C. K. Madsen and J. H. Zhao, "Postfabrication optimization of an autoregressive planar waveguide lattice filter," *Appl. Opt.*, vol. 36, no. 3, pp. 642-647, January 1997.
- [56] A. Melloni, "Synthesis of a parallel-coupled ring-resonator filter," *Opt. Lett.*, vol. 26, no. 12, pp. 917-919, June 2001.
- [57] B. E. Little et al., "Filter Synthesis for periodically coupled microring resonators," *Opt. Lett.*, vol. 25, no. 5, pp. 344-346, March 2000.

- [58] B. Moslehi et al., "Fiber-Optic Lattice Signal Processing," *Proc. IEEE*, vol. 72, no. 7, pp. 909-930, July 1984.
- [59] W. Glaser, *Photonik für Ingenieure*, Verlag Technik GmbH, Berlin 1997.
- [60] K. Okamoto: *Fundamentals of Optical waveguides*, Academic Press, New York, 2000.
- [61] A. Yariv, "Universal relations for coupling of optical power between microresonators and dielectric waveguides," *Electron. Lett.*, vol. 36, no. 4, pp. 321-322, February 2000.
- [62] Y. Yanagase et al., "Box-like Filter Response by Vertically Series Coupled Microring Resonator Filter," *Proc. ECOC'01*, Paper Th.A.3.3, pp. 634-635, October 2001.
- [63] S. Suzuki et al., "Integrated-Optic Double-Ring Resonators with a Wide Free Spectral Range of 100 GHz," *IEEE J. Lightwave Technol.*, vol. 13, no. 8, pp. 1766-1771, August 1995.
- [64] M. Ferri et al., "Analysis and experiments on a GaAs/AlGaAs Double Ring Resonator Filter," *WFPOC*, June 8 - 9, Pavia, Italy, 2000.
- [65] M. Sorel et al., "Semiconductor double ring waveguide resonator," *Electron. Lett.*, vol. 35, no. 18, pp. 1551-1552, September 1999.
- [66] G. Griffel, "Vernier Effect in Asymmetrical Ring Resonator Arrays," *IEEE Photon. Technol. Lett.*, vol. 12, no. 12, pp. 1642-1644, December 2000.
- [67] F. Fiedler and A. Schlachetzki, "Optical Parameters Of InP-Based Waveguides," *Solid-State Electronics*, vol. 30, no. 1, pp. 73-83, 1987.
- [68] K. Vreeburg: *InP-based Photonic Integrated Circuits for Wavelength Routing and switching*, Dissertation TU Delft, ISBN 90-9011143-3, 1997.
- [69] K. Utaoka et al., "Lasing Characteristics of 1.5-1.6  $\mu\text{m}$  GaInAsP / InP Integrated Twin-Guide Lasers with First-Order Distributed Bragg Reflectors," *IEEE J. Quantum Electron.*, vol. QE-17, no. 5, pp. 651-658, May 1981.
- [70] Private communications, M. Gravert and C. M. Weinert, internal HHI software tool.
- [71] K. J. Ebeling: *Integrierte Optoelektronik*, Springer Verlag, Berlin, Heidelberg, New York, 1992.
- [72] L. Spiekman: *Compact Integrated Optical Components for Telecommunication Networks*, Ph.D. Thesis, Delft University of Technology, ISBN 90-9009718-X, 1996.
- [73] M. K. Chin and S. T. Ho, "Design and Modeling of Waveguide-Coupled Single-Mode Microring Resonators," *IEEE J. Lightwave Technol.*, vol. 16, no. 8, pp. 1433-1446, August 1998.
- [74] D. L. Lee: *Electromagnetic Principles of Integrated Optics*, John Wiley, New York, pp. 128-142, 1986.

- [75] D. Marcuse: Light Transmission Optics, Van Nostrand Reinhold, New York, pp. 398-406, 1972
- [76] V. Subramaniam et al., "Measurement of Mode Field Profiles and Bending and Transition Losses in Curved Optical Channel Waveguides," IEEE J. Lightwave Technol., vol. 15, no. 6, pp. 990-997, June 1997.
- [77] E. G. Neumann, "Low Loss Dielectric Optical Waveguide Bends," Fiber and Integr. Optics, vol. 4, no. 2, pp. 203-211, 1982.
- [78] Private communications, R. Kaiser and M. Hamacher, HHI.
- [79] R. Grover et al., "Process development of methane-hydrogen-argon-based deep dry etching of InP for high aspect-ratio structures with vertical facet-quality sidewalls," J. Vac. Sci. Technol., vol. 19, no. 5, pp. 1694-1698, September/October 2001.
- [80] S. J. Choi et al., "CH<sub>4</sub>-based dry etching of high Q InP microdisks," J. Vac. Sci. Technol. B, vol. 20, no. 1, pp. 301-305, January/February 2002.
- [81] Y. Gottesman et al., "Monitoring of multimode imaging devices by use of optical low-coherence reflectometers in reflection and transmission modes," Appl. Opt., vol. 39, no. 13, pp. 2140-2144, May 2000.
- [82] Y. Gottesman et al., "A Novel Design Proposal to Minimize Reflections in Deep-Ridge Multimode Interference Couplers," IEEE Photon. Technol. Lett., vol. 12, no. 12, pp. 1662-1664, December 2000.
- [83] A. Küng et al., "Optical fiber ring resonator characterization by optical time-domain reflectometry," Opt. Lett. vol. 22, no. 2, pp. 90-92, January 1997.
- [84] M. Haruna et al., "Nondestructive and simple method of optical-waveguide loss measurement with optimization of end-fire coupling," Electron. Lett., vol. 28, no. 17, pp. 1612 – 1613, August 1992.
- [85] K. H. Park et al., "Nondestructive propagation loss and facet reflectance measurements of GaAs/AlGaAs strip-loaded waveguides," J. Appl. Phys., vol. 78, no. 10, pp. 6318-6320, November 1995.
- [86] L. B. Soldano and E. C. M. Pennings, "Optical Multi-Mode Interference Devices Based on Self-Imaging: Principles and Applications," IEEE J. Lightwave Technol., vol. 13, no. 4, pp. 615-627, April 1995.
- [87] C. M. Weinert and N. Agrawal, "Three-Dimensional Finite Difference Simulation of Coupling Behavior and Loss in Multimode Interference Devices," IEEE Photon. Technol. Lett., vol. 7, no. 5, pp. 529-531, May 1995.

- [88] Y. Ma et al., "Ultracompact Multimode Interference 3 dB Coupler with Strong Lateral Confinement by Deep Dry Etching," *IEEE Photon. Technol. Lett.*, vol. 12, no. 5, pp. 492-494, May 2000.
- [89] J. Leuthold and C. H. Joyner, "Multimode Interference Couplers with Tuneable Splitting Ratios," *Proc. ECOC'2000, Munich, Germany*, vol. 3, pp. 177-178, September 2000.
- [90] S. Tedjini, "All-Optical Networks as Microwave and Millimeter-Wave Circuits," *IEEE Transactions on Microwave Theory and Techniques*, vol. 43, no. 9, September 1995.
- [91] M. Hamacher et al., "Monolithic Integration of Lasers, Photodiodes, Waveguides and Spot Size Converters on GaInAsP / InP for Photonic IC Applications," in *Proceed. Internat. Conf. On Indium Phosphide and Related Materials (IPRM' 2000)*, Williamsburg, USA, Paper MA1.3, pp. 21-24, May 2000.
- [92] H. Heidrich et al., "Analysis of optical crosstalk within optoelectronic integrated circuits including lasers and photodetectors," *Appl. Phys. B*, vol. 73, pp. 581-583, October 2001.
- [93] Private communications, W. Rehbein, HHI.
- [94] F. Pommereau et al., "Optimization of Butt Coupling between Deep-Ridge and Buried Ridge Waveguides for the Realization of Monolithically Integrated Wavelength Selectors," *IPRM'99, Davos, Switzerland*, Paper WeA1-7, pp. 401-404, May 1999.
- [95] K. Kalli and D. A. Jackson, "Analysis of the dynamic response of a ring resonator to a time-varying input signal," *Opt. Lett.*, vol. 18, no. 6, pp. 465-467, March 1993.
- [96] K. Djordjev et al., "Active Semiconductor Microdisk Devices," *IEEE J. Lightwave Technol.*, vol. 20, no. 1, pp. 105-113, January 2002.
- [97] K. Djordjev et al., "High-Q Vertically Coupled InP Microdisk Resonators," *IEEE Photon. Technol. Lett.*, vol. 14, no. 3, pp. 331-333, March 2002.



## Index

- active – passive transition ..... 92, 102
- add/drop filter ..... 11
- arrayed waveguide grating..... 5
- atomic force microscope..... 69
- autoregressive ..... 3, 7
  - autoregressive filter ..... 19
  - autoregressive moving average filter.. 19
- butt joint..... 100
- chemical vapor deposition ..... 95
- conformal mapping ..... 49
- coupler ..... 65
  - codirectional coupler ..... 71
  - critical coupling ..... 23
  - multimode – interference – coupler.... 65
- cut-back-method ..... 62
- dispersion..... 9, 43
  - chromatic dispersion ..... 9, 43
  - dispersion compensation..... 9
  - material dispersion..... 43
  - negative dispersion ..... 9
  - positive dispersion ..... 9
- double ring resonator ..... 31
- effective index method ..... 49
- external cavity laser ..... 59
- Fabry-Perot interferometer ..... 4
- Fabry-Perot Resonator..... 62
- fiber Bragg grating..... 4
- fiber optic ring resonator ..... 7
- fiber-optic recirculating delay lines..... 8
- finesse ..... 22, 24
- Finite impulse response ..... 3
  - FIR ..... 3
- free spectral range..... 25
  - FSR ..... 25
- full-width at half-maximum..... 22
  - FWHM..... 22, 25
- group refractive index..... 44
- Infinite impulse response..... 3
  - IIR ..... 3
- interleaver ..... 13
- intrinsic losses..... 61
- ITU..... 7, 9, 2, 87
- Levinson algorithm..... 19
- lock-in amplifier ..... 59
- Mach-Zehnder interferometer..... 5, 11
- mesa ..... 95
  - support mesa ..... 93
- metal organic vapor phase epitaxy ..... 95
- moving average ..... 3
  - feed-forward..... 3
  - MA ..... 3
- notch filter ..... 11
- on-off ratio ..... 2, 8, 23, 29
- optical delay line ..... 9
- optical filters ..... 6
- optical frequency division multiplexing . 12
  - FDM..... 12
- optical low coherence reflectometry ..... 60
  - OLCR..... 84
- overlap..... 51, 66
- photo diode..... 10
  - PD..... 10
- photolithography ..... 54
- plane grating..... 3
- Plasma enhanced chemical vapor
  - deposition..... 53
- polarization division multiplexing ..... 12
  - PDM..... 12
- polarization mode dispersion ..... 43
- Pt-resistor ..... 77, 87
- Q* factor ..... 26
- quantum well..... 92
- reactive ion etching ..... 54
- reflection factor ..... 63
- resonance matching..... 87
- response time..... 119
- SAMOVPE..... 95
- semiconductor optical amplifier..... 91
- shape factor ..... 33
- single ring resonator..... 7
- TDM..... 1
- Thin film dielectric interference filter..... 5
- transparency current ..... 103
  - transparency current density ..... 103
- triple ring resonator..... 36, 115
  - parallel coupled triple ring resonator .. 38
- Vegard's law ..... 41
- Vernier effect ..... 40
- vertical coupling..... 12
- Wavelength stabilization..... 10
- WDM ..... 1, 3
- z - transform..... 17

## **Curriculum vitae**

**Name:** Dominik Gerhard Rabus

**Date of birth:** 21.07.1973 in Stuttgart, Germany

**Email:** dominik@rabusfamily.com

### **Professional experience**

Since 10/1999

PhD candidate at the Heinrich-Hertz-Institut für Nachrichtentechnik Berlin GmbH

10/1998 - 04/1999

Robert Bosch GmbH, Gerlingen-Schillerhöhe, Corporate Research and Development,  
Thin Films and Microsystems Technology: internship and assignment

06/1996 - 01/1998

Fraunhofer Institute Manufacturing Engineering and Automation, Stuttgart,  
Robot Systems: scientific employee

07/1994 - 09/1994

Robert Bosch GmbH, Leinfelden, business division power tools: internship

### **Education**

10/1994 – 9/1999

University of Stuttgart, Electrical Engineering and Information Technology,  
degree: Diplom Ingenieur (Dipl.-Ing.)

07/1993 - 06/1994

Navy: Frigate Bremen, specialization: ship's command and navigation

09/1988 - 06/1993

Hegel-Gymnasium, Stuttgart, major courses: mathematics and chemistry,  
degree: Abitur

03/1984 - 09/1988

Bangalore International School, Bangalore, India

08/1980 – 03/1984

Primary school, Pestalozzischule, Stuttgart

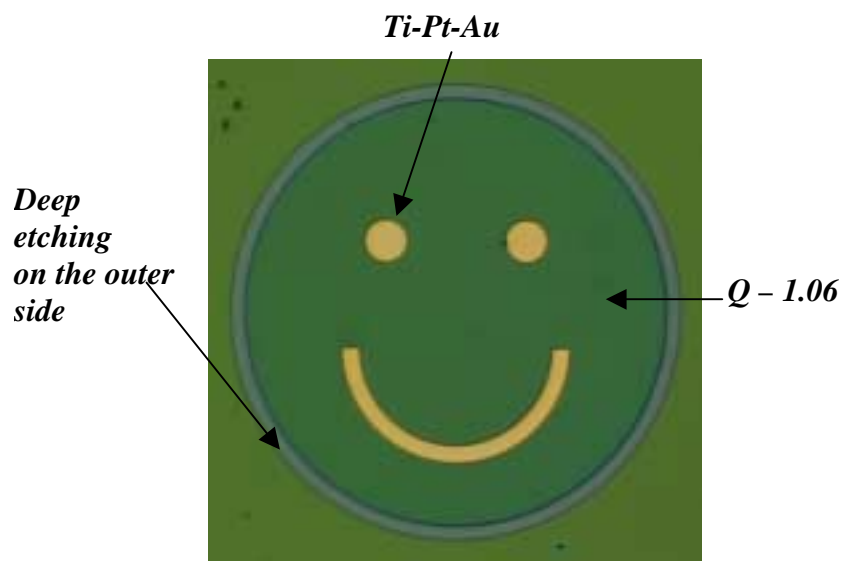
### **Extracurricular activities**

- Reviewer for IEEE - LEOS and IEE proceedings publications
- Exceptional reward “power engineering” at the 28. Landeswettbewerb of  
“Jugend forscht“, 1993
- 1. Environmental reward "Umweltwettbewerb der Terratec", 1993
- 1. Environmental reward of the city of Stuttgart, 1992



*This work was performed at the  
Heinrich – Hertz – Institut für Nachrichtentechnik Berlin GmbH*

*Also known as*



*The End*